Design and Preparation of Gelatin-Based Carriers for Imaging Probes to Visualize Cell Functions

Yuki Murata

2021

CONTENTS

PART I. DEVELOPMENT OF IMAGING PROBES AND CELLULAR DELIVERY CARRIERS TO VISUALIZE CELL FUNCTIONS

Chapter 1. Preparation of gelatin nanospheres incorporating quantum dots and iron oxide nanoparticles for multimodal cell imaging

Chapter 2. Preparation of cationized gelatin-molecular beacon complexes to visualize intracellular mRNA

Chapter 3. Preparation of cationized gelatin-molecular beacon complexes and cationized gelatin nanospheres incorporating molecular beacon for intracellular controlled release

Chapter 4. Preparation of cationized gelatin nanospheres incorporating molecular beacon to visualize cell proliferation ability

Chapter 5. Preparation of cationized gelatin nanospheres incorporating molecular beacon to visualize cell apoptosis

PART II. APPLICATION OF GELATIN-BASED CARRIERS FOR IMAGING PROBES TO MULTI-COLOR IMAGING AND THREE-DIMENSIONAL CELLS FABRICATE

Chapter 6. Preparation of cationized gelatin nanospheres incorporating molecular beacon to visualize energy metabolic pathways between undifferentiated and differentiated mouse embryonic stem cells

Chapter 7. Preparation of gelatin nanospheres incorporating quantum dots and iron oxide nanoparticles to visualize human induced pluripotent stem cells-derived three-dimensional cartilage tissue

Chapter 8. Preparation of cationized gelatin nanospheres incorporating molecular beacon to visualize apoptosis in three-dimensional cell aggregates

ABBREVIATIONS

2D	Two-dimensional
2-DG	2-deoxy-D-glucose
3D	Three-dimensional
6-FAM	6-carboxyfluorescein
Actb	β-actin
Act D	Actinomycin D
AFP	α-fetoprotein
ANOVA	Analysis of variance
α-SMA	α-smooth muscle actin
ATP	Adenosine 5’-triphosphate
Bax	Bcl-2-associated X protein
BCA	Bicinchonic acid
bFGF	Basic fibroblast growth factor
$\text{BHQ}^{\circledR}$	Black hole quencher
BMP-2	Bone morphogenic protein-2
CAR T cells	Chimeric antigen receptor T cells
CDK	Cyclin dependent kinases
cDNA	Complementary DNA
cGNS	Cationized gelatin nanospheres
cGNS_{MB}	cGNS incorporating MB
$\text{cGNS}_{\text{Actb MB}}$	cGNS incorporating Actb MB
$\text{cGNS}_{\text{casp3 MB}}$	cGNS incorporating caspase-3 MB
$\text{cGNS}_{\text{GAP MB}}$	cGNS incorporating GAPDH MB
$\text{cGNS}_{\text{Ki67 MB}}$	cGNS incorporating Ki67 MB
$\text{cGNS}_{\text{PDK1 MB}}$	cGNS incorporating PDK1 MB
$\text{cGNS}_{\text{PGC-1}\alpha\text{ MB}}$	cGNS incorporating PGC-1α MB
$\text{cGNS}_{\text{dual MB}}$	cGNS co-incorporating caspase-3 and GAPDH MB
$\text{cGNS}_{\text{multi MB}}$	cGNS co-incorporating PDK1, PGC-1α, and Actb MB
CPP	Cell-penetrating peptides
CPZ	Chlorpromazine
CRISPR/Cas9	Clustered regularly interspaced short palindromic repeats /CRISPR associated protein 9
CSC	Cancer stem cells
CT	Computed tomography
Cyto D	Cytochalasin D
DAB	3,3’-diaminobenzidine
DAPI	4’,6-diamidino-2-phenylindole

DCA	Dichloroacetate
DDS	Drug delivery system
DDW	Double-distilled water
DLS	Dynamic light scattering
DMEM	Dulbecco's Modified Eagle Medium
DNA	Deoxyribonucleic acid
EB	Embryoid body
ECAR	Extracellular acidification rate
ECM	Extracellular matrix
EDC	1-ethyl-3-(3-dimethylaminopropyl) carbodiimide hydrochloride salt
EDTA	Ethylenediaminetetra acetic acid
EGFP	Enhanced green fluorescent protein
ELS	Electrophoresis light scattering
ES cells	Embryonic stem cells
ETC	Electron transport chain
FACS	Fluorescence activated cell sorting
Fas Ab	Anti-Fas antibody
FCCP	Carbonyl cyanide-4-(trifluoromethoxy)phenylhydrazone
FCS	Fetal calf serum
FITC	Fluorescein isothiocyanate
FRET	Fluorescence resonance energy transfer
GA	Glutaraldehyde
GAPDH	Glyceraldehyde-3-phosphate dehydrogenase
GDF-5	Growth differentiation factor-5
GFP	Green fluorescent protein
Glut1	Glucose transporter 1
GMEM	Glasgow's Minimum Essential Medium
GNS	Gelatin nanospheres
$\mathrm{GNS_{IONP}}$	GNS incorporating IONP
$\mathrm{GNS_{QD}}$	GNS incorporating QD
$\mathrm{GNS_{QD+IONP}}$	GNS incorporating QD and IONP
$\mathrm{GNS_{3QD+IONP}}$	GNS co-incorporating three kinds of QD and IONP
HE	Hematoxylin and eosin
HK2	Hexokinase 2
Hoechst 33258	Bisbenzimide H33258 fluorochrome trihydrochloride
HVJ-E	Hemagglutinating Virus of Japan-envelope
IBFQ	Iowa Black®FQ
IBRQ	Iowa Black®RQ
IgG	Immunoglobulin G

IgM	Immunoglobulin M
IMDM	Iscove's Modified Dulbecco's Medium
IONP	Iron oxide nanoparticles
iPS cells	Induced pluripotent stem cells
ITS-X	Insulin, transferrin, selenium, and ethanolamine solution
JNK	c-Jun N-terminal kinase
KSR	Knockout serum replacement
LIF	Leukemia inhibitory factor
LNA	Locked nucleic acids
MB	Molecular beacons
MCM	Minichromosme maintenance proteins
mES cells	Mouse embryonic stem cells
miRNA	MicroRNA
MRI	Magnetic resonance imaging
mRNA	Messenger RNA
MSC	Mesenchymal stem cells
NADH	Reduced nicotinamide adenine dinucleotide
NEAA	Non-essential amino acid
NIR	Near infrared
OCR	Oxygen consumption rate
OXPHOS	Oxidative phosphorylation
PB	Phosphate buffer
PBS	Phosphate buffered-saline
PCNA	Proliferation cell nuclear antigen
PCR	Polymerase chain reaction
PDH	Pyruvate dehydrogenase
PDK1	Pyruvate dehydrogenase kinase 1
pDNA	Plasmid DNA
PEI	Poly(ethyleneimine)
PET	Positron emission tomography
PFKFB3	6-phosphofructo-2-kinase/fructose-2,6-biphosphatase 3
PGC-1α	Peroxisome proliferator-activated receptor γ, coactivator-1α
PI	Propidium iodide
PK	Pyruvate kinase
PLGA	Poly(lactic-co-glycolic acid)
PMSF	Phenylmethanesulfonyl fluoride
PNA	Protein nucleic acids
pPDH	Phosphorylated pyruvate dehydrogenase
PVA	Poly(vinyl alcohol)

PVDF	Poly(vinyliden difluoride)
QD	Quantum dots
qPCR	Quantitative real-time polymerase chain reaction
R8	Octa-arginine
RIPA buffer	Radioimmunoprecipitation buffer
RNA	Ribonucleic acid
SD	Standard deviation
SDS	Sodium lauryl sulfate
SDS-PAGE	Sodium lauryl sulfate-poly(acrylamide) gel electrophoresis
siRNA	Small interfering RNA
SLO	Streptolysin O
smFISH	Single molecule fluorescence *in situ* hybridization
Span 80	Sorbitan monooleate
SPECT	Single photon emission computed tomography
SSC buffer	Saline-sodium citrate buffer
T_2	Transverse relaxation time
TAT peptide	transactivator of transcription peptide
Tbp	TATA-box binding protein
TBST	Tris buffered-saline with Tween 20
TdT	Terminal deoxynucleotidyl transferase
TE	Echo time
TGF-β1	Transforming growth factor-β1
TGF-β3	Transforming growth factor-β3
TNBS	2,4,6-trinitrobenzene sulfonic acid
TR	Repetition time
Tubb III	βIII tubulin
TUNEL	TdT-mediated dUTP nick-end labeling
Tween 80	Poly(oxyethylene) sorbitan monooleate
WST-8	2-(2-methoxy-4-nitrophenyl)-3-(4-nitrophenyl)-5-(2,4-disulfophenyl)-2H-tetrazolium

GENERAL INTRODUCTION

With the rapid progress of basic biology and cell research, technologies and methodologies to enhance cell abilities have been widely developed. The advances of genetic engineering and genome editing enabled the artificial control of cell ability. For example, induced pluripotent stem (iPS) cells with high abilities for self-renewal and differentiation have been generated from the adult fibroblasts by genetically introducing the reprogramming factors [1, 2]. Recently, the chimeric antigen receptor (CAR) T cell therapy has been approved against leukemia and lymphoma [3]. The genetically engineered CAR T cells showed a high therapeutic ability against CD19 positive B cell malignances, while the further improvement of CAR T cells by the genome editing, including clustered regularly interspaced short palindromic repeats/CRISPR associated protein 9 (CRISPR/Cas9) system, is being conducted for the therapy universalization and enhancement of anti-tumor ability [4-7]. On the other hand, recent technologies of cell culture and tissue engineering allow cells to maintain the ability both *in vitro* and even *in vivo*, offering an appropriate environment for the exertion of their biological functions, (*i.e.* cell functions), such as survival, proliferation, and differentiation. Based on the cells with high potential and technologies to regulate the cell environments, various applications, including organoid research [8-11], drug discovery [12-16], cancer immunotherapy [17-20], and cell transplantation therapy [21-25], have been extensively studied to make full use of cell functions. For the support and further development of these research fields, it is indispensable to evaluate the cell functions.

Since the cell functions are regulated by the gene and its transcribed messenger RNA (mRNA), and the consequent translated protein, biochemical techniques have been widely applied to assess the cell functions. These techniques like polymerase chain reaction (PCR) and western blotting, have been conventionally used as the reliable methods to evaluate the expression of mRNA and protein. However, the biochemical techniques often require the cell destruction, resulting in the total information in cell population. It is also theoretically difficult to continuously evaluate the time course of cell function change for the same cell. On the other hand, the genetic engineering with reporter genes and its proteins, *e.g.* green fluorescent protein

(GFP), is another method to evaluate the cell functions. The reporter genes can be genetically fused with target genes to express the fused fluorescent proteins, which enable the continuous trace of cell functions at a genetic level. Various fluorescent proteins covering the wide range of fluorescent wavelength have been developed [26]. The combination with two fluorescent proteins based on the fluorescence resonance energy transfer (FRET) makes it possible to emit the specific fluorescence in response to bioactive small molecules [27-31], lipids in cell membrane [32], membrane charges [33], guanosine triphosphate-binding proteins [34-36], and various enzymatic activities [37-40]. The genetic engineering system has been widely recognized as a powerful tool, while there are several limitations in some cases. In general, the construction of plasmid DNA (pDNA) requires multi-complicated steps, and it is sometimes difficult to establish the cell line stably expressing the FRET proteins due to the low transfection efficiency and the gene recombination between fluorescent proteins. In addition, some fluorescent proteins have tendency to form dimers and oligomers, leading to the inaccurate FRET signal and the negative effect on host proteins [41-44]. The (over)expression of fused protein has possibility to disturb the physiological condition and the consequent cell function. Under these circumstances, it is of prime importance to develop technologies and methodologies to evaluate the cell functions without the cell destruction and the disturbance of original cell functions.

Molecular imaging is one of feasible approaches to visualize cell functions in individual living cells. The definition of molecular imaging is to spatio-temporally visualize the biological processes and phenomena at a molecular level in the living cells, tissues, and bodies. It is well recognized that the field of molecular imaging is quite interdisciplinary [45-47]. Imaging probes are designed and synthesized by the technologies of organic and material chemistry. After the probe delivery, the signals from probes are detected by imaging instruments. Finally, the detected signal is visualized and analyzed based on the informatics and mathematics. Since the imaging efficacy highly depends on the signal detection, it is necessary to efficiently deliver the imaging probes to the target molecules in the cells. The technologies and methodologies of drug delivery system (DDS) are practically applicable to the spatio-temporal regulation of probe concentration. It is highly conceivable to enhance the efficacy of cell function imaging by the combination of carrier materials with imaging probes. Therefore, both the development of imaging probes and cellular delivery carriers are essential keys to succeed in the cell function imaging in terms of material sciences.

For the imaging probes, it seems that the development of multimodal and activatable probes composed of two strategies. So far, various imaging modalities have been utilized, including positron emission tomography (PET) [48-50], single photon emission computed tomography (SPECT) [51-53], computed tomography (CT) [54-56], ultrasound [57-59] and photoacoustic imaging [60-63], optical imaging (bioluminescence [64-66], fluorescence [67-69], and phosphorescence [70-72]), and magnetic resonance imaging (MRI) [73-75]. It is well recognized that each imaging modality has advantages and disadvantages from the viewpoint of sensitivity, spatial and temporal resolutions, and tissue penetration in visualization [47, 76]. For example, the fluorescent imaging has a high sensitivity and a wide range of signal change to be visualized. However, considering the *in vivo* applications, the fluorescent imaging has some limitations on the penetration into the deep sites of tissues and bodies due to the absorption and scattering of light, as well as the autofluorescence [77]. In this circumstance, fluorescent dyes that absorb excitation light and emit fluorescence in the wavelength over the near infrared (NIR) region, so-called "biological optical window" (about 700-1000 nm; NIR I and 1000-1700 nm; NIR II), have been developed [78-80]. In addition, quantum dots (QD) of fluorescent nano-materials with intense fluorescence sufficiently detected *in vivo*, have been reported to be useful in many animal studies [81-85]. On the other hand, MRI has a high spatial resolution and theoretically no limitation on the penetration depth of visualization. The localization and distribution of cells transplanted *in vivo* have been successfully visualized following the cell labeling with the contrast agents, such as gadolinium [86], manganese [87], fluorine-19 [88], and iron oxide nanoparticles (IONP) [89-91], while the sensitivity has room to be improved. Considering the advantages and disadvantages of each modality, the multimodal imaging which combines more than two imaging modalities, is expected to compensate the disadvantages and overcome the limitations, leading to an enhanced reliability and the multiple information on the visualization [92-94]. For the achievement of multimodal imaging, it is technically necessary to develop the multimodal probes which can be simultaneously detected by more than two modalities. The development of multimodal probes would be one of key strategies to expand the applications of cell function imaging.

Another key strategy is the development of activatable probes which emit the signal responding to the change of target molecules and the resulting cell functions. In order to visualize the cell functions, it is necessary to detect the target molecules, including regulatory molecules and marker molecules, such as CD molecules and receptors on the cell membrane, proteins like enzymes, microRNA (miRNA), and mRNA, which are characteristic to the cell functions. Conventionally, the fluorescent imaging has been applied to the cell function imaging due to the high sensitivity and the wide range of signal change. The fluorescent probes are classified into two types: always-on and activatable types. The always-on fluorescent probes are selectively accumulated on the target molecules to emit the specific fluorescent signal from the targets and the consequent cell functions. The conjugation with antibodies [95-99], aptamers [100-103], and ligand molecules, such as folate [104], mannose [105], chlorotoxin [106], and other peptides [107] against target molecules, can be utilized to enhance the affinity and accumulation. On the other hand, the activatable fluorescent probes have some advantages over the conventional always-on probes. The activatable probes are designed to only emit the fluorescence after the conjugation and reaction with the target molecules. Because the activatable probes are not fluorescent in itself, the background signal can be drastically reduced to sensitively detect the slight change of cell functions. In addition, it is not required to wash out the excessive probes, leading to the reduced imaging time. The availability of activatable probes is one of advantages in the fluorescent imaging over other imaging modalities [108]. A variety of activatable probes including organic fluorescent dyes and QD, which emit the fluorescent signal in response to various cell environments, such as pH, metal ions, nitric oxide, hydrogen sulfide, glutathione, reactive oxygen species, and enzymes, have been reported [109-111]. For example, an activatable probe of hydroxymethyl rhodol derivative conjugated with β-galactoside (HMRef-βGal) was designed to be fluorescent after the enzymatic reaction with β-galactosidase which highly expresses in ovarian cancer cells [112]. The intracellular β-galactosidase activity *in vitro* and the peritoneal metastasis under the size of 1 mm from ovarian cancer *in vivo*, were fluorescently visualized with the HMRef-βGal probe. However, in many cases, both the always-on and activatable fluorescent probes are required to be designed individually to give the specificity against each target molecule of cell function. It is, thus, necessary to individually optimize the physicochemical properties of probes, including the binding and dissociation constants with the targets, after the probe design. In addition, many activatable probes to detect enzymatic activities are designed against the cleavage enzymes, such as matrix metalloproteinases [113-115], cathepsins [116-119], and caspases [120-122], which might limit the versatility of visualization. In this circumstance, the development of versatile activatable probes is expected to be explored for the sensitive and versatile system to visualize various cell functions.

Molecular beacons (MB) are known to be an activatable imaging probe to specifically detect nucleic acid molecules, such as mRNA and miRNA. MB are stem-loop structured nucleic acid derivatives composed of DNA bases. The fluorescent molecule and the corresponding quencher are conjugated at both the 5' and 3' ends of MB to be a quenched state based on the FRET mechanism. On the other hand, in the presence of target nucleic acids, the specific hybridization via the hydrogen bonds of bases between the MB loop and the target sequences causes the drastic structural change to emit the fluorescence (**Figure 1A**). The MB was originally reported as a PCR probe by Tyagi *et al* in 1996 [123] and 1998 [124], and many types of

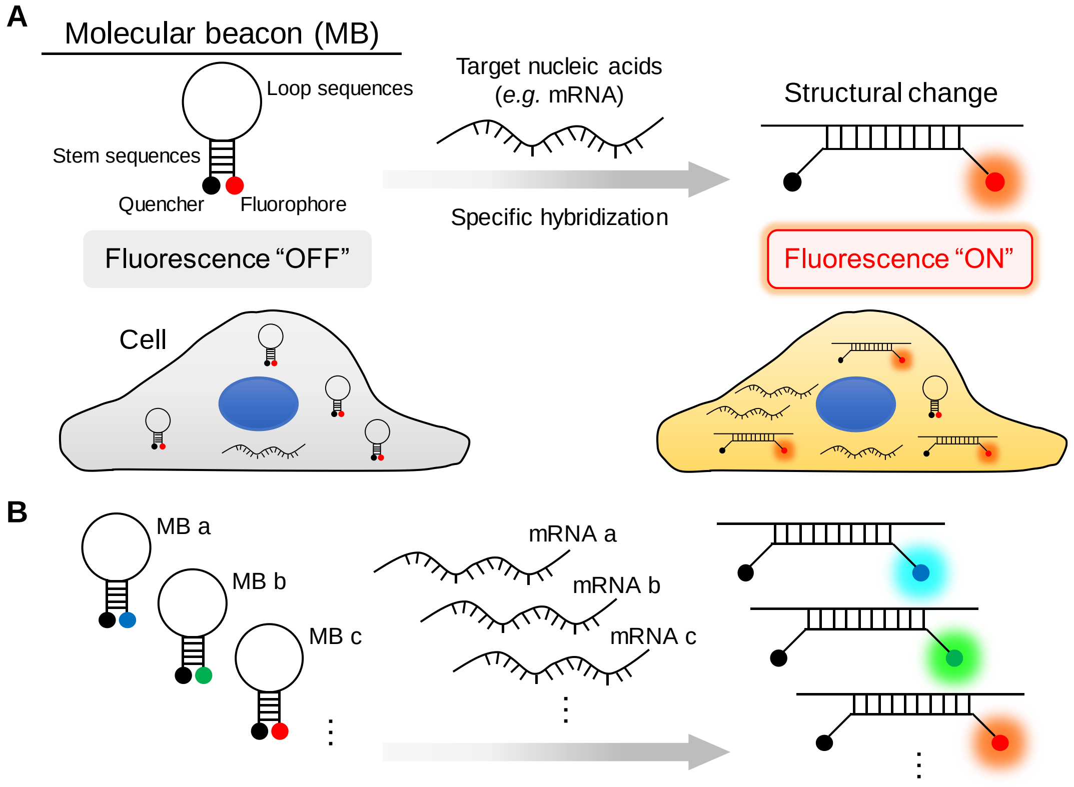

Figure 1. Fluorescent detection of target nucleic acids based on MB. (A) Fluorescent emission of MB via the specific hybridization with target nucleic acids. (B) Theoretically every mRNA can be detected by designing the sequences of MB in a versatile system.

MB, such as the modification with 2'-O-methylated RNA [125-127], phosphorothioate bonds [128, 129], morpholino [130], locked nucleic acids (LNA) [131-133], and peptide nucleic acids (PNA) [134, 135], and the combination with two MB (dual FRET MB) [136-138], have been reported in the research fields of nucleic acid chemistry, as well as the use in living cells following the intracellular delivery. One of major advantages of MB is the versatility. Simply designing the MB sequences based on the thermodynamic parameters like melting temperature [139-141], the MB can be designed against theoretically every mRNA which regulates various cell functions via its expression and the consequent protein synthesis. Therefore, as one trial, the utilization of MB would be promising to visualize the cell functions in a versatile system by detecting the intracellular mRNA and other nucleic acid molecules.

Since the MB are hardly internalized into cells because of the electrostatic repulsion force between the MB and cell membrane both with negative charges, it is technically necessary to deliver MB into cells. Physical methods used as gene transfection techniques, such as microinjection [142-144] and electroporation [145-147], have been widely applied to the MB delivery. However, these techniques require specialized instruments, and the internalization efficiency and cell viability are sometimes low. In some cases, the amount of MB internalized into each cell is variable, which might not be suitable for the imaging at a single cell level. In addition to the physical methods, streptolysin O (SLO) of a bacterial toxin has been utilized as well [148-150]. The SLO method reversibly permeabilizes the cell membrane via the binding with cholesterol and the subsequent formation of pores (about 25-30 nm). The limitation of SLO is that the internalization efficiency depends on the cell type because of the different compositions of cholesterol in the cell membrane, leading to the requirement for multiple optimizations. Moreover, cell-penetrating peptides (CPP), for example transactivator of transcription (TAT) peptide, have been chemically conjugated with MB to enhance the cell internalization [151-154]. On the other hand, various carrier materials of MB including transfection reagents, such as gold nanoparticles [155-159], dendrimers [160-162], cationized liposomes [163-167], and cationized polymers [168-172], have been reported so far. However, in many studies, the properties of carrier materials-MB complexes, such as cytotoxicity, cell internalization, and detection efficiency of MB fluorescence, have not been always investigated well although these properties are quite important in the materials design.

Gelatin is a biodegradable polymer, and has been extensively utilized for food, pharmaceutical, and medical purposes. The bio-safety and biocompatibility have been proven through their long-term history of practical applications as the biomaterial and drug ingredient. Gelatin is crosslinked to form hydrogels with varied shapes, such as sheets [173-175], sponges [176-178], nonwovens [179], microspheres [180, 181], and nanospheres [182-185], and many types of agents, including low-molecular weight drugs [186-190], peptides [191, 192], proteins like growth factors [193-195], platelet-rich plasma [196, 197], and imaging probes [198-200], can be incorporated into the hydrogel matrices. Various mechanisms have been reported to be involved in the incorporation of agents: physical entrapment, covalent conjugation, electrostatic, hydrophilic, and hydrophobic interactions, and hydrogen bonding [183-185]. The incorporation ability of gelatin hydrogels is advantageous for the design of multimodal probes which requires the incorporation of multiple imaging probes. As the carrier design for imaging probes, the gelatin nanospheres (GNS) are one of attractive candidates due to the high susceptibility to cell internalization in both non-phagocytic [201] and phagocytic cells [202]. In addition to the inherent nature of gelatin, it has been well recognized that the nano-sized particles are easily internalized into cells via an endocytotic pathway [203-206]. Therefore, the GNS would be internalized into cells by the simple incubation, and allow cells to label with imaging probes incorporated in the GNS. Moreover, a variety of surface modifications of GNS have been reported to be available, including folate, ligand peptides for epidermal growth factor receptor, poly(ethylene glycol), antibodies, carbohydrates like mannose and 4-sulfated N-acetyl galactosamine, heparin, fatty acids, and CPP like TAT peptide and octa-arginine (R8) [183-185]. These modifications would be practical methods to regulate the cell internalization of GNS.

Other advantages of gelatin are the availability of different physicochemical properties (isoelectric point and molecular weight), and the easiness of chemical modification due to the presence of functional groups (hydroxyl, amino, and carboxyl groups). Cationized gelatin can be readily prepared by introducing amino compounds to the carboxyl groups of gelatin [207-209]. Cationized gelatin enables to form a complex with nucleic acid molecules, such as pDNA [210] and small interfering RNA (siRNA) [211], with the nano-size and positive surface charge suitable for cell internalization and the subsequent gene expression or suppression. The previous study has demonstrated that, among the amino compounds (ethylenediamine, putrescine, spermidine, and spermine) introduced to gelatin, the introduction of spermine showed the highest transfection efficiency *in vitro* [210]. In agreement with the cationized gelatin, the highest gene expression was similarly observed in the spermine-introduced cationized dextran [212]. This is due to the pH buffering capacity of secondary amino groups in spermine, which leads to the acceleration of endosomal escape, so-called "proton sponge effect" although the mechanism is not always clarified well [213]. However, recent technologies of super-resolution microscopy have enabled the direct observation for sequential processes of endosomal escape: osmotic swelling and rupture of endosomes, release of polyion complex of siRNA and cationic polymer into the cytosol, and dissociation of siRNA and polymer in the cytosol [214]. The endosomal escape is advantageous for the carrier of MB because the mRNA of a MB target molecule exists in the cytosol. In other words, the active site of MB is in the cytosol. Based on the findings, it is highly expected that the spermine-introduced cationized gelatin is an effective as the carrier material of MB to deliver into cells, while the preparation condition needs optimization.

One of major problems of MB imaging to be solved is the short remaining time in the cells after the cell internalization and the consequent temporal fluorescent activity. Due to the reason, at present, many studies are limited to detect the MB fluorescence within 1 week. It has been demonstrated that the intracellular signal of MB diminished by the fourth day after transfection with a cationized polymer-based transfection reagent [215]. In addition, the naked MB following the SLO transfection led to more than 50% decrease of MB signal 3 days later [216]. On the other hand, in general, the cell functions change from time to time in the order from day to week. For example, mesenchymal stem cells (MSC) have an ability for differentiation into osteogenic, adipogenic, and chondrogenic lineages [217]. In these differentiation cultures, it is well recognized that the expression patterns of differentiation markers and the maturation states depend on the time period of differentiation cultures from 1 to 4 weeks [218-220]. Therefore, it is important to develop the technology to prolong the intracellular activity of MB for the continuous and long-term visualization of cell functions. As one trial to tackle this issue, the intracellular controlled release of MB is a feasible approach. The gelatin hydrogels can achieve the controlled release of various drugs, including pDNA and siRNA, to prolong its biological activities [211, 221-230]. As the release mechanism, it is highly possible that the molecules incorporated are released from the gelatin hydrogel together with the fragment of gelatin degraded as a result of enzymatic hydrogel degradation. Thus, the release profile can be readily regulated by the degradability of gelatin hydrogel. The concept can be expanded to the intracellular controlled release of nucleic acid molecules from the gelatin hydrogel nanospheres. Previous studies have demonstrated that the cationized GNS (cGNS) can achieve the intracellular controlled release of pDNA [231] and siRNA [232] following the cell internalization, and the biological activity of nucleic acids can be prolonged according to the degradability of cGNS. In addition, several researches have demonstrated that the intracellular controlled release of MB from the biodegradable poly(lactic-co-glycolic acid) (PLGA) nanoparticles continuously visualized the intracellular mRNA [233, 234]. Based on the findings, the intracellular controlled release of MB from the cGNS is expected to be feasible to chronologically visualize the time-course change of various cell functions for a long time period (**Figure 2**).

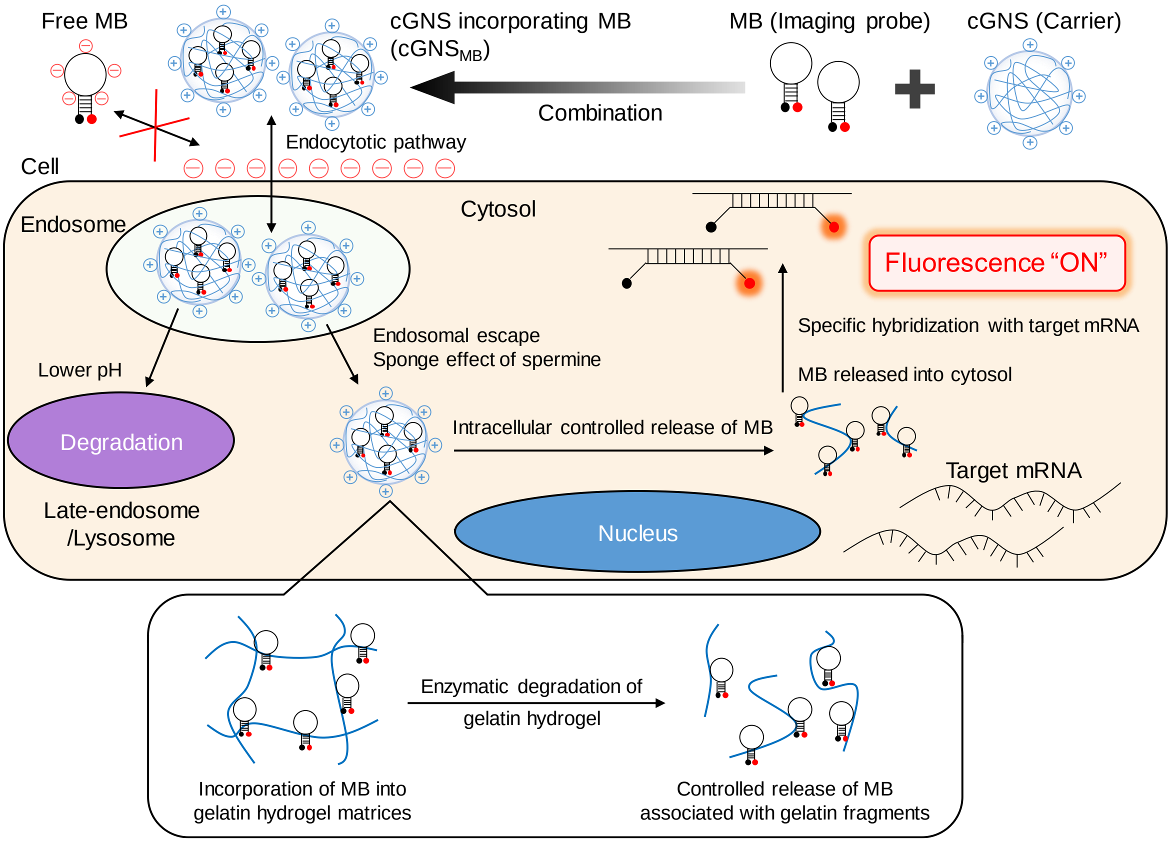

Figure 2. Schematic illustration of intracellular controlled release of MB from cGNS.

When cell functions are synergistically regulated by multiple biological processes, the ideal imaging system is to visualize multiple target molecules simultaneously. For example, the cell metabolism is a highly interactive cell function due to the many contributions of multiple metabolic pathways. Among them, the glycolysis and the oxidative phosphorylation (OXPHOS) are the main pathways of energy production. In stem cells including pluripotent and somatic stem cells, undifferentiated cells heavily rely the glycolysis for the fast production of adenosine 5'-triphosphate (ATP), and the nucleotides synthesis by the pentose phosphate pathway shunted from the glycolysis is enhanced to meet the requirements for rapid proliferation and self-renewal. On the other hand, the OXPHOS which produces ATP more efficiently than the glycolysis, is a main pathway in differentiated cells [235-238]. It has been demonstrated that the decrease of glycolysis and the opposite increase of OXPHOS are synergistically observed over the differentiation of stem cells [239-241]. Therefore, it is quite important to simultaneously detect target molecules corresponding to the glycolysis and OXPHOS to comprehensively visualize the energy metabolic pathways. Since the MB with different sequences and pairs of fluorophore and quencher can be designed, multiple MB to detect various mRNA with different colors can be synthesized. In addition, the cGNS can incorporate multiple types of MB simultaneously. Taken together, the multi-color imaging of cell functions will be achieved by utilizing cGNS incorporating multiple types of MB to detect multiple target mRNA of each biological process related to the cell functions.

The conventional biological researches have been performed with two-dimensional (2D) culture dishes. However, in the living body, most cells exist in the three-dimensional (3D) state organized where cells are surrounded by other cells and extracellular matrix (ECM) components. The cell functions in the 3D state are efficiently enhanced compared with the 2D state because the biochemical and mechanical signals are upregulated due to the close cell-cell and cell-ECM interactions [242, 243]. For example, embryonic stem (ES) cells initiate the spontaneous differentiation via the formation of 3D cells aggregate, so-called embryoid body (EB) [244, 245]. Actually, a lot of culture techniques to induce the differentiation of ES and iPS cells into specific linages, mediate the formation of EB in an initial step of differentiation [246-250]. Based on the background, the technologies and methodologies of 3D cells fabrication have been extensively developed [251-256], and applied to wide research fields which make use of cell functions enhanced. For example, cardiac cell sheets [257] and layered sheets [258], cartilage pellets [259], and spheroids of MSC [260, 261] and other cells [262] transplanted *in vivo* showed the high therapeutic effect against various disease models. The tumor spheroids were effective models in the drug screening [263-265]. In addition, the 3D self-organization of cells is essential in an organoid fabrication. Various types of organoid have been reported to study the developmental processes [266-268], disease modeling [269-271], and applications to drug discovery [272-275] and transplantation therapy [276-278]. Under these circumstances, it is undoubtedly important to develop the imaging technology to visualize the cell functions in the 3D cells fabricate. To this end, it is necessary to homogenously label the individual cells in the 3D fabricate with imaging probes. However, it has been reported that the homogenous labeling is sometimes difficult due to the poor penetration of imaging probes into the 3D fabricate [279, 280]. As one strategy, it is expected to be effective that cells are incubated with GNS incorporating imaging probes to label in a 2D culture, and then the cells labeled are fabricated to 3D constructs (**Figure 3**).

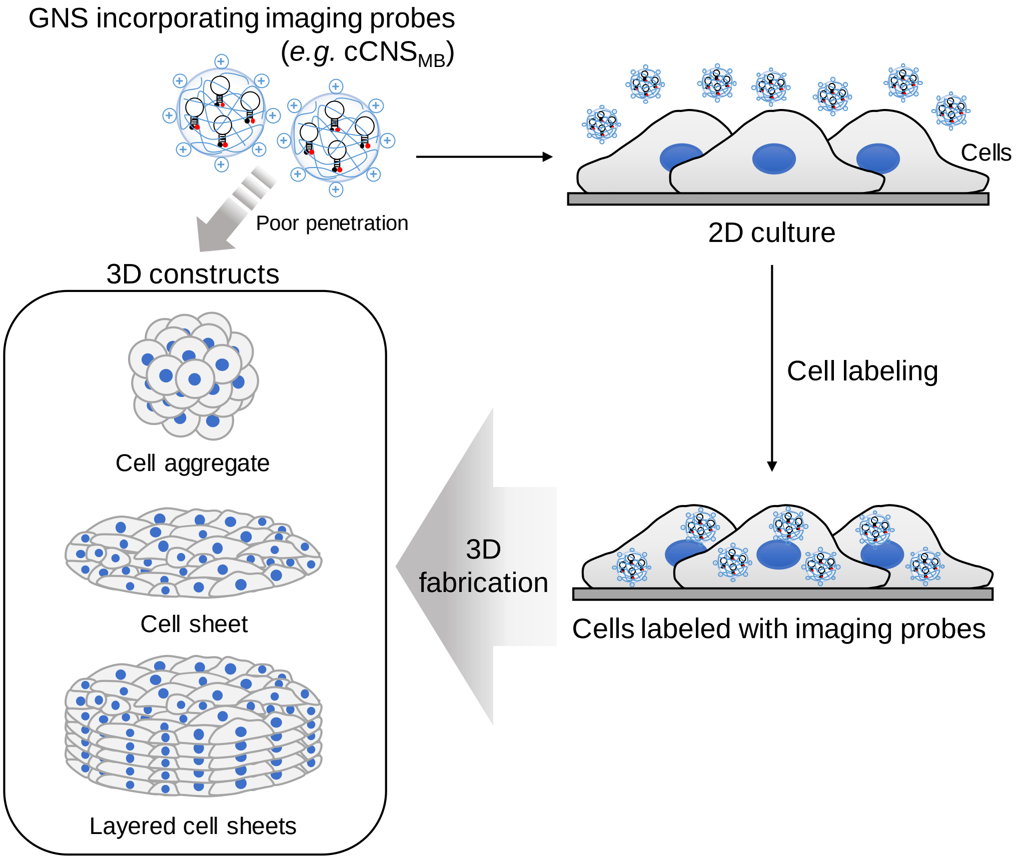

Figure 3. Labeling strategy of 3D cells fabricate combined with imaging probes.

Accordingly, even the cells interior of 3D fabricate can be homogenously labeled with imaging probes. One of advantages of this method is to fabricate various sizes and shapes of 3D constructs, such as aggregates, sheets, and layered sheets, after the labeling with imaging probes, which makes it possible to visualize the cell functions in the various 3D environments.

The objective of this thesis is to design and prepare gelatin-based carriers for imaging probes to visualize cell functions. In PART I, basic technologies of imaging system were developed. Imaging probes were complexed or incorporated into gelatin-based carriers, and the physicochemical properties were evaluated. The cells were incubated with the carries to be labeled with the imaging probes. In addition, the intracellular controlled release was evaluated to prolong the intracellular activity of MB. The cell proliferation ability and cell apoptosis of fundamental cell functions were visualized based on the intracellular controlled release of MB.

Chapter 1 describes the preparation of GNS incorporating QD and IONP ($\mathrm{GNS}_{\mathrm{QD+IONP}}$) as a multimodal imaging probe. The physicochemical properties of $\mathrm{GNS}_{\mathrm{QD+IONP}}$ were evaluated with various concentrations of glutaraldehyde (GA) of a crosslinking reagent in preparation. The apparent size and zeta potential of $\mathrm{GNS}_{\mathrm{QD+IONP}}$ were not affected by the GA concentration. On the other hand, the percentage of QD incorporated in $\mathrm{GNS}_{\mathrm{QD+IONP}}$ tended to decrease as the GA concentration increased, whereas that of IONP was constant. When treated with R8 of a CPP and incubated with human articular chondrocytes, $\mathrm{GNS}_{\mathrm{QD+IONP}}$ were efficiently internalized into the cells although their cytotoxicity was observed at the R8 concentration of 320 μM. The cells internalizing $\mathrm{GNS}_{\mathrm{QD+IONP}}$ could be visualized by both the fluorescent and MRI modalities.

Chapter 2 describes the preparation of cationized gelatin-MB complexes to visualize intracellular mRNA. The complexes were prepared from spermine-introduced cationized gelatins with different extents of cationization and different mixing ratios of MB to cationized gelatin. The apparent size of complexes was almost similar, while the zeta potential was different among the complexes. Irrespective of the preparation conditions, the complexes had a sequence specificity against the target oligonucleotides in hybridization. The cytotoxicity and the amount of complexes internalized into mouse bone marrow-derived MSC increased with an increase in the cationization extent and the concentration of cationized gelatin. After the incubation with complexes prepared from cationized gelatin with the highest extent of cationization and at mixing ratios of 10 and 20 pmole MB/μg cationized gelatin, a high fluorescent intensity was detected. On the other hand, the complex prepared with the mixing ratio at 20 pmole/μg did not show any cytotoxicity. The complex was the most effective to visualize the glyceraldehyde-3-phosphate dehydrogenase (GAPDH) mRNA endogenously present. In addition, even for an enhanced GFP (EGFP) mRNA exogenously transfected, the complex permitted to effectively detect it as well.

Chapter 3 describes the preparation of cationized gelatin-MB complexes and cGNS incorporating MB ($\mathrm{cGNS_{MB}}$) for the intracellular controlled release of MB. The cGNS with different degradabilities were prepared to incorporate the MB for GAPDH mRNA. There was no difference in the apparent size and zeta potential between the complexes and the $\mathrm{cGNS_{MB}}$, while the MB release from the complexes was faster than that from the $\mathrm{cGNS_{MB}}$. When mouse bone marrow-derived MSC were incubated with the complexes and $\mathrm{cGNS_{MB}}$, the amount of MB internalized into cells and cytotoxicity of complexes were higher than those of $\mathrm{cGNS_{MB}}$. However, in the amount range of non-cytotoxicity, the amount of MB internalized was at a similar level among them. The intracellular fluorescence of $\mathrm{cGNS_{MB}}$ was observed over 14 days, whereas that of complexes disappeared within 5 days. Moreover, the time period of $\mathrm{cGNS_{MB}}$ remaining in the cells prolonged with the increase of GA amount used in $\mathrm{cGNS_{MB}}$ preparation. As the result, it is likely that the intracellular fluorescence was retained at a high level for longer time periods. The intracellular controlled release of MB could be achieved by the use of $\mathrm{cGNS_{MB}}$, and prolonged the time period of mRNA visualization.

Chapter 4 describes the preparation of $\mathrm{cGNS_{MB}}$ to visualize the cell proliferation ability. In this chapter, two types of MB to detect mRNA were used. One is a Ki67 MB of a target for cell proliferation ability. The other is a GAPDH MB as a control of stable fluorescence in cells. The cGNS incorporating Ki67 MB and GAPDH MB ($\mathrm{cGNS_{Ki67\ MB}}$ and $\mathrm{cGNS_{GAP\ MB}}$) were prepared, respectively. There was no difference in the physicochemical properties and the cell internalization between the $\mathrm{cGNS_{Ki67\ MB}}$ and $\mathrm{cGNS_{GAP\ MB}}$. When basic fibroblast growth factor (bFGF) was added to mouse bone marrow-derived MSC, the expression of Ki67 and the cell proliferation increased with the bFGF concentration. After the incubation for the cell internalization of cGNS$_{\mathrm{MB}}$, the cells were further incubated for 24 hr with or without different concentrations of bFGF. The fluorescence of cGNS$_{\mathrm{Ki67\ MB}}$ significantly increased with the increase of bFGF concentration, whereas that of cGNS$_{\mathrm{GAP\ MB}}$ was constant, irrespective of the bFGF concentration. A timelapse imaging assay revealed that a fast enhancement of cGNS$_{\mathrm{Ki67\ MB}}$ fluorescence after the bFGF addition compared with no bFGF addition. On the other hand, for the cGNS$_{\mathrm{GAP\ MB}}$, a constant fluorescence was observed even at any time point after the bFGF addition. The cell proliferation ability could be chronologically visualized by the cGNS$_{\mathrm{MB}}$.

Chapter 5 describes the preparation of cGNS$_{\mathrm{MB}}$ to visualize the cell apoptosis. In this chapter, two types of MB to detect mRNA of caspase-3 as a target for cell apoptosis and GAPDH MB were incorporated in cGNS, respectively (cGNS$_{\mathrm{casp3\ MB}}$ and cGNS$_{\mathrm{GAP\ MB}}$). The MB incorporated in cGNS showed the sequence specificity against the target oligonucleotides in hybridization. The cGNS incorporation enabled MB to enhance the stability against nuclease to a significantly great extent compared with free MB. The cGNS$_{\mathrm{GAP\ MB}}$ were internalized into mouse bone marrow-derived MSC by an endocytotic pathway, and were not localized at the lysosomes. After the incubation with cGNS$_{\mathrm{MB}}$, the cell apoptosis was induced at different concentrations of camptothecin. No change in the intracellular fluorescence was observed for cGNS$_{\mathrm{GAP\ MB}}$. On the other hand, for the cGNS$_{\mathrm{casp3\ MB}}$, the fluorescent intensity significantly enhanced by the apoptosis induction of cells. The fluorescent enhancement even at the lower concentrations of camptothecin enabled the earlier detection of cell apoptosis compared with the conventional methods. The cell apoptosis could be visualized by the cGNS$_{\mathrm{MB}}$.

In PART II, the basic technologies developed in PART I were expanded to the multi-color imaging for the visualization of multiple cell functions. Imaging probes with different fluorescent wavelengths were simultaneously incorporated into the GNS. In addition, the homogenous labeling method of 3D cells fabricate was developed to visualize cell functions in the 3D environments.

Chapter 6 describes the preparation of cGNS$_{\mathrm{MB}}$ to visualize energy metabolic pathways. In this chapter, MB for the mRNA of pyruvate dehydrogenase kinase 1 (PDK1) and peroxisome proliferator-activated receptor γ, coactivator-1α (PGC-1α) which are upregulated in the glycolysis and the OXPHOS, respectively, were designed. As a control, MB for β-actin

(Actb) of a constant expressing gene was prepared. The $cGNS_{PDK1\ MB}$, $cGNS_{PGC\text{-}1\alpha\ MB}$, and $cGNS_{Actb\ MB}$ prepared were readily internalized into mouse embryonic stem (mES) cells, while their pluripotency was not modified by their internalization. The measurements of extracellular acidification rate (ECAR) and oxygen consumption rate (OCR) of representative metabolic indicators revealed that the undifferentiated cells showed an enhanced glycolytic profile. On the other hand, the OXPHOS profile increased as the induction of early and neural differentiations. For the $cGNS_{MB}$ imaging, the fluorescence of $cGNS_{PDK1\ MB}$ was strongly observed for the undifferentiated cells. On the contrary, the fluorescence of $cGNS_{PGC\text{-}1\alpha\ MB}$ significantly increased as the induction of early and neural differentiations, while the $cGNS_{Actb\ MB}$ fluorescence was similarly observed for both the undifferentiated and differentiated cells. The fluorescent intensity showed a good accordance with the metabolic profiles of undifferentiated and differentiated cells. In addition, cGNS co-incorporating PDK1, PGC-1α, and Actb MB ($cGNS_{multi\ MB}$) were prepared to perform the multi-color imaging in the same cell population. As the result, the intense fluorescence of PDK1 MB was homogenously observed for the undifferentiated cells. On the other hand, for the neural differentiation-induced cells, some fluorescence of PDK1 MB was observed around the intense fluorescence of PGC-1α MB. The energy metabolic pathways between undifferentiated and differentiated mES cells could be visualized by the $cGNS_{MB}$ with different colors.

Chapter 7 describes the preparation of GNS co-incorporating three kinds of QD and IONP ($GNS_{3QD+IONP}$) to visualize human iPS cells-derived 3D cartilage tissue. In this chapter, two labeling methods were performed. One is that a cartilage tissue was labeled directly by incubating with R8-treated $GNS_{3QD+IONP}$ (direct labeling method). The other is a "dissociation and labeling method". First, the cartilage tissue was dissociated to cells in a single dispersed state. Then, the cells were incubated with R8-$GNS_{3QD+IONP}$ in a monolayer culture. Finally, the cells labeled were fabricated to 3D pellets or cell sheets. By the direct labeling method, only cells residing in the surface surrounding site of cartilage tissue were labeled. On the other hand, the 3D cartilage pellets and the cell sheets were homogenously labeled, and maintained fluorescently visualized over 4 weeks with different colors. In addition, the cartilage properties were histologically detected even after the process of dissociation and labeling. The human iPS cells-derived 3D cartilage tissue could be homogenously labeled and visualized by the dissociation and labeling method with $\mathrm{GNS}_{\mathrm{3QD+IONP}}$.

Chapter 8 describes the preparation of $\mathrm{cGNS}_{\mathrm{MB}}$ to visualize the apoptosis in 3D cell aggregates. In this chapter, caspase-3 and GAPDH MB were incorporated in cGNS, respectively ($\mathrm{cGNS}_{\mathrm{casp3\ MB}}$ and $\mathrm{cGNS}_{\mathrm{GAP\ MB}}$). In addition to the single type of MB, cGNS co-incorporating caspase-3 and GAPDH MB ($\mathrm{cGNS}_{\mathrm{dual\ MB}}$) were prepared to perform the dual-color imaging for the same cell aggregate. The $\mathrm{cGNS}_{\mathrm{MB}}$ were incubated with mouse bone marrow-derived MSC to label with MB in the 2D culture. The cell apoptosis mediated by the addition of antibody for the death receptor Fas, was ratiometrically detected by the $\mathrm{cGNS}_{\mathrm{dual\ MB}}$ to the same extent as single MB. The cell aggregates were prepared from MB-labeled cells, and the MB fluorescence was detected from almost all of the cells even in the 3D aggregates to show the homogenous distribution. In addition to the Fas-mediated apoptosis, the aggregates were treated with camptothecin of a low-molecular weight apoptosis inducer. The fluorescence of caspase-3 MB was mainly distributed at the surface surrounding site of Fas-mediated apoptotic aggregates rather than the center site, while that of GAPDH MB was detected even in the interior site. On the other hand, in the camptothecin-induced apoptotic aggregates, both caspae-3 and GAPDH MB fluorescence were detected from the interior site of aggregates, as well as the surrounding site. It is likely that the MB fluorescence reflected the localization of apoptotic position caused by the different molecular sizes of apoptosis inducer and the consequent penetration into the aggregates. The apoptosis in 3D cell aggregates could be visualized by the $\mathrm{cGNS}_{\mathrm{MB}}$.

In summary, this thesis describes the feasibility of gelatin-based carriers for imaging probes to visualize various cell functions in both 2D and 3D environments. It is concluded that the effective cell function imaging can be achieved by the combination of gelatin-based carriers and imaging probes.

REFERENCES

1. Takahashi K, Yamanaka S. Induction of pluripotent stem cells from mouse embryonic and adult fibroblast cultures by defined factors. *Cell* 2006; **126**: 663-676.
2. Takahashi K, Tanabe K, Ohnuki M, Narita M, Ichisaka T, Tomoda K *et al.* Induction of pluripotent stem cells from adult human fibroblasts by defined factors. *Cell* 2007; **131**: 861-872.
3. June CH, O'Connor RS, Kawalekar OU, Ghassemi S, Milone MC. CAR T cell immunotherapy for human cancer. *Science* 2018; **359**: 1361-1365.
4. Eyquem J, Mansilla-Soto J, Giavridis T, van der Stegen SJ, Hamieh M, Cunanan KM *et al.* Targeting a CAR to the TRAC locus with CRISPR/Cas9 enhances tumour rejection. *Nature* 2017; **543**: 113-117.
5. Rupp LJ, Schumann K, Roybal KT, Gate RE, Ye CJ, Lim WA *et al.* CRISPR/Cas9-mediated PD-1 disruption enhances anti-tumor efficacy of human chimeric antigen receptor T cells. *Sci Rep* 2017; **7**: 737.
6. Gao Q, Dong X, Xu Q, Zhu L, Wang F, Hou Y *et al.* Therapeutic potential of CRISPR/Cas9 gene editing in engineered T-cell therapy. *Cancer Med* 2019; **8**: 4254-4264.
7. Shah NN, Fry TJ. Mechanisms of resistance to CAR T cell therapy. *Nat Rev Clin Oncol* 2019; **16**: 372-385.
8. Fatehullah A, Tan SH, Barker N. Organoids as an in vitro model of human development and disease. *Nat Cell Biol* 2016; **18**: 246-254.
9. Yin X, Mead BE, Safaee H, Langer R, Karp JM, Levy O. Engineering Stem Cell Organoids. *Cell Stem Cell* 2016; **18**: 25-38.
10. Drost J, Clevers H. Organoids in cancer research. *Nat Rev Cancer* 2018; **18**: 407-418.
11. Takebe T, Wells JM. Organoids by design. *Science* 2019; **364**: 956-959.
12. Brownjohn PW, Smith J, Portelius E, Serneels L, Kvartsberg H, De Strooper B *et al.* Phenotypic Screening Identifies Modulators of Amyloid Precursor Protein Processing in Human Stem Cell Models of Alzheimer's Disease. *Stem Cell Reports* 2017; **8**: 870-882.
13. Cho CF, Wolfe JM, Fadzen CM, Calligaris D, Hornburg K, Chiocca EA *et al.* Blood-

brain-barrier spheroids as an in vitro screening platform for brain-penetrating agents. *Nat Commun* 2017; **8**: 15623.

14. Moffat JG, Vincent F, Lee JA, Eder J, Prunotto M. Opportunities and challenges in phenotypic drug discovery: an industry perspective. *Nat Rev Drug Discov* 2017; **16**: 531-543.
15. Kokubu Y, Nagino T, Sasa K, Oikawa T, Miyake K, Kume A *et al.* Phenotypic Drug Screening for Dysferlinopathy Using Patient-Derived Induced Pluripotent Stem Cells. *Stem Cells Transl Med* 2019; **8**: 1017-1029.
16. Savoji H, Mohammadi MH, Rafatian N, Toroghi MK, Wang EY, Zhao Y *et al.* Cardiovascular disease models: A game changing paradigm in drug discovery and screening. *Biomaterials* 2019; **198**: 3-26.
17. Rezvani K, Rouce R, Liu E, Shpall E. Engineering Natural Killer Cells for Cancer Immunotherapy. *Mol Ther* 2017; **25**: 1769-1781.
18. Ferreira LMR, Muller YD, Bluestone JA, Tang Q. Next-generation regulatory T cell therapy. *Nat Rev Drug Discov* 2019; **18**: 749-769.
19. Pathria P, Louis TL, Varner JA. Targeting Tumor-Associated Macrophages in Cancer. *Trends Immunol* 2019; **40**: 310-327.
20. Riley RS, June CH, Langer R, Mitchell MJ. Delivery technologies for cancer immunotherapy. *Nat Rev Drug Discov* 2019; **18**: 175-196.
21. Alfaifi M, Eom YW, Newsome PN, Baik SK. Mesenchymal stromal cell therapy for liver diseases. *J Hepatol* 2018; **68**: 1272-1285.
22. Garcia SM, Tamaki S, Lee S, Wong A, Jose A, Dreux J *et al.* High-Yield Purification, Preservation, and Serial Transplantation of Human Satellite Cells. *Stem Cell Reports* 2018; **10**: 1160-1174.
23. Menasche P. Cell therapy trials for heart regeneration - lessons learned and future directions. *Nat Rev Cardiol* 2018; **15**: 659-671.
24. Soontararak S, Chow L, Johnson V, Coy J, Wheat W, Regan D *et al.* Mesenchymal Stem Cells (MSC) Derived from Induced Pluripotent Stem Cells (iPSC) Equivalent to Adipose-Derived MSC in Promoting Intestinal Healing and Microbiome Normalization

in Mouse Inflammatory Bowel Disease Model. *Stem Cells Transl Med* 2018; **7**: 456-467.

25. Doi D, Magotani H, Kikuchi T, Ikeda M, Hiramatsu S, Yoshida K *et al.* Pre-clinical study of induced pluripotent stem cell-derived dopaminergic progenitor cells for Parkinson's disease. *Nat Commun* 2020; **11**: 3369.
26. Chudakov DM, Matz MV, Lukyanov S, Lukyanov KA. Fluorescent proteins and their applications in imaging living cells and tissues. *Physiol Rev* 2010; **90**: 1103-1163.
27. Horikawa K, Yamada Y, Matsuda T, Kobayashi K, Hashimoto M, Matsu-ura T *et al.* Spontaneous network activity visualized by ultrasensitive Ca(2+) indicators, yellow Cameleon-Nano. *Nat Methods* 2010; **7**: 729-732.
28. Surdo NC, Berrera M, Koschinski A, Brescia M, Machado MR, Carr C *et al.* FRET biosensor uncovers cAMP nano-domains at beta-adrenergic targets that dictate precise tuning of cardiac contractility. *Nat Commun* 2017; **8**: 15031.
29. Yoshida T, Alfaqaan S, Sasaoka N, Imamura H. Application of FRET-Based Biosensor "ATeam" for Visualization of ATP Levels in the Mitochondrial Matrix of Living Mammalian Cells. *Methods Mol Biol* 2017; **1567**: 231-243.
30. Shen Y, Wu SY, Rancic V, Aggarwal A, Qian Y, Miyashita SI *et al.* Genetically encoded fluorescent indicators for imaging intracellular potassium ion concentration. *Commun Biol* 2019; **2**: 18.
31. Ahmad M, Anjum NA, Asif A, Ahmad A. Real-time monitoring of glutathione in living cells using genetically encoded FRET-based ratiometric nanosensor. *Sci Rep* 2020; **10**: 992.
32. Hertel F, Li S, Chen M, Pott L, Mehta S, Zhang J. Fluorescent Biosensors for Multiplexed Imaging of Phosphoinositide Dynamics. *ACS Chem Biol* 2020; **15**: 33-38.
33. Ma Y, Yamamoto Y, Nicovich PR, Goyette J, Rossy J, Gooding JJ *et al.* A FRET sensor enables quantitative measurements of membrane charges in live cells. *Nat Biotechnol* 2017; **35**: 363-370.
34. Shao S, Liao X, Xie F, Deng S, Liu X, Ristaniemi T *et al.* FRET biosensor allows spatio-temporal observation of shear stress-induced polar RhoGDIalpha activation. *Commun Biol* 2018; **1**: 224.

35. Shcherbakova DM, Cox Cammer N, Huisman TM, Verkhusha VV, Hodgson L. Direct multiplex imaging and optogenetics of Rho GTPases enabled by near-infrared FRET. *Nat Chem Biol* 2018; **14**: 591-600.

36. Marston DJ, Vilela M, Huh J, Ren J, Azoitei ML, Glekas G *et al.* Multiplexed GTPase and GEF biosensor imaging enables network connectivity analysis. *Nat Chem Biol* 2020; **16**: 826-833.

37. Stawarski M, Rutkowska-Wlodarczyk I, Zeug A, Bijata M, Madej H, Kaczmarek L *et al.* Genetically encoded FRET-based biosensor for imaging MMP-9 activity. *Biomaterials* 2014; **35**: 1402-1410.

38. Anand P, Fu A, Teoh SH, Luo KQ. Application of a fluorescence resonance energy transfer (FRET)-based biosensor for detection of drug-induced apoptosis in a 3D breast tumor model. *Biotechnol Bioeng* 2015; **112**: 1673-1682.

39. Bertolin G, Sizaire F, Herbomel G, Reboutier D, Prigent C, Tramier M. A FRET biosensor reveals spatiotemporal activation and functions of aurora kinase A in living cells. *Nat Commun* 2016; **7**: 12674.

40. Kim TJ, Lei L, Seong J, Suh JS, Jang YK, Jung SH *et al.* Matrix Rigidity-Dependent Regulation of Ca(2+) at Plasma Membrane Microdomains by FAK Visualized by Fluorescence Resonance Energy Transfer. *Adv Sci* 2019; **6**: 1801290.

41. Zacharias DA, Violin JD, Newton AC, Tsien RY. Partitioning of lipid-modified monomeric GFPs into membrane microdomains of live cells. *Science* 2002; **296**: 913-916.

42. Snapp EL, Hegde RS, Francolini M, Lombardo F, Colombo S, Pedrazzini E *et al.* Formation of stacked ER cisternae by low affinity protein interactions. *J Cell Biol* 2003; **163**: 257-269.

43. Piston DW, Kremers GJ. Fluorescent protein FRET: the good, the bad and the ugly. *Trends Biochem Sci* 2007; **32**: 407-414.

44. Wiedenmann J, Oswald F, Nienhaus GU. Fluorescent proteins for live cell imaging: opportunities, limitations, and challenges. *IUBMB Life* 2009; **61**: 1029-1042.

45. Massoud TF, Gambhir SS. Molecular imaging in living subjects: seeing fundamental

biological processes in a new light. *Genes Dev* 2003; **17**: 545-580.

46. Willmann JK, van Bruggen N, Dinkelborg LM, Gambhir SS. Molecular imaging in drug development. *Nat Rev Drug Discov* 2008; **7**: 591-607.

47. James ML, Gambhir SS. A molecular imaging primer: modalities, imaging agents, and applications. *Physiol Rev* 2012; **92**: 897-965.

48. Gambhir SS. Molecular imaging of cancer with positron emission tomography. *Nat Rev Cancer* 2002; **2**: 683-693.

49. Truillet C, Oh HLJ, Yeo SP, Lee CY, Huynh LT, Wei J *et al.* Imaging PD-L1 Expression with ImmunoPET. *Bioconjug Chem* 2018; **29**: 96-103.

50. Jeong HJ, Yoo RJ, Kim JK, Kim MH, Park SH, Kim H *et al.* Macrophage cell tracking PET imaging using mesoporous silica nanoparticles via in vivo bioorthogonal F-18 labeling. *Biomaterials* 2019; **199**: 32-39.

51. Khalil MM, Tremoleda JL, Bayomy TB, Gsell W. Molecular SPECT Imaging: An Overview. *Int J Mol Imaging* 2011; **2011**: 796025.

52. Cheng SH, Yu D, Tsai HM, Morshed RA, Kanojia D, Lo LW *et al.* Dynamic In Vivo SPECT Imaging of Neural Stem Cells Functionalized with Radiolabeled Nanoparticles for Tracking of Glioblastoma. *J Nucl Med* 2016; **57**: 279-284.

53. Rondon A, Schmitt S, Briat A, Ty N, Maigne L, Quintana M *et al.* Pretargeted radioimmunotherapy and SPECT imaging of peritoneal carcinomatosis using bioorthogonal click chemistry: probe selection and first proof-of-concept. *Theranostics* 2019; **9**: 6706-6718.

54. Chhour P, Naha PC, O'Neill SM, Litt HI, Reilly MP, Ferrari VA *et al.* Labeling monocytes with gold nanoparticles to track their recruitment in atherosclerosis with computed tomography. *Biomaterials* 2016; **87**: 93-103.

55. Zou Y, Wei Y, Wang G, Meng F, Gao M, Storm G *et al.* Nanopolymersomes with an Ultrahigh Iodine Content for High-Performance X-Ray Computed Tomography Imaging In Vivo. *Adv Mater* 2017; **29**: 1603997.

56. Dong YC, Hajfathalian M, Maidment PSN, Hsu JC, Naha PC, Si-Mohamed S *et al.* Effect of Gold Nanoparticle Size on Their Properties as Contrast Agents for Computed

Tomography. *Sci Rep* 2019; **9**: 14912.

57. Abou-Elkacem L, Bachawal SV, Willmann JK. Ultrasound molecular imaging: Moving toward clinical translation. *Eur J Radiol* 2015; **84**: 1685-1693.
58. Gao Y, Hernandez C, Yuan HX, Lilly J, Kota P, Zhou H *et al.* Ultrasound molecular imaging of ovarian cancer with CA-125 targeted nanobubble contrast agents. *Nanomedicine* 2017; **13**: 2159-2168.
59. Farhadi A, Ho GH, Sawyer DP, Bourdeau RW, Shapiro MG. Ultrasound imaging of gene expression in mammalian cells. *Science* 2019; **365**: 1469-1475.
60. Dhada KS, Hernandez DS, Suggs LJ. In Vivo Photoacoustic Tracking of Mesenchymal Stem Cell Viability. *ACS Nano* 2019; **13**: 7791-7799.
61. Moore C, Chen F, Wang J, Jokerst JV. Listening for the therapeutic window: Advances in drug delivery utilizing photoacoustic imaging. *Adv Drug Deliv Rev* 2019; **144**: 78-89.
62. Attia ABE, Balasundaram G, Moothanchery M, Dinish US, Bi R, Ntziachristos V *et al.* A review of clinical photoacoustic imaging: Current and future trends. *Photoacoustics* 2019; **16**: 100144.
63. Piao YJ, Kim HS, Moon WK. Noninvasive Photoacoustic Imaging of Dendritic Cell Stimulated with Tumor Cell-Derived Exosome. *Mol Imaging Biol* 2020; **22**: 612-622.
64. Mezzanotte L, van 't Root M, Karatas H, Goun EA, Lowik C. In Vivo Molecular Bioluminescence Imaging: New Tools and Applications. *Trends Biotechnol* 2017; **35**: 640-652.
65. Iwano S, Sugiyama M, Hama H, Watakabe A, Hasegawa N, Kuchimaru T *et al.* Single-cell bioluminescence imaging of deep tissue in freely moving animals. *Science* 2018; **359**: 935-939.
66. John S, Rolnick K, Wilson L, Wong S, Van Gelder RN, Pepple KL. Bioluminescence for in vivo detection of cell-type-specific inflammation in a mouse model of uveitis. *Sci Rep* 2020; **10**: 11377.
67. Ntziachristos V. Fluorescence molecular imaging. *Annu Rev Biomed Eng* 2006; **8**: 1-33.
68. Etrych T, Lucas H, Janouskova O, Chytil P, Mueller T, Mader K. Fluorescence optical imaging in anticancer drug delivery. *J Control Release* 2016; **226**: 168-181.

69. Wang C, Wang Z, Zhao T, Li Y, Huang G, Sumer BD *et al.* Optical molecular imaging for tumor detection and image-guided surgery. *Biomaterials* 2018; **157**: 62-75.
70. Tobita S, Yoshihara T. Intracellular and in vivo oxygen sensing using phosphorescent iridium(III) complexes. *Curr Opin Chem Biol* 2016; **33**: 39-45.
71. Raza A, Colley HE, Baggaley E, Sazanovich IV, Green NH, Weinstein JA *et al.* Oxygen Mapping of Melanoma Spheroids using Small Molecule Platinum Probe and Phosphorescence Lifetime Imaging Microscopy. *Sci Rep* 2017; **7**: 10743.
72. Cao X, Rao Allu S, Jiang S, Jia M, Gunn JR, Yao C *et al.* Tissue pO2 distributions in xenograft tumors dynamically imaged by Cherenkov-excited phosphorescence during fractionated radiation therapy. *Nat Commun* 2020; **11**: 573.
73. Bennett KM, Jo J, Cabral H, Bakalova R, Aoki I. MR imaging techniques for nano-pathophysiology and theranostics. *Adv Drug Deliv Rev* 2014; **74**: 75-94.
74. Jones KM, Pollard AC, Pagel MD. Clinical applications of chemical exchange saturation transfer (CEST) MRI. *J Magn Reson Imaging* 2018; **47**: 11-27.
75. Batsios G, Najac C, Cao P, Viswanath P, Subramani E, Saito Y *et al.* In vivo detection of gamma-glutamyl-transferase up-regulation in glioma using hyperpolarized gamma-glutamyl-[1-(13)C]glycine. *Sci Rep* 2020; **10**: 6244.
76. Baker M. Whole-animal imaging: The whole picture. *Nature* 2010; **463**: 977-980.
77. Leblond F, Davis SC, Valdes PA, Pogue BW. Pre-clinical whole-body fluorescence imaging: Review of instruments, methods and applications. *J Photochem Photobiol B* 2010; **98**: 77-94.
78. Luo S, Zhang E, Su Y, Cheng T, Shi C. A review of NIR dyes in cancer targeting and imaging. *Biomaterials* 2011; **32**: 7127-7138.
79. Zhu S, Tian R, Antaris AL, Chen X, Dai H. Near-Infrared-II Molecular Dyes for Cancer Imaging and Surgery. *Adv Mater* 2019; **31**: e1900321.
80. Li B, Zhao M, Feng L, Dou C, Ding S, Zhou G *et al.* Organic NIR-II molecule with long blood half-life for in vivo dynamic vascular imaging. *Nat Commun* 2020; **11**: 3102.
81. Michalet X, Pinaud FF, Bentolila LA, Tsay JM, Doose S, Li JJ *et al.* Quantum dots for live cells, in vivo imaging, and diagnostics. *Science* 2005; **307**: 538-544.

82. Onoshima D, Yukawa H, Baba Y. Multifunctional quantum dots-based cancer diagnostics and stem cell therapeutics for regenerative medicine. *Adv Drug Deliv Rev* 2015; **95**: 2-14.

83. Han HS, Niemeyer E, Huang Y, Kamoun WS, Martin JD, Bhaumik J *et al.* Quantum dot/antibody conjugates for in vivo cytometric imaging in mice. *Proc Natl Acad Sci U S A* 2015; **112**: 1350-1355.

84. Wegner KD, Hildebrandt N. Quantum dots: bright and versatile in vitro and in vivo fluorescence imaging biosensors. *Chem Soc Rev* 2015; **44**: 4792-4834.

85. Liu X, Braun GB, Zhong H, Hall DJ, Han W, Qin M *et al.* Tumor-Targeted Multimodal Optical Imaging with Versatile Cadmium-Free Quantum Dots. *Adv Funct Mater* 2016; **26**: 267-276.

86. Nicholls FJ, Rotz MW, Ghuman H, MacRenaris KW, Meade TJ, Modo M. DNA-gadolinium-gold nanoparticles for in vivo T1 MR imaging of transplanted human neural stem cells. *Biomaterials* 2016; **77**: 291-306.

87. Venter A, Szulc DA, Loai S, Ganesh T, Haedicke IE, Cheng HL. A manganese porphyrin-based T1 contrast agent for cellular MR imaging of human embryonic stem cells. *Sci Rep* 2018; **8**: 12129.

88. Bouchlaka MN, Ludwig KD, Gordon JW, Kutz MP, Bednarz BP, Fain SB *et al.* (19)F-MRI for monitoring human NK cells in vivo. *Oncoimmunology* 2016; **5**: e1143996.

89. Yukawa H, Nakagawa S, Yoshizumi Y, Watanabe M, Saito H, Miyamoto Y *et al.* Novel positively charged nanoparticle labeling for in vivo imaging of adipose tissue-derived stem cells. *PLoS One* 2014; **9**: e110142.

90. Azzabi F, Rottmar M, Jovaisaite V, Rudin M, Sulser T, Boss A *et al.* Viability, differentiation capacity, and detectability of super-paramagnetic iron oxide-labeled muscle precursor cells for magnetic-resonance imaging. *Tissue Eng Part C Methods* 2015; **21**: 182-191.

91. Dadfar SM, Roemhild K, Drude NI, von Stillfried S, Knuchel R, Kiessling F *et al.* Iron oxide nanoparticles: Diagnostic, therapeutic and theranostic applications. *Adv Drug Deliv Rev* 2019; **138**: 302-325.

92. Louie A. Multimodality imaging probes: design and challenges. *Chem Rev* 2010; **110**: 3146-3195.

93. Lee DE, Koo H, Sun IC, Ryu JH, Kim K, Kwon IC. Multifunctional nanoparticles for multimodal imaging and theragnosis. *Chem Soc Rev* 2012; **41**: 2656-2672.

94. Li X, Zhang XN, Li XD, Chang J. Multimodality imaging in nanomedicine and nanotheranostics. *Cancer Biol Med* 2016; **13**: 339-348.

95. Jaiswal JK, Mattoussi H, Mauro JM, Simon SM. Long-term multiple color imaging of live cells using quantum dot bioconjugates. *Nat Biotechnol* 2003; **21**: 47-51.

96. Tada H, Higuchi H, Wanatabe TM, Ohuchi N. In vivo real-time tracking of single quantum dots conjugated with monoclonal anti-HER2 antibody in tumors of mice. *Cancer Res* 2007; **67**: 1138-1144.

97. Gleysteen JP, Newman JR, Chhieng D, Frost A, Zinn KR, Rosenthal EL. Fluorescent labeled anti-EGFR antibody for identification of regional and distant metastasis in a preclinical xenograft model. *Head Neck* 2008; **30**: 782-789.

98. Yang K, Zhang FJ, Tang H, Zhao C, Cao YA, Lv XQ *et al.* In-vivo imaging of oral squamous cell carcinoma by EGFR monoclonal antibody conjugated near-infrared quantum dots in mice. *Int J Nanomedicine* 2011; **6**: 1739-1745.

99. Heath CH, Deep NL, Sweeny L, Zinn KR, Rosenthal EL. Use of panitumumab-IRDye800 to image microscopic head and neck cancer in an orthotopic surgical model. *Ann Surg Oncol* 2012; **19**: 3879-3887.

100. Shi H, Tang Z, Kim Y, Nie H, Huang YF, He X *et al.* In vivo fluorescence imaging of tumors using molecular aptamers generated by cell-SELEX. *Chem Asian J* 2010; **5**: 2209-2213.

101. Shi H, Cui W, He X, Guo Q, Wang K, Ye X *et al.* Whole cell-SELEX aptamers for highly specific fluorescence molecular imaging of carcinomas in vivo. *PLoS One* 2013; **8**: e70476.

102. Zeng Z, Parekh P, Li Z, Shi ZZ, Tung CH, Zu Y. Specific and sensitive tumor imaging using biostable oligonucleotide aptamer probes. *Theranostics* 2014; **4**: 945-952.

103. Farrar CT, William CM, Hudry E, Hashimoto T, Hyman BT. RNA aptamer probes as

optical imaging agents for the detection of amyloid plaques. *PLoS One* 2014; **9**: e89901.

104. van Dam GM, Themelis G, Crane LM, Harlaar NJ, Pleijhuis RG, Kelder W *et al.* Intraoperative tumor-specific fluorescence imaging in ovarian cancer by folate receptor-alpha targeting: first in-human results. *Nat Med* 2011; **17**: 1315-1319.
105. Kim JB, Park K, Ryu J, Lee JJ, Lee MW, Cho HS *et al.* Intravascular optical imaging of high-risk plaques in vivo by targeting macrophage mannose receptors. *Sci Rep* 2016; **6**: 22608.
106. Patil R, Galstyan A, Sun T, Shatalova ES, Butte P, Mamelak AN *et al.* Polymalic acid chlorotoxin nanoconjugate for near-infrared fluorescence guided resection of glioblastoma multiforme. *Biomaterials* 2019; **206**: 146-159.
107. Wang W, Hu Z. Targeting Peptide-Based Probes for Molecular Imaging and Diagnosis. *Adv Mater* 2019; **31**: e1804827.
108. Ogawa M, Kosaka N, Regino CA, Mitsunaga M, Choyke PL, Kobayashi H. High sensitivity detection of cancer in vivo using a dual-controlled activation fluorescent imaging probe based on H-dimer formation and pH activation. *Mol Biosyst* 2010; **6**: 888-893.
109. Urano Y. Novel live imaging techniques of cellular functions and in vivo tumors based on precise design of small molecule-based 'activatable' fluorescence probes. *Curr Opin Chem Biol* 2012; **16**: 602-608.
110. Chen C, Tian R, Zeng Y, Chu C, Liu G. Activatable Fluorescence Probes for "Turn-On" and Ratiometric Biosensing and Bioimaging: From NIR-I to NIR-II. *Bioconjug Chem* 2020; **31**: 276-292.
111. Luby BM, Charron DM, MacLaughlin CM, Zheng G. Activatable fluorescence: From small molecule to nanoparticle. *Adv Drug Deliv Rev* 2017; **113**: 97-121.
112. Asanuma D, Sakabe M, Kamiya M, Yamamoto K, Hiratake J, Ogawa M *et al.* Sensitive beta-galactosidase-targeting fluorescence probe for visualizing small peritoneal metastatic tumours in vivo. *Nat Commun* 2015; **6**: 6463.
113. Jeong S, Song J, Lee W, Ryu YM, Jung Y, Kim SY *et al.* Cancer-Microenvironment-Sensitive Activatable Quantum Dot Probe in the Second Near-Infrared Window. *Nano*

Lett 2017; **17**: 1378-1386.

114. Miampamba M, Liu J, Harootunian A, Gale AJ, Baird S, Chen SL *et al.* Sensitive in vivo Visualization of Breast Cancer Using Ratiometric Protease-activatable Fluorescent Imaging Agent, AVB-620. *Theranostics* 2017; **7**: 3369-3386.

115. Zhao X, Yang CX, Chen LG, Yan XP. Dual-stimuli responsive and reversibly activatable theranostic nanoprobe for precision tumor-targeting and fluorescence-guided photothermal therapy. *Nat Commun* 2017; **8**: 14998.

116. Ryu JH, Na JH, Ko HK, You DG, Park S, Jun E *et al.* Non-invasive optical imaging of cathepsin B with activatable fluorogenic nanoprobes in various metastatic models. *Biomaterials* 2014; **35**: 2302-2311.

117. Chen X, Lee D, Yu S, Kim G, Lee S, Cho Y *et al.* In vivo near-infrared imaging and phototherapy of tumors using a cathepsin B-activated fluorescent probe. *Biomaterials* 2017; **122**: 130-140.

118. Blau R, Epshtein Y, Pisarevsky E, Tiram G, Israeli Dangoor S, Yeini E *et al.* Image-guided surgery using near-infrared Turn-ON fluorescent nanoprobes for precise detection of tumor margins. *Theranostics* 2018; **8**: 3437-3460.

119. Narita Y, Shimizu K, Ikemoto K, Uchino R, Kosugi M, Maess MB *et al.* Macrophage-targeted, enzyme-triggered fluorescence switch-on system for detection of embolism-vulnerable atherosclerotic plaques. *J Control Release* 2019; **302**: 105-115.

120. Maxwell D, Chang Q, Zhang X, Barnett EM, Piwnica-Worms D. An improved cell-penetrating, caspase-activatable, near-infrared fluorescent peptide for apoptosis imaging. *Bioconjug Chem* 2009; **20**: 702-709.

121. Yuan Y, Zhang CJ, Kwok RTK, Mao D, Tang BZ, Liu B. Light-up probe based on AIEgens: dual signal turn-on for caspase cascade activation monitoring. *Chem Sci* 2017; **8**: 2723-2728.

122. Wang J, Zhou Z, Zhang F, Xu H, Chen W, Jiang T. A novel nanocomposite based on fluorescent turn-on gold nanostars for near-infrared photothermal therapy and self-theranostic caspase-3 imaging of glioblastoma tumor cell. *Colloids Surf B Biointerfaces* 2018; **170**: 303-311.

123. Tyagi S, Kramer FR. Molecular beacons: probes that fluoresce upon hybridization. *Nat Biotechnol* 1996; **14**: 303-308.

124. Tyagi S, Bratu DP, Kramer FR. Multicolor molecular beacons for allele discrimination. *Nat Biotechnol* 1998; **16**: 49-53.

125. Tsourkas A, Behlke MA, Bao G. Hybridization of 2'-O-methyl and 2'-deoxy molecular beacons to RNA and DNA targets. *Nucleic Acids Res* 2003; **31**: 5168-5174.

126. Ilieva M, Dufva M. SOX2 and OCT4 mRNA-expressing cells, detected by molecular beacons, localize to the center of neurospheres during differentiation. *PLoS One* 2013; **8**: e73669.

127. Yu S, Li F, Huang X, Dong C, Ren J. In Situ Study of Interactions between Endogenous c-myc mRNA with CRDBP in a Single Living Cell by Combining Fluorescence Cross-Correlation Spectroscopy with Molecular Beacons. *Anal Chem* 2020; **92**: 2988-2996.

128. Zhao D, Yang Y, Qu N, Chen M, Ma Z, Krueger CJ *et al.* Single-molecule detection and tracking of RNA transcripts in living cells using phosphorothioate-optimized 2'-O-methyl RNA molecular beacons. *Biomaterials* 2016; **100**: 172-183.

129. Wu X, Mao S, Yang Y, Rushdi MN, Krueger CJ, Chen AK. A CRISPR/molecular beacon hybrid system for live-cell genomic imaging. *Nucleic Acids Res* 2018; **46**: e80.

130. Chen J, Wu J, Hong Y. The morpholino molecular beacon for specific RNA visualization in vivo. *Chem Commun* 2016; **52**: 3191-3194.

131. Wu Y, Yang CJ, Moroz LL, Tan W. Nucleic acid beacons for long-term real-time intracellular monitoring. *Anal Chem* 2008; **80**: 3025-3028.

132. James AM, Baker MB, Bao G, Searles CD. MicroRNA Detection Using a Double Molecular Beacon Approach: Distinguishing Between miRNA and Pre-miRNA. *Theranostics* 2017; **7**: 634-646.

133. Bakthavathsalam P, Longatte G, Jensen SO, Manefield M, Gooding JJ. Locked nucleic acid molecular beacon for multiplex detection of loop mediated isothermal amplification. *Sensor Actuat B-Chem* 2018; **268**: 255-263.

134. Kam Y, Rubinstein A, Nissan A, Halle D, Yavin E. Detection of endogenous K-ras mRNA in living cells at a single base resolution by a PNA molecular beacon. *Mol Pharm*

2012; **9**: 685-693.

135. Wang Q, Chen L, Long Y, Tian H, Wu J. Molecular beacons of xeno-nucleic acid for detecting nucleic acid. *Theranostics* 2013; **3**: 395-408.

136. Santangelo PJ, Nix B, Tsourkas A, Bao G. Dual FRET molecular beacons for mRNA detection in living cells. *Nucleic Acids Res* 2004; **32**: e57.

137. King FW, Liszewski W, Ritner C, Bernstein HS. High-throughput tracking of pluripotent human embryonic stem cells with dual fluorescence resonance energy transfer molecular beacons. *Stem Cells Dev* 2011; **20**: 475-484.

138. Mao S, Ying Y, Wu X, Krueger CJ, Chen AK. CRISPR/dual-FRET molecular beacon for sensitive live-cell imaging of non-repetitive genomic loci. *Nucleic Acids Res* 2019; **47**: e131.

139. Goel G, Kumar A, Puniya AK, Chen W, Singh K. Molecular beacon: a multitask probe. *J Appl Microbiol* 2005; **99**: 435-442.

140. Bratu DP, Catrina IE, Marras SA. Tiny molecular beacons for in vivo mRNA detection. *Methods Mol Biol* 2011; **714**: 141-157.

141. Wile BM, Ban K, Yoon YS, Bao G. Molecular beacon-enabled purification of living cells by targeting cell type-specific mRNAs. *Nat Protoc* 2014; **9**: 2411-2424.

142. Tyagi S, Alsmadi O. Imaging native beta-actin mRNA in motile fibroblasts. *Biophys J* 2004; **87**: 4153-4162.

143. Catrina IE, Marras SA, Bratu DP. Tiny molecular beacons: LNA/2'-O-methyl RNA chimeric probes for imaging dynamic mRNA processes in living cells. *ACS Chem Biol* 2012; **7**: 1586-1595.

144. Miyoshi Y, Ohtsuki T, Kashida H, Asanuma H, Watanabe K. In-stem molecular beacon targeted to a 5'-region of tRNA inclusive of the D arm that detects mature tRNA with high sensitivity. *PLoS One* 2019; **14**: e0211505.

145. Ban K, Wile B, Cho KW, Kim S, Song MK, Kim SY *et al.* Non-genetic Purification of Ventricular Cardiomyocytes from Differentiating Embryonic Stem Cells through Molecular Beacons Targeting IRX-4. *Stem Cell Reports* 2015; **5**: 1239-1249.

146. Sadahiro H, Kang KD, Gibson JT, Minata M, Yu H, Shi J *et al.* Activation of the Receptor

Tyrosine Kinase AXL Regulates the Immune Microenvironment in Glioblastoma. *Cancer Res* 2018; **78**: 3002-3013.

147. Mao S, Ying Y, Wu X, Chen AK. Delivering Molecular Beacons via an Electroporation-Based Approach Enables Live-Cell Imaging of Single RNA Transcripts and Genomic Loci. *Methods Mol Biol* 2020; **2106**: 241-252.
148. Lennon FE, Hermann CD, Olivares-Navarrete R, Rhee WJ, Schwartz Z, Bao G *et al.* Use of molecular beacons to image effects of titanium surface microstructure on beta1 integrin expression in live osteoblast-like cells. *Biomaterials* 2010; **31**: 7640-7647.
149. Lee JH, Kim JA, Kwon MH, Kang JY, Rhee WJ. In situ single step detection of exosome microRNA using molecular beacon. *Biomaterials* 2015; **54**: 116-125.
150. Feng X, Kang W, Wu X, Wang S, Liu F. Quantitative Detection and Real-Time Monitoring of Endogenous mRNA at the Single Live Cell Level Using a Ratiometric Molecular Beacon. *ACS Appl Mater Interfaces* 2019; **11**: 28752-28761.
151. Nitin N, Santangelo PJ, Kim G, Nie S, Bao G. Peptide-linked molecular beacons for efficient delivery and rapid mRNA detection in living cells. *Nucleic Acids Res* 2004; **32**: e58.
152. Yeh HY, Yates MV, Mulchandani A, Chen W. Visualizing the dynamics of viral replication in living cells via Tat peptide delivery of nuclease-resistant molecular beacons. *Proc Natl Acad Sci U S A* 2008; **105**: 17522-17525.
153. Ganguli PS, Chen W, Yates MV. Detection of murine norovirus-1 by using TAT peptide-delivered molecular beacons. *Appl Environ Microbiol* 2011; **77**: 5517-5520.
154. Kam Y, Rubinstein A, Naik S, Djavsarov I, Halle D, Ariel I *et al.* Detection of a long non-coding RNA (CCAT1) in living cells and human adenocarcinoma of colon tissues using FIT-PNA molecular beacons. *Cancer Lett* 2014; **352**: 90-96.
155. Pan W, Zhang T, Yang H, Diao W, Li N, Tang B. Multiplexed detection and imaging of intracellular mRNAs using a four-color nanoprobe. *Anal Chem* 2013; **85**: 10581-10588.
156. Deng D, Li Y, Xue J, Wang J, Ai G, Li X *et al.* Gold nanoparticle-based beacon to detect STAT5b mRNA expression in living cells: a case optimized by bioinformatics screen. *Int J Nanomedicine* 2015; **10**: 3231-3244.

157. Liu J, Zhang L, Lei J, Ju H. MicroRNA-Responsive Cancer Cell Imaging and Therapy with Functionalized Gold Nanoprobe. *ACS Appl Mater Interfaces* 2015; **7**: 19016-19023.
158. Luan M, Yu L, Li Y, Pan W, Gao X, Wan X *et al.* Visualizing Breast Cancer Cell Proliferation and Invasion for Assessing Drug Efficacy with a Fluorescent Nanoprobe. *Anal Chem* 2017; **89**: 10601-10607.
159. Lio DCS, Liu C, Wiraja C, Qiu B, Fhu CW, Wang X *et al.* Molecular Beacon Gold Nanosensors for Leucine-Rich Alpha-2-Glycoprotein-1 Detection in Pathological Angiogenesis. *ACS Sens* 2018; **3**: 1647-1655.
160. Maksimenko A, Helin V, Bertrand JR, Gottikh M, Malvy C. Real-time detection and efficacy of antisense oligonucleotides delivered by PAMAM dendrimers in living cells. *J Drug Deliv Sci Tec* 2005; **15**: 75-79.
161. Zhang Y, Zhou C, Kwak KJ, Wang X, Yung B, Lee LJ *et al.* Efficient siRNA delivery using a polyamidoamine dendrimer with a modified pentaerythritol core. *Pharm Res* 2012; **29**: 1627-1636.
162. Kurita H, Haruta N, Uchihashi Y, Seto T, Takashima K. Strand breaks and chemical modification of intracellular DNA induced by cold atmospheric pressure plasma irradiation. *PLoS One* 2020; **15**: e0232724.
163. Kang WJ, Cho YL, Chae JR, Lee JD, Choi KJ, Kim S. Molecular beacon-based bioimaging of multiple microRNAs during myogenesis. *Biomaterials* 2011; **32**: 1915-1922.
164. Zhou C, Zhang Y, Yu B, Phelps MA, Lee LJ, Lee RJ. Comparative cellular pharmacokinetics and pharmacodynamics of siRNA delivery by SPANosomes and by cationic liposomes. *Nanomedicine* 2013; **9**: 504-513.
165. Carpi S, Fogli S, Giannetti A, Adinolfi B, Tombelli S, Da Pozzo E *et al.* Theranostic properties of a survivin-directed molecular beacon in human melanoma cells. *PLoS One* 2014; **9**: e114588.
166. Bohlander PR, Abba ML, Bestvater F, Allgayer H, Wagenknecht HA. Two wavelength-shifting molecular beacons for simultaneous and selective imaging of vesicular miRNA-21 and miRNA-31 in living cancer cells. *Org Biomol Chem* 2016; **14**: 5001-5006.

167. Ratajczak K, Krazinski BE, Kowalczyk AE, Dworakowska B, Jakiela S, Stobiecka M. Hairpin-Hairpin Molecular Beacon Interactions for Detection of Survivin mRNA in Malignant SW480 Cells. *ACS Appl Mater Interfaces* 2018; **10**: 17028-17039.
168. Lin X, Konno T, Ishihara K. Cell-membrane-permeable and cytocompatible phospholipid polymer nanoprobes conjugated with molecular beacons. *Biomacromolecules* 2014; **15**: 150-157.
169. Zhu HZ, An JH, Yao Q, Han J, Li XT, Jiang FL *et al.* Chitosan combined with molecular beacon for mir-155 detection and imaging in lung cancer. *Molecules* 2014; **19**: 14710-14722.
170. Vaidyanathan S, Chen J, Orr BG, Banaszak Holl MM. Cationic Polymer Intercalation into the Lipid Membrane Enables Intact Polyplex DNA Escape from Endosomes for Gene Delivery. *Mol Pharm* 2016; **13**: 1967-1978.
171. Guk K, Hwang SG, Lim J, Son HY, Choi Y, Huh YM *et al.* Fluorescence amplified sensing platforms enabling miRNA detection by self-circulation of a molecular beacon circuit. *Chem Commun* 2019; **55**: 3457-3460.
172. Xu C, He XY, Peng Y, Dai BS, Liu BY, Cheng SX. Facile Strategy To Enhance Specificity and Sensitivity of Molecular Beacons by an Aptamer-Functionalized Delivery Vector. *Anal Chem* 2020; **92**: 2088-2096.
173. Kim YH, Furuya H, Tabata Y. Enhancement of bone regeneration by dual release of a macrophage recruitment agent and platelet-rich plasma from gelatin hydrogels. *Biomaterials* 2014; **35**: 214-224.
174. Notodihardjo SC, Morimoto N, Kakudo N, Mitsui T, Le TM, Tabata Y *et al.* Efficacy of Gelatin Hydrogel Impregnated With Concentrated Platelet Lysate in Murine Wound Healing. *J Surg Res* 2019; **234**: 190-201.
175. Nakajima N, Hashimoto S, Sato H, Takahashi K, Nagoya T, Kamimura K *et al.* Efficacy of gelatin hydrogels incorporating triamcinolone acetonide for prevention of fibrosis in a mouse model. *Regen Ther* 2019; **11**: 41-46.
176. Yamamoto M, Hokugo A, Takahashi Y, Nakano T, Hiraoka M, Tabata Y. Combination of BMP-2-releasing gelatin/beta-TCP sponges with autologous bone marrow for bone

regeneration of X-ray-irradiated rabbit ulnar defects. *Biomaterials* 2015; **56**: 18-25.

177. Shujaa Addin A, Akizuki T, Hoshi S, Matsuura T, Ikawa T, Fukuba S *et al.* Biodegradable gelatin/beta-tricalcium phosphate sponges incorporating recombinant human fibroblast growth factor-2 for treatment of recession-type defects: A split-mouth study in dogs. *J Periodontal Res* 2017; **52**: 863-871.

178. Washio A, Teshima H, Yokota K, Kitamura C, Tabata Y. Preparation of gelatin hydrogel sponges incorporating bioactive glasses capable for the controlled release of fibroblast growth factor-2. *J Biomater Sci Polym Ed* 2019; **30**: 49-63.

179. Nakamura K, Saotome T, Shimada N, Matsuno K, Tabata Y. A Gelatin Hydrogel Nonwoven Fabric Facilitates Metabolic Activity of Multilayered Cell Sheets. *Tissue Eng Part C Methods* 2019; **25**: 344-352.

180. Tajima S, Tabata Y. Preparation and functional evaluation of cell aggregates incorporating gelatin microspheres with different degradabilities. *J Tissue Eng Regen Med* 2013; **7**: 801-811.

181. Inoo K, Bando H, Tabata Y. Enhanced survival and insulin secretion of insulinoma cell aggregates by incorporating gelatin hydrogel microspheres. *Regen Ther* 2018; **8**: 29-37.

182. Coester CJ, Langer K, van Briesen H, Kreuter J. Gelatin nanoparticles by two step desolvation--a new preparation method, surface modifications and cell uptake. *J Microencapsul* 2000; **17**: 187-193.

183. Elzoghby AO. Gelatin-based nanoparticles as drug and gene delivery systems: Reviewing three decades of research. *J Control Release* 2013; **172**: 1075-1091.

184. Sahoo N, Sahoo RK, Biswas N, Guha A, Kuotsu K. Recent advancement of gelatin nanoparticles in drug and vaccine delivery. *Int J Biol Macromol* 2015; **81**: 317-331.

185. Mahmoudi Saber M. Strategies for surface modification of gelatin-based nanoparticles. *Colloids Surf B Biointerfaces* 2019; **183**: 110407.

186. Tanigo T, Takaoka R, Tabata Y. Sustained release of water-insoluble simvastatin from biodegradable hydrogel augments bone regeneration. *J Control Release* 2010; **143**: 201-206.

187. Saito T, Tabata Y. Hypoxia-induced angiogenesis is increased by the controlled release

of deferoxiamine from gelatin hydrogels. *Acta Biomater* 2014; **10**: 3641-3649.

188. Sakai S, Sato K, Tabata Y, Kishi K. Local release of pioglitazone (a peroxisome proliferator-activated receptor gamma agonist) accelerates proliferation and remodeling phases of wound healing. *Wound Repair Regen* 2016; **24**: 57-64.

189. Tanaka T, Matsushita T, Nishida K, Takayama K, Nagai K, Araki D *et al.* Attenuation of osteoarthritis progression in mice following intra-articular administration of simvastatin-conjugated gelatin hydrogel. *J Tissue Eng Regen Med* 2019; **13**: 423-432.

190. Yamashita K, Tsunoda S, Gunji S, Murakami T, Suzuki T, Tabata Y *et al.* Intraperitoneal chemotherapy for peritoneal metastases using sustained release formula of cisplatin-incorporated gelatin hydrogel granules. *Surg Today* 2019; **49**: 785-794.

191. Kohara H, Tajima S, Yamamoto M, Tabata Y. Angiogenesis induced by controlled release of neuropeptide substance P. *Biomaterials* 2010; **31**: 8617-8625.

192. Al Mamun MA, Khan MAA, Alles N, Matsui M, Tabata Y, Ohya K *et al.* Gelatin hydrogel carrier with the W9-peptide elicits synergistic effects on BMP-2-induced bone regeneration. *J Oral Biosci* 2013; **55**: 217-223.

193. Young S, Patel ZS, Kretlow JD, Murphy MB, Mountziaris PM, Baggett LS *et al.* Dose effect of dual delivery of vascular endothelial growth factor and bone morphogenetic protein-2 on bone regeneration in a rat critical-size defect model. *Tissue Eng Part A* 2009; **15**: 2347-2362.

194. Nakaguchi K, Jinnou H, Kaneko N, Sawada M, Hikita T, Saitoh S *et al.* Growth factors released from gelatin hydrogel microspheres increase new neurons in the adult mouse brain. *Stem Cells Int* 2012; **2012**: 915160.

195. Kumagai M, Minakata K, Masumoto H, Yamamoto M, Yonezawa A, Ikeda T *et al.* A therapeutic angiogenesis of sustained release of basic fibroblast growth factor using biodegradable gelatin hydrogel sheets in a canine chronic myocardial infarction model. *Heart Vessels* 2018; **33**: 1251-1257.

196. Kakudo N, Morimoto N, Ogawa T, Hihara M, Notodihardjo PV, Matsui M *et al.* Angiogenic effect of platelet-rich plasma combined with gelatin hydrogel granules injected into murine subcutis. *J Tissue Eng Regen Med* 2017; **11**: 1941-1948.

197. Shibata M, Takagi G, Kudo M, Kurita J, Kawamoto Y, Miyagi Y *et al.* Enhanced Sternal Healing Through Platelet-Rich Plasma and Biodegradable Gelatin Hydrogel. *Tissue Eng Part A* 2018; **24**: 1406-1412.
198. Xu JH, Gao FP, Liu XF, Zeng Q, Guo SS, Tang ZY *et al.* Supramolecular gelatin nanoparticles as matrix metalloproteinase responsive cancer cell imaging probes. *Chem Commun* 2013; **49**: 4462-4464.
199. Tomitaka A, Jo J, Aoki I, Tabata Y. Preparation of biodegradable iron oxide nanoparticles with gelatin for magnetic resonance imaging. *Inflamm and Regen* 2014; **34**: 45-55.
200. Xia DL, Xu PP, Luo XY, Zhu JF, Gu HY, Huo D *et al.* Overcoming Hypoxia by Multistage Nanoparticle Delivery System to Inhibit Mitochondrial Respiration for Photodynamic Therapy. *Adv Funct Mater* 2019; **29**: 1807294.
201. Gupta AK, Gupta M, Yarwood SJ, Curtis AS. Effect of cellular uptake of gelatin nanoparticles on adhesion, morphology and cytoskeleton organisation of human fibroblasts. *J Control Release* 2004; **95**: 197-207.
202. Coester C, Nayyar P, Samuel J. In vitro uptake of gelatin nanoparticles by murine dendritic cells and their intracellular localisation. *Eur J Pharm Biopharm* 2006; **62**: 306-314.
203. Desai MP, Labhasetwar V, Walter E, Levy RJ, Amidon GL. The mechanism of uptake of biodegradable microparticles in Caco-2 cells is size dependent. *Pharm Res* 1997; **14**: 1568-1573.
204. Rejman J, Oberle V, Zuhorn IS, Hoekstra D. Size-dependent internalization of particles via the pathways of clathrin- and caveolae-mediated endocytosis. *Biochem J* 2004; **377**: 159-169.
205. Win KY, Feng SS. Effects of particle size and surface coating on cellular uptake of polymeric nanoparticles for oral delivery of anticancer drugs. *Biomaterials* 2005; **26**: 2713-2722.
206. Gratton SE, Ropp PA, Pohlhaus PD, Luft JC, Madden VJ, Napier ME *et al.* The effect of particle design on cellular internalization pathways. *Proc Natl Acad Sci U S A* 2008; **105**: 11613-11618.

207. Konat Zorzi G, Contreras-Ruiz L, Parraga JE, Lopez-Garcia A, Romero Bello R, Diebold Y *et al.* Expression of MUC5AC in ocular surface epithelial cells using cationized gelatin nanoparticles. *Mol Pharm* 2011; **8**: 1783-1788.

208. Mimi H, Ho KM, Siu YS, Wu A, Li P. Polyethyleneimine-based core-shell nanogels: a promising siRNA carrier for argininosuccinate synthetase mRNA knockdown in HeLa cells. *J Control Release* 2012; **158**: 123-130.

209. Zhang W, Han B, Lai X, Xiao C, Xu S, Meng X *et al.* Stiffness of cationized gelatin nanoparticles is a key factor determining RNAi efficiency in myeloid leukemia cells. *Chem Commun* 2020; **56**: 1255-1258.

210. Kushibiki T, Tomoshige R, Iwanaga K, Kakemi M, Tabata Y. In vitro transfection of plasmid DNA by cationized gelatin prepared from different amine compounds. *J Biomater Sci Polym Ed* 2006; **17**: 645-658.

211. Saito T, Tabata Y. Preparation of gelatin hydrogels incorporating small interfering RNA for the controlled release. *J Drug Target* 2012; **20**: 864-872.

212. Jo J, Nagane K, Yamamoto M, Tabata Y. Effect of amine type on the expression of plasmid DNA by cationized dextran. *J Biomater Sci Polym Ed* 2010; **21**: 225-236.

213. Vermeulen LMP, De Smedt SC, Remaut K, Braeckmans K. The proton sponge hypothesis: Fable or fact? *Eur J Pharm Biopharm* 2018; **129**: 184-190.

214. Wojnilowicz M, Glab A, Bertucci A, Caruso F, Cavalieri F. Super-resolution Imaging of Proton Sponge-Triggered Rupture of Endosomes and Cytosolic Release of Small Interfering RNA. *ACS Nano* 2019; **13**: 187-202.

215. Desai HV, Voruganti IS, Jayasuriya C, Chen Q, Darling EM. Live-cell, temporal gene expression analysis of osteogenic differentiation in adipose-derived stem cells. *Tissue Eng Part A* 2014; **20**: 899-907.

216. Yeo D, Wiraja C, Chuah YJ, Gao Y, Xu C. A Nanoparticle-based Sensor Platform for Cell Tracking and Status/Function Assessment. *Sci Rep* 2015; **5**: 14768.

217. Pittenger MF, Mackay AM, Beck SC, Jaiswal RK, Douglas R, Mosca JD *et al.* Multilineage potential of adult human mesenchymal stem cells. *Science* 1999; **284**: 143-147.

218. Sekiya I, Larson BL, Vuoristo JT, Cui JG, Prockop DJ. Adipogenic differentiation of human adult stem cells from bone marrow stroma (MSCs). *J Bone Miner Res* 2004; **19**: 256-264.

219. Meinel L, Hofmann S, Betz O, Fajardo R, Merkle HP, Langer R *et al.* Osteogenesis by human mesenchymal stem cells cultured on silk biomaterials: comparison of adenovirus mediated gene transfer and protein delivery of BMP-2. *Biomaterials* 2006; **27**: 4993-5002.

220. Noth U, Rackwitz L, Heymer A, Weber M, Baumann B, Steinert A *et al.* Chondrogenic differentiation of human mesenchymal stem cells in collagen type I hydrogels. *J Biomed Mater Res A* 2007; **83**: 626-635.

221. Tabata Y, Ikada Y. Protein release from gelatin matrices. *Adv Drug Deliv Rev* 1998; **31**: 287-301.

222. Yamamoto M, Ikada Y, Tabata Y. Controlled release of growth factors based on biodegradation of gelatin hydrogel. *J Biomater Sci Polym Ed* 2001; **12**: 77-88.

223. Fukunaka Y, Iwanaga K, Morimoto K, Kakemi M, Tabata Y. Controlled release of plasmid DNA from cationized gelatin hydrogels based on hydrogel degradation. *J Control Release* 2002; **80**: 333-343.

224. Kushibiki T, Tomoshige R, Fukunaka Y, Kakemi M, Tabata Y. In vivo release and gene expression of plasmid DNA by hydrogels of gelatin with different cationization extents. *J Control Release* 2003; **90**: 207-216.

225. Young S, Wong M, Tabata Y, Mikos AG. Gelatin as a delivery vehicle for the controlled release of bioactive molecules. *J Control Release* 2005; **109**: 256-274.

226. Kushibiki T, Tomoshige R, Iwanaga K, Kakemi M, Tabata Y. Controlled release of plasmid DNA from hydrogels prepared from gelatin cationized by different amine compounds. *J Control Release* 2006; **112**: 249-256.

227. Hori K, Sotozono C, Hamuro J, Yamasaki K, Kimura Y, Ozeki M *et al.* Controlled-release of epidermal growth factor from cationized gelatin hydrogel enhances corneal epithelial wound healing. *J Control Release* 2007; **118**: 169-176.

228. Lin X, Jo H, Ishii TM, Fujita M, Fu M, Tambara K *et al.* Controlled release of matrix

metalloproteinase-1 plasmid DNA prevents left ventricular remodeling in chronic myocardial infarction of rats. *Circ J* 2009; **73**: 2315-2321.

229. Obata Y, Nishino T, Kushibiki T, Tomoshige R, Xia Z, Miyazaki M *et al.* HSP47 siRNA conjugated with cationized gelatin microspheres suppresses peritoneal fibrosis in mice. *Acta Biomater* 2012; **8**: 2688-2696.
230. Kim YH, Tabata Y. Dual-controlled release system of drugs for bone regeneration. *Adv Drug Deliv Rev* 2015; **94**: 28-40.
231. Doi N, Jo J, Tabata Y. Preparation of Biodegradable Gelatin Nanospheres with a Narrow Size Distribution for Carrier of Cellular Internalization of Plasmid DNA. *J Biomater Sci Polym Ed* 2012; **23**: 991-1004.
232. Ishikawa H, Nakamura Y, Jo J, Tabata Y. Gelatin nanospheres incorporating siRNA for controlled intracellular release. *Biomaterials* 2012; **33**: 9097-9104.
233. Wiraja C, Yeo DC, Chong MS, Xu C. Nanosensors for Continuous and Noninvasive Monitoring of Mesenchymal Stem Cell Osteogenic Differentiation. *Small* 2016; **12**: 1342-1350.
234. Wiraja C, Yeo DC, Tham KC, Chew SWT, Lim X, Xu C. Real-Time Imaging of Dynamic Cell Reprogramming with Nanosensors. *Small* 2018; **14**: e1703440.
235. Zhang J, Nuebel E, Daley GQ, Koehler CM, Teitell MA. Metabolic regulation in pluripotent stem cells during reprogramming and self-renewal. *Cell Stem Cell* 2012; **11**: 589-595.
236. Folmes CD, Dzeja PP, Nelson TJ, Terzic A. Metabolic plasticity in stem cell homeostasis and differentiation. *Cell Stem Cell* 2012; **11**: 596-606.
237. Ito K, Suda T. Metabolic requirements for the maintenance of self-renewing stem cells. *Nat Rev Mol Cell Biol* 2014; **15**: 243-256.
238. Teslaa T, Teitell MA. Pluripotent stem cell energy metabolism: an update. *EMBO J* 2015; **34**: 138-153.
239. Zhang Y, Marsboom G, Toth PT, Rehman J. Mitochondrial respiration regulates adipogenic differentiation of human mesenchymal stem cells. *PLoS One* 2013; **8**: e77077.
240. Hopkinson BM, Desler C, Kalisz M, Vestentoft PS, Juel Rasmussen L, Bisgaard HC.

Bioenergetic Changes during Differentiation of Human Embryonic Stem Cells along the Hepatic Lineage. *Oxid Med Cell Longev* 2017; **2017**: 5080128.

241. Cliff TS, Wu T, Boward BR, Yin A, Yin H, Glushka JN *et al.* MYC Controls Human Pluripotent Stem Cell Fate Decisions through Regulation of Metabolic Flux. *Cell Stem Cell* 2017; **21**: 502-516.

242. Griffith LG, Swartz MA. Capturing complex 3D tissue physiology in vitro. *Nat Rev Mol Cell Biol* 2006; **7**: 211-224.

243. Baker BM, Chen CS. Deconstructing the third dimension: how 3D culture microenvironments alter cellular cues. *J Cell Sci* 2012; **125**: 3015-3024.

244. Itskovitz-Eldor J, Schuldiner M, Karsenti D, Eden A, Yanuka O, Amit M *et al.* Differentiation of human embryonic stem cells into embryoid bodies compromising the three embryonic germ layers. *Mol Med* 2000; **6**: 88-95.

245. Kurosawa H. Methods for inducing embryoid body formation: in vitro differentiation system of embryonic stem cells. *J Biosci Bioeng* 2007; **103**: 389-398.

246. Okada Y, Matsumoto A, Shimazaki T, Enoki R, Koizumi A, Ishii S *et al.* Spatiotemporal recapitulation of central nervous system development by murine embryonic stem cell-derived neural stem/progenitor cells. *Stem Cells* 2008; **26**: 3086-3098.

247. Czepiel M, Balasubramaniyan V, Schaafsma W, Stancic M, Mikkers H, Huisman C *et al.* Differentiation of induced pluripotent stem cells into functional oligodendrocytes. *Glia* 2011; **59**: 882-892.

248. Kattman SJ, Witty AD, Gagliardi M, Dubois NC, Niapour M, Hotta A *et al.* Stage-specific optimization of activin/nodal and BMP signaling promotes cardiac differentiation of mouse and human pluripotent stem cell lines. *Cell Stem Cell* 2011; **8**: 228-240.

249. Mahmood A, Harkness L, Schroder HD, Abdallah BM, Kassem M. Enhanced differentiation of human embryonic stem cells to mesenchymal progenitors by inhibition of TGF-beta/activin/nodal signaling using SB-431542. *J Bone Miner Res* 2010; **25**: 1216-1233.

250. Nakajima-Takagi Y, Osawa M, Oshima M, Takagi H, Miyagi S, Endoh M *et al.* Role of

SOX17 in hematopoietic development from human embryonic stem cells. *Blood* 2013; **121**: 447-458.

251. Knight E, Przyborski S. Advances in 3D cell culture technologies enabling tissue-like structures to be created in vitro. *J Anat* 2015; **227**: 746-756.

252. Ravi M, Paramesh V, Kaviya SR, Anuradha E, Solomon FD. 3D cell culture systems: advantages and applications. *J Cell Physiol* 2015; **230**: 16-26.

253. van Duinen V, Trietsch SJ, Joore J, Vulto P, Hankemeier T. Microfluidic 3D cell culture: from tools to tissue models. *Curr Opin Biotechnol* 2015; **35**: 118-126.

254. Nath S, Devi GR. Three-dimensional culture systems in cancer research: Focus on tumor spheroid model. *Pharmacol Ther* 2016; **163**: 94-108.

255. Duan B. State-of-the-Art Review of 3D Bioprinting for Cardiovascular Tissue Engineering. *Ann Biomed Eng* 2017; **45**: 195-209.

256. Ronaldson-Bouchard K, Vunjak-Novakovic G. Organs-on-a-Chip: A Fast Track for Engineered Human Tissues in Drug Development. *Cell Stem Cell* 2018; **22**: 310-324.

257. Iseoka H, Miyagawa S, Fukushima S, Saito A, Masuda S, Yajima S *et al.* Pivotal Role of Non-cardiomyocytes in Electromechanical and Therapeutic Potential of Induced Pluripotent Stem Cell-Derived Engineered Cardiac Tissue. *Tissue Eng Part A* 2018; **24**: 287-300.

258. Matsuo T, Masumoto H, Tajima S, Ikuno T, Katayama S, Minakata K *et al.* Efficient long-term survival of cell grafts after myocardial infarction with thick viable cardiac tissue entirely from pluripotent stem cells. *Sci Rep* 2015; **5**: 16842.

259. Yamashita A, Morioka M, Yahara Y, Okada M, Kobayashi T, Kuriyama S *et al.* Generation of scaffoldless hyaline cartilaginous tissue from human iPSCs. *Stem Cell Reports* 2015; **4**: 404-418.

260. Zhang X, Hu MG, Pan K, Li CH, Liu R. 3D Spheroid Culture Enhances the Expression of Antifibrotic Factors in Human Adipose-Derived MSCs and Improves Their Therapeutic Effects on Hepatic Fibrosis. *Stem Cells Int* 2016; **2016**: 4626073.

261. Petrenko Y, Sykova E, Kubinova S. The therapeutic potential of three-dimensional multipotent mesenchymal stromal cell spheroids. *Stem Cell Res Ther* 2017; **8**: 94.

262. Ong CS, Zhou X, Han J, Huang CY, Nashed A, Khatri S *et al.* In vivo therapeutic applications of cell spheroids. *Biotechnol Adv* 2018; **36**: 494-505.

263. Zanoni M, Piccinini F, Arienti C, Zamagni A, Santi S, Polico R *et al.* 3D tumor spheroid models for in vitro therapeutic screening: a systematic approach to enhance the biological relevance of data obtained. *Sci Rep* 2016; **6**: 19103.

264. Kessel S, Cribbes S, Dery O, Kuksin D, Sincoff E, Qiu J *et al.* High-Throughput 3D Tumor Spheroid Screening Method for Cancer Drug Discovery Using Celigo Image Cytometry. *SLAS Technol* 2017; **22**: 454-465.

265. Antunes J, Gaspar VM, Ferreira L, Monteiro M, Henrique R, Jeronimo C *et al.* In-air production of 3D co-culture tumor spheroid hydrogels for expedited drug screening. *Acta Biomater* 2019; **94**: 392-409.

266. Huch M, Koo BK. Modeling mouse and human development using organoid cultures. *Development* 2015; **142**: 3113-3125.

267. Takata N, Abbey D, Fiore L, Acosta S, Feng R, Gil HJ *et al.* An Eye Organoid Approach Identifies Six3 Suppression of R-spondin 2 as a Critical Step in Mouse Neuroretina Differentiation. *Cell Rep* 2017; **21**: 1534-1549.

268. Pollen AA, Bhaduri A, Andrews MG, Nowakowski TJ, Meyerson OS, Mostajo-Radji MA *et al.* Establishing Cerebral Organoids as Models of Human-Specific Brain Evolution. *Cell* 2019; **176**: 743-756.

269. Dutta D, Heo I, Clevers H. Disease Modeling in Stem Cell-Derived 3D Organoid Systems. *Trends Mol Med* 2017; **23**: 393-410.

270. Kim H, Park HJ, Choi H, Chang Y, Park H, Shin J *et al.* Modeling G2019S-LRRK2 Sporadic Parkinson's Disease in 3D Midbrain Organoids. *Stem Cell Reports* 2019; **12**: 518-531.

271. Sachs N, Papaspyropoulos A, Zomer-van Ommen DD, Heo I, Bottinger L, Klay D *et al.* Long-term expanding human airway organoids for disease modeling. *EMBO J* 2019; **38**: e100300.

272. Broutier L, Mastrogiovanni G, Verstegen MM, Francies HE, Gavarro LM, Bradshaw CR *et al.* Human primary liver cancer-derived organoid cultures for disease modeling and

drug screening. *Nat Med* 2017; **23**: 1424-1435.

273. Lee SH, Hu W, Matulay JT, Silva MV, Owczarek TB, Kim K *et al.* Tumor Evolution and Drug Response in Patient-Derived Organoid Models of Bladder Cancer. *Cell* 2018; **173**: 515-528.

274. Kim M, Mun H, Sung CO, Cho EJ, Jeon HJ, Chun SM *et al.* Patient-derived lung cancer organoids as in vitro cancer models for therapeutic screening. *Nat Commun* 2019; **10**: 3991.

275. Saito Y, Muramatsu T, Kanai Y, Ojima H, Sukeda A, Hiraoka N *et al.* Establishment of Patient-Derived Organoids and Drug Screening for Biliary Tract Carcinoma. *Cell Rep* 2019; **27**: 1265-1276.

276. Takebe T, Enomura M, Yoshizawa E, Kimura M, Koike H, Ueno Y *et al.* Vascularized and Complex Organ Buds from Diverse Tissues via Mesenchymal Cell-Driven Condensation. *Cell Stem Cell* 2015; **16**: 556-565.

277. Lebreton F, Lavallard V, Bellofatto K, Bonnet R, Wassmer CH, Perez L *et al.* Insulin-producing organoids engineered from islet and amniotic epithelial cells to treat diabetes. *Nat Commun* 2019; **10**: 4491.

278. Lenti E, Bianchessi S, Proulx ST, Palano MT, Genovese L, Raccosta L *et al.* Therapeutic Regeneration of Lymphatic and Immune Cell Functions upon Lympho-organoid Transplantation. *Stem Cell Reports* 2019; **12**: 1260-1268.

279. Ma HL, Jiang Q, Han S, Wu Y, Cui Tomshine J, Wang D *et al.* Multicellular tumor spheroids as an in vivo-like tumor model for three-dimensional imaging of chemotherapeutic and nano material cellular penetration. *Mol Imaging* 2012; **11**: 487-498.

280. Jarockyte G, Dapkute D, Karabanovas V, Daugmaudis JV, Ivanauskas F, Rotomskis R. 3D cellular spheroids as tools for understanding carboxylated quantum dot behavior in tumors. *Biochim Biophys Acta Gen Subj* 2018; **1862**: 914-923.

PART I

DEVELOPMENT OF IMAGING PROBES AND CELLULAR DELIVERY CARRIERS TO VISUALIZE CELL FUNCTIONS

Chapter 1

Preparation of gelatin nanospheres incorporating quantum dots and iron oxide nanoparticles for multimodal cell imaging

INTRODUCTION

Through the recent progress of tissue engineering as well as stem cell biology, some feasible results on tissue regeneration and repairing have been reported for animal models [1-3]. For the therapeutic achievement of tissue regenerative therapy, it is of prime importance to evaluate the process of cell-based tissue regeneration and repairing. Under these circumstances, the development of technologies and methodologies to visualize the localization and distribution of cells transplanted, is highly required for experimental and clinical purposes.

A multimodal imaging is one of the methods to visualize by more than two imaging modalities, which enable to compensate the disadvantages of each modality, leading to an enhanced reliability of visualization [4-9]. For the effective multimodal cell imaging, it is technically necessary to design and prepare a multimodal probe as well as the carrier to deliver the probe into the target cells.

In this chapter, a multimodal probe to be detected by both the fluorescent and magnetic resonance (MR) imaging modalities was prepared by incorporating the corresponding imaging probes into the nanospheres of gelatin. As the fluorescent and MR imaging probes, quantum dots (QD) with an intense fluorescence and narrow emission spectrum [10, 11] and iron oxide nanoparticles (IONP) of a negative contrast agent [12-14] were used. Various gelatin nanospheres (GNS) incorporating QD and IONP (GNS_{QD}, GNS_{IONP}, and $GNS_{QD+IONP}$) were prepared in different conditions and their physicochemical properties were evaluated. The $GNS_{QD+IONP}$ were treated with octa-arginine (R8) of a cell-penetrating peptide (CPP). When the $GNS_{QD+IONP}$ were incubated with human chondrocytes, the cell viability, the percentage of nanospheres internalized into the cells, and the fluorescent and MR imaging efficiency were investigated.

EXPERIMENTAL

Materials

Gelatin with an isoelectric point of 5.0 and the weight-averaged molecular weight of 100,000, prepared by an alkaline treatment of bovine bone collagen, was kindly supplied from Nitta Gelatin Inc., Osaka, Japan. Qdot 705 ITK Carboxyl Quantum Dots (QD, 8 µM in water) was purchased from Invitrogen Co., Tokyo, Japan. Alkali-treated dextran-coated magnetic iron oxide nanoparticles (IONP, 5 mg Fe/ml in water) was purchased from Meito Sangyo Co., Ltd, Nagoya, Japan. Isooctane, poly(oxyethylene) sorbitan monooleate (Tween 80), glutaraldehyde (GA, 25 wt% in water), glycine, and concentrated hydrochloric acid (HCl) were purchased from Nacalai Tesque. Inc., Kyoto, Japan. Sorbitan monooleate (Span 80) was purchased from Tokyo Chemical Industry Co., Ltd, Tokyo, Japan. R8 was purchased from Sigma-Aldrich Inc., St. Louis, MO, USA. The reagents were used without further purification.

Preparation of GNS, $\mathrm{GNS_{QD}}$, $\mathrm{GNS_{IONP}}$, and $\mathrm{GNS_{QD+IONP}}$

GNS incorporating both QD and IONP were prepared based on the conventional emulsion method [15]. The QD and IONP aqueous solutions (10 µl) were mixed with 2 ml of gelatin aqueous solution at different concentrations (2.0, 5.0, 10, 20, and 50 mg/ml). The mixed solution was added into 40 ml of isooctane containing Tween 80 (480 mg) and Span 80 (480 mg), and then sonicated for 3 min at room temperature to obtain gelatin/isooctane emulsion. The emulsions at various concentrations of GA aqueous solution (0.20, 0.50, 1.0, 2.0, 3.5, and 5.0 wt%) (200 µl) were mixed with isooctane (40 ml), followed by sonication by the same procedures described above to prepare the GA/isooctane emulsion. Then, the GA/isooctane emulsion was mixed with the gelatin/isooctane emulsion. After the sonication for 3 min on ice, the mixed emulsion was agitated by stirring for 3 hr at 4 ℃ to allow gelatin to crosslink in emulsion with GA. Next, the glycine/isooctane emulsion prepared similarly was added to block the aldehyde groups unreacted. The final reactant was centrifuged at 8,500 rpm for 60 min at 4 ℃ to collect the GNS incorporating QD and IONP. The nanospheres ware rinsed with acetone, and then double-distilled water (DDW) by the centrifugation of 5,000 rpm for 5 min at 4 ℃ and 20,000 rpm for 30 min at 4 ℃, respectively. Finally, the GNS incorporating both the QD and IONP ($GNS_{QD+IONP}$) were dispersed in 1 ml of DDW. In this study, other three types of nanospheres, such as empty GNS, GNS incorporating QD (GNS_{QD}), and GNS incorporating IONP (GNS_{IONP}), were also prepared in the same procedure except for using the corresponding QD and IONP at the same concentration.

Characterization of GNS, GNS_{QD}, GNS_{IONP}, and $GNS_{QD+IONP}$

The apparent size and surface zeta potential of nanospheres under a dispersed condition in 10 mM phosphate buffered-saline (PBS, pH7.4) were measured by the dynamic light scattering (DLS) and electrophoretic light scattering (ELS) using Zetasizer Nano-ZS (Malvern Instruments Ltd., Worcestershire, UK). Percentage of QD and IONP incorporated in the GNS was measured by an atomic absorption spectrophotometer of Cd and Fe (AA-6800, Shimadzu Corp., Kyoto, Japan). The experiment was independently performed three times for each of the samples unless otherwise mentioned.

Cell culture experiments

Normal human articular chondrocytes were purchased from Lonza Japan Ltd., Tokyo Japan. The cells were cultured in a chondrocyte basal medium supplemented with CGM^{TM} Bulletkit^{TM} (Lonza Japan Ltd, Tokyo, Japan) and 1 vol% penicillin and streptomycin at 37 °C in a 5% CO_2-95% air atmospheric condition. The cells were detached with 0.25 wt% trypsin-containing 1 mM ethylenediaminetetra acetic acid (EDTA) solution (Nacalai Tesque. Inc., Kyoto, Japan), and continued to culture in 100 mm cell culture dish (Corning Inc., Corning, NY, USA) to allow to grow until to 80% confluency.

Internalization evaluation of $GNS_{QD+IONP}$ into cells

Human chondrocytes were seeded on each well of 6 well multi-dish culture plate (Corning Inc., Corning, NY, USA) at a density of 1×10^5 cells/well, and cultured for 24 hr. The $GNS_{QD+IONP}$ prepared at 5.0 mg/ml of gelatin, 0.5 wt% of GA, and 8 nM of QD, were mixed with 0, 20, 80, and 320 μM of R8 in PBS solution, followed by incubating for 15 min at room temperature to treat the $GNS_{QD+IONP}$. The medium was changed to OPTI MEM (Thermo Fisher

Scientific Inc., Waltham, MA, USA), and then the $\mathrm{GNS_{QD+IONP}}$ treated with R8 were added to each well. After 3 hr incubation, the medium was removed and cells were washed with PBS, and then the fresh basal medium was added. Cells were observed by confocal laser microscopy FV1000-D IX81 (OLYMPUS Co., Ltd., Tokyo, Japan) after 12 hr incubation with $\mathrm{GNS_{QD+IONP}}$.

To evaluate the percentage of $\mathrm{GNS_{QD+IONP}}$ internalized into cells, a flow cytometry analysis was performed. Briefly, the cells were washed with PBS and detached with 0.25 wt% trypsin-containing 1 mM EDTA solution and suspended in 1 ml of PBS. The cell suspension was analyzed on fluorescence activated cell sorting FACSCanto II (Becton Dickinson and Company, Franklin Lakes, NJ, USA), with the excitation and emission wavelengths of 488 and 695 nm, respectively.

Evaluation of cell viability after incubation with $\mathrm{GNS_{QD+IONP}}$

Cells were similarly seeded in 96 well multi-dish culture plate (Corning Inc., Corning, NY, USA) at a density of 1×10^4 cells/well and cultured for 24 hr, and then incubated with $\mathrm{GNS_{QD+IONP}}$ at the same procedure described above. The cell viability was evaluated using a cell counting kit (Nacalai Tesque. Inc., Kyoto, Japan). After 12 hr incubation, the medium was changed to the fresh basal medium, and then 10 μl of 2-(2-methoxy-4-nitrophenyl)-3-(4-nitrophenyl)-5-(2,4-disulfophenyl)-2H-tetrazolium (WST-8) solution was added and further incubated for 3 hr. The absorbance of samples at 450 nm was measured using Multi-mode Microplate Reader (SpectraMax i3x, Molecular Devices Japan Co., Ltd., Tokyo, Japan). The percentage of cell viability was expressed as 100% for cells without $\mathrm{GNS_{QD+IONP}}$ incubation.

MRI measurement of cells incubated with $\mathrm{GNS_{QD+IONP}}$

After incubation with $\mathrm{GNS_{QD+IONP}}$ for 12 hr, cells were washed with PBS and detached similarly, and suspended with saline at a density of 1×10^7 cells/ml. The cell suspension was placed into a 0.2 ml plastic tube (Simport Plastics Ltd., Beloeil, Canada) and subjected to MRI measurement. The MRI measurement was performed using 1.5 T MRmini (DS Pharma Biomedical Co., Ltd, Osaka, Japan) with a computer-controlled console and a 38.5 mm Ø solenoid coil. The sample tube was set in the center of MRI coil and maintained at room temperature. The transverse relaxation time (T_2)-weighted images were obtained by 2D spin-echo multi-slice sequences. The imaging parameters were repetition time (TR)/echo time (TE) of 2000/69 msec, field of view of 40 mm^2, and average number of 1. Additionally, T_2 maps were acquired by different TR/TE ratios of 2000/69, 1880/89, and 1760/109, followed by calculation of T_2 value with Image J software (NIH, Bethesda, MD, USA) using MRI Calc Plugin (http://rsb.info.nih.gov/ij/plugins/mri-analysis.html).

Statistical analysis

The data were expressed as the average ± standard deviation (SD). All the statistical analysis was performed using one-way analysis of variance (ANOVA) with a post-hoc Tukey-Kramer multiple comparison test. *P* values less than 0.05 were considered to be statistically significant.

RESULTS

Characterization of GNS, GNS_{QD}, GNS_{IONP}, and $GNS_{QD+IONP}$

Figure 1A shows the apparent size of GNS, GNS_{QD}, and GNS_{IONP} prepared at different gelatin concentrations. The apparent size tended to increase with an increase in the gelatin concentration for any nanosphere. **Figure 1B** shows the percentage of QD and IONP incorporated in GNS. As the gelatin concentration increased, both the percentages increased and reached a plateau. The percentage of IONP incorporated was higher than that of QD at the corresponding gelatin concentration.

Figures 2A and **2B** show the apparent size and zeta potential of $GNS_{QD+IONP}$ prepared at the same gelatin concentration (5.0 mg/ml) and different GA concentrations. The size and zeta potential of $GNS_{QD+IONP}$ were 162 nm and -6.9 mV, irrespective of the GA concentration. The percentage of IONP incorporated in $GNS_{QD+IONP}$ was constant, whereas that of QD tended to decrease as the GA concentration increased (**Figure 2C**). The $GNS_{QD+IONP}$ prepared at 5.0 mg/ml of gelatin and 0.5 wt% of GA were used in the following experiments.

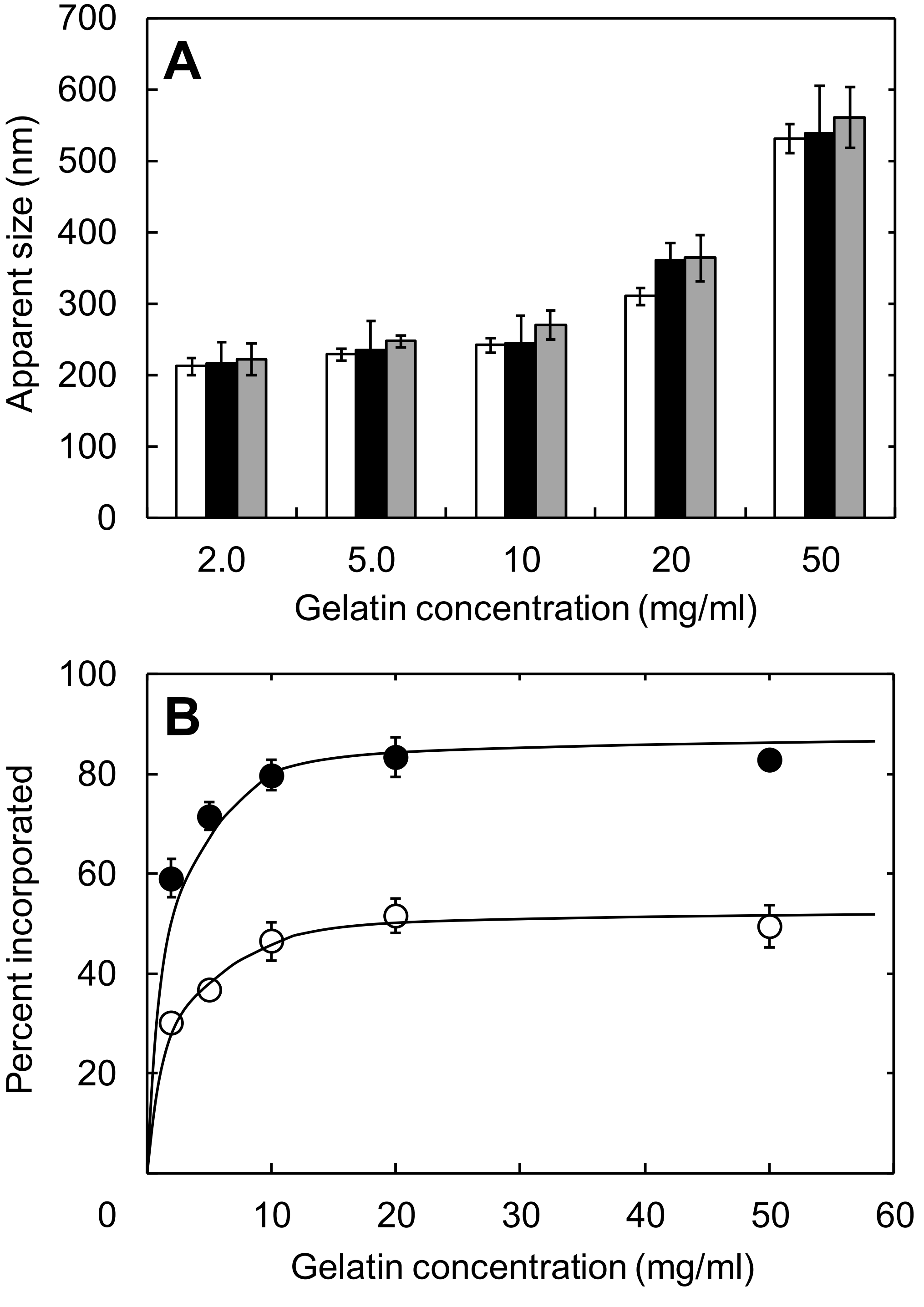

Figure 1. (A) The apparent size of GNS (□), GNS$_{QD}$ (■), and GNS$_{IONP}$ (▨) prepared at different gelatin concentrations. (B) The percentage of QD (○) and IONP (●) incorporated in GNS$_{QD}$ and GNS$_{IONP}$ prepared at different gelatin concentrations.

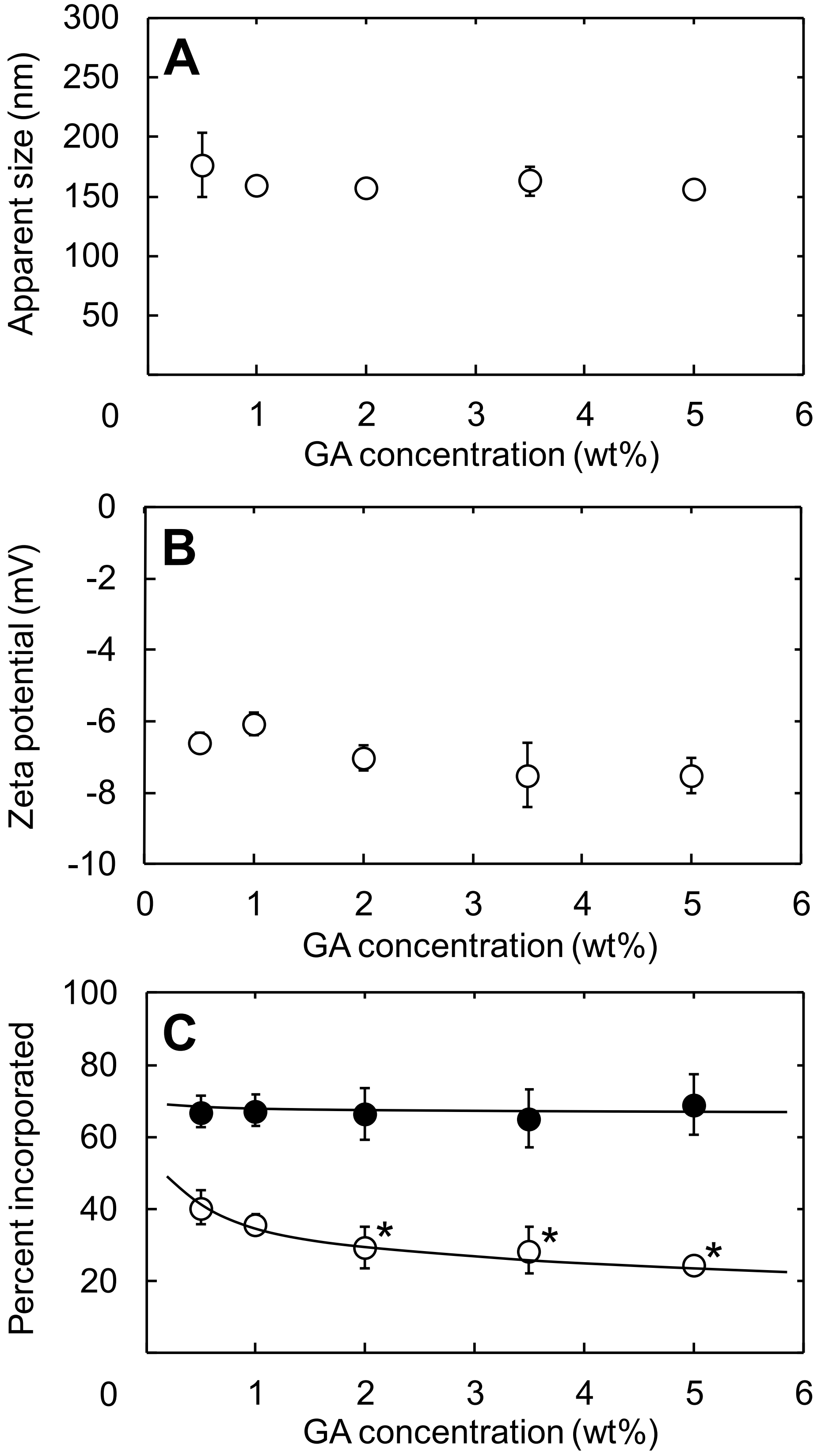

Figure 2. Characterization of GNS$_{QD+IONP}$ prepared at different GA concentrations. The gelatin concentration is all 5.0 mg/ml. (A) The apparent size, (B) zeta potential, and (C) the percentage of QD (○) and IONP (●) incorporated in GNS$_{QD+IONP}$. *, $p < 0.05$; significant against the percentage of QD at the GA concentration of 0.5 wt%.

Cell viability after incubation with $GNS_{QD+IONP}$

Figure 3 shows the cell viability 12 hr after incubation with $GNS_{QD+IONP}$ treated at different concentrations of R8. No cytotoxicity was observed for R8 treated $GNS_{QD+IONP}$ other than the highest concentration of R8 (320 μM).

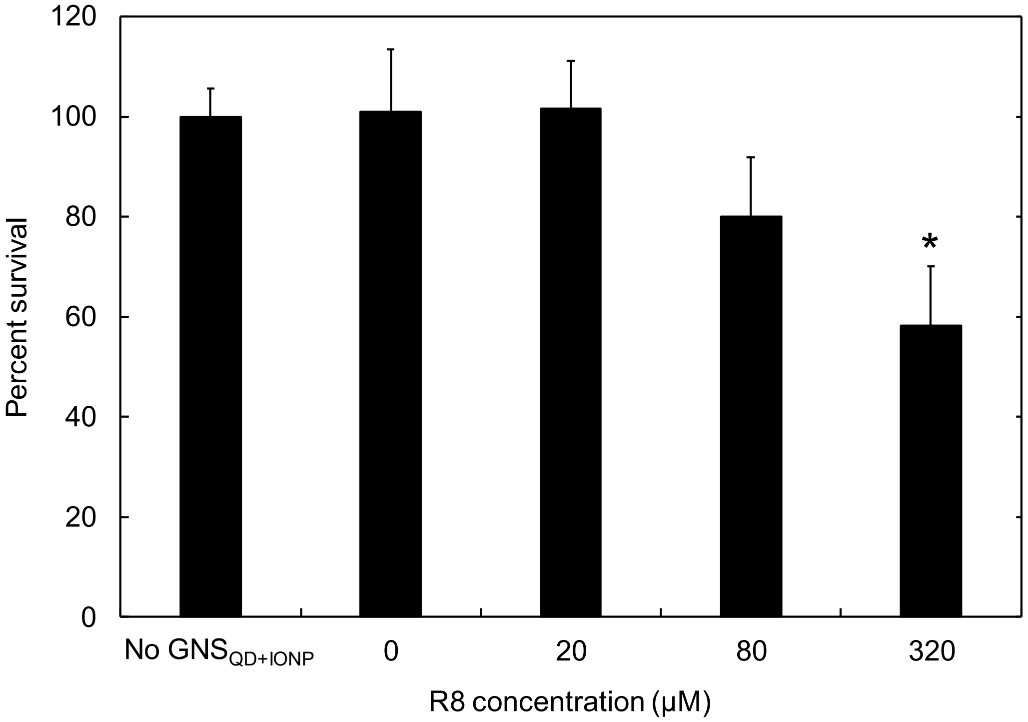

Figure 3. Viability of human chondrocytes 12 hr after incubation with $GNS_{QD+IONP}$ with or without R8 treatment at the concentration of 20, 80, and 320 μM. The viability of cells without $GNS_{QD+IONP}$ incubation is 100% (No $GNS_{QD+IONP}$). The amount of $GNS_{QD+IONP}$ incubated is 0.24 mg. *, $p < 0.05$; significant against the percent survival of cells incubated with no $GNS_{QD+IONP}$.

Internalization of $GNS_{QD+IONP}$ into cells

Figure 4A shows the confocal microscopic pictures of cells 12 hr after incubation with $GNS_{QD+IONP}$ treated with different concentrations of R8. Cell internalization was observed for every $GNS_{QD+IONP}$, irrespective of the R8 concentration. The $GNS_{QD+IONP}$ were homogenously internalized into the large portions of cells. When measured by the flow cytometry (**Figures 4B** and **4C**), the percentage of fluorescent-positive cells increased with increasing R8 concentration to treat $GNS_{QD+IONP}$. The highest percentage was observed at the R8 concentration of 80 μM.

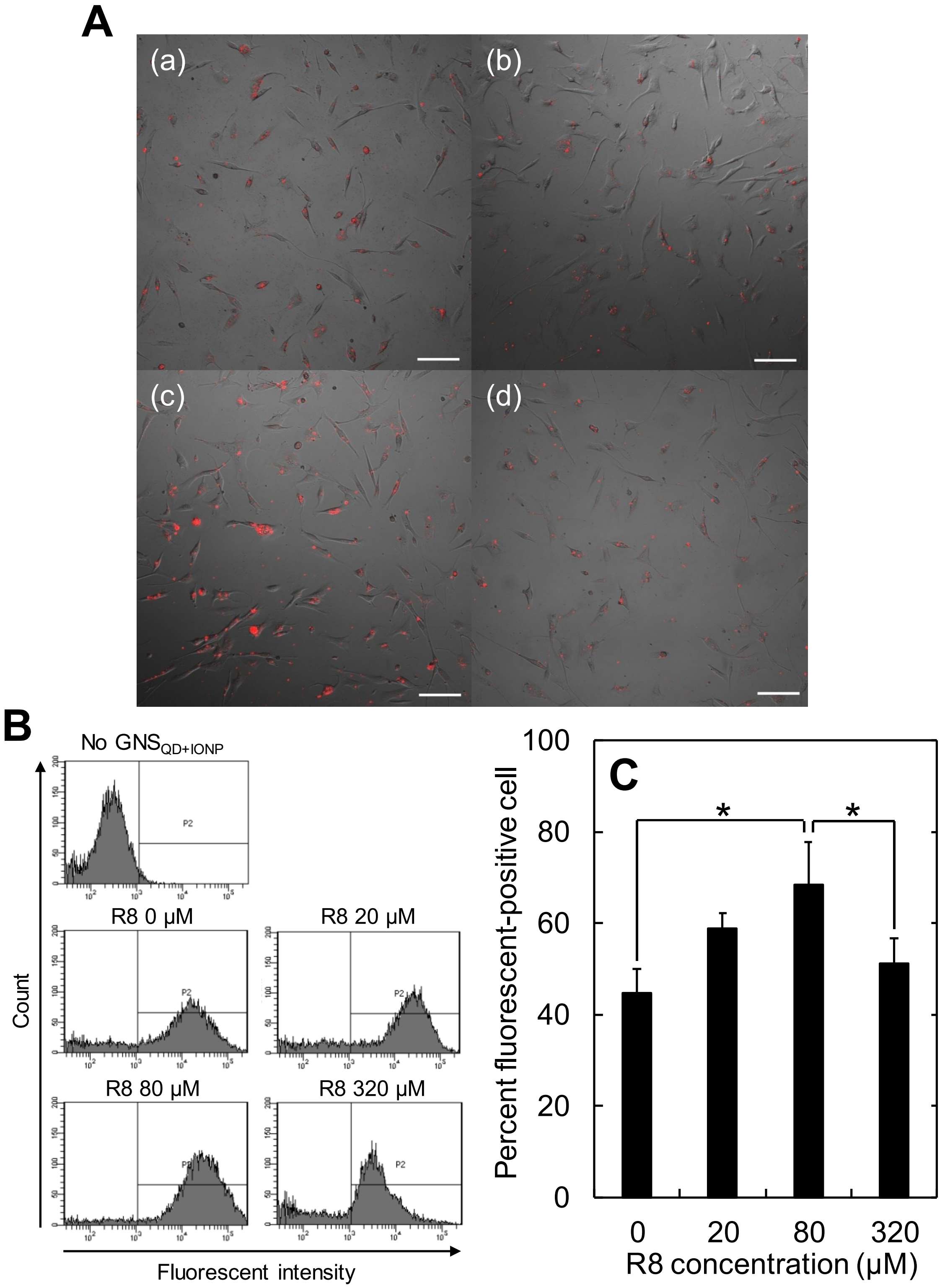

Figure 4. Fluorescent evaluation of human chondrocytes 12 hr after incubation with GNS$_{QD+IONP}$ with or without R8 treatment. (A) Confocal microscopic pictures of cells incubated with GNS$_{QD+IONP}$ treated at 0 (a), 20 (b), 80 (c), and 320 μM of R8 (d). The length of scale bars is 150 μm. (B) The flow cytometry analysis and (C) the percentage of cells labeled. The amount of GNS$_{QD+IONP}$ incubated is 2.4 mg. *, $p < 0.05$; significant between the two groups.

MRI of cells incubated with $GNS_{QD+IONP}$

Figure 5 shows the T_2-weighted MRI images of cells 12 hr after incubation with $GNS_{QD+IONP}$ treated with at the R8 concentration of 80 μM. A clear contrast was detected for cells incubated in contrast to cells without $GNS_{QD+IONP}$ incubation. When calculated from the T_2 map, the T_2 value of cells incubated (88 msec) was smaller than that of non-incubated cells (94 msec).

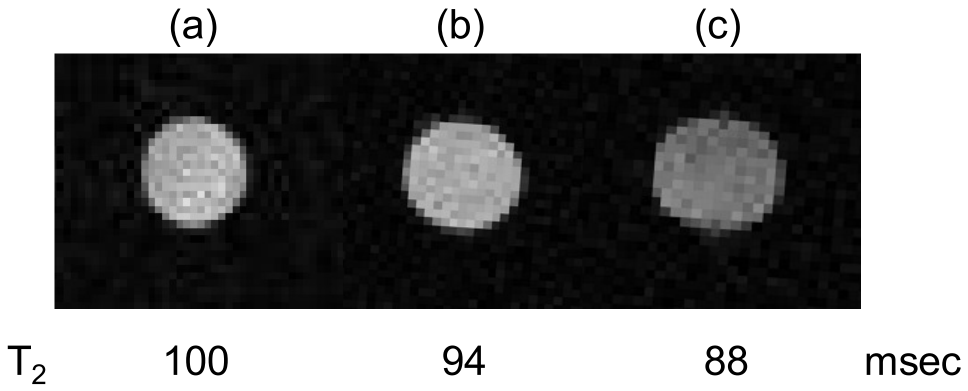

Figure 5. T_2-weighted MRI images and T_2 values of (a) saline, (b) original cells, and (c) human chondrocytes incubated with $GNS_{QD+IONP}$. The amount of $GNS_{QD+IONP}$ incubated is 48 mg.

DISCUSSION

The present study demonstrates that $GNS_{QD+IONP}$ were prepared by the conventional emulsion method, and readily internalized into human chondrocytes by treatment with R8 of a CPP. The cells were visualized by both the fluorescent and MR imaging modalities.

It has been reported that the GNS were prepared by various methods, such as coacervation [16-18], nanoprecipitation [19], and emulsion [20]. Among the preparation methods, nano-sized spheres are formed through the phase separation of gelatin solution by selecting a suitable solvent. To successfully incorporate a substance into GNS, it is technically important to consider the solubility of substance in solvent used for the preparation of GNS. When the solvent used for GNS preparation is miscible to that for the substance, the substance is equally distributed in both the solvents, resulting in the decreased substance incorporation in the GNS. In this study, the solubility of QD and IONP was investigated using acetone, 1-butanol, 2-

butanol, ethanol, and isooctane as the solvent for GNS preparation. Based on this, the poorest solubility of QD and IONP was observed for isooctane. Therefore, the isooctane-based emulsion method was selected to prepare GNS incorporating QD and IONP.

The gelatin concentration affected on the apparent size of GNS, irrespective of the QD and IONP incorporation (**Figure 1A**). It is likely that the water viscosity increased with an increase in the gelatin concentration, resulting in enhanced size of GNS. The gelatin concentration also modified the percentage of QD and IONP incorporated in GNS_{QD} and GNS_{IONP} (**Figure 1B**). This is because an increase in the gelatin concentration leads to an increase of gelatin molecules which can interact with QD and IONP in water phase. On the other hand, the number of gelatin molecules which do not contribute to the formation of nanospheres will increase as the gelatin concentration increases. Taken together, both the percentages of QD and IONP incorporated would increase and reach to a plateau level.

The percentage of QD incorporated in $GNS_{QD+IONP}$ tended to decrease with an increase in the concentration of GA, while that of IONP did not change (**Figure 2C**). The GA concentration affects not only the degree of crosslinking, but also the number of amino groups of GNS. It is possible that the amino groups of gelatin reduced with an increase in the degree of GA crosslinking. On the other hand, both the QD and IONP have a negative charge, although their charge densities are different. Therefore, the reason why the percent incorporation decreased only for QD may be due to the difference of electrostatic interaction strength with gelatin molecules in nanosphere preparation. To modify the internalization of nanospheres into cells, it is important to control the physicochemical properties of nanospheres, such as the apparent size and surface potential. It has been reported that nanospheres of around 150 nm were easy to be taken up by non-phagocytic cells [21]. In this point, $GNS_{QD+IONP}$ of 162 nm prepared are suitable to allow them to internalize into cells. In addition to the control of physicochemical properties, various methodologies have been explored to increase the extent of cell internalization for nanospheres, by making use of some enhancers of CPP [22, 23] or physical stimuli, such as electroporation [24, 25], sonoporation [26], and magnetoporation [27]. R8 is one of CPP widely utilized to allow nano- or micro-spheres or liposomes to internalize into cells [28-32]. Due to the electrostatic interaction between the positive charge of arginine and the negative charge of $GNS_{QD+IONP}$ (**Figure 2B**), it is highly conceivable that R8 easily interacts with $GNS_{QD+IONP}$ to modify the surface. This modification may make the GNS surface positive, resulting in the interaction with cell membranes. Therefore, $GNS_{QD+IONP}$ treated with different concentrations of R8 would be susceptible to the internalization into cells (**Figure 4**). The percentage of $GNS_{QD+IONP}$ internalized increased with an increase in the lower concentrations of R8, but it decreased in the highest concentration. This is because the highest concentration of R8 caused the cytotoxicity (**Figure 3**). It is reported that strong positive charges give cells toxicity [33, 34]. From the experiment, the optimized concentration of R8 is 80 μM in terms of the percent internalized and cytotoxicity (**Figures 3** and **4**). As the toxicity of GNS themselves, it has been experimentally demonstrated that the GNS with concentrations less than 200 μg/ml do not exhibit any cytotoxicity [15]. The $GNS_{QD+IONP}$ treated with the optimized R8 concentration showed a clear MRI image (**Figure 5**).

Gelatin is a biodegradable polymer and degrades enzymatically. Therefore, the GNS would be degraded by intracellular enzymes, such as collagenase, after the internalization into cells. The degradation of GNS is affected by the degree of crosslinking and could be controlled by the GA concentrations [35, 36]. In this study, since $GNS_{QD+IONP}$ can be prepared at different GA concentrations, it is highly expected that the remaining time of $GNS_{QD+IONP}$ in the cells could be controlled.

One of the target tissues is cartilage. As the cartilage injury, the transplantation of chondrocytes is one of promising therapeutic approaches. The survival rate of chondrocytes transplanted is one of the important factors contributing to the success of treatment. Since the self-repairing and regeneration abilities of cartilage tissue are poor [37, 38], it is necessary to develop the technologies and methodologies for the visualization of chondrocytes. In order to develop the chondrocytes transplantation, visualizing the localization and distribution of chondrocytes transplanted are required. Some researches on the imaging of chondrocytes by internalizing nanospheres into chondrocytes are reported [39, 40]. The present study indicates that $GNS_{QD+IONP}$ are efficiently internalized into chondrocytes (**Figure 4**).

Recently, QD have great attention due to the unique fluorescent properties and surface modification, and cells imaging with QD has been investigated [41, 42]. Intracellularly activatable

QD have been developed based on the mechanism of fluorescence resonance energy transfer (FRET) [43, 44] and cleavaged by an intracellular protease [45, 46]. On the other hand, IONP have been widely used for the biomedical applications [47, 48], such as magnetic cell sorting, hyperthermia effect, and excellent negative contrast agent of MRI. In this study, GNS incorporating both QD and IONP were designed to allow to simultaneously visualize cells by fluorescent and MR imaging modalities. When combined with the activatable QD, the nanospheres of the multimodal probe will function as an environment-responsive imaging system which can be changed by responding to a change of intracellular environment. The toxicity of $\mathrm{GNS}_{\mathrm{QD+IONP}}$ and the intracellular fate should be evaluated for the further biomedical applications.

REFERENCES

1. Tabata Y, Hijikata S, Muniruzzaman M, Ikada Y. Neovascularization effect of biodegradable gelatin microspheres incorporating basic fibroblast growth factor. *J Biomater Sci Polym Ed* 1999; **10**: 79-94.
2. Yamamoto M, Takahashi Y, Tabata Y. Controlled release by biodegradable hydrogels enhances the ectopic bone formation of bone morphogenetic protein. *Biomaterials* 2003; **24**: 4375-4383.
3. Bajada S, Mazakova I, Richardson JB, Ashammakhi N. Updates on stem cells and their applications in regenerative medicine. *J Tissue Eng Regen Med* 2008; **2**: 169-183.
4. Louie A. Multimodality imaging probes: design and challenges. *Chem Rev* 2010; **110**: 3146-3195.
5. Lee DE, Koo H, Sun IC, Ryu JH, Kim K, Kwon IC. Multifunctional nanoparticles for multimodal imaging and theragnosis. *Chem Soc Rev* 2012; **41**: 2656-2672.
6. Mitra RN, Doshi M, Zhang X, Tyus JC, Bengtsson N, Fletcher S *et al.* An activatable multimodal/multifunctional nanoprobe for direct imaging of intracellular drug delivery. *Biomaterials* 2012; **33**: 1500-1508.
7. Wen X, Wang Y, Zhang F, Zhang X, Lu L, Shuai X *et al.* In vivo monitoring of neural stem cells after transplantation in acute cerebral infarction with dual-modal MR imaging and optical imaging. *Biomaterials* 2014; **35**: 4627-4635.
8. Ye F, Barrefelt A, Asem H, Abedi-Valugerdi M, El-Serafi I, Saghafian M *et al.* Biodegradable polymeric vesicles containing magnetic nanoparticles, quantum dots and anticancer drugs for drug delivery and imaging. *Biomaterials* 2014; **35**: 3885-3894.
9. Li X, Zhang XN, Li XD, Chang J. Multimodality imaging in nanomedicine and nanotheranostics. *Cancer Biol Med* 2016; **13**: 339-348.
10. Michalet X, Pinaud FF, Bentolila LA, Tsay JM, Doose S, Li JJ *et al.* Quantum dots for live cells, in vivo imaging, and diagnostics. *Science* 2005; **307**: 538-544.
11. Wegner KD, Hildebrandt N. Quantum dots: bright and versatile in vitro and in vivo fluorescence imaging biosensors. *Chem Soc Rev* 2015; **44**: 4792-4834.
12. Jo J, Aoki I, Tabata Y. Design of iron oxide nanoparticles with different sizes and surface

charges for simple and efficient labeling of mesenchymal stem cells. *J Control Release* 2010; **142**: 465-473.

13. Yukawa H, Nakagawa S, Yoshizumi Y, Watanabe M, Saito H, Miyamoto Y *et al.* Novel positively charged nanoparticle labeling for in vivo imaging of adipose tissue-derived stem cells. *PLoS One* 2014; **9**: e110142.
14. Dadfar SM, Roemhild K, Drude NI, von Stillfried S, Knuchel R, Kiessling F *et al.* Iron oxide nanoparticles: Diagnostic, therapeutic and theranostic applications. *Adv Drug Deliv Rev* 2019; **138**: 302-325.
15. Tomitaka A, Jo J, Aoki I, Tabata Y. Preparation of biodegradable iron oxide nanoparticles with gelatin for magnetic resonance imaging. *Inflamm and Regen* 2014; **34**: 45-55.
16. Kommareddy S, Amiji M. Poly(ethylene glycol)-modified thiolated gelatin nanoparticles for glutathione-responsive intracellular DNA delivery. *Nanomedicine* 2007; **3**: 32-42.
17. Tseng CL, Wang TW, Dong GC, Yueh-Hsiu Wu S, Young TH, Shieh MJ *et al.* Development of gelatin nanoparticles with biotinylated EGF conjugation for lung cancer targeting. *Biomaterials* 2007; **28**: 3996-4005.
18. Wong C, Stylianopoulos T, Cui J, Martin J, Chauhan VP, Jiang W *et al.* Multistage nanoparticle delivery system for deep penetration into tumor tissue. *Proc Natl Acad Sci U S A* 2011; **108**: 2426-2431.
19. Lee EJ, Khan SA, Lim KH. Gelatin nanoparticle preparation by nanoprecipitation. *J Biomater Sci Polym Ed* 2011; **22**: 753-771.
20. Allouche J, Boissiere M, Hélary C, Livage J, Coradin T. Biomimetic core–shell gelatine/silica nanoparticles: a new example of biopolymer-based nanocomposites. *J Mater Chem* 2006; **16**: 3120-3125.
21. He C, Hu Y, Yin L, Tang C, Yin C. Effects of particle size and surface charge on cellular uptake and biodistribution of polymeric nanoparticles. *Biomaterials* 2010; **31**: 3657-3666.
22. Tunnemann G, Ter-Avetisyan G, Martin RM, Stockl M, Herrmann A, Cardoso MC. Live-cell analysis of cell penetration ability and toxicity of oligo-arginines. *J Pept Sci* 2008; **14**: 469-476.

23. Copolovici DM, Langel K, Eriste E, Langel U. Cell-penetrating peptides: design, synthesis, and applications. *ACS Nano* 2014; **8**: 1972-1994.

24. Matsuda T, Cepko CL. Electroporation and RNA interference in the rodent retina in vivo and in vitro. *Proc Natl Acad Sci U S A* 2004; **101**: 16-22.

25. Ferrauto G, Delli Castelli D, Terreno E, Aime S. In vivo MRI visualization of different cell populations labeled with PARACEST agents. *Magn Reson Med* 2013; **69**: 1703-1711.

26. Delalande A, Leduc C, Midoux P, Postema M, Pichon C. Efficient Gene Delivery by Sonoporation Is Associated with Microbubble Entry into Cells and the Clathrin-Dependent Endocytosis Pathway. *Ultrasound Med Biol* 2015; **41**: 1913-1926.

27. Liu D, Wang L, Wang Z, Cuschieri A. Magnetoporation and magnetolysis of cancer cells via carbon nanotubes induced by rotating magnetic fields. *Nano Lett* 2012; **12**: 5117-5121.

28. Takeuchi T, Kosuge M, Tadokoro A, Sugiura Y, Nishi M, Kawata M *et al.* Direct and rapid cytosolic delivery using cell-penetrating peptides mediated by pyrenebutyrate. *ACS Chem Biol* 2006; **1**: 299-303.

29. Nakase I, Konishi Y, Ueda M, Saji H, Futaki S. Accumulation of arginine-rich cell-penetrating peptides in tumors and the potential for anticancer drug delivery in vivo. *J Control Release* 2012; **159**: 181-188.

30. Ringhieri P, Diaferia C, Galdiero S, Palumbo R, Morelli G, Accardo A. Liposomal doxorubicin doubly functionalized with CCK8 and R8 peptide sequences for selective intracellular drug delivery. *J Pept Sci* 2015; **21**: 415-425.

31. Motoyama K, Nishiyama R, Maeda Y, Higashi T, Kawaguchi Y, Futaki S *et al.* Cholesterol-Lowering Effect of Octaarginine-Appended beta-Cyclodextrin in Npc1-Trap-CHO Cells. *Biol Pharm Bull* 2016; **39**: 1823-1829.

32. Komin A, Russell LM, Hristova KA, Searson PC. Peptide-based strategies for enhanced cell uptake, transcellular transport, and circulation: Mechanisms and challenges. *Adv Drug Deliv Rev* 2017; **110-111**: 52-64.

33. Fischer D, Li Y, Ahlemeyer B, Krieglstein J, Kissel T. In vitro cytotoxicity testing of polycations: influence of polymer structure on cell viability and hemolysis. *Biomaterials*

2003; **24**: 1121-1131.

34. Frohlich E. The role of surface charge in cellular uptake and cytotoxicity of medical nanoparticles. *Int J Nanomedicine* 2012; **7**: 5577-5591.

35. Doi N, Jo J, Tabata Y. Preparation of Biodegradable Gelatin Nanospheres with a Narrow Size Distribution for Carrier of Cellular Internalization of Plasmid DNA. *J Biomater Sci Polym Ed* 2012; **23**: 991-1004.

36. Ishikawa H, Nakamura Y, Jo J, Tabata Y. Gelatin nanospheres incorporating siRNA for controlled intracellular release. *Biomaterials* 2012; **33**: 9097-9104.

37. Newman AP. Articular cartilage repair. *Am J Sports Med* 1998; **26**: 309-324.

38. Yanaga H, Yanaga K, Imai K, Koga M, Soejima C, Ohmori K. Clinical application of cultured autologous human auricular chondrocytes with autologous serum for craniofacial or nasal augmentation and repair. *Plast Reconstr Surg* 2006; **117**: 2019-2030.

39. Ramaswamy S, Greco JB, Uluer MC, Zhang Z, Zhang Z, Fishbein KW *et al.* Magnetic resonance imaging of chondrocytes labeled with superparamagnetic iron oxide nanoparticles in tissue-engineered cartilage. *Tissue Eng Part A* 2009; **15**: 3899-3910.

40. Chen J, Wang F, Zhang Y, Jin X, Zhang L, Feng Y *et al.* In vivo tracking of superparamagnetic iron oxide nanoparticle labeled chondrocytes in large animal model. *Ann Biomed Eng* 2012; **40**: 2568-2578.

41. Onoshima D, Yukawa H, Baba Y. Multifunctional quantum dots-based cancer diagnostics and stem cell therapeutics for regenerative medicine. *Adv Drug Deliv Rev* 2015; **95**: 2-14.

42. Fan J, Sun Y, Wang S, Li Y, Zeng X, Cao Z *et al.* Inhibition of autophagy overcomes the nanotoxicity elicited by cadmium-based quantum dots. *Biomaterials* 2016; **78**: 102-114.

43. Maxwell T, Banu T, Price E, Tharkur J, Campos MGN, Gesquiere A *et al.* Non-Cytotoxic Quantum Dot–Chitosan Nanogel Biosensing Probe for Potential Cancer Targeting Agent. *Nanomaterials* 2015; **5**: 2359-2379.

44. Mattera L, Bhuckory S, Wegner KD, Qiu X, Agnese F, Lincheneau C *et al.* Compact quantum dot-antibody conjugates for FRET immunoassays with subnanomolar detection limits. *Nanoscale* 2016; **8**: 11275-11283.

45. Chang E, Miller JS, Sun J, Yu WW, Colvin VL, Drezek R *et al.* Protease-activated quantum dot probes. *Biochem Biophys Res Commun* 2005; **334**: 1317-1321.

46. Chung EY, Ochs CJ, Wang Y, Lei L, Qin Q, Smith AM *et al.* Activatable and Cell-Penetrable Multiplex FRET Nanosensor for Profiling MT1-MMP Activity in Single Cancer Cells. *Nano Lett* 2015; **15**: 5025-5032.

47. Tartaj P, Morales MD, Veintemillas-Verdaguer S, Gonzalez-Carreno T, Serna CJ. The preparation of magnetic nanoparticles for applications in biomedicine. *J Phys D Appl Phys* 2003; **36**: R182-R197.

48. Yen SK, Padmanabhan P, Selvan ST. Multifunctional iron oxide nanoparticles for diagnostics, therapy and macromolecule delivery. *Theranostics* 2013; **3**: 986-1003.

Chapter 2

Preparation of cationized gelatin-molecular beacon complexes to visualize intracellular mRNA

INTRODUCTION

For the achievement of cell function imaging with molecular beacons (MB), it is technically necessary to deliver MB into cells. Complexation with carrier materials including transfection reagents, enables MB to internalize into cells due to their nano-size and positive surface charge suitable for cell internalization. It has been reported various materials can be utilized as the carrier of MB [1-9]. In these previous studies, the MB function is mainly investigated, but the properties of carrier materials-MB complexes, such as cytotoxicity, cell internalization, and detection efficiency of MB fluorescence, have not been always investigated well although they are quite important in the materials design.

Gelatin can be readily cationized by simply introducing amino compounds to the carboxyl groups of gelatin to form the complex with nucleic acids [10, 11]. Among the amino compounds, it has been demonstrated that the introduction of spermine showed the highest transfection efficiency [10]. Based on the findings, the spermine-introduced cationized gelatin is focused to allow MB to effectively internalize into cells and subsequently detect the target messenger RNA (mRNA).

In this chapter, the fluorescent detection property of cationized gelatin-MB complexes prepared in various conditions was evaluated. Cationized gelatin with varied cationic extents was prepared for the complexation of MB. The complexes were prepared with different mixing ratios of MB to cationized gelatin to assess their physicochemical and hybridization properties. The cytotoxicity, the amount of cell internalization, and the intracellular fluorescence of complexes were investigated. To evaluate the fluorescent detection of MB, both an endogenous mRNA of glyceraldehyde-3-phosphate dehydrogenase (GAPDH) due to the constant expression and the mRNA of enhanced green fluorescent protein (EGFP) exogenously transfected, were used to optimize the preparation condition of the complexes in terms of MB visualization. As a target cell, mesenchymal stem cells (MSC) which are one of the most promising candidates in cell transplantation therapy due to their high abilities for differentiation, anti-inflammatory, anti-fibrotic and immunoregulation [12-17], were selected to evaluate the technological potential of MB-based imaging.

EXPERIMENTAL

Materials

Gelatin with an isoelectric point of 9.0 and the weight-averaged molecular weight of 99,000, prepared by an acidic treatment of pig skin, was kindly supplied from Nitta Gelatin Inc., Osaka, Japan. MB composed of DNA bases for mouse mRNA of GAPDH was designed by NIPPON GENE Co., Ltd, Tokyo, Japan. On the other hand, the sequence of MB for EGFP mRNA was obtained from the previous report [18]. The MB were synthesized by Integrated DNA Technologies, Inc., Coralville, IA, USA. Target oligonucleotides of DNA for GAPDH MB (specific and non-specific sequences) were synthesized by Hokkaido System Science Co., Ltd, Sapporo, Japan. The sequences of MB and target oligonucleotides were listed in **Table 1**. Spermine was purchased from Sigma-Aldrich Inc., St Louis, MO, USA. Concentrated hydrochloric acid (HCl) and 1-ethyl-3-(3-dimethylaminopropyl) carbodiimide hydrochloride salt (EDC) were purchased from Nacalai Tesque. Inc., Kyoto, Japan. The reagents were used without any purification.

Table 1. Sequences of MB and target oligonucleotides used.

MB and target oligonucleotides	Sequences (5' to 3')
GAPDH MB	[TYE®665]-CTGGTAATCCGTTCACACCGACCTTCACCAG-[IBRQ]
EGFP MB	[TYE®665]-ACGCCTTCTCGTTGGGGTCTTTGCTCGGCGT-[IBRQ]
GAPDH specific target	TGGTGAAGGTCGGTGTGAACGGATT
GAPDH non-specific target	TTTCTGAATGGCCCAGGT

MB: molecular beacons
GAPDH: glyceraldehyde-3-phosphate dehydrogenase
EGFP: enhanced green fluorescent protein
IBRQ: Iowa Black®RQ
underline: stem structure

Preparation of cationized gelatin

Cationized gelatin was prepared according to the method previously reported [10, 19]. Briefly, spermine was added at molar ratios of 1, 3, 5, 10, 20, and 50 to the carboxyl groups of gelatin into 50 ml of double-distilled water (DDW) containing 2.0 g of gelatin. Immediately after that, the solution pH was adjusted to 5.0 with 11 M HCl. EDC was added at the molar ratio of 3 to the carboxyl groups of gelatin before the addition of DDW into solution to adjust the total volume of 100 ml. Then, the solution was stirred at 40 °C for 18 hr and dialyzed against DDW for 3 days with a dialysis membrane (molecular weight cut off = 12,000 to 14,000, Viskase Companies, Inc., Willowbrook, IL, USA) at room temperature. The solution was freeze-dried to obtain cationized gelatins. To determine the percentage of spermine introduced into the carboxyl groups of gelatin, the conventional 2,4,6-trinitrobenzene sulfonic acid (TNBS, FUJIFILM Wako Pure Chemical Inc., Osaka, Japan) method was performed [20]. The names of cationized gelatin (percent introduced: 3.17, 16.9, 25.6, 35.4, 42.9, and 55.2 mole%) were defined as SM1, SM3, SM5, SM10, SM20, and SM50, respectively.

Preparation of cationized gelatin-MB complexes

The complexation of cationized gelatin and MB was performed by simply mixing cationized gelatin solution and MB in DDW at different mixing ratios (5, 10, 20, 40, and 200 pmole MB/µg cationized gelatin). The mixed solution was incubated for 15 min at room temperature to obtain the cationized gelatin-MB complexes. The apparent size of complexes resuspended in 10 mM phosphate buffered saline solution (PBS, pH7.4) was measured by dynamic light scattering (DLS, Zetasizer Nano-ZS, Malvern Instruments Ltd., Worcestershire, UK). On the other hand, the zeta potential of complexes resuspended in 10 mM phosphate buffer solution (PB, pH7.4) was measured by electrophoresis light scattering (ELS, Zetasizer Nano-ZS, Malvern Instruments Ltd., Worcestershire, UK). The measurements were independently performed three times unless otherwise mentioned.

Radiolabeling of MB

MB were labeled with radioactive iodine (^{125}I), as the methods previously reported with slight modification [21]. Briefly, MB (5 µl, 50 µM in 0.2 M sodium acetate and 40 mM acetic acid solution, pH5.0) was incubated at 60 °C for 50 min with 2 µl of 0.3 mM Na_2SO_3, 5 µl of $Na^{125}I$ (740 MBq/ml in 0.1 M NaOH aqueous solution, PerkinElmer Inc., Waltham, MA, USA), and 5 µl of 4 mM $TlCl_3$. Then, 100 µl of 0.1 M Na_2SO_3, and 900 µl of 0.1 M NaCl, 50 mM Tris, and 1 mM ethylenediaminetetraacetic acid (EDTA) were added to the solution. After the incubation for 30 min at 60 °C, the mixture was applied on the PD-10 column (GE Healthcare Bio-Sciences Corp. Piscataway, NJ, USA) to remove the free ^{125}I by the gel filtration. The radioactivity of ^{125}I was measured with a gamma counter (Auto Well Gamma System ARC-380 CL, Aloka Co., Ltd, Tokyo, Japan).

Hybridization assay

Various concentrations of target oligonucleotides (GAPDH specific or non-specific sequences, 0, 50, 100, 500, 1000, and 5000 nM) and free GAPDH MB or the complexes were mixed in PBS containing 0.5 mM $MgCl_2$ and 0.9 mM $CaCl_2$. The mixture was incubated for 1 hr at room temperature protected from light. The fluorescent intensity was measured by Multi-mode Microplate Reader (SpectraMax i3x, Molecular Devices Japan Co., Ltd., Tokyo, Japan). The fluorescent intensity was normalized by that of free MB or complex without the target incubation (0 nM).

Cell culture experiments

KUM6 cells (JCRB1202) of a mouse bone marrow-derived MSC line were purchased from JCRB Cell Bank (National Institute of Biomedical Innovation, Health and Nutrition, Osaka, Japan). The cells were cultured in Iscove’s Modified Dulbecco’s Medium (IMDM, Thermo Fisher Scientific Inc., Waltham, MA, USA) containing 10 vol% bovine fetal calf serum (FCS, GE healthcare Life Sciences Hyclone laboratories inc., Logan, UT, USA) and 1 vol% penicillin/streptomycin (Nacalai Tesque. Inc., Kyoto, Japan) at 37 °C in a 5% CO_2-95% air atmospheric condition. The cells were detached with 0.25 wt% trypsin-containing 1 mM EDTA solution (Nacalai Tesque. Inc., Kyoto, Japan) and continued to culture in 100 mm cell culture dish (Corning Inc., Corning, NY, USA) to allow to grow until to 80% confluency.

Evaluation of cell viability after incubation with complexes

Cells were seeded on each well of 96 well multi-dish culture plate (Corning Inc., Corning, NY, USA) at a density of 1 × 10^4 cells/well and cultured for 24 hr. Then, the medium was changed to OPTI MEM (Thermo Fisher Scientific Inc., Waltham, MA, USA), followed by the addition of complexes prepared at different mixing ratios (5, 10, 20, 40, and 200 pmole MB/µg cationized gelatin) to each well. The final concentration of GAPDH MB was 200 nM. The cell viability was evaluated using a cell counting kit (Nacalai Tesque. Inc., Kyoto, Japan). After the incubation for 3 hr, 10 µl of 2-(2-methoxy-4-nitrophenyl)-3-(4-nitrophenyl)-5-(2,4-disulfophenyl)-2H-tetrazolium (WST-8) solution was added to each well and further incubated for 1 hr. The absorbance of samples at 450 nm was measured by the microplate reader. The percentage of cell viability was expressed as 100% for cells without incubation of complexes.

Evaluation of cell internalization

The cells were similarly seeded on each well of 6 well multi-dish culture plate (Corning Inc., Corning, NY, USA) at a density of 5 × 10^4 cells/well and cultured for 24 hr. The medium was changed to OPTI MEM before the complexes prepared at different mixing ratios (5, 10, 20, 40, and 200 pmole MB/µg cationized gelatin) were added. The final concentration of GAPDH MB was 200 nM. After the incubation for 3 hr, the cells were washed with PBS, trypsinized, and collected by centrifugation of 2,000 g for 3 min at room temperature. Then, the radioactivity of ^{125}I-labeled MB in the cells was evaluated by the gamma counter. On the other hand, the number of cells after the incubation with the complexes was evaluated by determining the DNA amount [22]. Briefly, the cells were washed with PBS and lysed with saline-sodium citrate (SSC) buffer containing 0.2 mg/ml sodium lauryl sulfate (SDS) solution. Next, 40 µl of cell lysate and 160 µl of 1.25 µg/ml bisbenzimide H33258 fluorochrome trihydrochloride (Hoechst 33258) solution (Nacalai Tesque. Inc., Kyoto, Japan) were mixed to measure the fluorescent intensity by the microplate reader. The cell number was evaluated from the DNA amount determined by the standard curve of cell suspension with different cell numbers.

Evaluation of intracellular fluorescence and imaging of endogenous GAPDH mRNA

The cells were seeded on a glass bottom dish of 35 mm in diameter (Matsunami Glass Industries, Ltd., Tokyo, Japan) at a density of 5 × 10^4 cells/dish and cultured for 24 hr. The medium was changed to OPTI MEM, and cells were incubated with complexes prepared at different mixing ratios (5, 10, 20, 40, and 200 pmole MB/μg cationized gelatin) for 3 hr. The final concentration of GAPDH MB was 200 nM. After the further incubation of 24 hr, the cells were observed by a fluorescent microscope (BZ-X700, KEYENCE Co., Ltd., Osaka, Japan) with a 20× objective lens. To quantitatively evaluate the fluorescent intensity of MB, flow cytometry analysis was performed. The cells were washed with PBS to remove the dead cells, and collected by the trypsinization and suspended in PBS. The cell suspension was analyzed on fluorescence activated cell sorting FACSCanto II (Becton Dickinson and Company, Franklin Lakes, NJ, USA) by counting 10,000 cells. On the other hand, to evaluate the intracellular localization of MB, cells which had been incubated with the complex prepared at 20 pmole MB/μg cationized gelatin, were fixed with 4 vol% paraformaldehyde for 20 min, and then the nuclei of cells were stained with 300 nM 4’,6-diamidino-2-phenylindole (DAPI, Thermo Fisher Scientific Inc., Waltham, MA, USA) for 10 min. The fluorescent images were taken by the fluorescent microscopy with an oil-immersed 100× objective lens.

Fluorescent imaging of EGFP mRNA exogenously transfected

The cells were similarly seeded on the glass bottom dish and cultured for 24 hr. Then, the complex prepared at 20 pmole/μg were added (final 200 nM EGFP MB) at the same procedure described above. As a control, the direct delivery of MB to the cytosol via a membrane fusion was performed by using a transfection reagent: Hemagglutinating Virus of Japan (HVJ)-envelope (HVJ-E) (GenomONE™-Si, ISHIHARA SANGYO KAISHA, LTD, Osaka, Japan) according to the manufacture’s instruction. After the incubation with complexes and HVJ-E for 3 hr, the mRNA of EGFP (5000 ng/dish, TriLink BioTechnologies, Inc., San Diego, CA, USA) was transfected by Lipofectamine® MessengerMAX™ (Thermo Fisher Scientific Inc., Waltham, MA, USA) according to the manufacture’s protocol. The cells were observed by the fluorescent microscopy with the oil-immersed 100× objective lens 36 hr later.

Statistical analysis

The data were expressed as the average ± standard deviation (SD). All the statistical analysis was performed using one-way analysis of variance (ANOVA) with a post-hoc Tukey-Kramer multiple comparison test. *P* values less than 0.05 were considered to be statistically significant.

RESULTS

Preparation of cationized gelatin

Table 2 shows the percentage of spermine introduced into the carboxyl groups of gelatin. The percent introduced increased with the increase of spermine addition. In the following experiments, three types of cationized gelatin (SM1, SM10, and SM50) with different extents of cationization were used. The percentages of spermine introduction (cationization extent) were 3.17, 35.4, and 55.2 mole% for SM1, SM10, and SM50, respectively

Table 2. Preparation of cationized gelatin.

Name of cationized gelatin	Molar ratio [a)]	Percent introduced
SM1	1	3.17 ± 0.39 [b)]
SM3	3	16.9 ± 1.55
SM5	5	25.6 ± 1.26
SM10	10	35.4 ± 2.56
SM20	20	42.9 ± 2.54
SM50	50	55.2 ± 3.23

a) Molar ratio of spermine added to the carboxyl groups of gelatin in preparation.
b) Average ± SD.

Characterization of complexes

Tables 3 and **4** show the apparent size and the zeta potential of complexes prepared at different mixing ratios of MB/cationized gelatin, respectively. The apparent size was almost similar, irrespective of the mixing ratio and the cationization extent, while it was around 300 nm. On the other hand, the zeta potential of complexes was influenced by the preparation conditions. The apparent size and zeta potential of complexes prepared at 200 pmole MB/µg cationized gelatin were not detected.

Table 3. Apparent size of complexes prepared.

	Apparent size of complexes (nm)		
Mixing ratio (pmole/µg) [a)]	SM1	SM10	SM50
5	286.0 ± 39.9 [b)]	290.3 ± 38.2	302.3 ± 67.0
10	307.3 ± 53.5	306.1 ± 63.4	299.2 ± 75.4
20	280.8 ± 38.7	307.9 ± 39.1	315.8 ± 28.5
40	309.3 ± 7.50	303.2 ± 32.4	325.3 ± 32.4
200	N.D. [c)]	N.D.	N.D.

a) The amount of MB per 1 µg of cationized gelatin.
b) Average ± SD.
c) Not detected.

Table 4. Zeta potential of complexes prepared.

	Zeta potential of complexes (mV)		
Mixing ratio (pmole/µg) [a)]	SM1	SM10	SM50
5	4.47 ± 0.57 [b)]	8.78 ± 0.27	9.00 ± 0.52
10	3.59 ± 0.22	9.23 ± 0.12	8.31 ± 0.61
20	-5.35 ± 1.53	8.41 ± 0.10	8.58 ± 0.35
40	-15.0 ± 1.11	-14.4 ± 1.38	-21.0 ± 1.66
200	N.D. [c)]	N.D.	N.D.

a) The amount of MB per 1 µg of cationized gelatin.
b) Average ± SD.
c) Not detected.

Hybridization specificity of complexes

The hybridization specificity of free MB and complexes was evaluated (**Figure 1**). The fluorescent intensity of free MB increased with an increase of the specific target concentration. On the contrary, when incubated with the non-specific target, the fluorescent intensity remained as low as that without the target incubation (**Figure 1A**). For the complexes prepared with different cationized gelatins (**Figures 1B**, **1C**, and **1D**), the fluorescent intensity incubated with the specific target became low as the increase of cationization extent. However, the fluorescent intensity incubated with the non-specific target was as low as free MB without target oligonucleotides for any type of complexes.

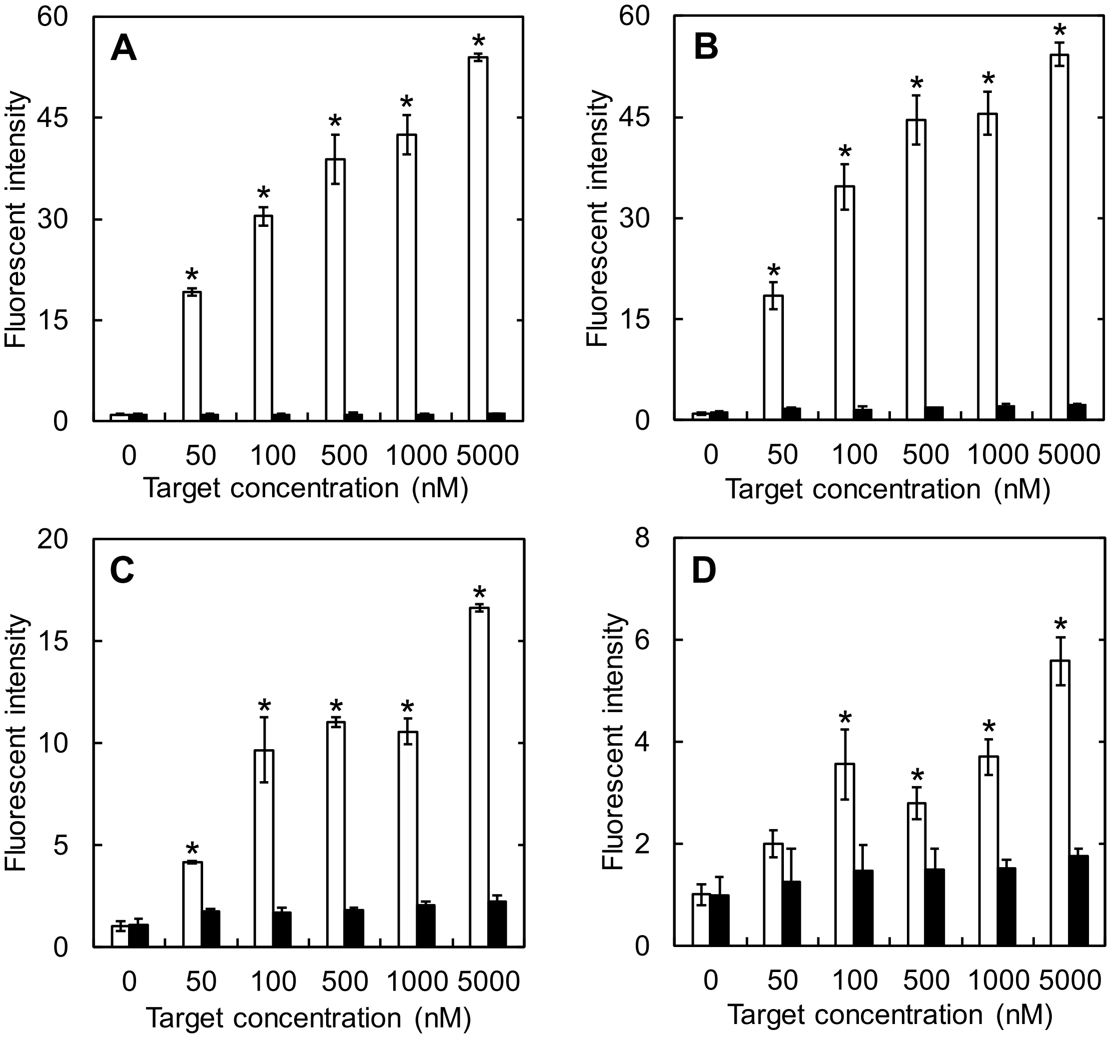

Figure 1. Hybridization specificity of free MB and MB incorporated in complexes. The fluorescent intensity of free MB (A), SM1 (B), SM10 (C), and SM50 complexes (D) mixed with different concentrations of specific (□) and non-specific target oligonucleotides (■). The concentration of GAPDH MB is 100 nM. *, $p < 0.05$; significant against the fluorescent intensity of non-specific target at the corresponding concentration.

Cell viability and MB internalization after incubation with complexes

Figure 2 shows the viability of cells incubated with complexes. The percent survival decreased with a decrease of the mixing ratio, irrespective of the complex type. In addition, the higher cytotoxicity of complexes was observed for the higher extent of cationization. Significant cytotoxicity was observed at 5 and 10 pmole MB/μg cationized gelatin of SM50 complexes and 5 pmole MB/μg cationized gelatin of SM10 complex. For other samples, any cytotoxicity was not seen.

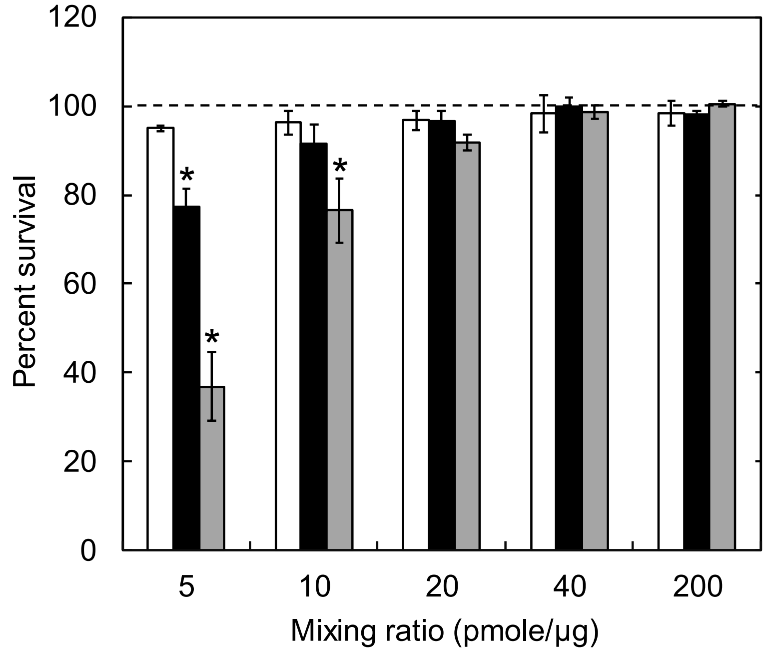

Figure 2. Viability of cells incubated with complexes prepared at various conditions. The cells were incubated with 1, 5, 10, 20, and 40 µg/ml SM1 (☐), SM10 (■), and SM50 complexes (▨). The GAPDH MB concentration is 200 nM. The viability of cells incubated without complex is expressed as 100%. *, $p < 0.05$; significant against the percent survival of cells incubated without complexes at the corresponding mixing ratio.

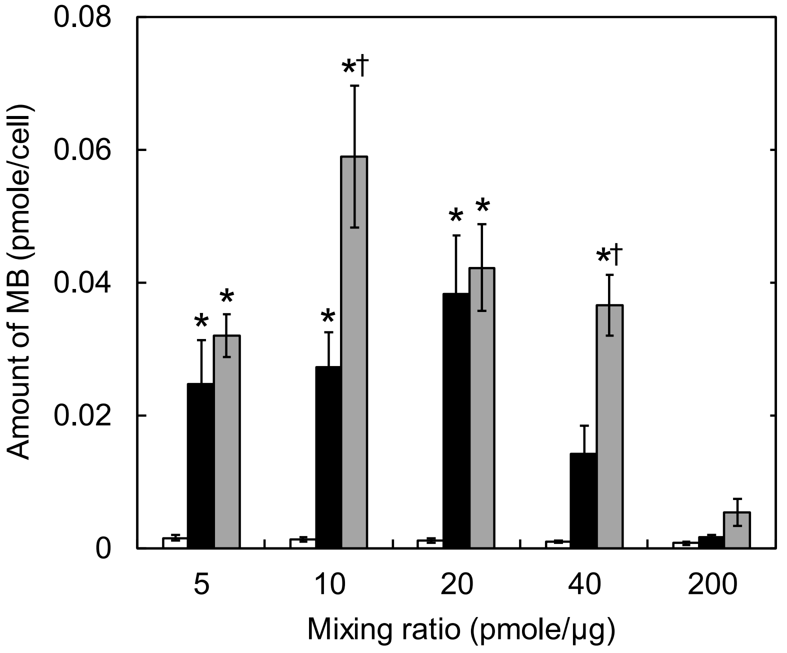

Figure 3. The amounts of MB internalized into cells incubated with complexes prepared at various conditions. The cells were incubated with SM1 (☐), SM10 (■), and SM50 complexes (▨) prepared at different mixing ratios. The GAPDH MB concentration is 200 nM. *, $p < 0.05$; significant against the fluorescent intensity of SM1 complexes at the corresponding mixing ratio. †, $p < 0.05$; significant against the fluorescent intensity of SM10 complexes at the corresponding mixing ratio.

The amounts of complexes internalized into cells were evaluated as a function of mixing ratio (**Figure 3**). For the SM10 and SM50 complexes, the amounts increased and then decreased as the mixing ratio of complexes increased. The highest amount of MB internalized was observed for the SM50 complex prepared at 10 pmole MB/μg cationized gelatin. On the contrary, for the SM1complex, few complexes were internalized into cells.

Evaluation of intracellular fluorescence and imaging of endogenous GAPDH mRNA

GAPDH mRNA was selected as the endogenous target because of the constant expression in each cell. **Figure 4** shows the fluorescent microscopic images of cells incubated with SM1, SM10 and SM50 complexes prepared at various mixing ratios. The fluorescence of SM1 complexes was hardly detected at any mixing ratio (**Figure 4A**). For the complexes

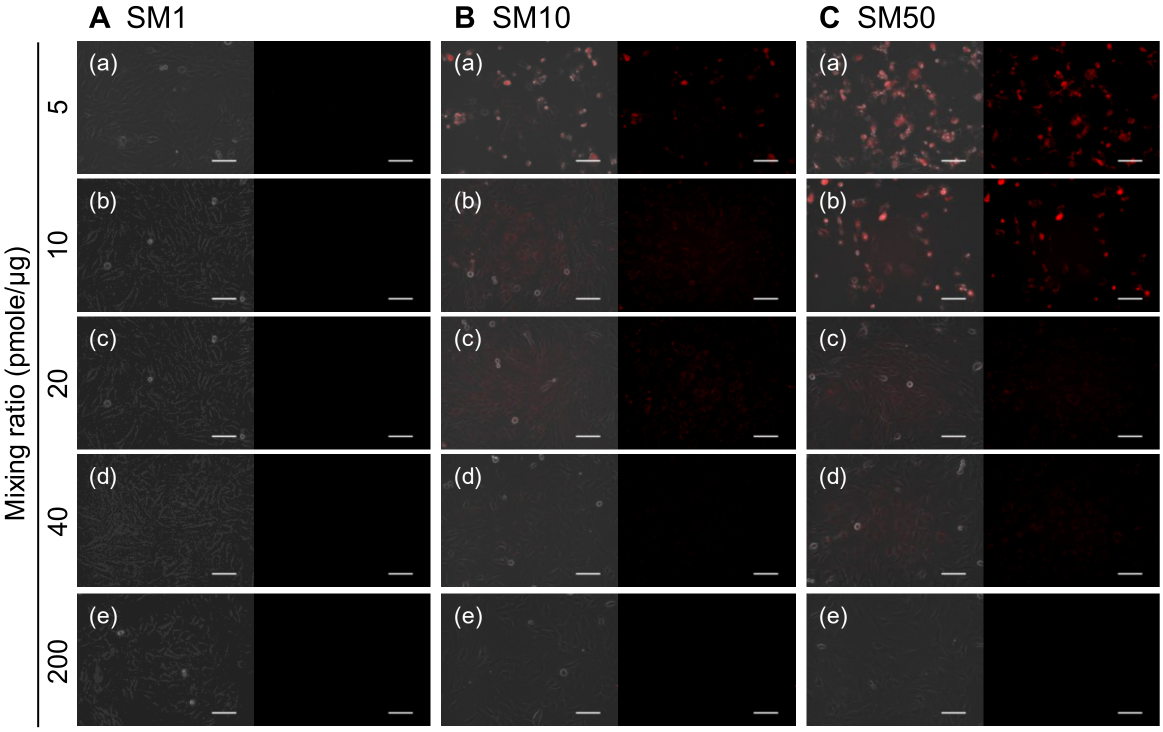

Figure 4. Fluorescent microscopic images of cells incubated with complexes prepared at various conditions. The cells were incubated with SM1 (A), SM10 (B), and SM50 complexes (C) prepared at mixing ratios of 5 (a), 10 (b), 20 (c), 40 (d), and 200 pmole MB/μg cationized gelatin (e). The GAPDH MB concentration is 200 nM. After incubation with complexes for 24 hr, the images were taken. The left panel shows the merged images of phase contrast and MB fluorescence, while the right panel shows the MB fluorescence. Scale bar is 100 μm.

prepared with SM10 and SM50 at 5 pmole MB/μg cationized gelatin (**Figures 4B (a)** and **4C (a)**) and with SM50 at 10 pmole MB/μg cationized gelatin (**Figure 4C (b)**), strong fluorescent spots were observed in dead cells. When compared at the same mixing ratio, the fluorescence tended to become strong with an increase of the cationization extent.

Figure 5 shows the flow cytometric analysis of complexes after the elimination of dead cells. The fluorescent intensity became stronger as the cationization extent increased although this tendency was not seen at the mixing ratio of 200 pmole MB/μg cationized gelatin. Considering the cytotoxicity and fluorescent intensity, the complexes prepared at 20 pmole/μg was used in the following experiments.

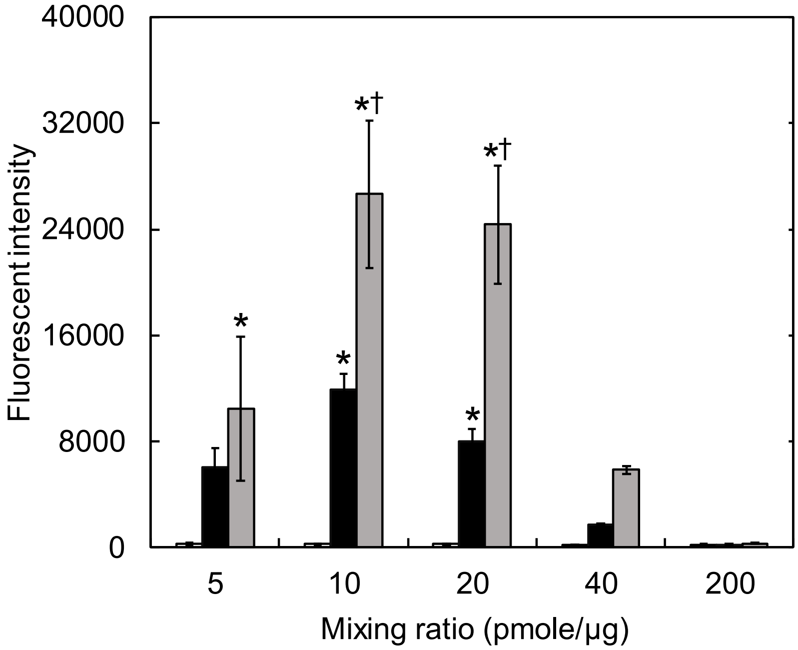

Figure 5. Flow cytometric analysis of cells incubated with complexes prepared at various conditions. The cells were incubated with SM1 (☐), SM10 (■), and SM50 complexes (▨) prepared at different mixing ratios. The GAPDH MB concentration is 200 nM. *, $p < 0.05$; significant against the fluorescent intensity of SM1 complexes at the corresponding mixing ratio. †, $p < 0.05$; significant against the fluorescent intensity of SM10 complexes at the corresponding mixing ratio.

Figure 6 shows the fluorescent microscopic images of cells incubated with the SM1, SM10 and SM50 complexes prepared at 20 pmole MB/μg cationized gelatin. The fluorescence of SM10 and SM50 complexes was observed in the cells, whereas that of SM1 complex was hardly observed. The fluorescent intensity and the number of fluorescent cells incubated with SM50 complex were larger than those incubated with the SM10 complex.

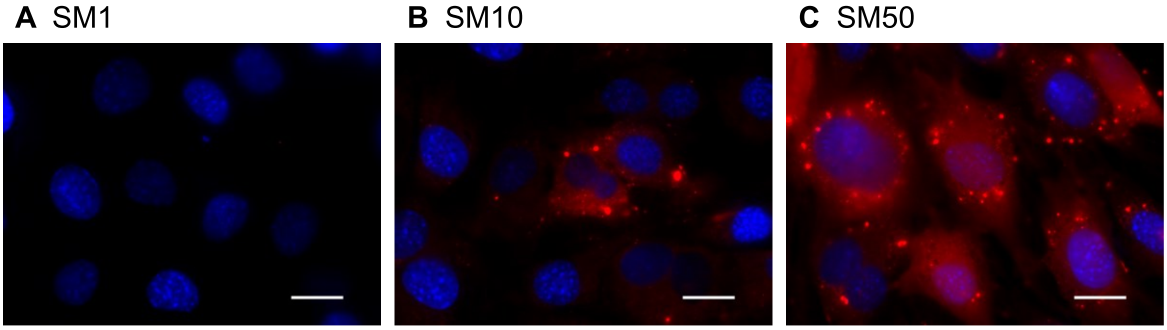

Figure 6. Fluorescent microscopic images of cells incubated with GAPDH MB complexes prepared at 20 pmole/μg. The cells were incubated with SM1 (A), SM10 (B), and SM50 complexes (C) prepared at the mixing ratio of 20 pmole MB/μg cationized gelatin. The GAPDH MB concentration is 200 nM. After the incubation with complexes for 24 hr, the images were taken. Red: GAPDH MB. Blue: nuclei. Scale bar is 20 μm.

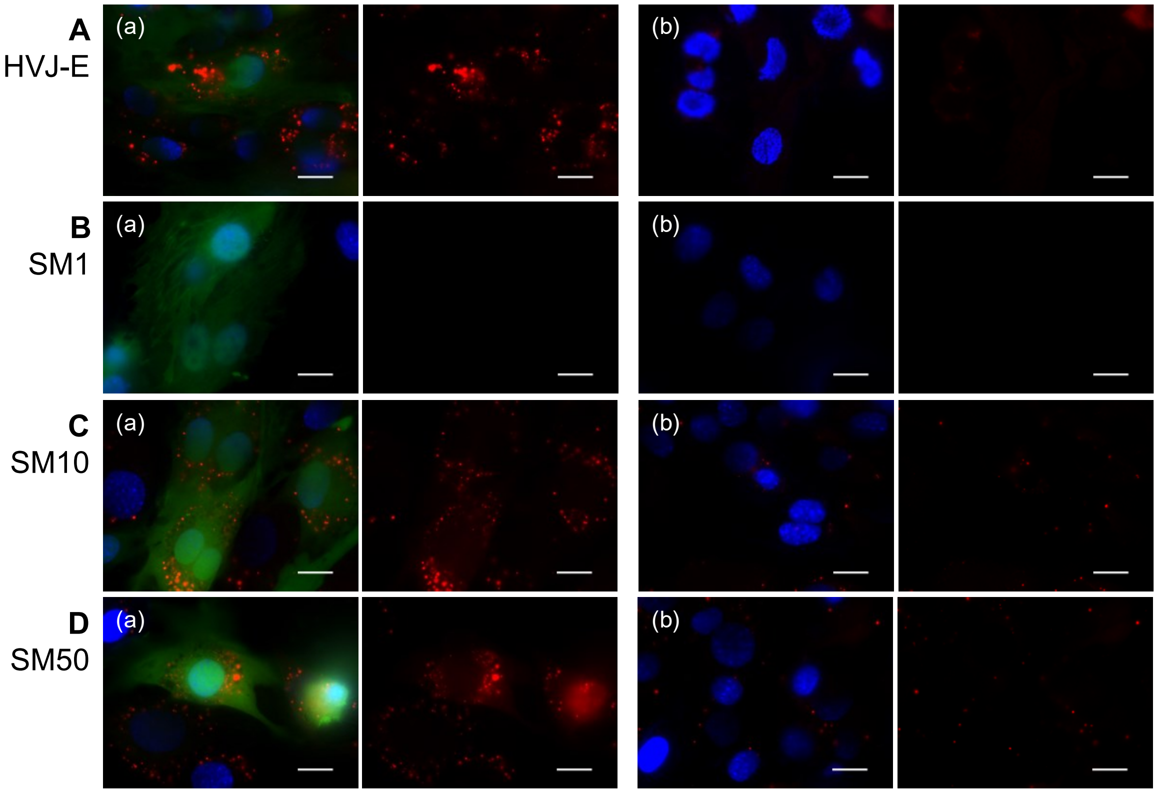

Figure 7. Fluorescent microscopic images of cells incubated with EGFP MB complexes prepared at 20 pmole/μg. The cells were incubated with HVJ-E (A), SM1 (B), SM10 (C), and SM50 complexes (D) prepared at the mixing ratio of 20 pmole MB/μg cationized gelatin. The EGFP MB concentration is 200 nM. After incubation with complexes, (a) EGFP mRNA was transfected by Lipofectamine® MessengerMAX™ 3 hr later or (b) not transfected. The fluorescent images were taken after the transfection for 36 hr. Red: EGFP MB. Green: EGFP. Blue: nuclei. The left panel shows the merged fluorescence, while the right panel shows the MB fluorescence. Scale bar is 20μm.

Imaging of the EGFP mRNA exogenously transfected

To further evaluate the function of complexes, the mRNA of EGFP was exogenously transfected to detect the MB visualization. **Figure 7** shows the fluorescent microscopic images of cells with or without transfection of target EGFP mRNA after incubation with the SM1, SM10, and SM50 complexes prepared at 20 pmole/μg or HVJ-E complexes. For the HVJ-E complex, a stronger fluorescence was detected by the transfection of EGFP mRNA. The fluorescence of SM1 complex was hardly detected, irrespective of the EGFP mRNA transfection. On the contrary, for cells incubated with SM10 and SM50 complexes, a stronger fluorescence was detected by the transfection of EGFP mRNA. Fluorescence was hardly observed even though the EGFP mRNA was not transfected (**Figures 7A (b)**, **7B (b)**, and **7C (b)**).

DISCUSSION

The present study demonstrates that the preparation conditions of cationized gelatin-MB complexes affect their physicochemical properties. In particular, the cationization extent of cationized gelatin was essential. The cytotoxicity, cell internalization, and MB imaging were evaluated by the culture of cells with various complexes. The complexes of highly cationized gelatin at a low mixing ratio showed a high cytotoxicity. On the other hand, for the complexes, the amount of MB internalized into cells was large. This may be because the cationic extent was high or the mixing ratio was low. The fluorescent intensity of complexes in the cells, in other words, the MB detection efficacy, was the highest for the SM50 complex mixed at 20 pmole MB/μg cationized gelatin. This MB detection was observed both the endogenous GAPDH mRNA and EGFP mRNA exogenously transfected. It is possible that this result is due to a balance of cytotoxicity and the MB amount internalized.

The percentage of amino groups introduced increased as the increase of spermine amount to the carboxyl groups in preparation (**Table 2**). However, the percent introduced did not increase even when the molar ratio was higher than 50. It is likely that when the number of spermine conjugated with gelatin increased, new spermine molecules cannot introduce due to the steric hindrance. SM3, SM5, and SM20 were used to preliminarily evaluate both the hybridization and cytotoxicity. The SM3 or SM5 and SM20 showed the intermediate results between SM1 and SM10, and between SM10 and SM50, respectively. These findings suggest that their properties change monotonically as the spermine introduction rate increases. Based on this, to comprehensively evaluate the effect of different spermine introduction extents on the properties of complexes, three types of SM1, SM10, and SM50 cationized gelatin composites with maximum, minimum, and medium percentages of spermine introduced were selected.

It is apparent in **Table 3** that significant change in the complexes size was not observed, irrespective of the mixing ratio. It is conceivable that only some portions of cationized gelatin contribute to the complexation of MB. Consequently, the mixing ratio would not affect the apparent size of complexes. On the other hand, the zeta potential of complexes was influenced by the preparation conditions to change the values (**Table 4**). This can be explained in terms of increased cationic nature of complexes and decreased amount of anionic MB associated with the complexes. The apparent size and zeta potential of complexes prepared at 200 pmole MB/μg cationized gelatin were not measured. It might be possible that the complexes prepared at the mixing ratio of 200 pmole/μg were aggregated to each other by the presence of excessive MB in the solution. In addition, the aggregated complexes might have a heterogeneous size distribution with different surface charges. It is highly conceivable that this heterogeneous aggregation would prevent the accurate measurements of apparent size and zeta potential.

The fluorescent intensity in the hybridization assay of complexes depended on the percent introduced of spermine or the sequences of target nucleotides (**Figure 1**). As one possible reason that the fluorescent intensity decreased as the increase in the percent introduce, the hybridization would be inhibited by the electrostatic interaction of MB with the strongly cationized gelatin. However, it should be noted that the fluorescent intensity of MB incubated with the specific sequence was significantly higher than that with the non-specific sequence for any type of complexes used.

The cell viability decreased as the decreased mixing ratio or the increased percentage of amino groups introduced (**Figure 2**). Since the same amount of MB was incubated with cells, the concentration of cationized gelatin increased with the decreased mixing ratio. Consequently, the cytotoxicity would become higher. At the cationized gelatin concentrations of 40, 40, and 20 μg/ml for SM50, SM10, and SM50, respectively, a significant cytotoxicity was observed. The cationic extent of complexes generally increases with an increase in the percent introduced. This will cause the decreased cell viability. The zeta potential of complexes became large for complexes with a decreased mixing ratio (**Table 4**). It is well known that highly cationic materials show a high cytotoxicity [23-25]. The result of this study is consistent with the reports. Since the cell membrane is of anionic charge, it is likely that cationic materials easily internact with the cell membrane, leading to the subsequent internalization [26, 27]. The same influence of cationized extent on the amount of MB internalized was observed (**Figure 3**). It may be that the amount of complexes internalized is well corresponded with that of MB internalized, since the MB is always associated with the complex.

There was no fluorescence detection for the SM1 complex or complexes prepared at the high mixing ratios (**Figure 4**). Bright spots were observed for the SM50 complexes mixed at 5 or 10 pmole/μg and the SM10 complex mixed at 5 pmole/μg at death cells (**Figure 4**). It is apparent in **Figure 3** that only the small amount of MB was internalized into cells. Taken together, it is highly possible that the cell membrane is damaged, and consequently complexes are easily internalized into cells, leading to a strong fluorescence in cells.

The fluorescent intensity of MB internalized in the flow cytometry assay comes from only the living cells (**Figure 5**), since the death cells were removed before the assay. The fluorescent intensity of the SM50 complex was higher than that of the SM1 and SM10 complexes. The large amount of MB was internalized into cells for the SM50 complex (**Figure 3**). The MB presence in cells would increase the probability of MB reacting with the target mRNA, resulting in an enhanced MB fluorescence. For the complexes at low mixing ratios, the cytotoxicity was high (**Figure 2**). This is due to the high concentration of cationized gelatin, leading to the low fluorescent intensity. In other words, since the dead cells internalizing a large amount of complexes were removed, only the living cells which had internalized a small amount of complexes, were evaluated with the flow cytometry. On the other hand, for the complexes at high mixing ratios, the fluorescent intensity was low (**Figure 5**). Considering the balance between the cytotoxicity and the fluorescent intensity, it is concluded that the SM50 complex prepared at a mixing ratio of 20 pmole MB/μg cationized gelatin is an optimal system to detect the intracellular mRNA in the condition of this study.

In the panels of **Figure 6** for the SM10 and SM50 complexes, the MB was spotted in the cell. It has been demonstrated that the intracellular mRNA was observed as dots in single molecule fluorescence *in situ* hybridization (smFISH) [28].

In the experiment to detect exogenous EGFP mRNA, HVJ-E was used as a positive control. HVJ-E is the particle prepared by inactivating the Hemagglutinating Virus of Japan and has an inherent ability of membrane fusion [29]. Since it is neither infectious nor proliferative, it has been used as a non-viral transfection tool for the genetic materials [29-31]. Because of the membrane fusion ability of HVJ-E, the cargo was directly transfected into cytosol. In the case of HVJ-E complex, MB is inserted into cytoplasm, and hybridize with the target mRNA to allow the fluorescence detection. On the other hand, in the case of cationized gelatin-MB complexes, the mechanism of MB detection is considered as shown below. The complexes are generally internalized into cells by an endocytotic pathway similarly to other transfection reagents of cationic liposome [32]. Since the spermine conjugated to the gelatin facilitates the endosomal escape of complexes by the pH buffering capacity of secondary amino groups in spermine [33], it is likely that the complexes were released in the cytosol and consequently hybridize with the target mRNA. Incidentally, the weak fluorescence of MB was observed even in the cells that is not transfected EGFP mRNA (**Figure 7**). Moreover, in both the GAPDH and EGFP MB, fluorescent dots with different sizes and brightness and the diffused fluorescent background were observed. The reason why fluorescent dots varied and diffused background signal was observed is not clear at present. The background signal might be due to the non-specific fluorescence of MB (**Figure 1**). In the case of smFISH, the detection reactions of mRNA are performed in fixed and dead cells. On the other hand, MB were internalized into living cells in this study. It is highly possible that the local concentrations of intracellular target mRNA and MB are different between the living and fixed/dead cells in terms of spatio-temporal reaction. In addition, the degradation of MB by nucleases [34] and the non-specific interaction with intracellular proteins [35] will be possible reasons of these results. In the preliminary experiments, the SM1, SM10, and SM50 complexes prepared at the mixing ratio of 20 pmole

MB/μg cationized gelatin showed an increased stability against the nuclease (DNase I) with the increase of cationization extent. This can be due to the limited access of DNase I to the MB incorporated in the complexes as well as the inhibited recognition of MB as a substrate of the nuclease. Therefore, the anti-nuclease stability would be enhanced compared with the free MB although further study is required to comprehensively investigate the incorporation ability of MB and the consequent stability for various complexes prepared with different cationized gelatins and mixing ratios. Some modified MB, including 2’-O-methylated RNA [36, 37], locked nucleic acids (LNA) [36, 38], and protein nucleic acids (PNA) [39], have been reported to be effective in avoiding the false-positive signal of MB. In addition to the carrier design of MB, chemical modifications of nucleic acids themselves would be utilized to further increase the specificity of MB and detection accuracy of target mRNA.

In addition to gelatin, various materials are known as carriers to internalize nucleic acid substances into cells [40-45]. In these studies, the cytotoxicity or transfection efficiency is evaluated based on the N/P ratio; the molar ratios of the amino groups of carrier materials to the phosphate groups of nucleic acids, as a main factor. The cytotoxicity and transfection efficacy increase as the N/P ratios increase. This is because the complexes are easily internalized into cells, since the electrostatic interaction between the complexes and the cell membrane becomes stronger [43]. In addition, it is reported that when the N/P ratio increases, the transfection efficiency will reach a maximum, and then decrease [40, 42, 44]. It is claimed that the interaction between the carrier and nucleic acid substance is too strong, which may inhibit the release of nucleic acid in cells [44]. **Table 5** shows the N/P ratios of complexes used in this study. The cytotoxicity and fluorescent intensity of complexes used in this study are evaluated by the N/P ratio. The cytotoxicity increased with the increasing N/P ratios (**Figure 2** and **Table 5**). When compared between the complexes prepared with the same cationized gelatin, the fluorescent intensity increased with an increase of the N/P ratio, reached a maximum value, and then decreased (**Figure 5** and **Table 5**). The decrease of MB fluorescence can be explained in terms of the strong electrostatic interaction between the cationized gelatin and MB in the higher N/P ratios as well as the decreased MB amount internalized into cells (**Figure 3**). The fluorescence was hardly detected with the SM1 complexes, irrespective of the N/P ratios. The fluorescent intensity was influenced by the N/P ratios, and also the amounts of spermine introduced into gelatin.

Table 5. N/P [a)] ratio of complexes prepared.

Mixing ratio (pmole/μg) [b)]	N/P ratio of complexes SM1	 SM10	 SM50
5	2.3	4.0	4.8
10	1.2	2.0	2.4
20	0.58	1.0	1.2
40	0.29	0.51	0.60
200	0.058	0.10	0.12

a) The molar ratio of the amino groups of cationized gelatin to the phosphate groups of MB.
b) The amount of MB per 1 μg of cationized gelatin.

In the present study, the fluorescent detection property of carrier material-MB complexes was focused. The complexes were prepared at various conditions and optimized to visualize both the intracellular endogenous and exogenous mRNA. The physicochemical and hybridization properties, cytotoxicity, the amount of MB internalized into cells, and the resulting fluorescent detection efficacy of MB, were greatly influenced by the preparation conditions of complexes. The findings in this study would be informative for wide research fields, and will contribute to the design of carrier materials used for the delivery of nucleic acids, such as plasmid DNA (pDNA), small interfering RNA (siRNA), as well as MB. To establish the imaging methods with MB, it is technically necessary to improve the sequence specificity of MB by adjusting the nucleotide sequence and to develop MB that emits stronger fluorescence, in addition to optimize the preparation conditions of complexes. This imaging method is not only useful for basic researches, but also applications to the fields of drug discovery, cancer diagnosis, and regenerative medicine including cell transplantation therapy.

REFERENCES

1. Zhang Y, Zhou C, Kwak KJ, Wang X, Yung B, Lee LJ *et al.* Efficient siRNA delivery using a polyamidoamine dendrimer with a modified pentaerythritol core. *Pharm Res* 2012; **29**: 1627-1636.
2. Lin X, Konno T, Ishihara K. Cell-membrane-permeable and cytocompatible phospholipid polymer nanoprobes conjugated with molecular beacons. *Biomacromolecules* 2014; **15**: 150-157.
3. Zhu HZ, An JH, Yao Q, Han J, Li XT, Jiang FL *et al.* Chitosan combined with molecular beacon for mir-155 detection and imaging in lung cancer. *Molecules* 2014; **19**: 14710-14722.
4. Deng D, Li Y, Xue J, Wang J, Ai G, Li X *et al.* Gold nanoparticle-based beacon to detect STAT5b mRNA expression in living cells: a case optimized by bioinformatics screen. *Int J Nanomedicine* 2015; **10**: 3231-3244.
5. Luan M, Yu L, Li Y, Pan W, Gao X, Wan X *et al.* Visualizing Breast Cancer Cell Proliferation and Invasion for Assessing Drug Efficacy with a Fluorescent Nanoprobe. *Anal Chem* 2017; **89**: 10601-10607.
6. Adinolfi B, Pellegrino M, Tombelli S, Trono C, Giannetti A, Domenici C *et al.* Polymeric nanoparticles promote endocytosis of a survivin molecular beacon: Localization and fate of nanoparticles and beacon in human A549 cells. *Life Sci* 2018; **215**: 106-112.
7. Lio DCS, Liu C, Wiraja C, Qiu B, Fhu CW, Wang X *et al.* Molecular Beacon Gold Nanosensors for Leucine-Rich Alpha-2-Glycoprotein-1 Detection in Pathological Angiogenesis. *ACS Sens* 2018; **3**: 1647-1655.
8. Ratajczak K, Krazinski BE, Kowalczyk AE, Dworakowska B, Jakiela S, Stobiecka M. Hairpin-Hairpin Molecular Beacon Interactions for Detection of Survivin mRNA in Malignant SW480 Cells. *ACS Appl Mater Interfaces* 2018; **10**: 17028-17039.
9. Xu C, He XY, Peng Y, Dai BS, Liu BY, Cheng SX. Facile Strategy To Enhance Specificity and Sensitivity of Molecular Beacons by an Aptamer-Functionalized Delivery Vector. *Anal Chem* 2020; **92**: 2088-2096.
10. Kushibiki T, Tomoshige R, Iwanaga K, Kakemi M, Tabata Y. In vitro transfection of

plasmid DNA by cationized gelatin prepared from different amine compounds. *J Biomater Sci Polym Ed* 2006; **17**: 645-658.

11. Saito T, Tabata Y. Preparation of gelatin hydrogels incorporating small interfering RNA for the controlled release. *J Drug Target* 2012; **20**: 864-872.
12. English K. Mechanisms of mesenchymal stromal cell immunomodulation. *Immunol Cell Biol* 2013; **91**: 19-26.
13. Meier RP, Muller YD, Morel P, Gonelle-Gispert C, Buhler LH. Transplantation of mesenchymal stem cells for the treatment of liver diseases, is there enough evidence? *Stem Cell Res* 2013; **11**: 1348-1364.
14. Spees JL, Lee RH, Gregory CA. Mechanisms of mesenchymal stem/stromal cell function. *Stem Cell Res Ther* 2016; **7**: 125.
15. Fu Y, Karbaat L, Wu L, Leijten J, Both SK, Karperien M. Trophic Effects of Mesenchymal Stem Cells in Tissue Regeneration. *Tissue Eng Part B Rev* 2017; **23**: 515-528.
16. Samsonraj RM, Raghunath M, Nurcombe V, Hui JH, van Wijnen AJ, Cool SM. Concise Review: Multifaceted Characterization of Human Mesenchymal Stem Cells for Use in Regenerative Medicine. *Stem Cells Transl Med* 2017; **6**: 2173-2185.
17. Shi Y, Wang Y, Li Q, Liu K, Hou J, Shao C *et al.* Immunoregulatory mechanisms of mesenchymal stem and stromal cells in inflammatory diseases. *Nat Rev Nephrol* 2018; **14**: 493-507.
18. Wiraja C, Yeo DC, Tham KC, Chew SWT, Lim X, Xu C. Real-Time Imaging of Dynamic Cell Reprogramming with Nanosensors. *Small* 2018; **14**: e1703440.
19. Kushibiki T, Tomoshige R, Iwanaga K, Kakemi M, Tabata Y. Controlled release of plasmid DNA from hydrogels prepared from gelatin cationized by different amine compounds. *J Control Release* 2006; **112**: 249-256.
20. Snyder SL, Sobocinski PZ. An improved 2,4,6-trinitrobenzenesulfonic acid method for the determination of amines. *Anal Biochem* 1975; **64**: 284-288.
21. Commerford SL. Iodination of nucleic acids in vitro. *Biochemistry* 1971; **10**: 1993-2000.
22. Anamizu M, Tabata Y. Design of injectable hydrogels of gelatin and alginate with ferric

ions for cell transplantation. *Acta Biomater* 2019; **100**: 184-190.

23. Fischer D, Li Y, Ahlemeyer B, Krieglstein J, Kissel T. In vitro cytotoxicity testing of polycations: influence of polymer structure on cell viability and hemolysis. *Biomaterials* 2003; **24**: 1121-1131.

24. Frohlich E. The role of surface charge in cellular uptake and cytotoxicity of medical nanoparticles. *Int J Nanomedicine* 2012; **7**: 5577-5591.

25. Shao XR, Wei XQ, Song X, Hao LY, Cai XX, Zhang ZR *et al.* Independent effect of polymeric nanoparticle zeta potential/surface charge, on their cytotoxicity and affinity to cells. *Cell Prolif* 2015; **48**: 465-474.

26. Win KY, Feng SS. Effects of particle size and surface coating on cellular uptake of polymeric nanoparticles for oral delivery of anticancer drugs. *Biomaterials* 2005; **26**: 2713-2722.

27. He C, Hu Y, Yin L, Tang C, Yin C. Effects of particle size and surface charge on cellular uptake and biodistribution of polymeric nanoparticles. *Biomaterials* 2010; **31**: 3657-3666.

28. Tsanov N, Samacoits A, Chouaib R, Traboulsi AM, Gostan T, Weber C *et al.* smiFISH and FISH-quant - a flexible single RNA detection approach with super-resolution capability. *Nucleic Acids Res* 2016; **44**: e165.

29. Shimamura M, Morishita R, Endoh M, Oshima K, Aoki M, Waguri S *et al.* HVJ-envelope vector for gene transfer into central nervous system. *Biochem Biophys Res Commun* 2003; **300**: 464-471.

30. Oshima K, Shimamura M, Mizuno S, Tamai K, Doi K, Morishita R *et al.* Intrathecal injection of HVJ-E containing HGF gene to cerebrospinal fluid can prevent and ameliorate hearing impairment in rats. *FASEB J* 2004; **18**: 212-214.

31. Mima H, Tomoshige R, Kanamori T, Tabata Y, Yamamoto S, Ito S *et al.* Biocompatible polymer enhances the in vitro and in vivo transfection efficiency of HVJ envelope vector. *J Gene Med* 2005; **7**: 888-897.

32. Cardarelli F, Digiacomo L, Marchini C, Amici A, Salomone F, Fiume G *et al.* The intracellular trafficking mechanism of Lipofectamine-based transfection reagents and its

implication for gene delivery. *Sci Rep* 2016; **6**: 25879.

33. Jo J, Nagane K, Yamamoto M, Tabata Y. Effect of amine type on the expression of plasmid DNA by cationized dextran. *J Biomater Sci Polym Ed* 2010; **21**: 225-236.
34. Chen AK, Behlke MA, Tsourkas A. Avoiding false-positive signals with nuclease-vulnerable molecular beacons in single living cells. *Nucleic Acids Res* 2007; **35**: e105.
35. Chen AK, Behlke MA, Tsourkas A. Efficient cytosolic delivery of molecular beacon conjugates and flow cytometric analysis of target RNA. *Nucleic Acids Res* 2008; **36**: e69.
36. Catrina IE, Marras SA, Bratu DP. Tiny molecular beacons: LNA/2'-O-methyl RNA chimeric probes for imaging dynamic mRNA processes in living cells. *ACS Chem Biol* 2012; **7**: 1586-1595.
37. Yu S, Li F, Huang X, Dong C, Ren J. In Situ Study of Interactions between Endogenous c-myc mRNA with CRDBP in a Single Living Cell by Combining Fluorescence Cross-Correlation Spectroscopy with Molecular Beacons. *Anal Chem* 2020; **92**: 2988-2996.
38. Wu Y, Yang CJ, Moroz LL, Tan W. Nucleic acid beacons for long-term real-time intracellular monitoring. *Anal Chem* 2008; **80**: 3025-3028.
39. Kam Y, Rubinstein A, Nissan A, Halle D, Yavin E. Detection of endogenous K-ras mRNA in living cells at a single base resolution by a PNA molecular beacon. *Mol Pharm* 2012; **9**: 685-693.
40. Ishii T, Okahata Y, Sato T. Mechanism of cell transfection with plasmid/chitosan complexes. *Biochim Biophys Acta* 2001; **1514**: 51-64.
41. Mao Z, Ma L, Yan J, Yan M, Gao C, Shen J. The gene transfection efficiency of thermoresponsive N,N,N-trimethyl chitosan chloride-g-poly(N-isopropylacrylamide) copolymer. *Biomaterials* 2007; **28**: 4488-4500.
42. Thakor D, Spigelman I, Tabata Y, Nishimura I. Subcutaneous peripheral injection of cationized gelatin/DNA polyplexes as a platform for non-viral gene transfer to sensory neurons. *Mol Ther* 2007; **15**: 2124-2131.
43. Brgles M, Santak M, Halassy B, Forcic D, Tomasic J. Influence of charge ratio of liposome/DNA complexes on their size after extrusion and transfection efficiency. *Int J Nanomedicine* 2012; **7**: 393-401.

44. Cordeiro RA, Santo D, Farinha D, Serra A, Faneca H, Coelho JFJ. High transfection efficiency promoted by tailor-made cationic tri-block copolymer-based nanoparticles. *Acta Biomater* 2017; **47**: 113-123.

45. Maiti B, Kamra M, Karande AA, Bhattacharya S. Transfection efficiencies of alpha-tocopherylated cationic gemini lipids with hydroxyethyl bearing headgroups under high serum conditions. *Org Biomol Chem* 2018; **16**: 1983-1993.

Chapter 3

Preparation of cationized gelatin-molecular beacon complexes and cationized gelatin nanospheres incorporating molecular beacon for intracellular controlled release

INTRODUCTION

One of major limitations of molecular beacons (MB) imaging is the temporal fluorescent activity due to their short remaining time (within several days to 1 week) in the living cells [1, 2]. On the other hand, it is well recognized that cell functions continuously change in the order from day to week. Therefore, it is of prime importance to prolong the intracellular activity of MB to realize the continuous and long-term visualization of cell functions. As one trial to tackle this problem, it is highly expected that the intracellular controlled release of MB from the cationized gelatin nanospheres (cGNS) is a feasible system. In the previous studies, it has been demonstrated that the cGNS can achieve the intracellular controlled release of nucleic acid molecules, such as plasmid DNA (pDNA) [3] and small interfering RNA (siRNA) [4], to prolong their biological activity in the cells. In addition, Chapter 2 demonstrated that the spermine-introduced cationized gelatin was an effective carrier material of MB to visualize the intracellular messenger RNA (mRNA). The preparation condition of cationized gelatin-MB complexes (*i.e.* cationization extent and mixing ratio of MB to cationized gelatin) was optimized from the viewpoint of cytotoxicity, MB amount internalized into cells, and the consequent detection efficiency of MB fluorescence. Based on the findings, the cGNS are prepared to incorporate MB under the optimized condition, and the intracellular controlled release of MB are compared between the cGNS incorporating MB ($\mathrm{cGNS_{MB}}$) and the cationized gelatin-MB complexes. For the easy comparison of MB fluorescence, MB for mRNA of glyceraldehyde-3-phosphate dehydrogenase (GAPDH) of a constantly expressing housekeeping gene is used as a control of stable fluorescence in the cell.

In this chapter, the $\mathrm{cGNS_{MB}}$ and the cationized gelatin-MB complexes (complex) were prepared to evaluate the time period of mRNA visualized. Since the release profile of bioactive molecules from the gelatin hydrogels is regulated by the hydrogel degradability [5-11], the cGNS with different degradabilities were prepared by changing the amount of glutaraldehyde (GA) of a crosslinking reagent to incorporate MB. The release profile of MB was compared between the cGNS$_{MB}$ and complex. The cytotoxicity, the cell internalization, the mechanism of internalization, and the intracellular localization were also investigated. After the cell internalization of cGNS$_{MB}$ and complex, the time period of mRNA visualization was evaluated in terms of the intracellular remaining of MB.

EXPERIMENTAL

Materials

Gelatin with an isoelectric point of 9.0 and the weight-averaged molecular weight of 99,000, prepared by an acidic process of pig skin, was kindly supplied from Nitta Gelatin Inc., Osaka, Japan. MB for mouse mRNA of GAPDH was designed by NIPPON GENE Co., Ltd, Tokyo, Japan, and synthesized by Eurogentec S.A., Seraing, Belgium. The sequence of MB was 5'-[Cy®5]-CTGGTAATCCGTTCACACCGACCTTCACCAG-[BHQ®-2]-3' (BHQ: black hole quencher, underline: stem structure). GA (25 wt% in water), glycine, concentrated hydrochloric acid (HCl), acetone, and 1-ethyl-3-(3-dimethylaminopropyl) carbodiimide hydrochloride salt (EDC) were purchased from Nacalai Tesque. Inc., Kyoto, Japan. Collagenase D was purchased from Roche Diagnostics, Indianapolis, IN, USA. Spermine was purchased from Sigma-Aldrich Inc., St. Louis, MO, USA. The reagents were used without further purification.

Preparation of cationized gelatin

Cationized gelatin was prepared according to the method described in Chapter 2. In brief, spermine was added at molar ratios of 3, 5, 7, 10, 20, and 50 to the carboxyl groups of gelatin into 50 ml of double-distilled water (DDW) containing 2.0 g of gelatin. The solution pH was immediately adjusted to 5.0 by adding 11 M HCl, and DDW was added into the solution to give the final volume of 100 ml. Then, EDC was added at a molar ratio of 3 to the carboxyl groups of gelatin, followed by the agitation at 40 °C for 18 hr and dialysis against DDW for 3 days with a dialysis membrane (molecular weight cut off = 12,000 to 14,000, Viskase Companies, Inc., Willowbrook, IL, USA) at room temperature. The dialyzed solution was freeze-dried to obtain cationized gelatins. The conventional 2,4,6-trinitrobenzene sulfonic acid (TNBS, FUJIFILM Wako Pure Chemical Inc., Osaka, Japan) method was performed to determine the percentage of amino groups introduced into the carboxyl groups of gelatin (percent introduced) [12].

Preparation of cGNS, $cGNS_{MB}$ and complex

According to the preparation procedure previously reported [4], cGNS were prepared by the conventional coacervation method. Briefly, 5 ml of acetone was added to 1.25 ml of cationized gelatin aqueous solution (50 mg/ml) at 40 °C to form coacervate. Immediately after that, GA (20, 40, 60, 80, and 100 µl) was added to the solution, followed by chemically crosslinking for 6 hr. Next, 2 ml of glycine aqueous solution (0.5 M) was added to the solution for the blocking of aldehyde groups unreacted. The resulting solution was agitated overnight at 40 °C and the residual acetone was evaporated. Then, cGNS were collected by the centrifugation of 14,000 rpm for 30 min at 25 °C and resuspended in DDW. The centrifugation and resuspension were repeated three times to wash cGNS.

The cGNS (200 µg/ml) and MB (4 µM) were mixed in DDW (20 pmole MB/µg cGNS) and incubated for 15 min at room temperature. The mixture was centrifuged at 14,000 rpm for 30 min at 25 °C and resuspended in DDW to obtain $cGNS_{MB}$.

The complexation of cationized gelatin and MB was performed by simply mixing cationized gelatin (100 µg/ml) and MB (1.5 µM) in DDW (15 pmole MB/µg cationized gelatin). The mixture was incubated for 15 min at room temperature to obtain a cationized gelatin-MB complex.

Radiolabeling of MB

According to the method described in Chapter 2, MB was labeled with radioactive iodine (^{125}I) [13]. The MB (5 µl, 10 µM in 0.2 M sodium acetate and 40 mM acetic acid solution, pH5.0) was incubated at 60 °C for 50 min with 2 µl of 0.3 mM Na_2SO_3, 5 µl of $Na^{125}I$ (740

MBq/ml in 0.1 M NaOH aqueous solution, PerkinElmer Inc., Waltham, MA, USA), and 5 μl of 4 mM $TlCl_3$. Mixed 100 μl of 0.1 M Na_2SO_3, and 900 μl of 0.1 M NaCl, 50 mM Tris, and 1 mM ethylenediaminetetra acetic acid (EDTA) were added to the solution. After the incubation for 30 min at 60 °C, the mixture was applied on the PD-10 column (GE Healthcare Bio-Sciences Corp., Piscataway, NJ, USA) to separate free ^{125}I from ^{125}I-labeled MB by the gel filtration. The radioactivity of ^{125}I was measured using a gamma counter (Auto Well Gamma System ARC-380 CL, Aloka Co., Ltd, Tokyo, Japan).

Characterization of cGNS, $cGNS_{MB}$, and complex

The apparent size of cGNS, $cGNS_{MB}$, and complex resuspended in 10 mM phosphate buffered-saline solution (PBS, pH7.4) was measured by dynamic light scattering (DLS, Zetasizer Nano-ZS, Malvern Instruments Ltd., Worcestershire, UK). On the other hand, the zeta potential of cGNS, $cGNS_{MB}$, and complex resuspended in 10 mM phosphate buffered solution (PB, pH7.4) was measured by electrophoresis light scattering (ELS, Zetasizer Nano-ZS, Malvern Instruments Ltd., Worcestershire, UK). The amount of MB incorporated in cGNS was determined by the radioactivity of $cGNS_{MB}$ prepared with the ^{125}I-labeled MB. These experiments were performed independently three times for each of the samples unless otherwise mentioned.

Degradation test of cGNS

The cGNS crosslinked with 20, 60, and 100 μl of GA (200 μg) were suspended in 1 ml of PBS, and then incubated at 37 °C. At different time intervals, the PBS supernatant was collected by the centrifugation (14,000 rpm for 10 min at 25 °C) and the nanospheres were resuspended in the same volume of fresh PBS. After 9 hr incubation, PBS was changed to PBS containing 50 μg/ml collagenase, and the supernatant was collected at sampling time points. The amount of cationized gelatin in the supernatant was determined by Micro BCA^{TM} Protein Assay Kit (Thermo Fisher Scientific Inc., Waltham, MA, USA). The standard curve was plotted using bovine serum albumin, and the percent degraded was determined by the total amount detected by the assay and the time point of cGNS disappeared.

Release test of MB from complex and cGNS$_{MB}$

The complex and cGNS$_{MB}$ (200 µg) crosslinked with 20 µl of GA which had been incorporated by the ^{125}I-labeled MB, were suspended in 1 ml of PBS, put into a dialysis bag (Spectra/Por® Float-A-Lyzer® G2, molecular weight cut off = 1,000,000, Repligen Corporation, Waltham, MA, USA), and dialyzed against 50 ml of PBS at 37 °C. At different time intervals, 50 ml of PBS was changed by the same volume of fresh PBS. After 9 hr dialysis, collagenase was added into the dialysis bag (50 µg/ml), and PBS was changed to PBS containing 50 µg/ml collagenase. The amount of MB released into the PBS collected was determined by the radioactivity measurement.

Evaluation of cell viability after incubation with complex and cGNS$_{MB}$

KUM6 cells of mouse bone marrow-derived mesenchymal stem cells (MSC) (JCRB Cell Bank, National Institute of Biomedical Innovation, Health and Nutrition, Osaka, Japan) were seeded into each well of 96 well multi-dish culture plate (Corning Inc., Corning, NY, USA) at a density of 1×10^4 cells/well. The cells were cultured in 100 µl of Iscove’s Modified Dulbecco’s Medium (IMDM, Thermo Fisher Scientific Inc., Waltham, MA, USA) containing 10 vol% bovine fetal calf serum (FCS, GE healthcare Life Sciences Hyclone laboratories inc., Logan, UT, USA) and 1 vol% penicillin/streptomycin at 37 °C in a 5% CO_2-95% air atmospheric condition for 24 hr. The medium was changed to OPTI MEM (Thermo Fisher Scientific Inc., Waltham, MA, USA), and then complex or cGNS$_{MB}$ crosslinked with 20, 60, and 100 µl of GA, were added to each well at different concentrations (1, 5, 10, 15, and 20 µg/ml). The cell viability was evaluated using a cell counting kit (Nacalai Tesque. Inc., Kyoto, Japan). After the incubation of 3 hr with complex or nanospheres, 10 µl of 2-(2-methoxy-4-nitrophenyl)-3-(4-nitrophenyl)-5-(2,4-disulfophenyl)-2H-tetrazolium (WST-8) solution was added to each well and further incubated for 1 hr. The absorbance of samples at 450 nm was measured by Multi-mode Microplate Reader (SpectraMax i3x, Molecular Devices Japan Co., Ltd., Tokyo, Japan). The percentage of cell viability was expressed as 100% for cells without incubation of complex or cGNS$_{MB}$.

Quantification of cell internalization after incubation with complex and $cGNS_{MB}$

Cells were seeded in each well of 6 well multi-dish culture plate (Corning Inc., Corning, NY, USA) at a density of 5 × 10^4 cells/well, and cultured for 24 hr. The medium was changed to OPTI MEM, and then complex or $cGNS_{MB}$ crosslinked with 20, 60, and 100 μl of GA which had been incorporated by the ^{125}I-labeled MB were added to each well at different concentrations (1, 5, 10, 15, and 20 μg/ml). After the incubation of 3 hr with complex or $cGNS_{MB}$, the cells were washed with PBS and detached with 0.25 wt% trypsin-containing 1 mM EDTA solution (Nacalai Tesque. Inc., Kyoto, Japan). The amount of MB was determined by the radioactivity measurement of cells collected.

Evaluation of cell internalization mechanism

To evaluate the cell internalization mechanism of complex and $cGNS_{MB}$, various endocytosis inhibitors were used to evaluate the effect [14-16]. In brief, cells were similarly seeded in each well of 6 well multi-dish culture plate at a density of 5 × 10^4 cells/well, and cultured for 24 hr. The cells were then treated with 10 mM 2-deoxy-D-glucose (2-DG) and 10 mM sodium azide, 6.25 μg/ml chlorpromazine (CPZ), 2.5 μg/ml filipin III, 1.5 μg/ml cytochalasin D (cyto D), and 50 μg/ml amiloride for 1 hr at 37 °C. After the treatment of inhibitors, cells were washed with PBS and complex or $cGNS_{MB}$ crosslinked with 20 μl of GA which had been incorporated by the ^{125}I-labeled MB were added (5 μg/ml), and incubated for 3 hr. In addition to the inhibitor treatments, the cells incubation with complex or $cGNS_{MB}$ were performed at 4 °C for 3 hr. The cells were washed with PBS and collected by their trypsinization. The amount of MB was determined by the radioactivity measurement, and the amount without the endocytosis inhibitors was expressed as 100%.

Evaluation of intracellular localization

Cells were seeded in a glass bottom dish of 35 mm in diameter (Matsunami Glass Industries Ltd., Tokyo, Japan) at a density of 5 × 10^4 cells/dish, and cultured for 24 hr. After the medium change to OPTI MEM, the cells were incubated with 5 μg/ml complex or $cGNS_{MB}$ crosslinked with 20 μl of GA for 3 hr. After the incubation of 5 and 12 hr with complex or cGNS$_{MB}$, the lysosomes of cells were stained with 80 nM LysoTracker® Red DND-99 (Thermo Fisher Scientific Inc., Waltham, MA, USA), and fixed with 4 vol% paraformaldehyde and the cell nuclei were stained with 300 nM 4',6-diamidino-2-phenylindole (DAPI, Thermo Fisher Scientific Inc., Waltham, MA, USA), and then the fluorescent images were taken by a fluorescent microscope (BZ-X700, KEYENCE Co., Ltd., Osaka, Japan). The fluorescence was expressed as a pseudo color.

Continuous fluorescent imaging of mRNA and intracellular remaining of MB

Cells were similarly seeded in the glass bottom dish at a density of 5×10^4 cells/dish, and cultured for 24 hr. After the medium change to OPTI MEM, the cells were incubated with 5 µg/ml complex or cGNS$_{MB}$ crosslinked with 20, 60, and 100 µl of GA for 3 hr, and cultured further for 14 days. The cells were observed by the fluorescent microscopy 1, 2, 3, 5, 7, 9, and 14 days later.

To evaluate the intracellular remaining of MB, cells were similarly seeded in each well of 6 well multi-dish culture plate at a density of 5×10^4 cells/well, and cultured for 24 hr. After the medium change to OPTI MEM, complex or cGNS$_{MB}$ crosslinked with 20, 60, and 100 µl of GA which had been incorporated by the ^{125}I-labeled MB were added (5 µg/ml) and incubated for 3 hr. The cells were further cultured, and trypsinized to collect at days 0, 1, 2, 3, 5, 7, 9, and 14. The amount of MB was determined by the radioactivity measurement, and the amount at day 0 was expressed as 100%.

Statistical analysis

The data were expressed as the average ± standard deviation (SD). All the statistical analysis was performed using one-way analysis of variance (ANOVA) with a post-hoc Tukey-Kramer multiple comparison test. *P* values less than 0.05 were considered to be statistically significant.

RESULTS

Preparation of cationized gelatin

Figure 1 shows the cationization extent of gelatin plotted as a function of the molar ratio of spermine added. The percent introduced increased as the increase of spermine addition ratio. In the following experiments, the cationized gelatin with the highest extent of cationization (44.8 mole%) was used.

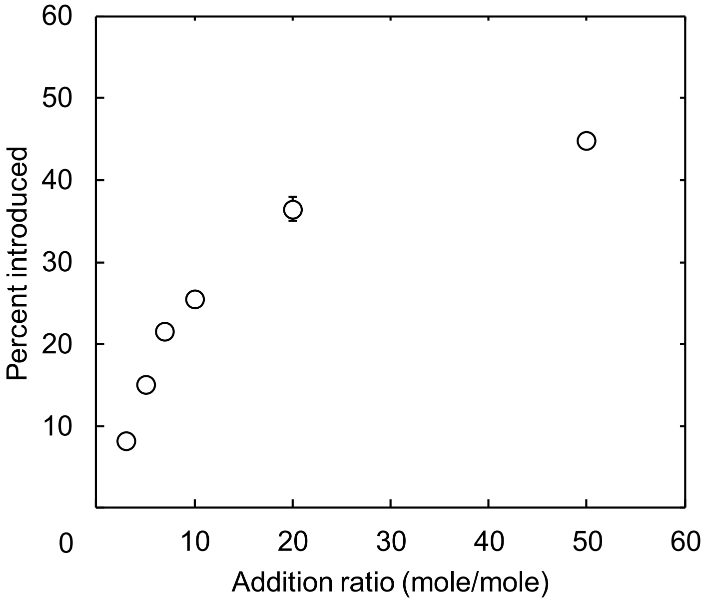

Figure 1. Cationization extent of gelatin as a function of the molar ratio of spermine added to the carboxyl groups of gelatin.

Characterization of cGNS

Figure 2 shows the apparent size and zeta potential of cGNS crosslinked with different amounts of GA. Both the apparent size and zeta potential were constant, irrespective of the GA amounts. **Figure 3** shows the degradation time profiles of cGNS crosslinked with different amounts of GA. In the collagenase-free PBS, 58, 44, and 38 wt% of gelatin were released within 9 hr from cGNS crosslinked with GA 20, 60, and 100 μl, respectively. The gelatin release in hydrogel degradation for every cGNS was observed even in PBS containing collagenase, although it tended to become slowly with an increase of GA amounts used in preparation. The fastest degradation was observed for cGNS (GA 20 μl), and the cGNS disappeared at the time point of 15 hr.

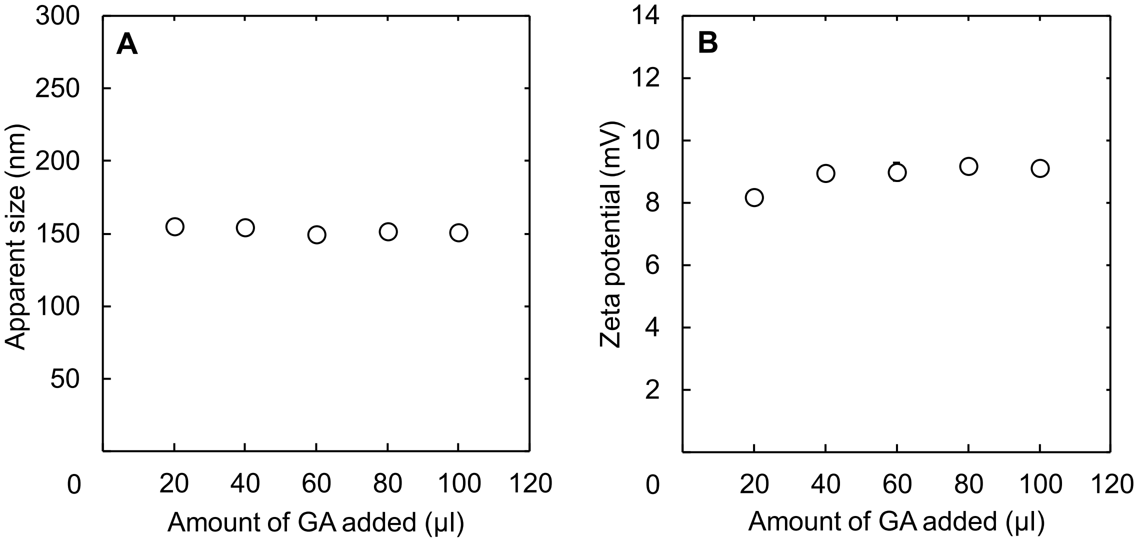

Figure 2. Apparent size (A) and zeta potential (B) of cGNS prepared at different amounts of GA.

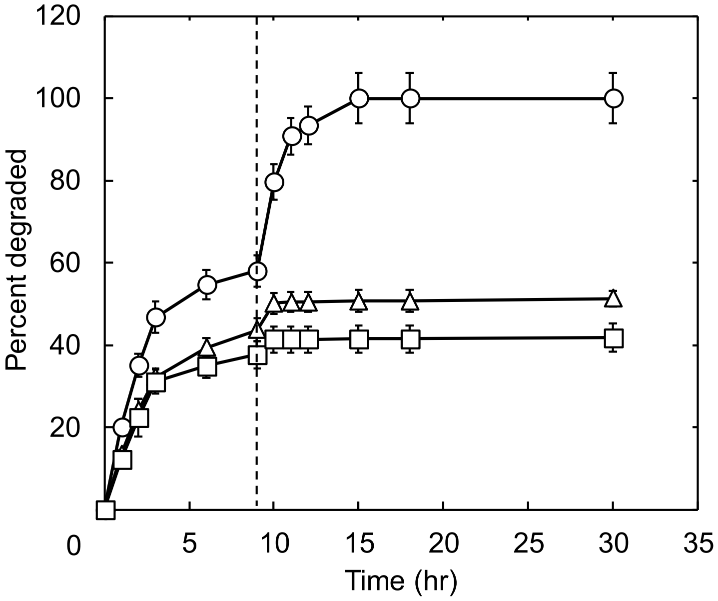

Figure 3. Time profiles of degradation of cGNS crosslinked with 20 (○), 60 (△), and 100 μl of GA (□). The degradation test was performed in PBS for the initial 9 hr, and thereafter in PBS containing collagenase at 37 °C.

Characterization of complex and cGNS$_{MB}$

Table 1 shows the physicochemical properties of complex and cGNS$_{MB}$. The apparent size of cGNS$_{MB}$ was constant, irrespective of the GA amounts. On the other hand, the MB amount incorporated and the zeta potential of cGNS$_{MB}$ slightly decreased with an increase of GA amount. The apparent size and zeta potential of complex were similar to those of cGNS$_{MB}$.

Table 1. Physicochemical properties of complex and cGNS$_{MB}$.

	Amount of MB incorporated (pmole/μg)	Apparent size (nm)	Zeta potential (mV)
Complex	15	223.6 ± 42.3	7.55 ± 0.90
cGNS$_{MB}$ (GA20 μl) [a)]	15.1 ± 0.1 [b)]	225.9 ± 19.8	9.23 ± 1.12
cGNS$_{MB}$ (GA40 μl)	14.7 ± 0.2	231.8 ± 13.4	8.40 ± 1.32
cGNS$_{MB}$ (GA60 μl)	13.6 ± 1.2	223.8 ± 19.3	6.84 ± 0.89
cGNS$_{MB}$ (GA80 μl)	13.8 ± 0.4	249.3 ± 21.6	5.94 ± 0.47
cGNS$_{MB}$ (GA100 μl)	13.5 ± 0.4	251.5 ± 27.5	2.90 ± 1.09

a) The volume of GA added in cGNS preparation.
b) Average ± SD.

Figure 4 shows the release profiles of MB from complex and cGNS$_{MB}$ crosslinked with 20 μl of GA. In the collagenase-free PBS, 16 and 3 wt% of MB were released from complexes and cGNS$_{MB}$, respectively. After the solution was changed to PBS containing collagenase, the MB release from complex was accelerated. On the other hand, the MB was slowly released from cGNS$_{MB}$, irrespective of the collagenase addition.

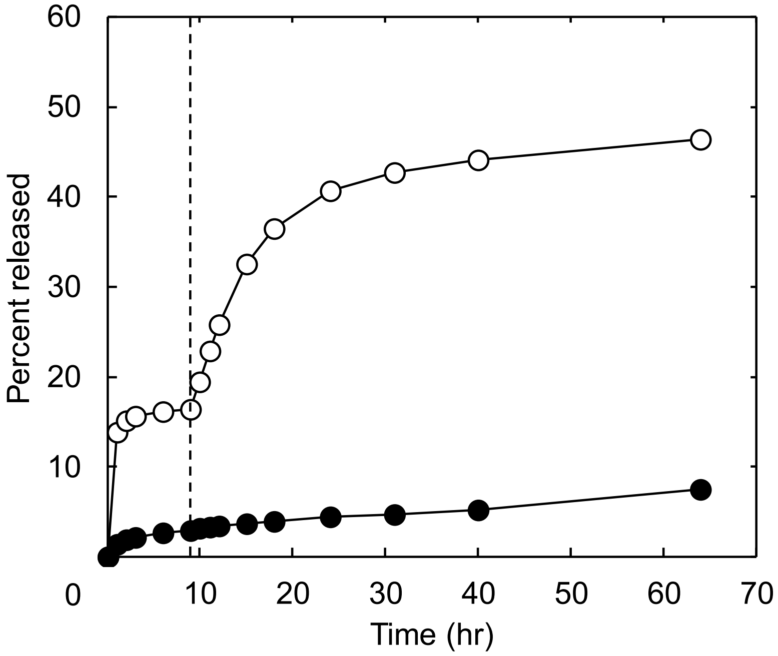

Figure 4. Time profiles of MB release from complex (○) and cGNS$_{MB}$ (●) crosslinked with 20 μl of GA. The release test was performed in PBS for the initial 9 hr, and thereafter in PBS containing collagenase at 37 °C.

Cell viability and cell internalization after incubation with complex and cGNSMB

The cytotoxicity and the amount of MB internalized into the cells were evaluated (**Figure 5**). The percentage of survived cells decreased as the increase of complex and cGNSMB concentration. Significant cytotoxicity was observed at 10 µg/ml of complex and 15 µg/ml of cGNSMB (GA 20 µl) or higher. However, no cytotoxicity was observed at any concentration for cGNSMB crosslinked with GA 60 and 100 µl. The amount of MB internalized into the cells increased when the concentration increased for both the complex and cGNSMB. When complex and cGNSMB were incubated at low concentrations of 1 and 5 µg/ml, the similar amount level of MB internalized was observed between the complex and cGNSMB. On the other hand, at high concentrations of 10, 15, and 20 µg/ml, the amount of complex internalized was larger than that of cGNSMB crosslinked with GA 20, 60, and 100 µl.

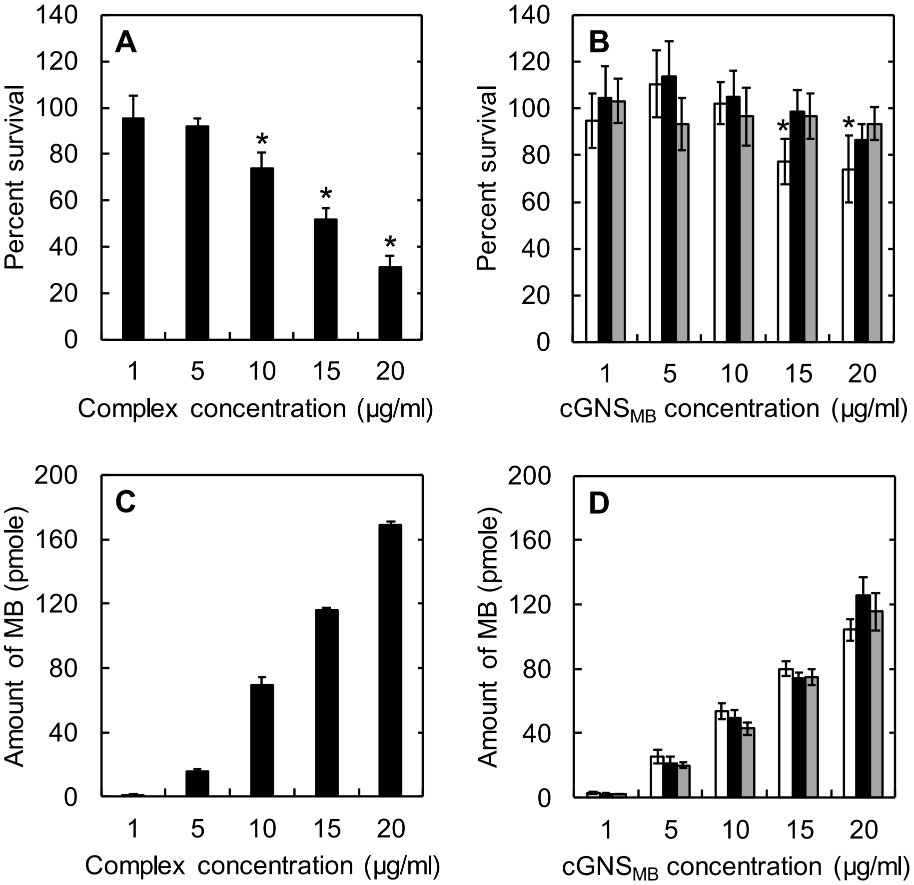

Figure 5. Cell viability (A and B) and amount of MB internalized into the cells (C and D) incubated with different concentrations of complex (A and C) and cGNSMB (B and D) crosslinked with 20 (☐), 60 (■), and 100 µl (▨) of GA. The viability of cells incubated without complex nor cGNSMB was expressed as 100%. *, $p < 0.05$; significant against the percent survival of cells without complex nor cGNSMB.

Mechanism of cell internalization and intracellular localization

The cell internalization pathway of complex and cGNS$_{\text{MB}}$ was evaluated by the pre-treatment of various endocytosis inhibitors (**Figure 6**). The amount of MB internalized was the most significantly decreased by the 4 °C incubation for both the complex and cGNS$_{\text{MB}}$. In addition, various endocytosis inhibitors, such as 2-DG and sodium azide (energy depended endocytosis), CPZ (clathrin-mediated endocytosis), filipin III (caveolae-mediated endocytosis), cyto D (phagocytosis and macropinocytosis), and amiloride (macropinocytosis) were pre-treated with the cells before the internalization culture of complex and cGNS$_{\text{MB}}$. For the complex, the pre-treatment with filipin III and amiloride significantly decreased the internalization. On the other hand, the pre-treatment with all kinds of inhibitors, especially CPZ caused the significant decrease of cGNS$_{\text{MB}}$ internalization.

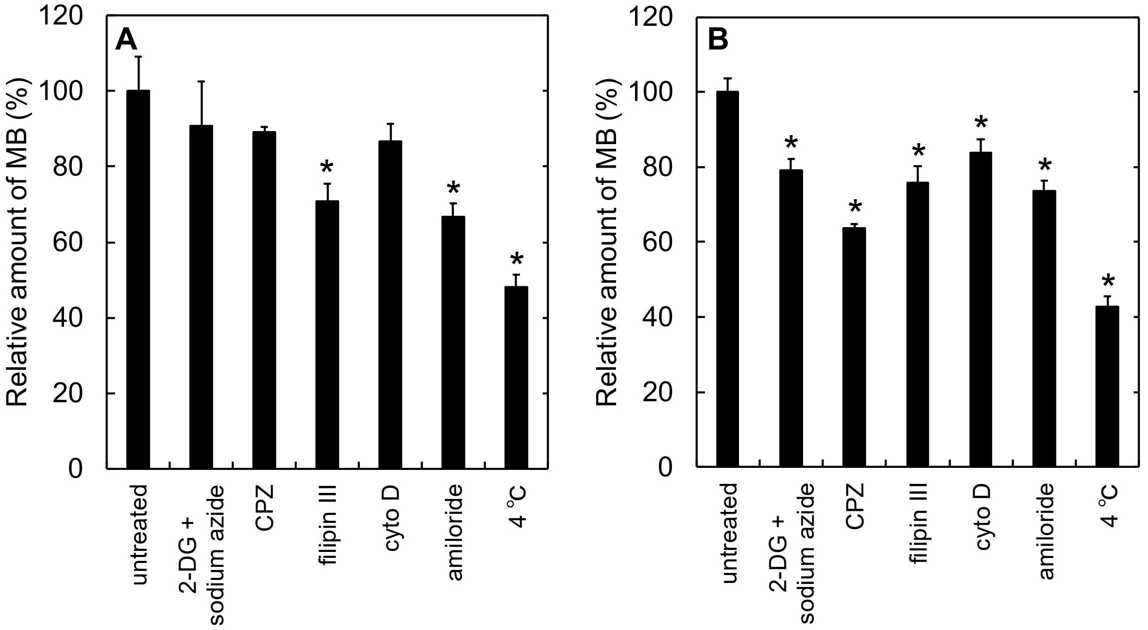

Figure 6. The effect of endocytosis inhibitors on the amount of MB internalized into cells. The cells were pre-treated with 2-DG and sodium azide, CPZ, filipin III, cyto D, and amiloride for 1 hr, followed by incubating with 5 µg/ml of complex (A) or cGNS$_{\text{MB}}$ crosslinked with 20 µl of GA (B). Incubation with complex or cGNS$_{\text{MB}}$ were also performed at 4 °C. The amount of MB without the endocytosis inhibitor (untreated) was expressed as 100%. *, $p < 0.05$; significant against the amount of MB internalized into the untreated cells.

Figure 7 shows the intracellular localization after 5 and 12 hr incubation with complex or cGNS$_{MB}$. For both the complex and cGNS$_{MB}$, the fluorescence of MB and lysosomes was not co-localized at 5 and 12 hr. The fluorescence of complex and cGNS$_{MB}$ were detected at a similar level at 5 hr. However, the fluorescence of complex disappeared at 12 hr, whereas that of cGNS$_{MB}$ was still observed.

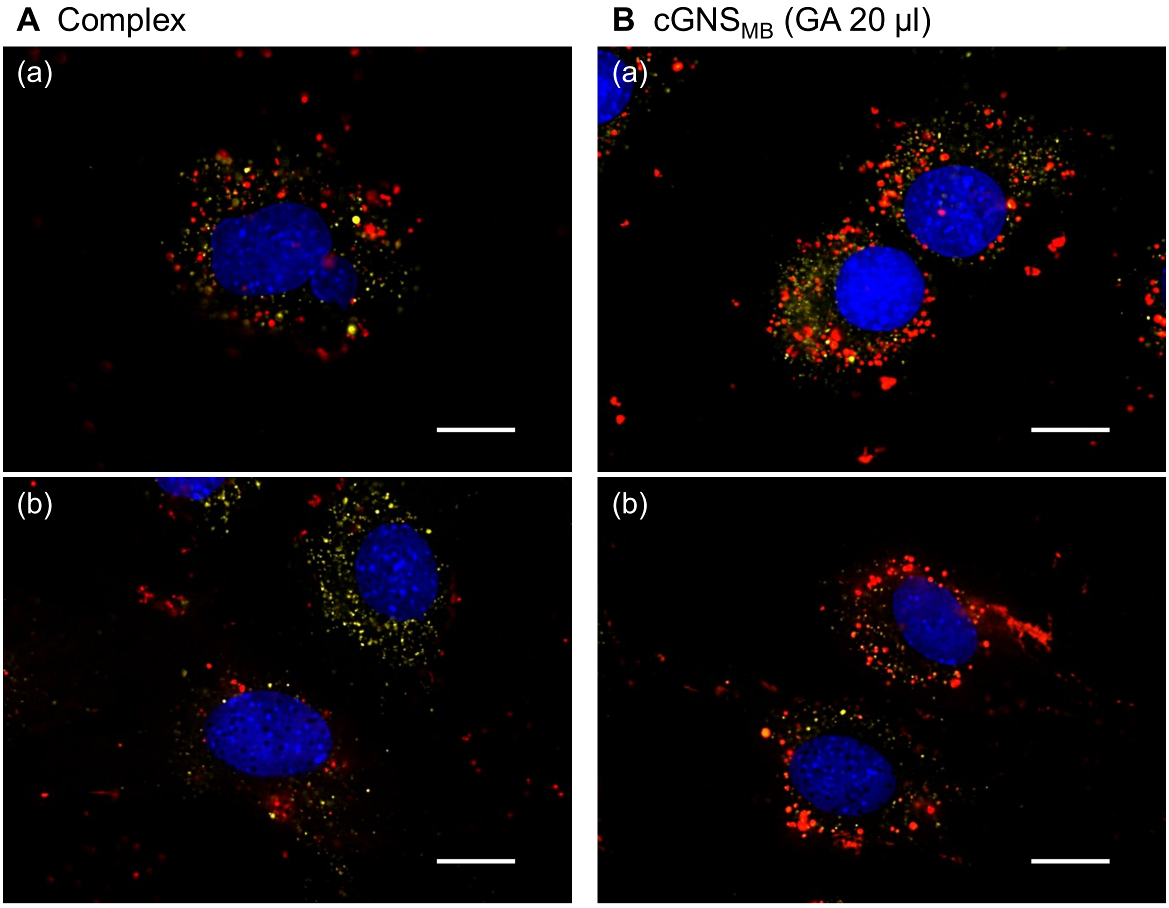

Figure 7. Fluorescent microscopic images of cells after the incubation with 5 μg/ml of complex (A) and cGNS$_{MB}$ crosslinked with 20 μl of GA (B). After the incubation with complex or cGNS$_{MB}$, the images were taken at 5 (a) and 12 hr later (b). Red: MB. Yellow: lysosomes. Blue: nuclei. Scale bar is 20 μm.

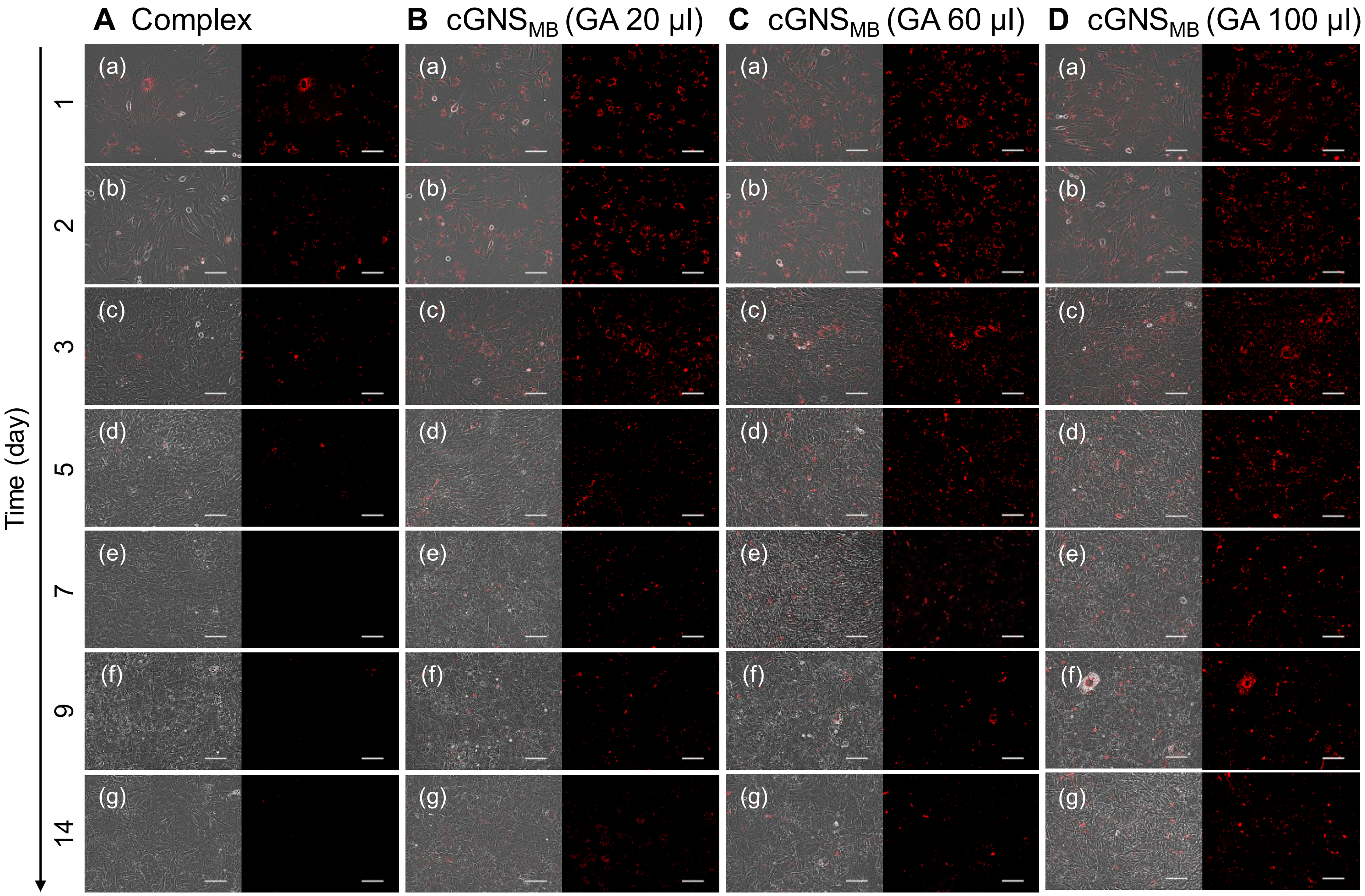

Figure 8. Fluorescent microscopic images of cells incubated with 5 µg/ml of complex (A) and cGNS$_{MB}$ crosslinked with 20 (B), 60 (C), and 100 µl of GA (D) for different time periods: 1 (a), 2 (b), 3 (c), 5 (d), 7 (e), 9 (f), and 14 days later (g). The left panel shows the merged images of phase contrast and MB fluorescence, while the right panel shows the MB fluorescence. Scale bar is 100 µm.

Continuous fluorescent imaging of mRNA and intracellular remaining of MB

Figure 8 shows the fluorescent microscopic images of cells incubated with complex or cGNS$_{MB}$ for different time periods. The fluorescence of complex was hardly detected after 5 days incubation, whereas the fluorescence of cGNS$_{MB}$ was sufficiently observed even after 14 days. The level of intracellular fluorescence at days 1 and 2 was almost same among cGNS$_{MB}$ crosslinked with GA 20, 60, and 100 μl. When compared at the same time point, the intracellular fluorescence of cGNS$_{MB}$ increased as the increase of GA amount after 3 days incubation.

Figure 9 shows the percent remaining of MB in the cells after the incubation with complex or different types of cGNS$_{MB}$. One day later, only 12 wt% of complex was remained and the percent remaining slightly decreased in a time dependent manner. On the contrary, at day 1, the percent remaining of cGNS$_{MB}$ was 53, 58, and 65 wt% for the volume of GA 20, 60, and 100 μl used in preparation, respectively, although it decreased with time. The intracellular remaining of cGNS$_{MB}$ became higher as the GA amount increased.

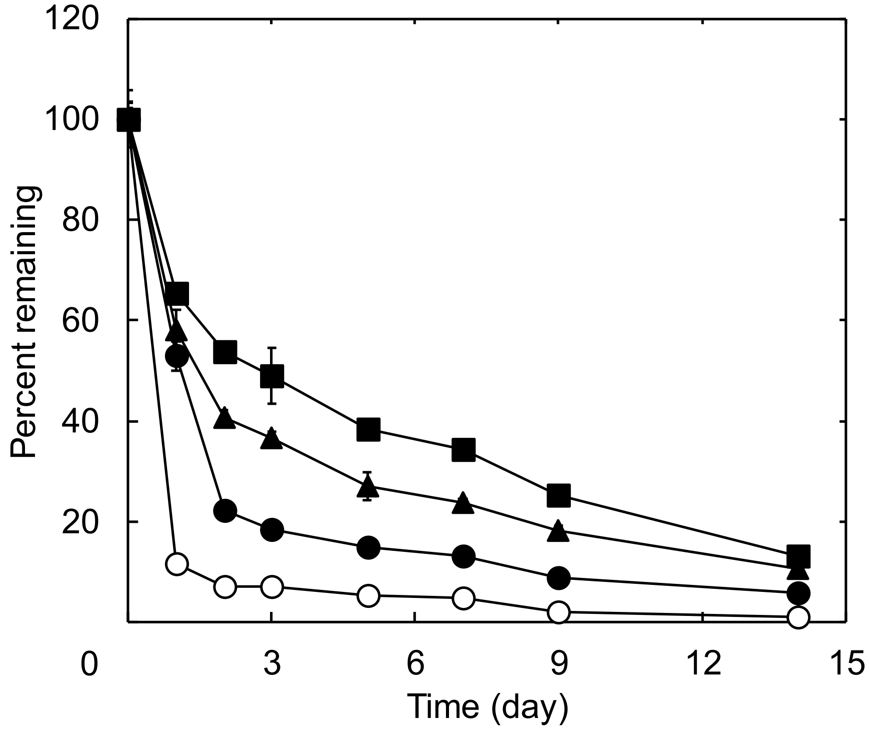

Figure 9. Intracellular remaining of complex (○) and cGNS$_{MB}$ crosslinked with 20 (●), 60 (▲), and 100 μl of GA (■). The amount of MB at day 0 was expressed as 100%.

DISCUSSION

The present study demonstrates that the $\mathrm{cGNS_{MB}}$ and the cationized gelatin-MB complexes were readily internalized into the cells via an endocytotic pathway, but not co-localized with lysosomes. The release profile of MB was different between the complex and $\mathrm{cGNS_{MB}}$. The intracellular fluorescence of complex disappeared at day 5, while that of nanospheres was observed over 14 days. This is because the intracellular rate of complex release was faster than that of $\mathrm{cGNS_{MB}}$. In addition, the decrease of intracellular $\mathrm{cGNS_{MB}}$ became slower as the increase of GA amount used in preparation. It is likely that, as the results, the intracellular fluorescence was retained at a high level. To our knowledge, this study is the first report to compare cell internalization between the complex and nanospheres prepared from the same starting material. In addition, this is the first investigation to estimate the intracellular activity of MB in terms of the time period of mRNA visualization. The time period could be regulated by changing the degradability of $\mathrm{cGNS_{MB}}$.

The apparent size and zeta potential of cGNS prepared were constant, irrespective of the GA amount (**Figure 2**). On the other hand, the time profile of degradation became slower as the increase of GA amount (**Figure 3**). In this study, collagenase was used to simulate the intracellular environment although the concentration is not clear. In addition, the reason of cGNS degradation in the absence of collagenase may be due to the release of gelatin which did not contribute to the crosslinking. The cGNS crosslinked with 20 μl of GA was completely degraded at the time point of 15 hr, whereas those of 60 and 100 μl were not completed. This is because the concentration of collagenase was not high enough to allow cGNS to degrade completely. However, it should be noted that the degradability of cGNS can be controlled only by the amount of GA of a crosslinking reagent. The apparent size of $\mathrm{cGNS_{MB}}$ was constant, while the amount of MB incorporated and zeta potential slightly decreased as the increase of GA amount. It is conceivable that the increase of GA amount increases the crosslinking extent of gelatin hydrogel, leading to the smaller mesh size of gelatin in hydrogel. Since the smaller mesh size prevents the incorporation of MB into the hydrogel, the number of MB molecules on the surface of nanospheres would increase with the increase of GA amount, resulting in an enhanced apparent size and reduced zeta potential. It is apparent from **Table 1** that the apparent size of complex and $\mathrm{cGNS_{MB}}$ were similar, and both of them had a similar positive charge. It is well recognized that the range of small size (around 200 nm) and positive charge is favorably internalized into cells [17, 18]. **Figure 4** shows that the release of MB from complex was faster than that from $\mathrm{cGNS_{MB}}$ crosslinked with 20 μl of GA. The cGNS (GA 20 μl) which degraded in the fastest profile (**Figure 3**) was used to compare with the complex. It has been reported that nucleic acids complexed with cationized gelatin and incorporated in cGNS were released with the fragment of gelatin degraded [4, 19]. This can be explained in terms of gelatin crosslinking. It is highly possible that complex which was physicochemically associated, but not crosslinked is easily degraded by collagenase compared with $\mathrm{cGNS_{MB}}$ crosslinked with GA. The constant MB release from $\mathrm{cGNS_{MB}}$, irrespective of collagenase addition, was observed. The $\mathrm{cGNS_{MB}}$ tended to be aggregated in the PBS containing collagenase. This aggregation might prevent the $\mathrm{cGNS_{MB}}$ from the collagenase degradation. Therefore, MB would be slowly released from the surface of aggregate degraded by the collagenase.

Figure 5 shows the cytotoxicity and the amount of MB internalized into the cells after incubation with the complex and $\mathrm{cGNS_{MB}}$. When complex and $\mathrm{cGNS_{MB}}$ were incubated at high concentrations of 10, 15, and 20 μg/ml, the amount of complex internalized was larger than that of $\mathrm{cGNS_{MB}}$. On the other hand, significant cytotoxicity of complex was observed over 10 μg/ml. However, the reason why higher cytotoxicity and better internalization of complex over $\mathrm{cGNS_{MB}}$ is not clear at present. In general, it is well known that cationic substances tend to show the cytotoxicity, although the better internalization into cells was observed [20-22]. The complex and $\mathrm{cGNS_{MB}}$ had a similar apparent size and zeta potential, but the $\mathrm{cGNS_{MB}}$ was crosslinked with GA. It is possible, therefore, that the cationized gelatin molecules of complex might be more flexible than that of $\mathrm{cGNS_{MB}}$. More flexible positive gelatin molecules of complex would interact with the surface of cells more strongly. This difference of molecular flexibility might cause the higher cytotoxicity and better internalization of complex over $\mathrm{cGNS_{MB}}$. In addition, it is likely that the presence of free cationized gelatin which did not contribute to the complex formation causes the higher cytotoxicity. Another possible reason of different cytotoxicities might be due to the different release profiles of MB and cationized gelatin fragment. Faster release of cationized gelatin fragments might lead to the higher cytotoxicity. Considering the non-cytotoxic condition and similar amount of cell internalization, in this study, 5 μg/ml was selected for comparison between the complex and $cGNS_{MB}$.

The pre-treatment of endocytosis inhibitors was performed to evaluate the mechanism of cell internalization (**Figure 6**). The amount of MB internalized was the most significantly decreased by 4 °C incubation for both the complex and $cGNS_{MB}$. This result indicates that both the complex and $cGNS_{MB}$ were internalized into the cells by the endocytotic pathway. The decreased internalization of complex by the pre-treatment with filipin III and amiloride experimentally confirms that the complex was internalized mainly via the caveolae-mediated endocytosis and macropinocytosis. On the other hand, for the $cGNS_{MB}$, the decreased internalization was observed by the pre-treatment with all kinds of inhibitors, especially CPZ. This indicates that there are many pathways for the $cGNS_{MB}$ internalization, although the clathrin-mediated endocytosis and macropinocytosis are mainly contributed. The reason of a small difference in endocytotic pathways between the complex and $cGNS_{MB}$ is not clear at present. However, it is highly conceivable that they were internalized into cells via the endocytosis pathway. The molecular flexibility on the surface of complex and $cGNS_{MB}$ might contribute to the endocytotic pathways. For both the complex and $cGNS_{MB}$, the fluorescence of MB was not co-localized with lysosomes after 5 and 24 hr incubation (**Figure 7**). Taken together, it is demonstrated that both the complex and $cGNS_{MB}$ were endosomally escaped following their endocytosis. This endosomal escape may be due to the pH buffering effect by the secondary amino groups of spermine [23]. As shown in **Figure 8**, the intracellular fluorescence of complex disappeared at day 5, while that of $cGNS_{MB}$ was observed over 14 days. It is reported that the intracellular fluorescence of MB diminished by fourth day after transfection with xtreamGENE HP^{TM} reagent which is a complex-based transfection reagent [1]. The results in this study well correspond to the report. In addition, it has been demonstrated that more than 50% of intracellular MB signal diminished by 96 hr after the streptolysin O (SLO) transfection [2]. This is due to the degradation of naked MB by endogenous nucleases and the resulting clearance from the cells. The different time periods of intracellular fluorescence decrement between the complex and $cGNS_{MB}$ may be due to the degradability and the consequent MB release profile (**Figures 3** and **4**). This is also experimentally confirmed from the intracellular remaining of

MB (**Figure 9**). The decrease of intracellular cGNS$_{MB}$ became slower as the increase of GA amount, leading to a prolonged high level of intracellular fluorescence. These findings demonstrate that the time period of mRNA visualization is controlled by the degradability of cGNS$_{MB}$ which can consequently modify the intracellular release profile of MB. The detailed mechanism of the MB release into the cytosol and the cellular clearance is not clear at present. It is reported that the polyion complex of a poly(ethyleneimine) (PEI) and pDNA were internalized into cells via the caveolae- and clathrin-mediated endocytosis, followed by the rapid rupture of endosomes due to the high buffering ability of PEI [24, 25]. The complex and cGNS$_{MB}$ which have secondary amino groups of spermine should be also released into cytosol as well as the polyion complex of PEI. On the other hand, the MB release is thought to be driven by the degradation of cationized gelatin which might occur in late-endosomes and lysosomes containing matrix metalloproteinases. The degraded fragment of cationized gelatin with MB might also be released into cytosol. Therefore, it is possible that the degradability affected the existence probability in the cytosol, and the resulting intracellular remaining. Further study is needed to investigate the intracellular event after the internalization of complex and cGNS$_{MB}$ to clarify the mechanism of intracellular MB release and the cellular clearance.

In this study, the feasibility of intracellular controlled release of MB to prolong the time period of mRNA visualization is clearly demonstrated. The complexation-based cell internalization has been widely applied in gene transfection. However, the short time period of gene expression or suppression is a challenging problem [26]. On the other hand, the intracellular release of nucleic acids enables the prolongation of its bioactivity because the intracellular concentration is kept high [4, 27, 28]. This study directly proved that the intracellular controlled release prolongs the intracellular activity of nucleic acid comparing with the complexation-based cell internalization. This intracellular controlled release of MB must be a versatile tool to visualize the long-term cellular biological functions. Wiraja *et al.* have reported that MB intracellular release from poly(lactic-co-glycolic acid) (PLGA) nanoparticles continuously visualized the mRNA of β-actin [2, 15], osteogenesis [29], and chondrogenesis [30] of MSC. The intracellular release of MB from the PLGA nanoparticles enabled the mRNA visualization over 28 days. The present study focused on regulating the time period of mRNA visualization by changing the degradability of $\mathrm{cGNS}_{\mathrm{MB}}$. The advantage of cGNS over PLGA nanoparticles would be the simplicity of controlling degradability and the consequent controllability of nucleic acids release profile. The time period of mRNA visualization and the intracellular remaining of MB was readily regulated by the degradability of $\mathrm{cGNS}_{\mathrm{MB}}$ (**Figures 8** and **9**). This controlled release system based on the degradation of cationized gelatin has been applied extracellularly [7, 8, 10, 19, 31, 32] and intracellularly [3, 4] to prolong the bioactivity of nucleic acids. Another strategy to prolong the intracellular MB activity is the modification of MB, such as locked nucleic acid (LNA) [33, 34] and 2'-O-methylation [34-36], based on nucleic acid chemistry. These modifications enhance the specificity in hybridization with the target mRNA and the stability against nucleases. It has been reported that 2'-O-methyl modified MB visualizing Oct-3/4 mRNA of a pluripotent marker were persistent in human embryonic stem (ES) cells at least for 7 days after the electroporation-based transfection [35]. In addition to the intracellular controlled release of MB based on material sciences, the modifications of MB could be combined to $\mathrm{cGNS}_{\mathrm{MB}}$ for the further prolongation of intracellular activity. In the near future, biological functions of cells which change in a time dependent manner, will be visualized based on the intracellular controlled release of MB.

REFERENCES

1. Desai HV, Voruganti IS, Jayasuriya C, Chen Q, Darling EM. Live-cell, temporal gene expression analysis of osteogenic differentiation in adipose-derived stem cells. *Tissue Eng Part A* 2014; **20**: 899-907.
2. Yeo D, Wiraja C, Chuah YJ, Gao Y, Xu C. A Nanoparticle-based Sensor Platform for Cell Tracking and Status/Function Assessment. *Sci Rep* 2015; **5**: 14768.
3. Doi N, Jo J, Tabata Y. Preparation of Biodegradable Gelatin Nanospheres with a Narrow Size Distribution for Carrier of Cellular Internalization of Plasmid DNA. *J Biomater Sci Polym Ed* 2012; **23**: 991-1004.
4. Ishikawa H, Nakamura Y, Jo J, Tabata Y. Gelatin nanospheres incorporating siRNA for controlled intracellular release. *Biomaterials* 2012; **33**: 9097-9104.
5. Tabata Y, Ikada Y. Protein release from gelatin matrices. *Adv Drug Deliv Rev* 1998; **31**: 287-301.
6. Yamamoto M, Ikada Y, Tabata Y. Controlled release of growth factors based on biodegradation of gelatin hydrogel. *J Biomater Sci Polym Ed* 2001; **12**: 77-88.
7. Fukunaka Y, Iwanaga K, Morimoto K, Kakemi M, Tabata Y. Controlled release of plasmid DNA from cationized gelatin hydrogels based on hydrogel degradation. *J Control Release* 2002; **80**: 333-343.
8. Kushibiki T, Tomoshige R, Fukunaka Y, Kakemi M, Tabata Y. In vivo release and gene expression of plasmid DNA by hydrogels of gelatin with different cationization extents. *J Control Release* 2003; **90**: 207-216.
9. Young S, Wong M, Tabata Y, Mikos AG. Gelatin as a delivery vehicle for the controlled release of bioactive molecules. *J Control Release* 2005; **109**: 256-274.
10. Kushibiki T, Tomoshige R, Iwanaga K, Kakemi M, Tabata Y. Controlled release of plasmid DNA from hydrogels prepared from gelatin cationized by different amine compounds. *J Control Release* 2006; **112**: 249-256.
11. Kim YH, Tabata Y. Dual-controlled release system of drugs for bone regeneration. *Adv Drug Deliv Rev* 2015; **94**: 28-40.
12. Snyder SL, Sobocinski PZ. An improved 2,4,6-trinitrobenzenesulfonic acid method for

the determination of amines. *Anal Biochem* 1975; **64**: 284-288.

13. Commerford SL. Iodination of nucleic acids in vitro. *Biochemistry* 1971; **10**: 1993-2000.
14. Yukawa H, Nakagawa S, Yoshizumi Y, Watanabe M, Saito H, Miyamoto Y *et al.* Novel positively charged nanoparticle labeling for in vivo imaging of adipose tissue-derived stem cells. *PLoS One* 2014; **9**: e110142.
15. Wiraja C, Yeo DC, Chew SY, Xu C. Molecular beacon-loaded polymeric nanoparticles for non-invasive imaging of mRNA expression. *J Mater Chem B* 2015; **3**: 6148-6156.
16. George E, Barai A, Shirke P, Majumder A, Sen S. Engineering interfacial migration by collective tuning of adhesion anisotropy and stiffness. *Acta Biomater* 2018; **72**: 82-93.
17. Win KY, Feng SS. Effects of particle size and surface coating on cellular uptake of polymeric nanoparticles for oral delivery of anticancer drugs. *Biomaterials* 2005; **26**: 2713-2722.
18. He C, Hu Y, Yin L, Tang C, Yin C. Effects of particle size and surface charge on cellular uptake and biodistribution of polymeric nanoparticles. *Biomaterials* 2010; **31**: 3657-3666.
19. Saito T, Tabata Y. Preparation of gelatin hydrogels incorporating small interfering RNA for the controlled release. *J Drug Target* 2012; **20**: 864-872.
20. Fischer D, Li Y, Ahlemeyer B, Krieglstein J, Kissel T. In vitro cytotoxicity testing of polycations: influence of polymer structure on cell viability and hemolysis. *Biomaterials* 2003; **24**: 1121-1131.
21. Frohlich E. The role of surface charge in cellular uptake and cytotoxicity of medical nanoparticles. *Int J Nanomedicine* 2012; **7**: 5577-5591.
22. Shao XR, Wei XQ, Song X, Hao LY, Cai XX, Zhang ZR *et al.* Independent effect of polymeric nanoparticle zeta potential/surface charge, on their cytotoxicity and affinity to cells. *Cell Prolif* 2015; **48**: 465-474.
23. Jo J, Nagane K, Yamamoto M, Tabata Y. Effect of amine type on the expression of plasmid DNA by cationized dextran. *J Biomater Sci Polym Ed* 2010; **21**: 225-236.
24. Rejman J, Conese M, Hoekstra D. Gene transfer by means of lipo- and polyplexes: role of clathrin and caveolae-mediated endocytosis. *J Liposome Res* 2006; **16**: 237-247.

25. ur Rehman Z, Hoekstra D, Zuhorn IS. Mechanism of polyplex- and lipoplex-mediated delivery of nucleic acids: real-time visualization of transient membrane destabilization without endosomal lysis. *ACS Nano* 2013; **7**: 3767-3777.

26. Raemdonck K, Vandenbroucke RE, Demeester J, Sanders NN, De Smedt SC. Maintaining the silence: reflections on long-term RNAi. *Drug Discov Today* 2008; **13**: 917-931.

27. Raemdonck K, Naeye B, Hogset A, Demeester J, De Smedt SC. Prolonged gene silencing by combining siRNA nanogels and photochemical internalization. *J Control Release* 2010; **145**: 281-288.

28. Xue HY, Wong HL. Tailoring nanostructured solid-lipid carriers for time-controlled intracellular siRNA kinetics to sustain RNAi-mediated chemosensitization. *Biomaterials* 2011; **32**: 2662-2672.

29. Wiraja C, Yeo DC, Chong MS, Xu C. Nanosensors for Continuous and Noninvasive Monitoring of Mesenchymal Stem Cell Osteogenic Differentiation. *Small* 2016; **12**: 1342-1350.

30. Tay LM, Wiraja C, Yeo DC, Wu Y, Yang Z, Chuah YJ *et al.* Noninvasive Monitoring of Three-Dimensional Chondrogenic Constructs Using Molecular Beacon Nanosensors. *Tissue Eng Part C Methods* 2017; **23**: 12-20.

31. Lin X, Jo H, Ishii TM, Fujita M, Fu M, Tambara K *et al.* Controlled release of matrix metalloproteinase-1 plasmid DNA prevents left ventricular remodeling in chronic myocardial infarction of rats. *Circ J* 2009; **73**: 2315-2321.

32. Obata Y, Nishino T, Kushibiki T, Tomoshige R, Xia Z, Miyazaki M *et al.* HSP47 siRNA conjugated with cationized gelatin microspheres suppresses peritoneal fibrosis in mice. *Acta Biomater* 2012; **8**: 2688-2696.

33. Wu Y, Yang CJ, Moroz LL, Tan W. Nucleic acid beacons for long-term real-time intracellular monitoring. *Anal Chem* 2008; **80**: 3025-3028.

34. Catrina IE, Marras SA, Bratu DP. Tiny molecular beacons: LNA/2'-O-methyl RNA chimeric probes for imaging dynamic mRNA processes in living cells. *ACS Chem Biol* 2012; **7**: 1586-1595.

35. King FW, Liszewski W, Ritner C, Bernstein HS. High-throughput tracking of pluripotent human embryonic stem cells with dual fluorescence resonance energy transfer molecular beacons. *Stem Cells Dev* 2011; **20**: 475-484.

36. Yu S, Li F, Huang X, Dong C, Ren J. In Situ Study of Interactions between Endogenous c-myc mRNA with CRDBP in a Single Living Cell by Combining Fluorescence Cross-Correlation Spectroscopy with Molecular Beacons. *Anal Chem* 2020; **92**: 2988-2996.

Chapter 4

Preparation of cationized gelatin nanospheres incorporating molecular beacon to visualize cell proliferation ability

INTRODUCTION

Proliferation ability is one of the fundamental biological functions of cells. It is quite important to evaluate the proliferation ability of cells in the research fields of biology and medicine. For example, highly proliferative cancer cells are one of the characteristic features of malignant cancers [1]. For the cell therapy in regenerative medicine, the survival and proliferation of cells transplanted *in vivo* lead to an improvement of therapeutic efficiency. In addition, a variety of trials have been reported to enhance the proliferation ability of cells, such as the application of bioreactors [2-4], and growth factors [5, 6]. However, at present, it is experimentally difficult to continuously assess the time course of cell proliferation ability. It has been well recognized that Ki67 is one of the representative proliferation markers extensively used in the fields of basic cell research [7] and pathology [8, 9]. As the conventional assay of Ki67 expression, immunohistological and immunofluorescent stainings, western blotting, and polymerase chain reaction (PCR) are used to evaluate the proliferation ability of cells. However, the techniques require cell destruction, and can only detect the temporal situation of cells at the sampling time. Under these circumstances, it is of prime importance to develop the imaging technologies and methodologies to continuously visualize the time course of cell proliferation ability.

Based on the results in Chapter 3, it was demonstrated that the intracellular controlled release of molecular beacons (MB) is an effective system to continuously visualize intracellular messenger RNA (mRNA) which regulates various cell functions. The cationized gelatin nanospheres (cGNS) incorporating MB ($cGNS_{MB}$) are easily internalized into cells, and the MB released into cytosol from the cGNS can specifically detect intracellular target mRNA over 2 weeks. To visualize the cell proliferation ability, MB to detect mRNA of Ki67 as a target of proliferation ability is designed to be incorporated in the cGNS. In addition, MB for mRNA of glyceraldehyde-3-phosphate dehydrogenase (GAPDH) of a constantly expressing housekeeping gene is used as a control of stable fluorescence in cells.

In this chapter, the cell proliferation ability was visualized based on the $\mathrm{cGNS_{MB}}$ imaging system. The cGNS incorporating Ki67 and GAPDH MB ($\mathrm{cGNS_{Ki67\ MB}}$ and $\mathrm{cGNS_{GAP\ MB}}$, respectively) were prepared and internalized into KUM6 cells of a mouse bone marrow-derived mesenchymal stem cell (MSC) line. Basic fibroblast growth factor (bFGF) was used to enhance the proliferation ability of cells. In addition to the cell proliferation, the effect of bFGF concentration on the mRNA and protein expressions of Ki67 was investigated. The fluorescent intensity of cells incubated with $\mathrm{cGNS_{Ki67\ MB}}$ and $\mathrm{cGNS_{GAP\ MB}}$ in the presence or absence of bFGF was evaluated in terms of the MB function to visualize the cell proliferation ability. A timelapse imaging of cells after the bFGF addition was performed to assess the time course of proliferation ability enhancement.

EXPERIMENTAL

Materials

Gelatin with an isoelectric point of 9.0 and the weight-averaged molecular weight of 99,000, prepared by an acidic process of pig skin, was kindly supplied from Nitta Gelatin Inc., Osaka, Japan. MB for mouse mRNA of GAPDH was designed by NIPPON GENE Co., Ltd, Tokyo, Japan, while that for Ki67 was designed by Beacon Designer$^{\mathrm{TM}}$ (PREMIER Biosoft, Palo Alto, CA, USA). The secondary structure of MB was estimated by an RNA/DNA folding software (UNAFold, Integrated DNA Technologies, Inc., Coralville, IA, USA.) to confirm the stem-loop structure. The MB were synthesized by Integrated DNA Technologies, Inc. Coralville, IA, USA. The sequences of MB were listed in **Table 1**. Basic fibroblast growth factor (bFGF, KCB-1) was kindly supplied from Kaken Pharmaceutical Co., Ltd., Tokyo, Japan. Glutaraldehyde (GA, 25 wt% in water), glycine, concentrated hydrochloric acid (HCl), acetone, and 1-ethyl-3-(3-dimethylaminopropyl) carbodiimide hydrochloride salt (EDC) were purchased from Nacalai Tesque. Inc., Kyoto, Japan. Spermine was purchased from Sigma-Aldrich Inc., St. Louis, MO, USA. The reagents were used without further purification.

Table 1. Sequences of MB and PCR primers used.

MB and PCR primers	Sequences (5’ to 3’)
Ki67 MB	[Alexa Fluor®488]-CGCGATCTGTATCACTCATCTGCTGCTGCGATCGCG-[IBFQ]
GAPDH MB	[TYE®665]-CTGGTAATCCGTTCACACCGACCTTCACCAG-[IBRQ]
Ki67 forward	CATCCATCAGCCGGAGTCA
Ki67 reverse	TGTTTCGCAACTTTCGTTTGTG
GAPDH forward	AACTTTGGCATTGTGGAAGG
GAPDH reverse	GGAGACAACCTGGTCCTCAG

MB: molecular beacons
PCR: polymerase chain reaction
GAPDH: glyceraldehyde-3-phosphate dehydrogenase
IBFQ: Iowa Black®FQ
IBRQ: Iowa Black®RQ
underline: stem structure

Preparation of cationized gelatin

Cationized gelatin was prepared by conjugating spermine with the carboxyl groups of gelatin as described in Chapter 2. In brief, spermine was added at a molar ratio of 50 to the carboxyl groups of gelatin into 50 ml of gelatin aqueous solution (40 mg/ml). Immediately after that, the solution pH was adjusted to 5.0 by adding 11 M HCl. Double-distilled water (DDW) was added to give the final volume of 100 ml. Next, EDC was added at a molar ratio of 3 to the carboxyl groups of gelatin, followed by the agitation at 40 °C for 18 hr and dialysis against DDW for 3 days with a dialysis membrane (molecular weight cut off = 12,000 to 14,000, Viskase Companies, Inc., Willowbrook, IL, USA) at room temperature. The dialyzed solution was freeze-dried to obtain the cationized gelatin. The percentage of amino groups introduced into gelatin was determined by the conventional 2,4,6-trinitrobenzene sulfonic acid (TNBS, FUJIFILM Wako Pure Chemical Inc., Osaka, Japan) method [10]. The percentage was 59.8 mole% per the carboxyl groups of gelatin.

Preparation of cGNS

According to the preparation procedure described in Chapter 3, cGNS were prepared by the conventional coacervation method. Briefly, 5 ml of acetone was added to 1.25 ml of cationized gelatin aqueous solution (50 mg/ml) at 40 °C to form coacervate. Aqueous solution of 25 wt% GA (20 μl) was immediately added to the solution, followed by chemically crosslinking of cationized gelatin for 6 hr. After that, an excessive amount of 0.5 M glycine aqueous solution (2 ml) was added for the blocking of aldehyde groups unreacted. The resulting solution was agitated overnight at 40 °C and the residual acetone was evaporated. Then, cGNS were collected by the centrifugation of 16,000 g for 30 min at 25 °C and resuspended in DDW. The centrifugation and resuspension procedures were repeated three times to wash cGNS. The apparent size of cGNS dispersed in 10 mM phosphate buffered-saline solution (PBS, pH7.4) was measured by dynamic light scattering (DLS, Zetasizer Nano-ZS, Malvern Instruments Ltd., Worcestershire, UK). On the other hand, the zeta potential of cGNS dispersed in 10 mM phosphate buffer (PB, pH7.4) was measured by electrophoresis light scattering (ELS, Zetasizer Nano-ZS, Malvern Instruments Ltd., Worcestershire, UK). The apparent size and zeta potential of cGNS were 155.3 ± 0.92 nm and 8.05 ± 0.17 mV, respectively.

Radiolabeling of MB

According to the method described in Chapter 2, MB was labeled with radioactive iodine (^{125}I) [11]. The MB (5 μl, 50 μM in 0.2 M sodium acetate and 40 mM acetic acid solution, pH5.0) were incubated at 60 °C for 50 min with 2 μl of 0.3 mM Na_2SO_3, 5 μl of Na^{125}I (740 MBq/ml in 0.1 M NaOH aqueous solution, PerkinElmer Inc., Waltham, MA, USA), and 5 μl of 4 mM $TlCl_3$. Next, mixed 100 μl of 0.1 M Na_2SO_3 and 900 μl of 0.1 M NaCl, 50 mM Tris, and 1 mM ethylenediaminetetra acetic acid (EDTA) solution was added to the MB solution. After the incubation for 30 min at 60 °C, the reactant was applied on the PD-10 column (GE Healthcare Bio-Sciences Corp., Piscataway, NJ, USA) to purify the ^{125}I-labeled MB by the gel filtration. The radioactivity of ^{125}I was measured using a gamma counter (Auto Well Gamma System ARC-380 CL, Aloka Co., Ltd, Tokyo, Japan).

Preparation of $\mathrm{cGNS_{MB}}$

The cGNS (200 μg/ml) and MB (Ki67 and GAPDH, each 4 μM) were mixed in DDW at the MB/cGNS ratio of 20 pmole/μg. After the incubation for 15 min at room temperature, the mixture was centrifuged at 16,000 g for 15 min at 25 °C and resuspended in DDW to obtain cGNS incorporating Ki67 and GAPDH MB ($\mathrm{cGNS_{Ki67\ MB}}$ and $\mathrm{cGNS_{GAP\ MB}}$). The amount of MB incorporated in cGNS was determined by the radioactivity of $\mathrm{cGNS_{MB}}$ prepared with ^{125}I-labeled MB. The apparent size and zeta potential of $\mathrm{cGNS_{MB}}$ were determined by DLS and ELS measurements, respectively. These measurements were performed independently three times for each sample.

Cell culture experiments

KUM6 cells (JCRB1202) of a mouse bone marrow-derived MSC line were purchased from JCRB Cell Bank (National Institute of Biomedical Innovation, Health and Nutrition, Osaka, Japan). The cells were cultured in Iscove's Modified Dulbecco's Medium (IMDM, Thermo Fisher Scientific Inc., Waltham, MA, USA) supplemented with 10 vol% bovine fetal calf serum (FCS, GE healthcare Life Sciences Hyclone laboratories inc., Logan, UT, USA) and 1 vol% penicillin and streptomycin (Nacalai Tesque. Inc., Kyoto, Japan) at 37 °C in a 5% CO_2-95% air atmospheric condition. The cells were detached with 0.25 wt% trypsin-containing 1 mM EDTA solution (Nacalai Tesque. Inc., Kyoto, Japan) and continued to culture in 100 mm cell culture dish (Corning Inc., Corning, NY, USA) to allow to grow until to 80% confluency.

Analysis of mRNA expression

The cells were seeded on each well of 6 well multi-dish culture plate (Corning Inc., Corning, NY, USA) at a density of 5×10^4 cells/well, and cultured for 24 hr. After that, bFGF was added to the cells at different final concentrations (0, 5, 10, 20, 40, and 100 ng/ml), and cultured further for 24 hr. Then, the total RNA was extracted from the cells by RNeasy Plus Mini Kit (QIAGEN, Hilden, Germany) according to the manufacture's instructions. The total RNA was reverse-transcribed to complementary DNA (cDNA) using a SuperScript VILO cDNA synthesis kit (Thermo Fisher Scientific Inc., Waltham, MA, USA). The cDNA (100 ng, 1 µl), forward and reverse primers (20 µM, each 0.5 µl), 12.5 µl of Power SYBR Green PCR Master Mix (Applied Biosystems, Foster City, CA, USA), and 10.5 µl of RNase-free water were mixed, and quantitative real-time polymerase chain reaction (qPCR) was performed on a Prism 7500 real-time PCR thermal cycler (Applied Biosystems, Foster City, CA, USA). The sequences of primers used were listed in **Table 1**. The following qPCR conditions were used: 95 °C for 10 min, followed by 40 cycles of 95 °C for 15 sec and 60 °C for 1 min. The level of Ki67 expression was normalized by that of GAPDH, and the expression level was analyzed by ΔΔCt method comparing with the cells cultured without bFGF (0 ng/ml).

Immunofluorescent staining

The cells were seeded on a glass bottom dish of 35 mm in diameter (Matsunami Glass Industries Ltd., Tokyo, Japan) at a density of 5×10^4 cells/dish. After the incubation for 24 hr, different concentrations of bFGF was added to the cells, and cultured further for 24 hr as described above. The cells were fixed with 4 vol% paraformaldehyde for 20 min, and permeabilized with 0.2 vol% TritonX-100 for 45 min at room temperature. After the blocking (ImmunoBlock$^{\text{TM}}$, KAC Co. Ltd., Kyoto, Japan), the cells were incubated with 1 µg/ml rabbit polyclonal anti-Ki67 antibody (ab15580, Abcam, Cambridge, UK) overnight at 4 °C. Next, the cells were washed with PBS three times, followed by the incubation with the secondary goat anti-rabbit IgG (H + L) antibody conjugated with Alexa Fluor$^{®}$546 (A11010, Thermo Fisher Scientific Inc., Waltham, MA, USA) for 1 hr at room temperature. The cell nuclei were stained with 300 nM 4’,6-diamidino-2-phenylindole (DAPI, Thermo Fisher Scientific Inc., Waltham, MA, USA), and then the fluorescent images were taken by a fluorescent microscope (BZ-X700, KEYENCE Co., Ltd., Osaka, Japan).

Evaluation of cell proliferation

The cells were seeded on each well of 6 well multi-dish culture plate at a density of 5×10^4 cells/well supplemented with different concentrations of bFGF (0, 5, 20, and 40 ng/ml). The medium was changed every 3 days. After the different time periods of culture, the cells were detached with 0.25 wt% trypsin containing 1 mM EDTA solution (Nacalai Tesque. Inc., Kyoto, Japan) and collected by the centrifugation at 1,000 rpm for 3 min. The cell number was counted by using a hemocytometer after the staining of dead cells with 0.4% trypan blue solution (Thermo Fisher Scientific Inc., Waltham, MA, USA).

Evaluation of $cGNS_{MB}$ internalization into cells

The cells were seeded on each well of 6 well multi-dish culture plate at a density of 5×10^4 cells/well, and cultured for 24 hr. The medium was changed to OPTI MEM (Thermo Fisher Scientific Inc., Waltham, MA, USA), and then $cGNS_{Ki67\ MB}$ and $cGNS_{GAP\ MB}$ which had been labeled with ^{125}I (10 μg/ml) were added to each well. After the incubation for 1 hr, the cells were washed with PBS and detached by the trypsinization. The amount of MB internalized into the cells was determined by the radioactivity measurement of cells collected.

Fluorescent imaging of $cGNS_{MB}$-incubated cells cultured with or without bFGF

The cells were seeded on the glass bottom dish at a density of 5×10^4 cells/dish, and cultured for 24 hr. After the medium changed to OPTI MEM, the cells were incubated with 10 μg/ml $cGNS_{Ki67\ MB}$ and $cGNS_{GAP\ MB}$ for 1 hr. Next, bFGF (0, 5, and 20 ng/ml) was added to the cells, and cultured further for 24 hr. The cells were observed by BZ-X700 fluorescent microscopy. To evaluate the fluorescent intensity, six images were taken at random and analyzed by BZ-X Analyzer equipped with the microscope. The fluorescent area in the cells was extracted and the averaged brightness of the area was measured as fluorescent intensity.

Timelapse imaging of $cGNS_{MB}$-incubated cells cultured with or without bFGF

The cells were similarly seeded on the glass bottom dish, and cultured for 24 hr. After the incubation with $cGNS_{Ki67\ MB}$ and $cGNS_{GAP\ MB}$ as described above, 0 and 20 ng/ml bFGF was added to the cells. Immediately after that, the timelapse imaging was performed at the time interval of 10 min for 24 hr by the fluorescent microscopy.

Statistical analysis

The data were expressed as the average ± standard deviation (SD). All the statistical analysis was performed using one-way analysis of variance (ANOVA) with a post-hoc Tukey-Kramer multiple comparison test. *P* values less than 0.05 were considered to be statistically significant.

RESULTS

Characterization of cGNS$_{\mathrm{MB}}$

Figure 1 shows the amount of MB incorporated in cGNS, the apparent size, and the zeta potential of cGNS$_{\mathrm{Ki67\ MB}}$ and cGNS$_{\mathrm{GAP\ MB}}$. There was no difference in the values between cGNS$_{\mathrm{Ki67\ MB}}$ and cGNS$_{\mathrm{GAP\ MB}}$. Over 85% of MB was incorporated in the cGNS, while the apparent size and the zeta potential were around 230 nm and 8.8 mV, respectively.

Effect of bFGF concentration on the expression of Ki67 and the cell proliferation

To investigate the effect of bFGF on the cell proliferation, the expression of Ki67 and the cell proliferation were evaluated. The mRNA expression of Ki67 after the incubation at different concentrations of bFGF for 24 hr was evaluated by the qPCR analysis (**Figure 2**). The expression level significantly increased as the increase of bFGF concentration, and the level was saturated over 20 ng/ml. Consistent with the mRNA expression, the protein expression of Ki67 detected by the immunofluorescent staining increased depending on the bFGF concentration (**Figure 3**). In addition, the fluorescence of Ki67 was similarly observed over 20 ng/ml. **Figure 4** shows the proliferation curve of cells cultured at different concentrations of bFGF. The proliferation was accelerated by the addition of bFGF, and the cell number at the time points of days 2 and 3 was significantly higher than that after culturing without bFGF (0 ng/ml). However, there was no difference in the acceleration of cell proliferation between 20 and 40 ng/ml bFGF. The following experiments were performed using the bFGF concentrations of 0, 5, and 20 ng/ml.

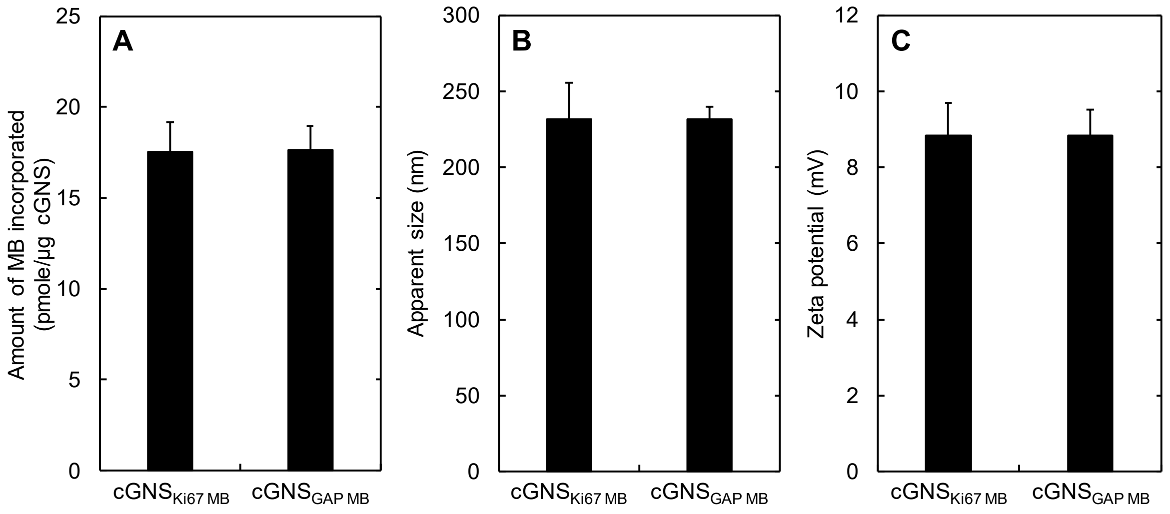

Figure 1. Characterization of cGNS$_{MB}$. Amount of MB incorporated in cGNS (A), apparent size (B), and zeta potential of cGNS$_{MB}$ (C).

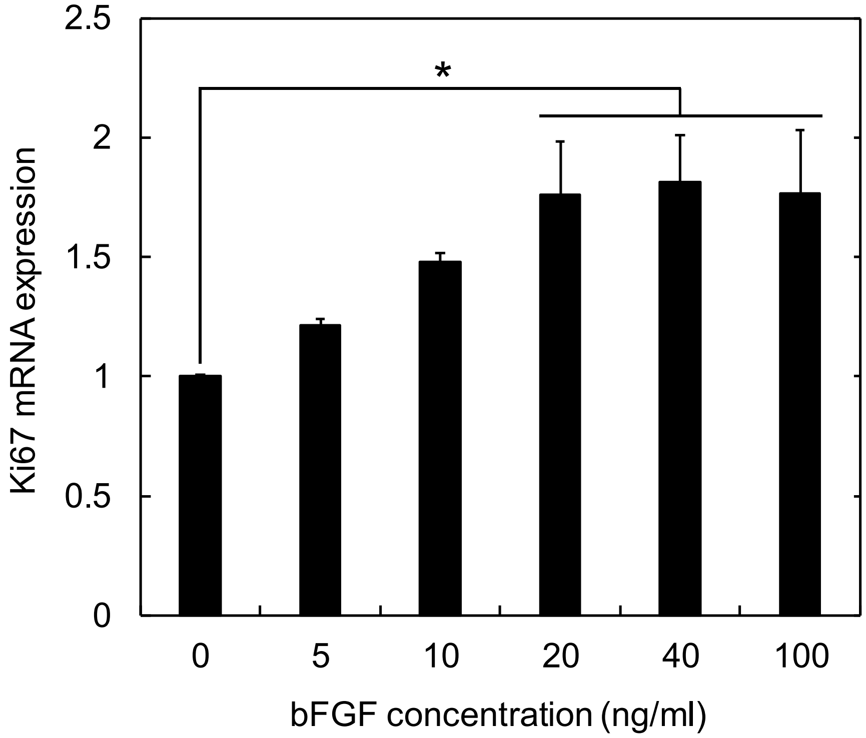

Figure 2. Effect of bFGF concentration on the mRNA expression of Ki67. The cells were cultured at different concentrations of bFGF for 24 hr. *, $p < 0.05$; significant against the expression level at 0 ng/ml bFGF.

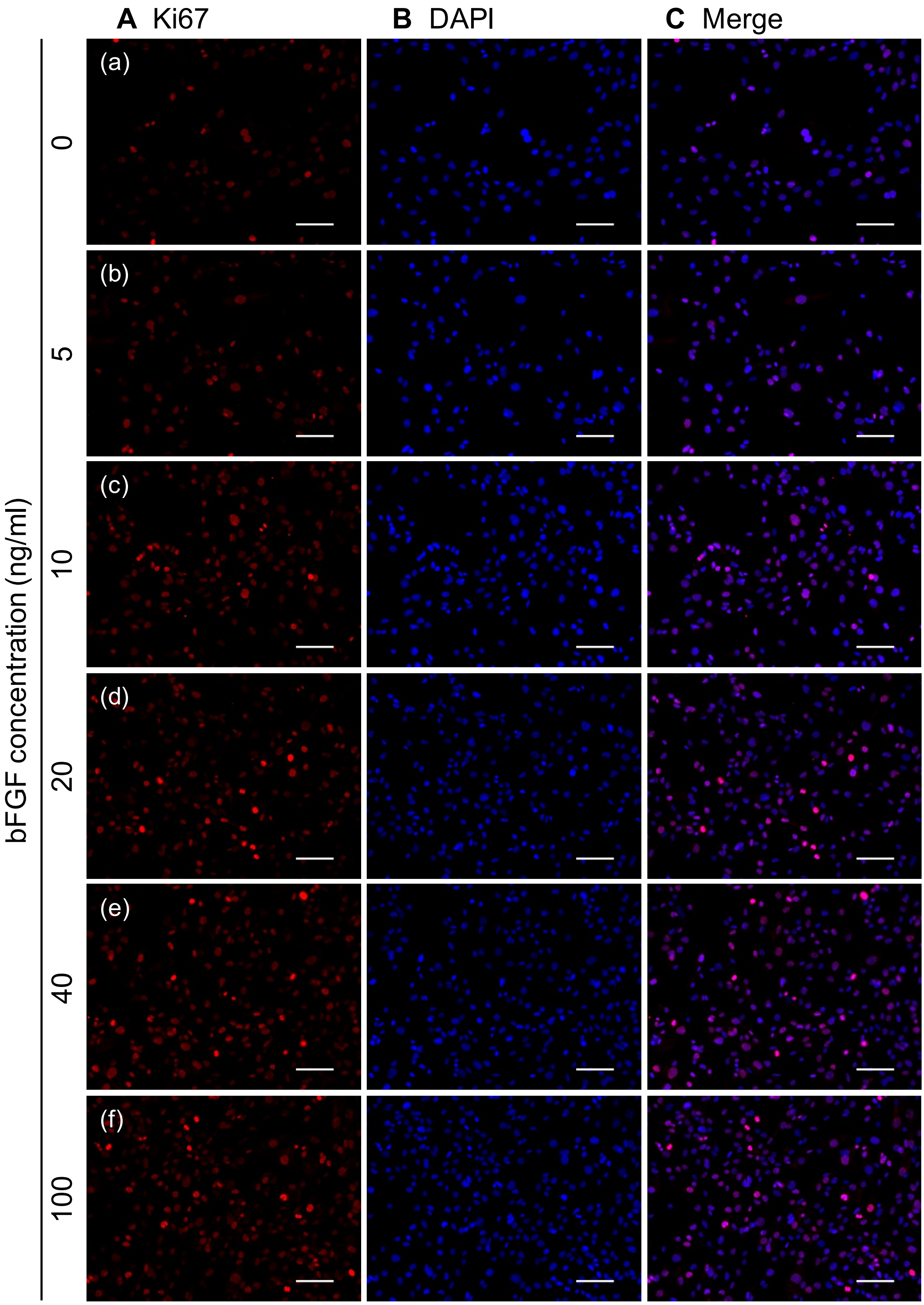

Figure 3. Immunofluorescent staining of Ki67: (A) Red: Ki67, (B) Blue: DAPI (nuclei), and (C) Merged fluorescent images. The cells were cultured with 0 (a), 5 (b), 10 (c), 20 (d), 40 (e), and 100 ng/ml bFGF (f) for 24 hr. Scale bar is 100 μm.

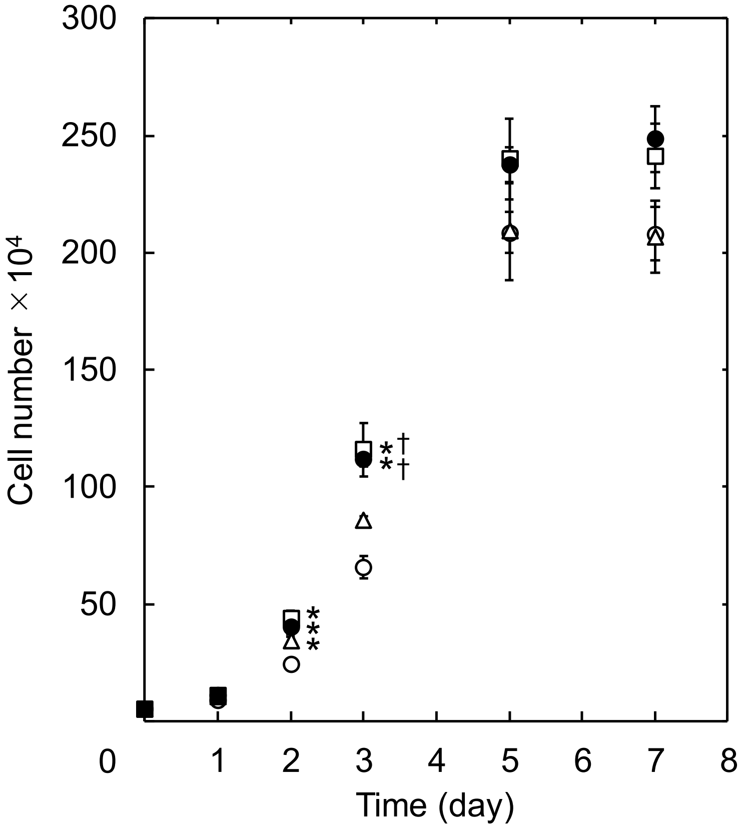

Figure 4. Time profile of cell proliferation at different concentrations of bFGF. The cells were cultured with 0 (○), 5 (△), 20 (□), and 40 ng/ml bFGF (●), and were trypsinized to count the cell number at different time points. *, $p < 0.05$; significant against the cell number cultured with 0 ng/ml bFGF at the corresponding time point. †, $p < 0.05$; significant against the cell number cultured with 5 ng/ml bFGF at the corresponding time point.

Cell internalization of $cGNS_{MB}$ and fluorescent imaging of proliferation ability of $cGNS_{MB}$-incubated cells cultured with or without bFGF

The cell internalization of $cGNS_{MB}$ was quantified in terms of the amount of MB internalized into the cells based on the radioactivity of ^{125}I labeled MB (**Figure 5**). There was no difference in the amount of $cGNS_{MB}$ internalization between $cGNS_{Ki67\ MB}$ and $cGNS_{GAP\ MB}$, and the internalization efficiency of MB was around 10%.

After the incubation for $cGNS_{MB}$ internalization, the cells after 24 hr incubation at different concentrations of bFGF, were observed by the fluorescent microscopy (**Figure 6**). The fluorescence of $cGNS_{GAP\ MB}$ was not changed by the addition of bFGF (**Figure 6B**). On the contrary, for the $cGNS_{Ki67\ MB}$, the fluorescence intensity became larger with the increasing bFGF concentration (**Figure 6A**). **Figure 7** shows the fluorescent intensity of cells incubated with $cGNS_{Ki67\ MB}$ and $cGNS_{GAP\ MB}$, followed by further cultured with bFGF. Similarly, the fluorescent intensity of $cGNS_{GAP\ MB}$ was constant at any concentration of bFGF. However, the fluorescence of $cGNS_{Ki67\ MB}$ became significantly stronger in the bFGF concentration manner.

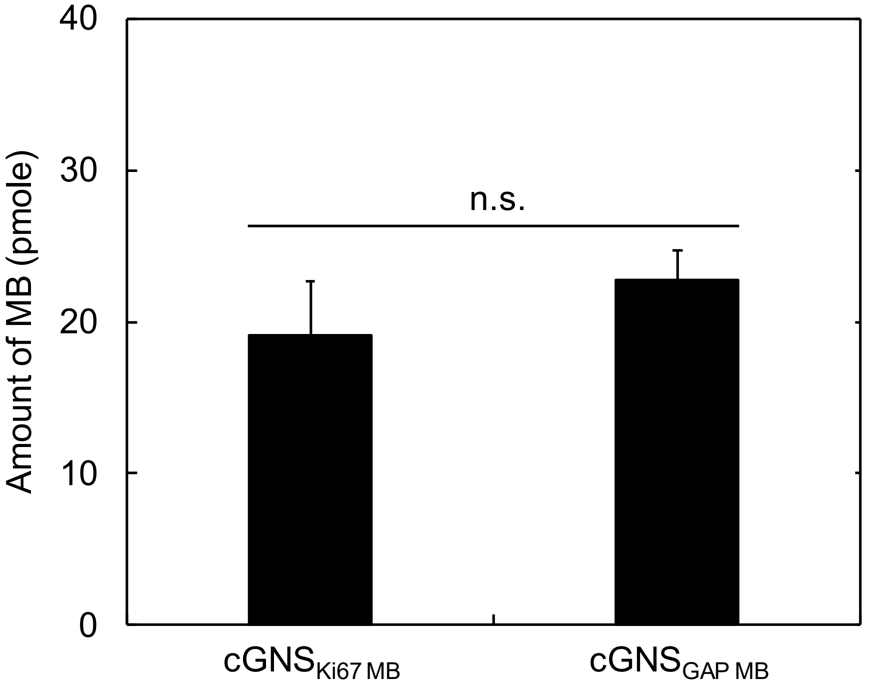

Figure 5. Amount of MB internalized into the cells. The cells were incubated with 10 µg/ml cGNS$_{MB}$ for 1 hr. n.s.; not significant.

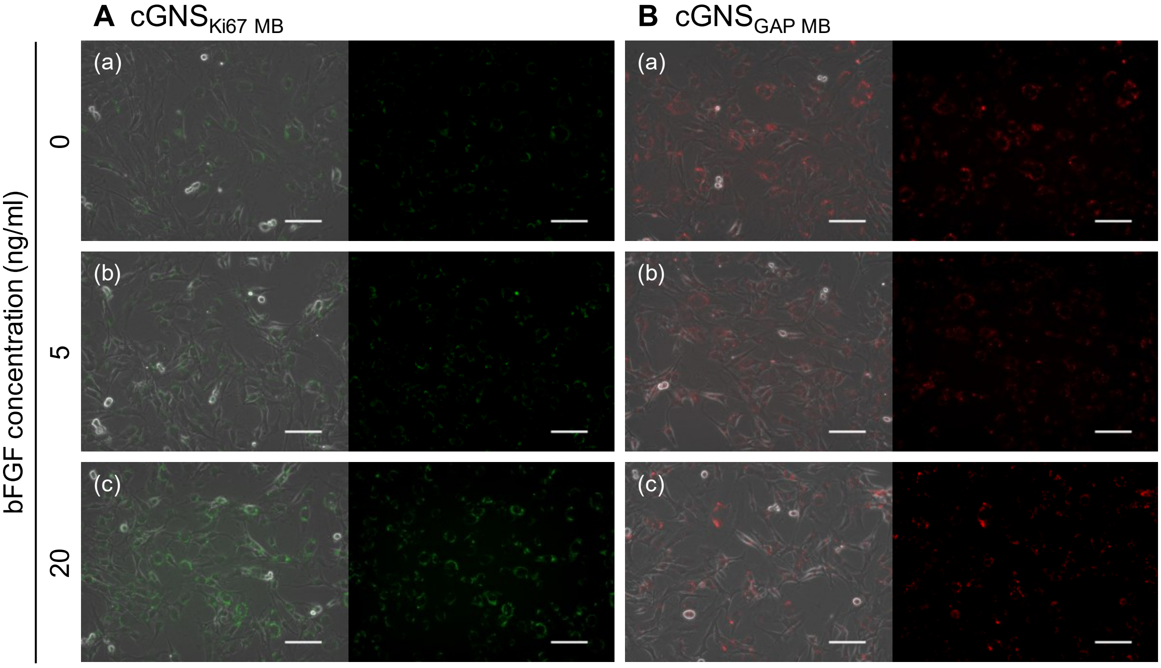

Figure 6. Fluorescent microscopic images of cGNS$_{MB}$-incubated cells cultured with or without bFGF. The cells were incubated with 10 µg/ml cGNS$_{Ki67\ MB}$ (A) and cGNS$_{GAP\ MB}$ (B) for 1 hr, and further for 24 hr in the presence of 0 (a), 5 (b), and 20 ng/ml bFGF (c). The left panel shows the merged images of phase contrast and MB fluorescence, while the right panel shows the MB fluorescence. Scale bar is 100 µm.

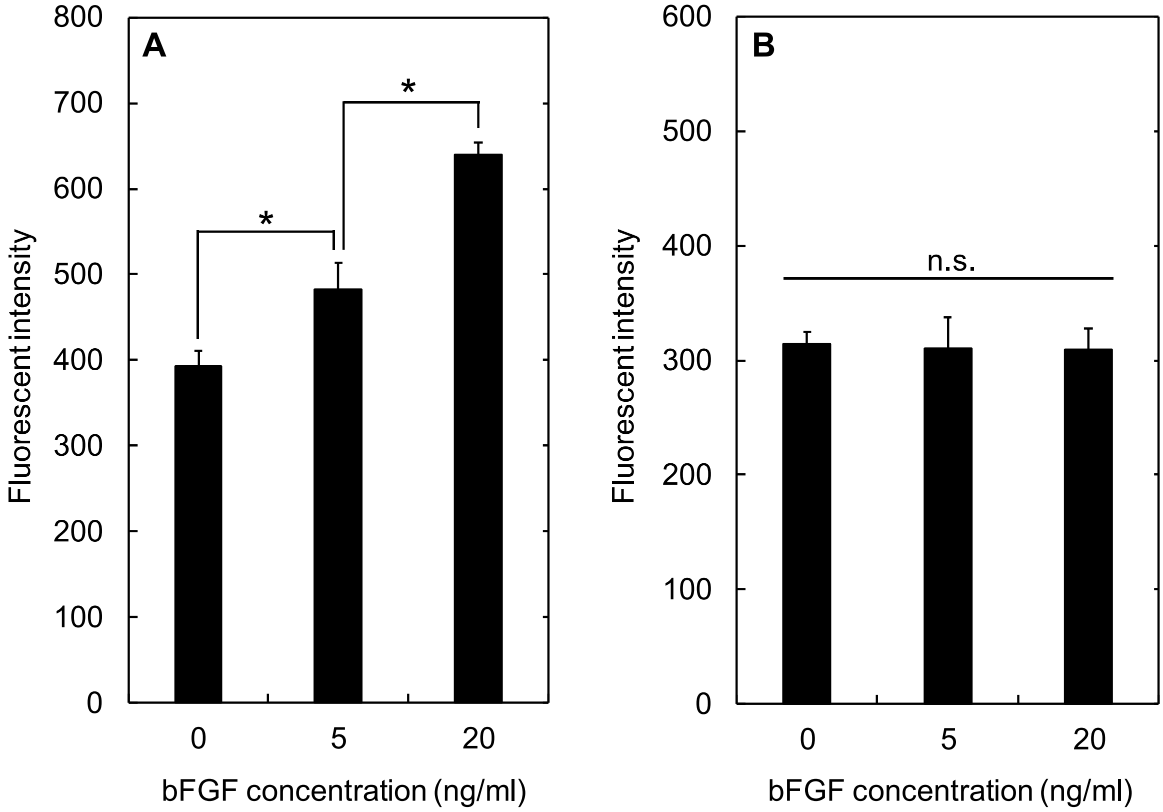

Figure 7. Proliferation assay of cGNS$_{MB}$-incubated cells cultured with or without bFGF. The cells were incubated with 10 μg/ml cGNS$_{Ki67\ MB}$ (A) and cGNS$_{GAP\ MB}$ (B) for 1 hr, and further for 24 hr in the presence of 0, 5, and 20 ng/ml bFGF. n.s.; not significant. *, $p < 0.05$; significant between the groups.

To continuously visualize the enhancement of proliferation ability after the addition of bFGF, the timelapse imaging was performed. **Figure 8** shows the fluorescent images of cells at different time points after the addition of 0 and 20 ng/ml bFGF. The fluorescence of cGNS$_{GAP\ MB}$ was constantly observed between 0 and 20 ng/ml bFGF at any time point (**Figure 8B**), and the fluorescence of cGNS$_{GAP\ MB}$ was retained at a similar level over the cell division. Similarly, the fluorescence of cGNS$_{Ki67\ MB}$ was observed between 0 and 20 ng/ml bFGF at the time point of 0 hr. However, at 20 ng/ml bFGF, the cGNS$_{Ki67\ MB}$ fluorescence increased faster from that of at 0 ng/ml bFGF (**Figure 8A**).

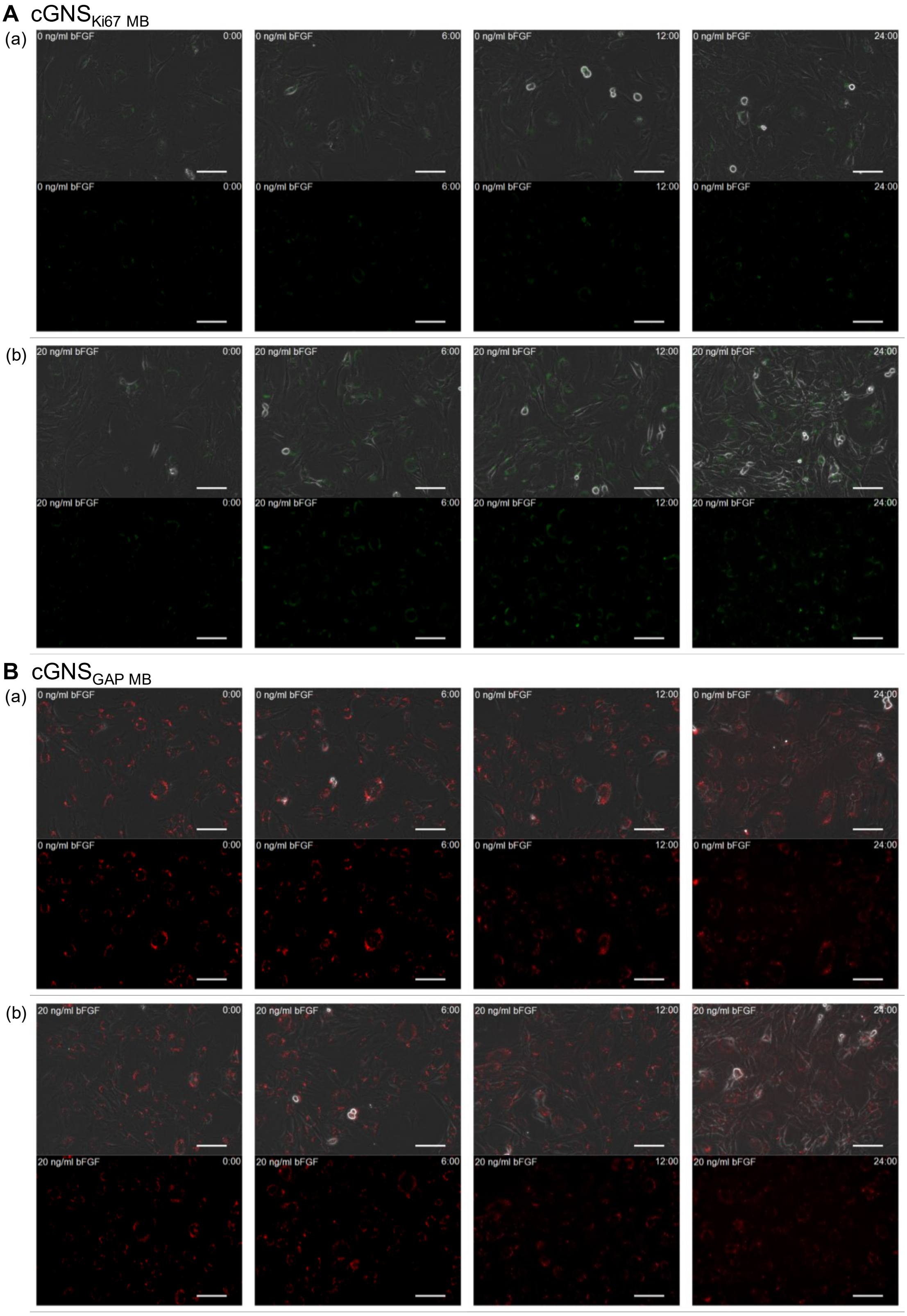

Figure 8. Timelapse imaging of cGNS$_{MB}$-incubated cells cultured with or without bFGF. The cells were incubated with 10 μg/ml cGNS$_{Ki67\ MB}$ (A) and cGNS$_{GAP\ MB}$ (B) for 1 hr, and further for 24 hr in the presence of 0 (a) and 20 ng/ml bFGF (b). The upper panel shows the merged images of phase contrast and MB fluorescence, while the lower panel shows the MB fluorescence. The fluorescent images at the time point of 0, 6, 12, and 24 hr after bFGF addition are shown. Scale bar is 100 μm.

DISUSSION

The present study demonstrates the methodological feasibility of $\mathrm{cGNS_{MB}}$ to visualize the proliferation ability of cells. The mRNA expression of Ki67 was significantly upregulated by the addition of bFGF over 20 ng/ml, as well as the protein expression. In addition, the cell proliferation was significantly accelerated by the bFGF addition. The $\mathrm{cGNS_{MB}}$ prepared were readily internalized into KUM6 cells, and emitted the fluorescence depending on the bFGF concentration added. The timelapse imaging experiments indicate that the fluorescence of $\mathrm{cGNS_{GAP\ MB}}$ was maintained at an almost same level over the cell division. On the contrary, the enhancement of $\mathrm{cGNS_{Ki67\ MB}}$ fluorescence at 20 ng/ml bFGF was faster than that without the bFGF addition.

There was no significant difference in the amount of MB incorporated, apparent size, and zeta potential between $\mathrm{cGNS_{Ki67\ MB}}$ and $\mathrm{cGNS_{GAP\ MB}}$ (**Figure 1**). The results indicate that the physicochemical properties of $\mathrm{cGNS_{MB}}$ did not depend on the sequence of MB. In addition, it is apparent from **Figure 5** that the amount of MB internalized into the cells was almost same, irrespective of the MB. This is due to the similar physicochemical properties of $\mathrm{cGNS_{MB}}$. The apparent size of around 230 nm and the positive charge of $\mathrm{cGNS_{MB}}$ is advantageous for the cell internalization in terms of the easy interaction with cell membrane and the subsequent endocytosis. In Chapter 3, at lower than 10 μg/ml of $\mathrm{cGNS_{MB}}$ concentration, 3 hr of incubation time did not show any cytotoxicity. In addition, it was demonstrated that the $\mathrm{cGNS_{MB}}$ were internalized into cells via endocytotic pathways, followed by the endosomal escape into the cytosol to specifically detect the target mRNA. Taken together, it is highly conceivable that the $\mathrm{cGNS_{Ki67\ MB}}$ and $\mathrm{cGNS_{GAP\ MB}}$ used in this study could specifically detect both the intracellular target mRNA of Ki67 and GAPDH.

The mRNA expression of Ki67 increased with an increase of bFGF concentration, and became constant over 20 ng/ml (**Figure 2**). The result was consistent with the immunofluorescent staining of Ki67 (**Figure 3**). In addition to the Ki67 expression after the bFGF addition for 24 hr, the cell proliferation was accelerated by the bFGF addition (**Figure 4**). The acceleration extent became greater as the increase of bFGF concentration, but there was no difference in the proliferation acceleration between 20 and 40 ng/ml. The result well corresponded to the expression of Ki67. In other words, Ki67 is a promising target of MB for the proliferation ability of cells. The cell proliferation at day 1 did not significantly change even in the presence of bFGF. On the other hand, after day 2, the cell proliferation significantly accelerated. The results indicate that the early enhancement of proliferation ability within 24 hr led to the latter cell proliferation. The cGNS$_{MB}$ imaging system developed in this study might allow us to judge the cell situation whether the cells can proliferate or not. Ki67 has been well recognized as the conventional proliferation marker, and the expression is upregulated during cell cycles except for the G0 phase. Other proliferation markers, such as cyclins and cyclin dependent kinases (CDK) [12], proliferation cell nuclear antigen (PCNA) [13], minichromosme maintenance proteins (MCM) [14], could be used as potential candidates for the MB target. These proliferation markers, including Ki67, are useful in the field of pathology for the cancer prognosis [1]. Among them, in this study, Ki67 was selected as a MB target for the cell proliferation ability because the long history of practical applications in the basic biology [7, 15, 16] and the clinical diagnosis as the labeling index of Ki67 [8, 9, 17]. Recently, the biological function of Ki67 over the cell division has been reported [18]. The protein of Ki67 functioned as a surfactant to prevent chromosomes from aggregation during the mitosis [19]. Therefore, the Ki67 expression should be essential for the cells capable of proliferation. On the other hand, the effect of bFGF on the proliferation and cell cycle of human umbilical cord-derived MSC has been reported [20]. The cell proliferation at different concentrations of bFGF (5, 10, 20, and 40 ng/ml) was evaluated by the 3H-thymidine incorporation assay. The proliferation significantly increased as the increase of bFGF concentration, which was consistent with the results in this study. However, as a slightly different point from the result of no difference in the cell proliferation between 20 and 40 ng/ml (**Figure 4**), the cell proliferation with 40 ng/ml bFGF was higher than that with 20 ng/ml. This might be due to the difference of cell type and the evaluation method of cell proliferation. The expressions of cyclin D1 and D2 of cell cycle proteins were upregulated by the addition of bFGF to reduce the cell population in G0/G1 phase and increase S and G2/M phases. In the present study, considering the expression of Ki67 except for the G0 phase, the addition of bFGF should reduce the G0 phase population to allow cells to increase the Ki67 expression.

After the incubation for $cGNS_{MB}$ internalization, different concentrations of bFGF were added to the cells, followed by further incubation for 24 hr (**Figures 6** and **7**). The fluorescent intensity of $cGNS_{Ki67\ MB}$ significantly increased with the increase of bFGF concentration added, whereas that of $cGNS_{GAP\ MB}$ did not. The fluorescent increase of $cGNS_{Ki67\ MB}$ well corresponded to the mRNA expression of Ki67 (**Figure 2**). These findings indicate that the $cGNS_{MB}$ could accurately detect the intracellular mRNA. In addition, the fluorescent localization of Ki67 MB was different from the immunofluorescent staining of Ki67 (**Figure 3**). This is due to the different intracellular localizations of target molecules. The Ki67 protein mainly localizes at cell nucleus. On the other hand, the Ki67 mRNA of MB target exists in the cytosol. Consistent with the results in this study, it has been reported that the Ki67 MB incorporated in poly(lactic-co-glycolic acid) (PLGA) nanoparticles could detect the Ki67 mRNA during the chondrogenesis of human MSC [21]. The culture conditions of chondrogenesis, such as the time period of supplementation with transforming growth factor-β3 (TGF-β3) and bFGF, to promote the differentiation into proliferative chondrocytes were optimized based on the MB signals. One of the advantages of $cGNS_{MB}$ over the PLGA nanoparticles is the easiness of cell internalization. The surface of PLGA nanoparticles were coated with poly-L-lysine to enhance the internalization, and a longer incubation of overnight at relatively higher concentration (1 mg/ml) needed for cell internalization of nanoparticles. On the contrary, $cGNS_{MB}$ were easily internalized into the cells at the concentration of 10 μg/ml and incubated only for 1 hr. The shorter incubation time period for the cell internalization of $cGNS_{MB}$ enough to give an efficient MB signal allows cells to detect the situation and functions timely.

It is apparent from **Figure 8A** that the fluorescent signal of $cGNS_{Ki67\ MB}$ for cells incubated at 20 ng/ml bFGF was stronger than that for the cells without bFGF. Compared with the case of 0 ng/ml bFGF, the fast increase of fluorescence which is responded by the bFGF addition, was observed within several hours. It is likely that the $cGNS_{Ki67\ MB}$ could detect the increase of Ki67 mRNA caused by the bFGF addition which might occur within several hours at single cell level. On the other hand, the fluorescence of $cGNS_{GAP\ MB}$ was constant between 0 and 20 ng/ml bFGF at any time point (**Figure 8B**). This is because the expression of intracellular target mRNA of GAPDH is sufficient and constant enough to be detected by $cGNS_{GAP\ MB}$, irrespective of the bFGF addition. The timelapse imaging revealed that the fluorescence of $\text{cGNS}_{\text{GAP MB}}$ did not change over the cell division. In general, it is recognized that the intracellular signal of imaging probes tends to become weak due to the dilution of intracellular concentration by the cell division [22]. On the contrary, in the system of intracellular controlled release of MB from cGNS, an excessive amount of quenched MB is continuously released into the cytosol according to the degradation of cGNS. It is highly possible that the sufficient amount of activatable MB enough to detect the target mRNA could be kept high even after the cell division. This is the reason why the fluorescence of $\text{cGNS}_{\text{GAP MB}}$ was retained at a similar level over the cell division. Further studies to investigate the time profile of mRNA expression and the intracellular concentration and localization of MB during the process of cell division should be needed.

This study demonstrates the feasibility of cGNS_{MB} system to visualize the proliferation ability of live cells without cells destruction at the sampling point. To our knowledge, this is the first report to chronologically visualize the cellular proliferation ability enhanced by different concentrations of bFGF, and the time course of enhancement in detail. In the development of anti-tumor drugs, the cGNS_{MB} system could be applied to monitor the proliferation ability of tumor cells and surrounding normal cells. This would be beneficial to judge the anti-tumor efficacy and the side effects of drugs over the course of treatment. In the fields of tissue engineering, the proliferation ability of cells applied to scaffolds could be visualized without the destruction of cells and scaffolds. In addition, the efficacy of growth factors like bFGF, and the combination with bioreactors to promote the proliferation ability could be tested both in two-dimensional (2D) and three-dimensional (3D) cultures in the scaffold. The applications would lead to the further development of tissue and disease modeling for basic cell research, drug discovery, and transplantation *in vivo*. In the future, the proliferation ability should be visualized by the cGNS_{MB} system for a longer time period in various situations of cell culture, as well as different cell types for the further applications.

REFERENCES

1. Whitfield ML, George LK, Grant GD, Perou CM. Common markers of proliferation. *Nat Rev Cancer* 2006; **6**: 99-106.
2. Gardel LS, Serra LA, Reis RL, Gomes ME. Use of perfusion bioreactors and large animal models for long bone tissue engineering. *Tissue Eng Part B Rev* 2014; **20**: 126-146.
3. Tang Y, Xu Y, Xiao Z, Zhao Y, Li J, Han S *et al.* The combination of three-dimensional and rotary cell culture system promotes the proliferation and maintains the differentiation potential of rat BMSCs. *Sci Rep* 2017; **7**: 192.
4. Kwok CK, Ueda Y, Kadari A, Gunther K, Ergun S, Heron A *et al.* Scalable stirred suspension culture for the generation of billions of human induced pluripotent stem cells using single-use bioreactors. *J Tissue Eng Regen Med* 2018; **12**: e1076-e1087.
5. Rodrigues M, Griffith LG, Wells A. Growth factor regulation of proliferation and survival of multipotential stromal cells. *Stem Cell Res Ther* 2010; **1**: 32.
6. Zhang X, Wang Y, Gao Y, Liu X, Bai T, Li M *et al.* Maintenance of high proliferation and multipotent potential of human hair follicle-derived mesenchymal stem cells by growth factors. *Int J Mol Med* 2013; **31**: 913-921.
7. Basak O, van de Born M, Korving J, Beumer J, van der Elst S, van Es JH *et al.* Mapping early fate determination in Lgr5+ crypt stem cells using a novel Ki67-RFP allele. *EMBO J* 2014; **33**: 2057-2068.
8. Pathmanathan N, Balleine RL. Ki67 and proliferation in breast cancer. *J Clin Pathol* 2013; **66**: 512-516.
9. Melling N, Kowitz CM, Simon R, Bokemeyer C, Terracciano L, Sauter G *et al.* High Ki67 expression is an independent good prognostic marker in colorectal cancer. *J Clin Pathol* 2016; **69**: 209-214.
10. Snyder SL, Sobocinski PZ. An improved 2,4,6-trinitrobenzenesulfonic acid method for the determination of amines. *Anal Biochem* 1975; **64**: 284-288.
11. Commerford SL. Iodination of nucleic acids in vitro. *Biochemistry* 1971; **10**: 1993-2000.
12. Hydbring P, Malumbres M, Sicinski P. Non-canonical functions of cell cycle cyclins and cyclin-dependent kinases. *Nat Rev Mol Cell Biol* 2016; **17**: 280-292.

13. Wang SC. PCNA: a silent housekeeper or a potential therapeutic target? *Trends Pharmacol Sci* 2014; **35**: 178-186.
14. Yu S, Wang G, Shi Y, Xu H, Zheng Y, Chen Y. MCMs in Cancer: Prognostic Potential and Mechanisms. *Anal Cell Pathol* 2020; **2020**: 3750294.
15. Zhang R, Takebe T, Sekine K, Koike H, Zheng Y, Taniguchi H. Identification of proliferating human hepatic cells from human induced pluripotent stem cells. *Transplant Proc* 2014; **46**: 1201-1204.
16. Motamedi M, Xu L, Elahi S. Correlation of transferrin receptor (CD71) with Ki67 expression on stimulated human and mouse T cells: The kinetics of expression of T cell activation markers. *J Immunol Methods* 2016; **437**: 43-52.
17. Li LT, Jiang G, Chen Q, Zheng JN. Ki67 is a promising molecular target in the diagnosis of cancer (review). *Mol Med Rep* 2015; **11**: 1566-1572.
18. Sun X, Kaufman PD. Ki-67: more than a proliferation marker. *Chromosoma* 2018; **127**: 175-186.
19. Cuylen S, Blaukopf C, Politi AZ, Muller-Reichert T, Neumann B, Poser I *et al.* Ki-67 acts as a biological surfactant to disperse mitotic chromosomes. *Nature* 2016; **535**: 308-312.
20. Ramasamy R, Tong CK, Yip WK, Vellasamy S, Tan BC, Seow HF. Basic fibroblast growth factor modulates cell cycle of human umbilical cord-derived mesenchymal stem cells. *Cell Prolif* 2012; **45**: 132-139.
21. Tay LM, Wiraja C, Wu Y, Yang Z, Lee EH, Xu C. The effect of temporal manipulation of transforming growth factor beta 3 and fibroblast growth factor 2 on the derivation of proliferative chondrocytes from mensenchymal stem cells-A study monitored by quantitative reverse transcription polymerase chain reaction and molecular beacon based nanosensors. *J Biomed Mater Res A* 2018; **106**: 895-904.
22. Jensen EC. Use of fluorescent probes: their effect on cell biology and limitations. *Anat Rec* 2012; **295**: 2031-2036.

Chapter 5

Preparation of cationized gelatin nanospheres incorporating molecular beacon to visualize cell apoptosis

INTRODUCTION

Cell transplantation is one of the promising therapies in regenerative medicine to induce the regeneration and repairing of damaged tissues and organs [1-8]. For the development of cell transplantation, the non-invasive technologies and methodologies to visualize the localization, distribution, and biological functions of cells transplanted in the living body are highly required. Imaging technologies are effective in non-invasively evaluating the localization and distribution of cells transplanted [9-17]. Various therapeutic effects have been reported based on the biological functions of cells transplanted, although the cell functions are not always clear [18-20]. On the other hand, it is reported that the majority of cells transplanted undergo apoptosis [21]. Under these circumstances, it is of prime importance to non-invasively visualize the apoptosis of cells transplanted which is a key to evaluate the therapeutic efficacy.

In Chapter 3, it was demonstrated that the intracellular controlled release of molecular beacons (MB) from cationized gelatin nanospheres (cGNS) is an effective system to continuously visualize intracellular messenger RNA (mRNA) over 2 weeks. In addition, Chapter 4 demonstrated that the cell proliferation ability was visualized by detecting the mRNA of Ki67 based on the intracellular controlled release of MB. To visualize the cell apoptosis, MB to detect caspase-3 mRNA of an apoptosis target expressing in apoptotic cells is designed to be incorporated in the cGNS. As a control of stable fluorescence, glyceraldehyde-3-phosphate dehydrogenase (GAPDH) MB which can detect GAPDH mRNA of a housekeeping gene constantly expressing in cells is used.

In this chapter, cGNS incorporating caspase-3 and GAPDH MB ($\mathrm{cGNS_{casp3\ MB}}$ and $\mathrm{cGNS_{GAP\ MB}}$, respectively) were prepared aiming at the visualization of cell apoptosis. The $\mathrm{cGNS_{MB}}$ preparation was performed in different conditions to optimize their physicochemical properties for cell internalization. The sequence specificity in hybridization and the stability of $\mathrm{cGNS_{MB}}$ against nuclease were evaluated. The cytotoxicity, cell internalization, and intracellular localization of $\mathrm{cGNS_{MB}}$ were investigated. The fluorescent intensity change of cells incubated with the $\mathrm{cGNS_{MB}}$ was evaluated to analyze the functional response of MB. Apoptosis was induced by the treatment of camptothecin of a common apoptosis inducer for cells which had been incubated with the $\mathrm{cGNS_{MB}}$. The conventional analysis of cell apoptosis and the mRNA expression of caspase-3 were investigated to compare with the $\mathrm{cGNS_{MB}}$ imaging.

EXPERIMENTAL

Materials

Gelatin with an isoelectric point of 9.0 and the weight-averaged molecular weight of 99,000, prepared by an acidic process of pig skin, was kindly supplied from Nitta Gelatin Inc., Osaka, Japan. MB for mouse mRNA of GAPDH and caspase-3 were designed by NIPPON GENE Co., Ltd, Tokyo, Japan, and synthesized by Eurogentec S.A., Seraing, Belgium. Target oligonucleotides of DNA for MB (GAPDH specific and caspase-3 specific sequence) were synthesized by Hokkaido System Science Co., Ltd, Sapporo, Japan. The sequences of MB and target oligonucleotides were listed in **Table 1**. Glutaraldehyde (GA, 25 wt% in water), glycine, concentrated hydrochloric acid (HCl), acetone, and 1-ethyl-3-(3-dimethylaminopropyl) carbodiimide hydrochloride salt (EDC) were purchased from Nacalai Tesque. Inc., Kyoto, Japan. Spermine was purchased from Sigma-Aldrich Inc., St. Louis, MO, USA. The reagents were used without further purification.

Preparation of cationized gelatin

Cationized gelatin was prepared by conjugating spermine with the carboxyl groups of gelatin as described in Chapter 2. In brief, spermine was added at a molar ratio of 50 to the carboxyl groups of gelatin into 50 ml of gelatin aqueous solution (40 mg/ml). Immediately after that, the solution pH was adjusted to 5.0 by adding 11 M HCl. Double-distilled water (DDW) was added to give the final volume of 100 ml. Next, EDC was added at a molar ratio of 3 to the carboxyl groups of gelatin, followed by the agitation at 40 °C for 18 hr and dialysis against DDW for 3 days with a dialysis membrane (molecular weight cut off = 12,000 to 14,000, Viskase Companies, Inc., Willowbrook, IL, USA) at room temperature. The dialyzed solution was freeze-dried to obtain the cationized gelatin. The percentage of amino groups introduced into gelatin was determined by the conventional 2,4,6-trinitrobenzene sulfonic acid (TNBS, FUJIFILM Wako Pure Chemical Inc., Osaka, Japan) method [22]. The percentage was 44.8 mole% per the carboxyl groups of gelatin.

Table 1. Sequences of MB, target oligonucleotides, and PCR primers used.

MB, target oligonucleotides, and PCR primers	Sequences (5’ to 3’)
GAPDH MB	[Cy®5]-CTGGTAATCCGTTCACACCGACCTTCACCAG-[BHQ®-2]
Caspase-3 MB	[6-FAM]-GTCACATACAGGAAGTCAGCCTCCACCGTGAC-[BHQ®-1]
GAPDH specific target	TGGTGAAGGTCGGTGTGAACGGATT
Caspase-3 specific target	CGGTGGAGGCTGACTTCCTGTATG
GAPDH forward	AACTTTGGCATTGTGGAAGG
GAPDH reverse	GGAGACAACCTGGTCCTCAG
Caspase-3 forward	TGTCATCTCGCTCTGGTACG
Caspase-3 reverse	AAATGACCCCTTCATCACCA

MB: molecular beacons
PCR: polymerase chain reaction
GAPDH: glyceraldehyde-3-phosphate dehydrogenase
6-FAM: 6-carboxyfluorescein
BHQ®: black hole quencher
underline: stem structure

Preparation of $\mathrm{cGNS}_{\mathrm{MB}}$

According to the preparation procedure described in Chapter 3, cGNS were prepared by the conventional coacervation method. Briefly, 1.25 ml of cationized gelatin aqueous solution (50 mg/ml) was warmed up to 40 °C. Next, 5 ml of acetone was added to the solution, and the coacervate was formed. GA (20 µl) were added, followed by chemically crosslinking cGNS for 6 hr. For the blocking of aldehyde groups unreacted, 2 ml of glycine aqueous solution (0.5 M) was added. The resulting solution was agitated overnight at 40 °C and the residual acetone was evaporated. cGNS were collected by the centrifugation of 14,000 rpm for 30 min at 25 °C and resuspended in DDW. The centrifugation and resuspension were repeated three times to wash cGNS.

Two types of MB for GAPDH and caspase-3 were used in this study. MB and cGNS were mixed at various ratios (2, 10, 20, 30, and 40 pmole MB/μg cGNS) and incubated for 15 min at room temperature. The mixture was centrifuged at 14,000 rpm for 30 min at 25 °C and resuspended in DDW to obtain cGNS incorporating GAPDH MB ($\mathrm{cGNS_{GAP\ MB}}$) and caspase-3 MB ($\mathrm{cGNS_{casp3\ MB}}$).

Radiolabeling of MB

According to the method described in Chapter 2, MB was labeled with radioactive iodine (^{125}I) [23]. The MB (5 μl, 10 μM in 0.2 M sodium acetate and 40 mM acetic acid solution, pH5.0) were incubated at 60 °C for 50 min with 2 μl of 0.3 mM Na_2SO_3, 5 μl of $Na^{125}I$ (740 MBq/ml in 0.1 M NaOH aqueous solution, PerkinElmer Inc., Waltham, MA, USA), and 5 μl of 4 mM $TlCl_3$. Next, mixed 100 μl of 0.1 M Na_2SO_3 and 900 μl of 0.1 M NaCl, 50 mM Tris, and 1 mM ethylenediaminetetra acetic acid (EDTA) solution was added to the MB solution. After the incubation for 30 min at 60 °C, the reactant was applied on the PD-10 column (GE Healthcare Bio-Sciences Corp., Piscataway, NJ, USA) to purify the ^{125}I-labeled MB by the gel filtration. The radioactivity of ^{125}I was measured using a gamma counter (Auto Well Gamma System ARC-380 CL, Aloka Co., Ltd, Tokyo, Japan).

Characterization of cGNS with or without MB incorporation

cGNS, $\mathrm{cGNS_{GAP\ MB}}$, and $\mathrm{cGNS_{casp3\ MB}}$ were resuspended in 10 mM phosphate buffered-saline solution (PBS, pH7.4), and the apparent size of nanospheres was measured by dynamic light scattering (DLS, Zetasizer Nano-ZS, Malvern Instruments Ltd., Worcestershire, UK). On the other hand, nanospheres were resuspended in 10 mM phosphate buffer solution (PB, pH7.4), and the zeta potential was measured by electrophoresis light scattering (ELS, Zetasizer Nano-ZS, Malvern Instruments Ltd., Worcestershire, UK). The amount of MB incorporated in cGNS was determined by the radioactivity of $\mathrm{cGNS_{GAP\ MB}}$ and $\mathrm{cGNS_{casp3\ MB}}$

prepared with the ^{125}I-labeled MB. The experiment was independently performed three times for each sample unless otherwise mentioned.

Hybridization assay

Various concentrations of target oligonucleotides (GAPDH specific and caspase-3 specific, 0, 50, 100, 500, 1000, and 5000 nM) and free MB (GAPDH MB and casppae-3 MB, 100 nM) or $cGNS_{MB}$ ($cGNS_{GAP\ MB}$ and $cGNS_{casp3\ MB}$, 100 nM MB) were mixed in hybridization buffer (20 mM Tris-HCl buffer containing 50 mM KCl and 5 mM $MgCl_2$, pH8.0). After the incubation of 1 hr at room temperature under light protection, the fluorescent intensity was measured by Multi-mode Microplate Reader (SpectraMax i3x, Molecular Devices Japan Co., Ltd., Tokyo, Japan).

Evaluation of nuclease stability

The stability of free MB and $cGNS_{MB}$ against DNase I (QIAGEN, Hilden, Germany) was evaluated. Various concentrations of DNase I (0, 0.5, 1, 5, 10, 15, 20, 30, and 40 U/ml) and free MB (GAPDH MB and caspase-3 MB, 100 nM) or $cGNS_{MB}$ ($cGNS_{GAP\ MB}$ and $cGNS_{casp3\ MB}$, 100 nM MB) were mixed in PBS containing 0.5 mM $MgCl_2$ and 0.9 mM $CaCl_2$. After the incubation of 15 min at 37 °C in a condition of light protection, the fluorescent intensity was measured by the microplate reader described above.

Cell culture experiments

KUM6 cells (JCRB1202) of a mouse bone marrow-derived mesenchymal stem cells (MSC) line were purchased from JCRB Cell Bank (National Institute of Biomedical Innovation, Health and Nutrition, Osaka, Japan). The cells were cultured in Iscove's Modified Dulbecco's Medium (IMDM, Thermo Fisher Scientific Inc., Waltham, MA, USA) containing 10 vol% bovine fetal calf serum (FCS, GE healthcare Life Sciences Hyclone laboratories inc., Logan, UT, USA) and 1 vol% penicillin/streptomycin (Nacalai Tesque. Inc., Kyoto, Japan) at 37 °C in a 5% CO_2-95% air atmospheric condition. The cells were detached with 0.25 wt% trypsin-containing 1 mM EDTA solution (Nacalai Tesque. Inc., Kyoto, Japan) and continued to culture in 100 mm cell culture dish (Corning Inc., Corning, NY, USA) to allow to grow until to 80% confluency.

Evaluation of cell viability after incubation with cGNS$_{MB}$

Cells were seeded on each well of 96 well multi-dish culture plate (Corning Inc., Corning, NY, USA) at a density of 1 × 10^4 cells/well and cultured for 24 hr. The medium was changed to OPTI MEM (Thermo Fisher Scientific Inc., Waltham, MA, USA), and then cGNS$_{GAP\ MB}$ or cGNS$_{casp3\ MB}$ (1, 5, 10, 15, and 20 μg/ml) were added to each well. The cell viability was evaluated using a cell counting kit (Nacalai Tesque. Inc., Kyoto, Japan). After the incubation for 3 hr with nanospheres, 10 μl of 2-(2-methoxy-4-nitrophenyl)-3-(4-nitrophenyl)-5-(2,4-disulfophenyl)-2H-tetrazolium (WST-8) solution was added to each well and further incubated for 1 hr. The absorbance of samples at 450 nm was measured by the microplate reader. The percentage of cell viability was expressed as 100% for cells without nanospheres incubation.

Evaluation of cell internalization

Cells were seeded in each well of 6 well multi-dish culture plate (Corning Inc., Corning, NY, USA) at a density of 5 × 10^4 cells/well, and cultured for 24 hr. The medium was changed to OPTI MEM, and then cGNS$_{GAP\ MB}$ prepared with the ^{125}I-labeled MB (1, 5, 10, 15, and 20 μg/ml) was added to each well. After the incubation of 3 hr with nanospheres, the medium was removed and cells were washed with PBS, and then the medium was added. The cells treated with nanospheres were collected by the trypsinization at 12 hr after nanospheres added. The amount of MB was determined by the radioactivity measurement.

For the inhibition of endocytosis, cells were similarly seeded in each well of 6 well multi-dish culture plate at a density of 5 × 10^4 cells/well, and cultured for 24 hr. The medium was changed to OPTI MEM, and cGNS$_{GAP\ MB}$ (10 μg/ml, 153 pmole of MB) was added, followed by incubating for 3 hr at 4 °C. GAPDH MB (153 pmole) were similarly incubated with the cells to measure the amount of MB internalized into the cells based on the radioactivity.

Evaluation of intracellular localization

To fluorescently label cGNS, fluorescein isothiocyanate isomer I (FITC, 200 μg/ml, Sigma-Aldrich Inc., St. Louis, MO, USA) and cGNS (5 mg/ml) were mixed in carbonate-bicarbonate buffer solution (0.1 M, pH9.6) at room temperature. After the incubation of 8 hr, the mixture was centrifuged at 14,000 rpm for 30 min at 25 °C and resuspended in DDW. The centrifugation and resuspension were repeated three times, and finally cGNS labeled with FITC (FITC-cGNS) were dispersed in DDW. FITC labeled-cGNS$_{GAP\ MB}$ (FITC-cGNS$_{GAP\ MB}$) were prepared by mixing GAPDH MB and FITC-cGNS at the same procedure described above.

Cells were seeded in a glass bottom dish of 35 mm in diameter (Matsunami Glass Industries Ltd., Tokyo, Japan) at a density of 5×10^4 cells/dish, and cultured for 24 hr. After the medium change to OPTI MEM, the cells were incubated with FITC-cGNS$_{GAP\ MB}$ (10 μg/ml) for 3 hr, and further cultured for 9 hr. The lysosomes of cells treated with nanospheres were stained with 80 nM LysoTracker® Red DND-99 (Thermo Fisher Scientific Inc., Waltham, MA, USA), followed by wash with PBS and fixation with 4 vol% paraformaldehyde for 20 min. The nuclei of cells were stained with 300 nM 4’,6-diamidino-2-phenylindole (DAPI, Thermo Fisher Scientific Inc., Waltham, MA, USA). The fluorescent images of cells were taken by a fluorescent microscope (BZ-X700, KEYENCE Co., Ltd., Osaka, Japan). The fluorescence was expressed as a pseudo color.

Fluorescent imaging of apoptosis

After the incubation of 12 hr with cGNS$_{GAP\ MB}$ or cGNS$_{casp3\ MB}$ (10 μg/ml), apoptosis was induced by camptothecin (Enzo Life Sciences, Inc., Farmingdale, NY, USA) [24]. In brief, various concentrations of camptothecin (final concentrations of 1, 2, 5, 10, and 20 μM) were added to the cells, and cultured for 12 hr to induce the cell apoptosis. After the apoptosis induction, the cells were observed by the fluorescent microscopy. Six fluorescent images were taken at random and quantified by BZ-X Analyzer equipped with the microscope. The fluorescence of images was calculated according to the following equation:

Fluorescent intensity = Fluorescent Area × Mean Fluorescent Intensity

Apoptosis analysis

Apoptosis of cells was evaluated by flow cytometry analysis using FITC Annexin V Apoptosis Detection Kit I (Becton Dickinson and Company, Franklin Lakes, NJ, USA) according to the manufacture's protocol. Briefly, cells were seeded in each well of 6 well multi-dish culture plate at a density of 1×10^5 cells/well, and cultured for 24 hr. Camptothecin (final concentrations of 0, 1, 2, 5, 10, and 20 μM) was added to the cells, and cultured for 12 hr. The cells were collected by the trypsinization and washed with cold PBS twice. Finally, the cells were suspended in 10 mM HEPES/NaOH solution containing 140 mM NaCl and 2.5 mM $CaCl_2$ (pH7.4), and FITC-conjugated annexin V and propidium iodide (PI) were added to the suspension. The cell suspension was analyzed on FACSCanto II flow cytometer and FACSDiva software (Becton Dickinson and Company, Franklin Lakes, NJ, USA) by counting 10,000 cells.

mRNA expression analysis

Cells were seeded in each well of 6 well multi-dish culture plate at a density of 1×10^5 cells/well, and induced apoptosis by camptothecin at the same procedure described above. After the apoptosis induction for 12 hr, the total RNA was extracted using RNeasy Plus Mini Kit (QIAGEN, Hilden, Germany) according to the manufacture's instructions. Complementary DNA (cDNA) was synthesized using a SuperScript VILO cDNA synthesis kit (Thermo Fisher Scientific Inc., Waltham, MA, USA). The cDNA (100 ng, 1 μl), forward and reverse primers (10 μM, each 0.5 μl), 12.5 μl of Power SYBR Green PCR Master Mix (Applied Biosystems, Foster City, CA, USA), and 10.5 μl of RNase-free water were mixed, and quantitative real-time polymerase chain reaction (qPCR) was performed on a Prism 7500 real-time PCR thermal cycler (Applied Biosystems, Foster City, CA, USA). The sequences of primers used were listed in **Table 1**. The following qPCR conditions were used: 95 °C for 10 min, followed by 40 cycles of 95 °C for 15 sec and 60 °C for 1 min. The level of caspase-3 expression was normalized by that of GAPDH, and the expression level was analyzed by $\Delta\Delta$Ct method comparing with the untreated cells.

Statistical analysis

The data were expressed as the average ± standard deviation (SD). All the statistical analysis was performed using one-way analysis of variance (ANOVA) with a post-hoc Tukey-Kramer multiple comparison test. *P* values less than 0.05 were considered to be statistically significant.

RESULTS

Characterization of cGNS with or without MB incorporation

The apparent size and zeta potential of MB-free, empty cGNS were 155.1 ± 2.8 nm and 8.18 ± 0.06 mV, respectively. **Figure 1** shows the amount of MB incorporated in cGNS, the apparent size, and the zeta potential of cGNS$_{\text{GAP MB}}$ and cGNS$_{\text{casp3 MB}}$. Both the cGNS$_{\text{GAP MB}}$ and cGNS$_{\text{casp3 MB}}$ showed similar physicochemical properties. The amount of MB incorporated in cGNS increased as an increase of MB amount added. The apparent size also increased, whereas the zeta potential tended to decrease as the amount of MB added increased. The following experiments were performed using the nanospheres prepared at the MB amount of 20 pmole/µg cGNS.

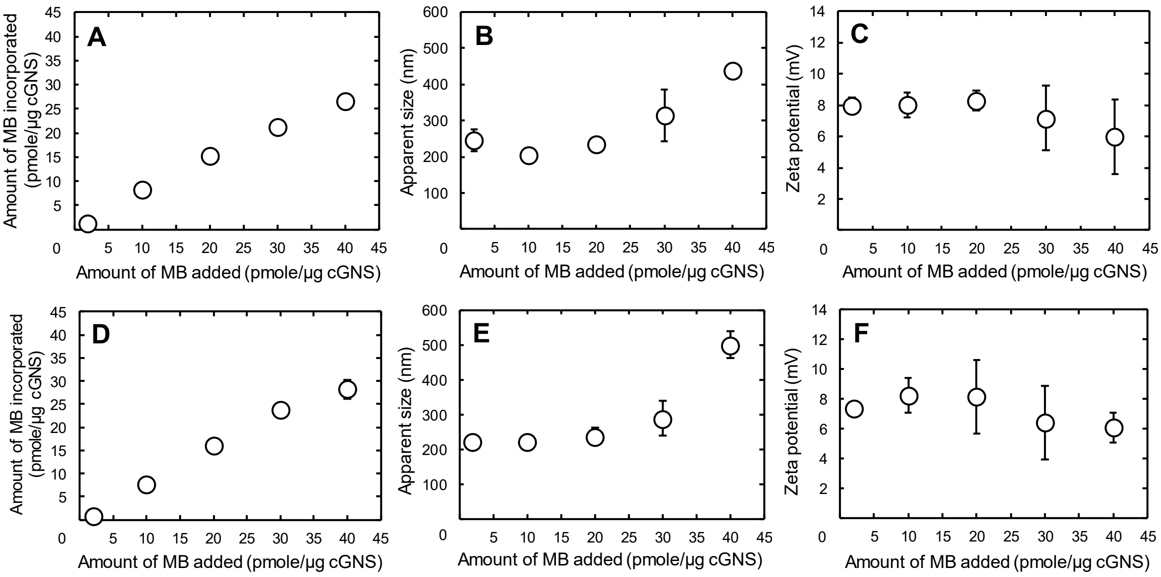

Figure 1. The amount of MB incorporated (A and D), apparent size (B and E), and zeta potential (C and F) of cGNS$_{\text{GAP MB}}$ (A, B, and C) and cGNS$_{\text{casp3 MB}}$ (D, E, and F) prepared at different ratios of MB to cGNS.

Hybridization specificity and nuclease stability of MB incorporated in cGNS

Figure 2 shows the hybridization specificity of free MB and MB incorporated in cGNS. Both the fluorescent intensities of free GAPDH MB and caspase-3 MB increased with the increased specific target concentration. On the other hand, an increase of non-specific target concentration did not affect the free MB fluorescent intensity (**Figures 2A** and **2B**). The fluorescent intensity of both GAPDH MB and caspase-3 MB incorporated in cGNS increased as the increase of specific target concentration. However, compared with free MB, the increase was small at the low concentrations of specific target. In addition, the fluorescent intensity of MB incorporated in cGNS was slightly increased as the increase of non-specific target concentration (**Figures 2C** and **2D**).

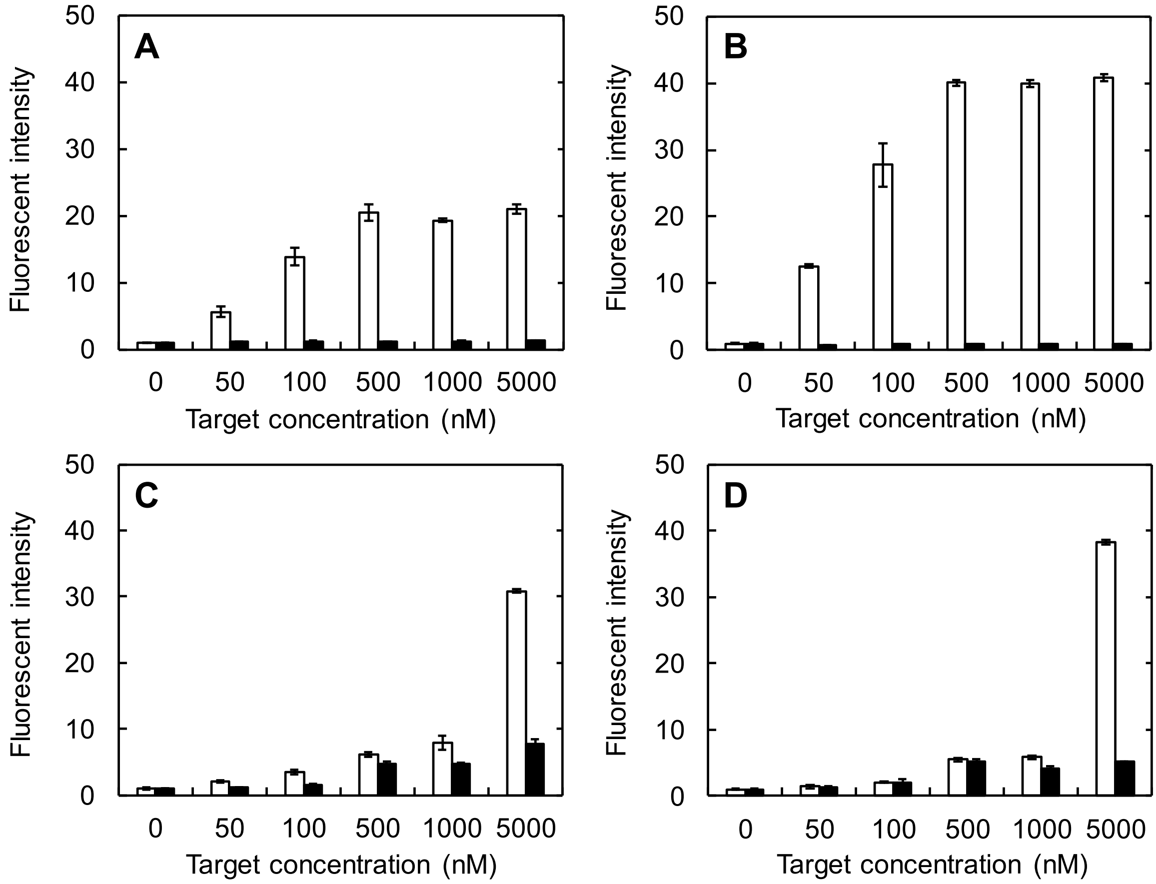

Figure 2. Hybridization specificity of free MB and MB incorporated in cGNS. The fluorescent intensity of free GAPDH MB (A), free caspase-3 MB (B), cGNS$_{\mathrm{GAP\ MB}}$ (C), and cGNS$_{\mathrm{casp3\ MB}}$ (D) mixed with different concentrations of specific (☐) and non-specific target oligonucleotides (■). The concentration of MB is all 100 nM.

Figure 3 shows the nuclease stability of free MB and MB incorporated in cGNS. Both the free GAPDH MB and caspase-3 MB were degraded and the fluorescent intensity increased with the DNase I concentration. On the other hand, the fluorescent intensity of both GAPDH MB and caspase-3 MB incorporated in cGNS was constant at any DNase I concentration.

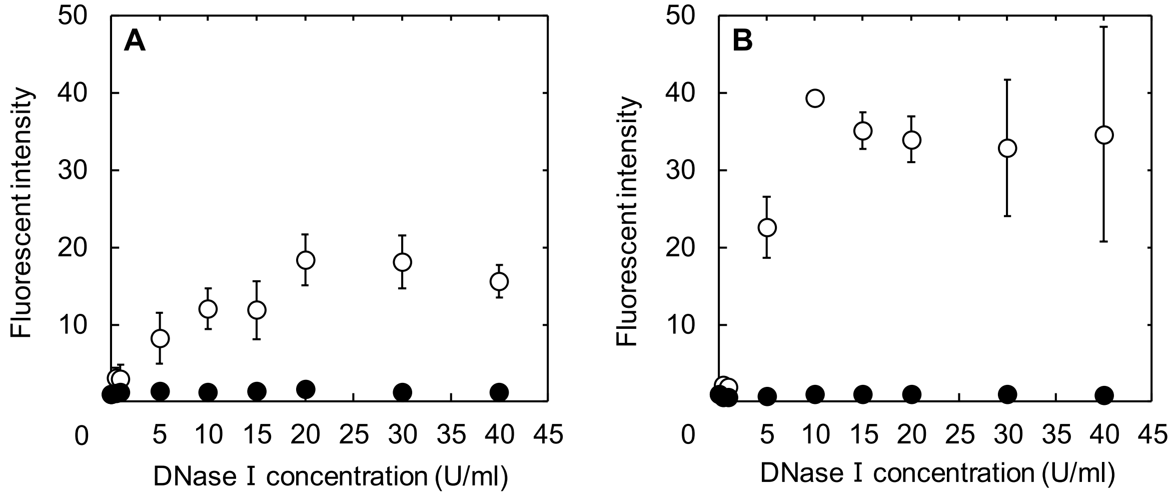

Figure 3. Nuclease stability of free MB (○) and MB incorporated in cGNS (●). The fluorescent intensity after mixing GAPDH MB (A) and caspae-3 MB (B) with different concentrations of DNase I. The concentration of MB is all 100 nM.

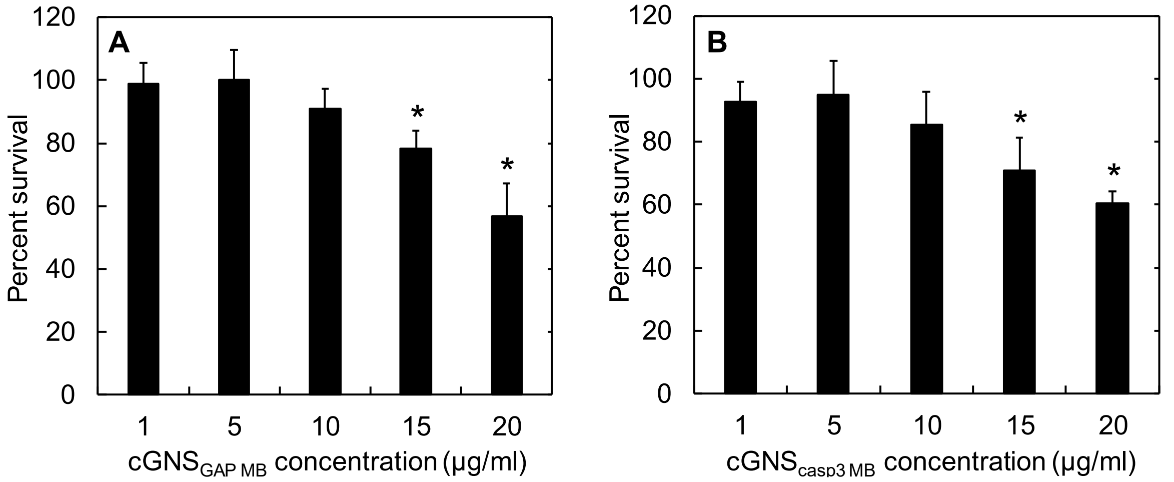

Figure 4. Viability of cells incubated with different concentrations of cGNS$_{GAP\ MB}$ (A) and cGNS$_{casp3\ MB}$ (B). The viability of cells without incubation with cGNS$_{MB}$ was expressed 100%. *, $p < 0.05$; significant against the percent survival of cells without cGNS$_{MB}$ incubation.

Cell viability after incubation with cGNS$_{\mathrm{MB}}$

Figure 4 shows the cell viability after incubation with cGNS$_{\mathrm{MB}}$. The percentage of cells survived tended to decrease as the increase of cGNS$_{\mathrm{MB}}$ concentration for both the cGNS$_{\mathrm{GAP\ MB}}$ and cGNS$_{\mathrm{casp3\ MB}}$. Significant cytotoxicity was observed at the concentrations of 15 and 20 µg/ml.

Cell internalization and intracellular localization

Figure 5A shows the cell internalization amount of MB incorporated in cGNS. The amount of MB internalized became higher with the increase of cGNS$_{\mathrm{MB}}$ concentration, and reached a plateau level. When the cell internalization of MB incorporated in cGNS was investigated at 37 and 4 °C incubation, the amount of MB internalized at 4 °C incubation was significantly lower than that at 37 °C (**Figure 5B**). In addition, free MB were hardly internalized into the cells both at 37 and 4 °C (**Figure 5C**).

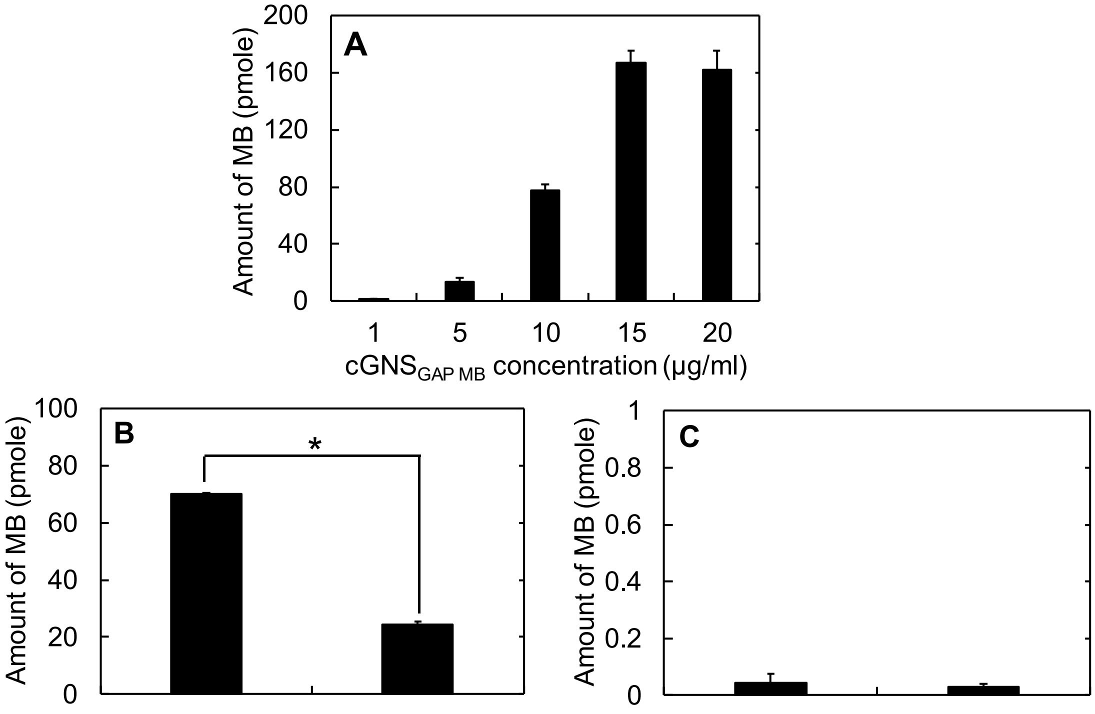

Figure 5. Cell internalization of free GAPDH MB and cGNS$_{\mathrm{GAP\ MB}}$. (A) The effect of cGNS$_{\mathrm{GAP\ MB}}$ concentration on the amount of MB internalized into the cells. (B) The amount of MB internalized into cells after incubation with cGNS$_{\mathrm{GAP\ MB}}$ (10 µg/ml, 153 pmole of GAPDH MB) at 37 and 4 °C. (C) The amount of MB internalized into cells after incubation with free GAPDH MB (153 pmole) at 37 and 4 °C. *, $p < 0.05$; significant against the amount at 37 °C.

Figure 6 shows the cell internalization of FITC-cGNS$_{GAP\ MB}$ and the intracellular localization of cGNS or MB, lysosomes, and nuclei. Both the cGNS and MB were localized in the cells in a similar distribution pattern. **Figure 6B (a)** shows the co-localization for all the MB and cGNS. It is apparent from **Figure 6B (b)** that the MB-cGNS complexes were not distributed at the lysosomes (magenta) of cells.

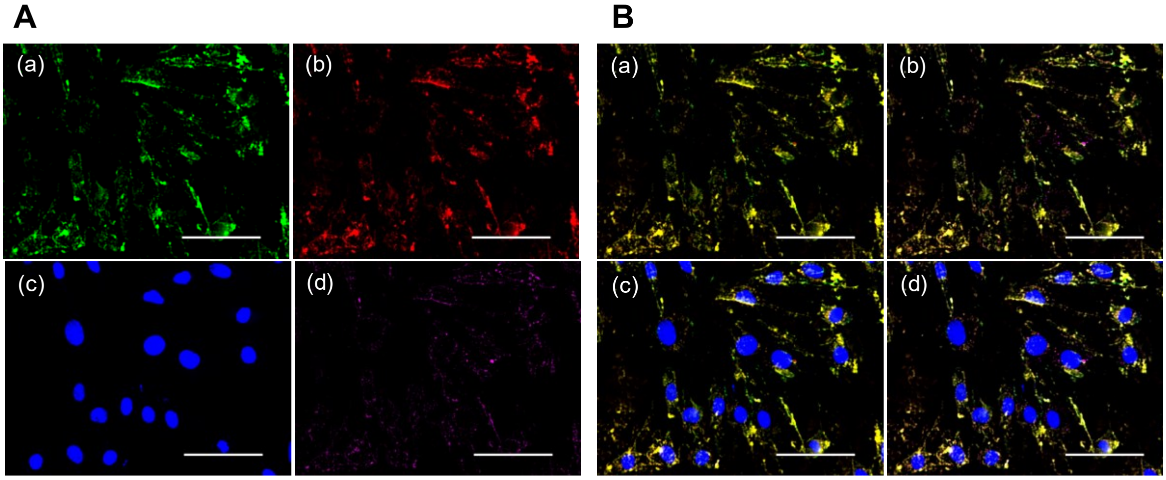

Figure 6. Fluorescent microscopic images of FITC-cGNS$_{GAP\ MB}$ internalized into cells. (A) Fluorescent images of cells after incubation with FITC-cGNS$_{GAP\ MB}$ (10 µg/ml): (a) Green: cGNS, (b) Red: GAPDH MB, (c) Blue: nuclei, and (d) Magenta: lysosomes. (B) Merged fluorescent images: (a) cGNS and MB, (b) cGNS, MB, and lysosomes, (c) cGNS, MB, and nuclei, and (d) cGNS, MB, nuclei, and lysosomes. Scale bar is 100 µm.

Fluorescent imaging of apoptosis

After the cell incubation and internalization of cGNS$_{MB}$, the cells following the addition of various concentrations of camptothecin, were observed by the fluorescent microscopy (**Figure 7**). **Figures 7A** and **7B** show the fluorescent images of cells incubated with cGNS$_{GAP\ MB}$ and cGNS$_{casp3\ MB}$, respectively. The fluorescence of GAPDH MB was constantly observed, irrespective of the camptothecin addition. On the contrary, for the caspase-3 MB, fluorescence was observed only after the camptothecin addition.

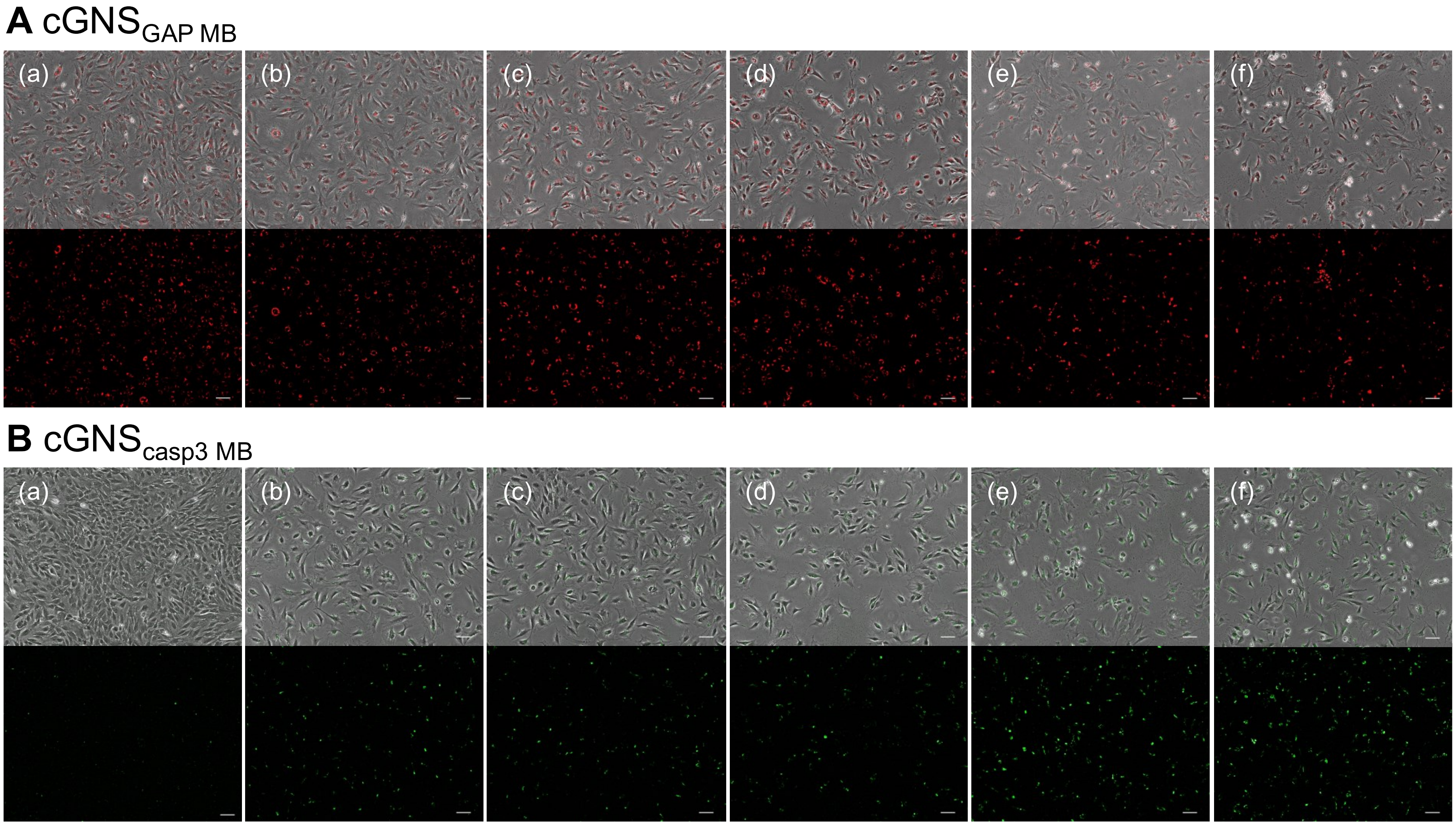

Figure 7. Fluorescent microscopic images of cellular apoptosis. Fluorescent images of cells incubated with 10 µg/ml cGNS$_{\text{GAP MB}}$ (A) and cGNS$_{\text{casp3 MB}}$ (B). Fluorescent images of cells after incubation with 0 (a), 1 (b), 2 (c), 5 (d), 10 (e), and 20 µM of camptothecin (f). The upper panel shows the merged images of phase contrast and MB fluorescence, while the lower panel shows the MB fluorescence. Scale bar is 100 µm.

Figure 8 shows the fluorescent intensity of cells incubated with $cGNS_{GAP\ MB}$ and $cGNS_{casp3\ MB}$ after the addition of camptothecin. The fluorescence of cells incubated with $cGNS_{GAP\ MB}$ was constant at any camptothecin concentration. On the other hand, the fluorescence of cells incubated with $cGNS_{casp3\ MB}$ significantly increased after the addition of camptothecin.

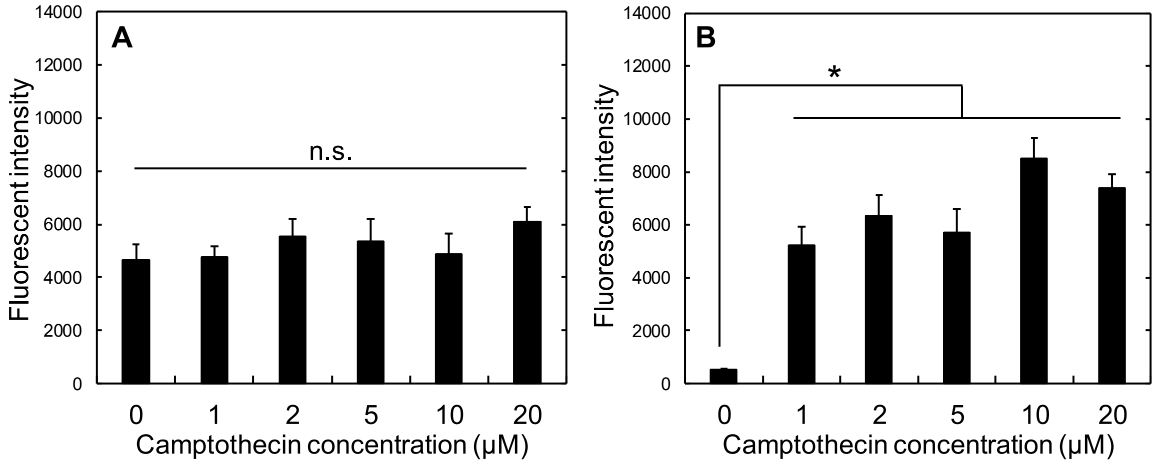

Figure 8. Apoptosis evaluation of cells incubated with $cGNS_{GAP\ MB}$ and $cGNS_{casp3\ MB}$. Fluorescent intensity of cells after incubation with 10 μg/ml $cGNS_{GAP\ MB}$ (A) and $cGNS_{casp3\ MB}$ (B). n.s.; not significant. *, $p < 0.05$; significant against the fluorescent intensity of cells at 0 μM camptothecin.

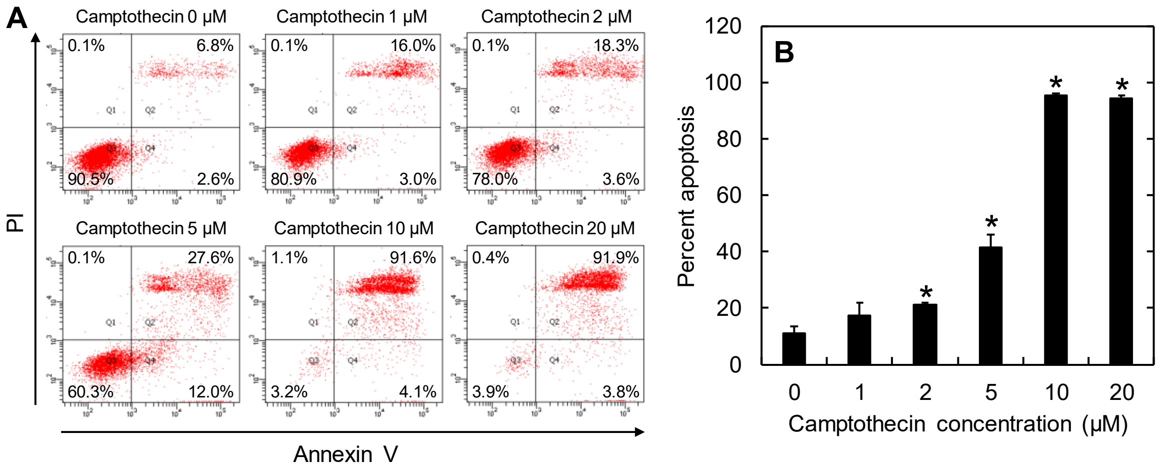

Figure 9. Apoptosis analysis of cells after incubation with different concentrations of camptothecin. (A) Flow cytometric plots of cell population and (B) the percentage of apoptotic cells 12 hr after incubation with different camptothecin concentrations. *, $p < 0.05$; significant against the percent apoptosis at 0 μM camptothecin.

Apoptosis analysis

Figure 9 shows the flow cytometry results of the conventional apoptosis analysis. As the concentration of camptothecin increased, the number of PI and annexin V double positive cells increased, whereas PI and annexin V double negative cells decreased. At the concentrations of 10 and 20 μM, more than 90% of cells were in an apoptosis condition.

mRNA expression analysis

Figure 10 shows the expression level of caspase-3 mRNA. Compared with the original cells, the expression level increased with the increase of camptothecin concentrations. Moreover, at the concentrations of 10 and 20 μM, the expression of caspase-3 mRNA was the same level as that of the original cells at 0 μM of camptothecin.

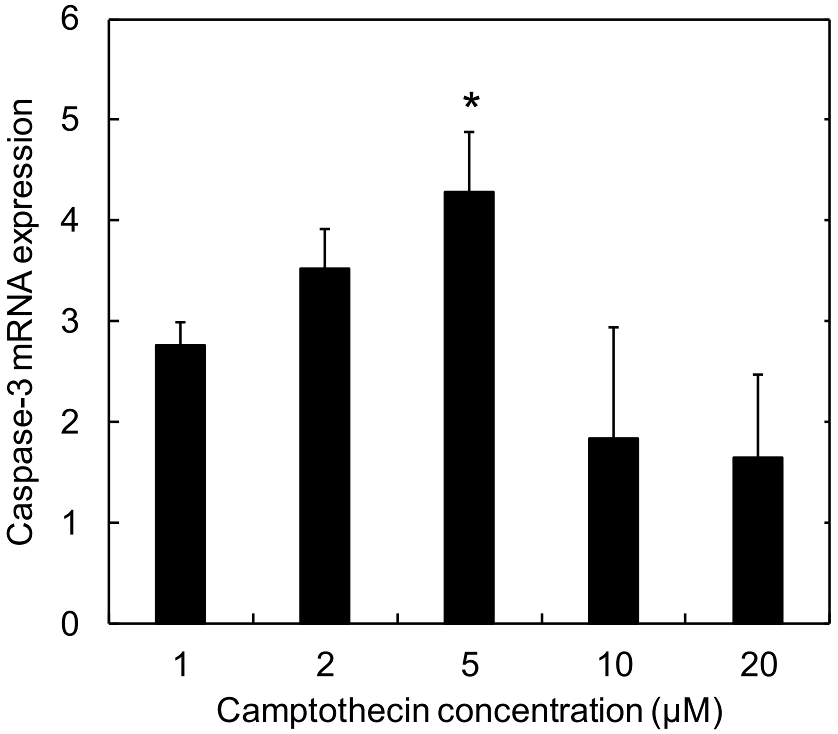

Figure 10. Expression analysis of caspase-3 mRNA 12 hr after incubation with different camptothecin concentrations. *, $p < 0.05$; significant against the expression level at 0 μM camptothecin.

DISCUSSION

The present study demonstrates that $cGNS_{MB}$ prepared were readily internalized into the cells as expected. The hybridization assay revealed that MB incorporated in cGNS showed the sequence specificity. In addition, the higher stability against the nuclease was observed than free MB. When the apoptotic cells were prepared by the camptothecin addition, the $cGNS_{casp3\ MB}$ showed the intracellular fluorescence expression according to the induction of cell apoptosis.

The mixing ratio of MB to cGNS in the $cGNS_{MB}$ preparation had an influence on the apparent size and zeta potential of $cGNS_{MB}$ (**Figure 1**). An increased amount of MB added increased the apparent size, but decreased the zeta potential. The MB-free, empty cGNS have a positive zeta potential, whereas the MB have a negative charge. Therefore, it is likely that the increased amount of MB added might cause the aggregation of nanospheres due to the electrostatic interaction. The apparent size of $cGNS_{MB}$ is larger than that of MB-free, empty cGNS. The aggregation of nanospheres might be due to the association among the nanospheres with MB. This formation change would become the increased size and decreased zeta potential. It is considered that some MB are on the surface of nanospheres, whereas the majority of MB are incorporated due to the small size of MB (31 and 32 bases of GAPDH MB and caspase-3 MB, respectively) and the constant zeta potential (8 mV of the MB-free, empty cGNS and $cGNS_{MB}$ prepared at 2, 10, and 20 pmole MB/µg cGNS). In this study, since the $cGNS_{MB}$ have a positive charge and a small size of 200 nm for better cell internalization [25, 26], the cGNS prepared at the ratio of 20 pmole MB/µg cGNS were selected, although the MB amount increased with an increase in the MB/cGNS ratio. Similar physicochemical properties had for both the $cGNS_{GAP\ MB}$ and $cGNS_{casp3\ MB}$. This finding demonstrates that the physicochemical properties of $cGNS_{MB}$ are not influenced by the sequence of MB. Considering the biological function of MB, it is important to evaluate the sequence specificity of MB and MB incorporated in cGNS for the hybridization [27, 28]. The hybridization study indicated that the fluorescent recovery of both MB and MB incorporated in cGNS was specific for the target sequences (**Figure 2**). Compared with free MB, the fluorescent recovery of MB incorporated in cGNS was small at the low concentrations of specific target. This is because the incorporation of MB in the cGNS prevents the target oligonucleotides from the specific association. However, sufficient fluorescent recovery was observed at the high concentrations of specific target. It is conceivable that the higher concentration contributes to an increase in the molecular association. The reason of slight fluorescent increase of MB incorporated in cGNS with the non-specific target is unclear at present. The cationized gelatin and MB are electrostatically interacted to each other, and the negative charge of MB may be shielded by the positive charge of cationized gelatin. It is possible that this contributes to the slight increase of fluorescent intensity with non-specific target. However, at the target concentration of 5000 nM, the fluorescent intensity with the specific target was sufficiently higher than that with non-specific target (four and seven times for GAPDH MB and caspase-3 MB, respectively). In addition to the hybridization specificity, the stability against nuclease is also important in terms of the cellular signal accuracy of MB [29, 30]. The free MB were readily degraded depending on the DNase I concentrations. In contrast, MB incorporated in cGNS were hardly degraded by DNase I (**Figure 3**). It is highly conceivable that the poor approach of DNase I to MB incorporated in the cGNS, resulting in an inhibited enzymatic reaction to MB.

It is apparent in **Figure 4** that the high concentrations of $\mathrm{cGNS_{MB}}$ showed significant cytotoxicity. It is well known that cationic substances have a cytotoxic nature [31-33]. The amount of MB internalized into the cells increased as the increase of $\mathrm{cGNS_{MB}}$ concentration, but reached a plateau level (**Figure 5A**). The cytotoxicity might be due to the increased cell internalization of $\mathrm{cGNS_{MB}}$. However, the amount of $\mathrm{cGNS_{MB}}$ internalized into the cells saturated over 15 μg/ml of $\mathrm{cGNS_{MB}}$ concentration. It is possible, therefore, that an excess amount of $\mathrm{cGNS_{MB}}$ which does not contribute to the cell internalization, might cause the cytotoxicity. Considering the non-cytotoxic concentration, 10 μg/ml was selected for the amount of $\mathrm{cGNS_{MB}}$ used in the experiment. In addition, 10 μg/ml of $\mathrm{cGNS_{MB}}$ did not affect the cell proliferation (data not shown).

The amount of MB internalized into the cells at 4 °C was significantly lower than that at 37 °C (**Figure 5B**). This suggests that $\mathrm{cGNS_{MB}}$ were internalized into the cells mainly via endocytosis. On the contrary, free MB were hardly internalized both at 37 and 4 °C (**Figure 5C**), and no fluorescence was observed in the cells. This higher internalization of MB for the $\mathrm{cGNS_{MB}}$, so-called the concentration effect of MB, is one of the reasons to enhance the MB response in the cells. The red color of MB and the green color of cGNS were well co-localized, which can be confirmed by the yellow color in the cells (**Figure 6B (a)**). This result indicates that both the MB and cGNS were internalized in the cells in the complex state. Moreover, MB-cGNS complexes (yellow) were not co-localized with lysosomes (magenta) in the cells (**Figure 6B (b)**). This finding demonstrates that the $cGNS_{MB}$ were endosomally escaped following the endocytosis. This may be due to the pH buffering effect by the secondary amino groups of spermine [34]. Taken together, MB-cGNS complexes internalized into the cells via endocytosis, were released into cytosol, and specifically responded with the intracellular mRNA without the degradation by the nucleases (**Figures 2**, **3**, **5B**, and **6**).

In this study, camptothecin was used as an apoptosis inducer commonly used. As the mechanism to induce the cell apoptosis, it is reported that camptothecin conjugates with an DNA-topoisomerase I complex to inhibit the topoisomerase I activity [35, 36]. For the cells incubated with $cGNS_{GAP\ MB}$, constant fluorescence was observed, irrespective of the apoptosis induction (**Figures 7** and **8**). On the contrary, $cGNS_{casp3\ MB}$ were not fluorescent for the original non-apoptotic cells, but after the apoptosis induction, the fluorescence was detected. This experimentally confirms that $cGNS_{MB}$ successfully functioned to detect the intracellular target mRNA. The fluorescent intensity of $cGNS_{casp3\ MB}$ was almost constant at any concentration of camptothecin except for 0 μM. This might be considered that the fluorescent recovery due to the hybridization of caspase-3 MB with the target mRNA is saturated even at low concentrations of camptothecin. For the conventional apoptosis detection, the apoptosis analysis of annexin V / PI staining was performed. PI stains the late apoptotic and dead cells because PI is only permeable to the membrane of damaged cells. The annexin V stains only the apoptotic cells because it conjugates with the phosphatidylserine of an apoptotic marker [37]. The flow cytometric assay revealed that the cell population was moved to the apoptotic fraction depending on the concentrations of camptothecin, and at the high concentrations (10 and 20 μM) more than 90% cells showed to be apoptotic (**Figure 9**). The advantages of $cGNS_{MB}$ over the conventional apoptosis detection are to visualize the intracellular localization of apoptosis target and detect which cells are in an apoptotic condition. In addition, $cGNS_{MB}$ could detect the apoptotic cells after the addition of 1 and 2 μM camptothecin which were less than 20%

apoptotic cell. This is also the advantage of $\mathrm{cGNS_{MB}}$ due to the detection of apoptosis target mRNA which expresses in the earlier apoptotic stage. The expression level of caspase-3 mRNA evaluated by the qPCR (**Figure 10**) tended to increase with the camptothecin concentration. However, at the concentrations of 10 and 20 μM, the expression levels were similar to those of the original cells. This is because the majority of cells after the addition of 10 and 20 μM camptothecin was in the late apoptosis state (**Figure 9**), and the intracellular mRNA might be degraded. On the other hand, for $\mathrm{cGNS_{casp3\ MB}}$, the increased fluorescence could be detected even after the addition of 10 and 20 μM camptothecin. The fluorescent intensity of MB was constant at the high target concentrations (**Figure 2**). This finding indicates that few amount loss of intracellular target mRNA might not lead to decrease in the MB fluorescence. The conventional mRNA expression analysis by qPCR is not generally detect the caspase-3 mRNA in late apoptotic cells. On the contrary, $\mathrm{cGNS_{casp3\ MB}}$ system specifically detects the caspase-3 mRNA. This is another advantage of $\mathrm{cGNS_{MB}}$.

The present study demonstrates the feasibility that $\mathrm{cGNS_{MB}}$ functioned well to visualize the cell apoptosis. To our knowledge, this is the first time to visualize the cell apoptosis using MB. Based on the results in Chapter 3, it is highly conceivable that the MB are intracellularly released into the cytosol with the degradation of cGNS. The release profile of MB can be readily regulated by the degradability of cGNS to prolong the time period of mRNA detection, leading to the prolonged and controlled visualization of cell functions. On the other hand, the advantage of MB is of high versatility because the target is mRNA. Only by simply designing and changing the MB sequences [38-40], multiple intracellular mRNA can be detected. This detection method will be able to be universal. In the near future, a prolonged visualization of cell apoptosis and other cell functions, including cell proliferation ability, will be achieved by the $\mathrm{cGNS_{MB}}$ imaging system based on the intracellular controlled release of MB.

REFERENCES

1. Bajada S, Mazakova I, Richardson JB, Ashammakhi N. Updates on stem cells and their applications in regenerative medicine. *J Tissue Eng Regen Med* 2008; **2**: 169-183.
2. Shibata T, Naruse K, Kamiya H, Kozakae M, Kondo M, Yasuda Y *et al.* Transplantation of bone marrow-derived mesenchymal stem cells improves diabetic polyneuropathy in rats. *Diabetes* 2008; **57**: 3099-3107.
3. Delcroix GJ, Schiller PC, Benoit JP, Montero-Menei CN. Adult cell therapy for brain neuronal damages and the role of tissue engineering. *Biomaterials* 2010; **31**: 2105-2120.
4. Alfaifi M, Eom YW, Newsome PN, Baik SK. Mesenchymal stromal cell therapy for liver diseases. *J Hepatol* 2018; **68**: 1272-1285.
5. Garcia SM, Tamaki S, Lee S, Wong A, Jose A, Dreux J *et al.* High-Yield Purification, Preservation, and Serial Transplantation of Human Satellite Cells. *Stem Cell Reports* 2018; **10**: 1160-1174.
6. Menasche P. Cell therapy trials for heart regeneration - lessons learned and future directions. *Nat Rev Cardiol* 2018; **15**: 659-671.
7. Soontararak S, Chow L, Johnson V, Coy J, Wheat W, Regan D *et al.* Mesenchymal Stem Cells (MSC) Derived from Induced Pluripotent Stem Cells (iPSC) Equivalent to Adipose-Derived MSC in Promoting Intestinal Healing and Microbiome Normalization in Mouse Inflammatory Bowel Disease Model. *Stem Cells Transl Med* 2018; **7**: 456-467.
8. Doi D, Magotani H, Kikuchi T, Ikeda M, Hiramatsu S, Yoshida K *et al.* Pre-clinical study of induced pluripotent stem cell-derived dopaminergic progenitor cells for Parkinson's disease. *Nat Commun* 2020; **11**: 3369.
9. Yukawa H, Nakagawa S, Yoshizumi Y, Watanabe M, Saito H, Miyamoto Y *et al.* Novel positively charged nanoparticle labeling for in vivo imaging of adipose tissue-derived stem cells. *PLoS One* 2014; **9**: e110142.
10. Onoshima D, Yukawa H, Baba Y. Multifunctional quantum dots-based cancer diagnostics and stem cell therapeutics for regenerative medicine. *Adv Drug Deliv Rev* 2015; **95**: 2-14.
11. Sato N, Wu H, Asiedu KO, Szajek LP, Griffiths GL, Choyke PL. (89)Zr-Oxine Complex

PET Cell Imaging in Monitoring Cell-based Therapies. *Radiology* 2015; **275**: 490-500.

12. Azzabi F, Rottmar M, Jovaisaite V, Rudin M, Sulser T, Boss A *et al.* Viability, differentiation capacity, and detectability of super-paramagnetic iron oxide-labeled muscle precursor cells for magnetic-resonance imaging. *Tissue Eng Part C Methods* 2015; **21**: 182-191.
13. Cheng SH, Yu D, Tsai HM, Morshed RA, Kanojia D, Lo LW *et al.* Dynamic In Vivo SPECT Imaging of Neural Stem Cells Functionalized with Radiolabeled Nanoparticles for Tracking of Glioblastoma. *J Nucl Med* 2016; **57**: 279-284.
14. Bouchlaka MN, Ludwig KD, Gordon JW, Kutz MP, Bednarz BP, Fain SB *et al.* (19)F-MRI for monitoring human NK cells in vivo. *Oncoimmunology* 2016; **5**: e1143996.
15. Nicholls FJ, Rotz MW, Ghuman H, MacRenaris KW, Meade TJ, Modo M. DNA-gadolinium-gold nanoparticles for in vivo T1 MR imaging of transplanted human neural stem cells. *Biomaterials* 2016; **77**: 291-306.
16. Jeong HJ, Yoo RJ, Kim JK, Kim MH, Park SH, Kim H *et al.* Macrophage cell tracking PET imaging using mesoporous silica nanoparticles via in vivo bioorthogonal F-18 labeling. *Biomaterials* 2019; **199**: 32-39.
17. Piao YJ, Kim HS, Moon WK. Noninvasive Photoacoustic Imaging of Dendritic Cell Stimulated with Tumor Cell-Derived Exosome. *Mol Imaging Biol* 2020; **22**: 612-622.
18. Ishikane S, Ohnishi S, Yamahara K, Sada M, Harada K, Mishima K *et al.* Allogeneic injection of fetal membrane-derived mesenchymal stem cells induces therapeutic angiogenesis in a rat model of hind limb ischemia. *Stem Cells* 2008; **26**: 2625-2633.
19. Iinuma S, Aikawa E, Tamai K, Fujita R, Kikuchi Y, Chino T *et al.* Transplanted bone marrow-derived circulating PDGFRα+ cells restore type VII collagen in recessive dystrophic epidermolysis bullosa mouse skin graft. *J Immunol* 2015; **194**: 1996-2003.
20. Fontaine MJ, Shih H, Schafer R, Pittenger MF. Unraveling the Mesenchymal Stromal Cells' Paracrine Immunomodulatory Effects. *Transfus Med Rev* 2016; **30**: 37-43.
21. Hyun JS, Tran MC, Wong VW, Chung MT, Lo DD, Montoro DT *et al.* Enhancing stem cell survival in vivo for tissue repair. *Biotechnol Adv* 2013; **31**: 736-743.
22. Snyder SL, Sobocinski PZ. An improved 2,4,6-trinitrobenzenesulfonic acid method for

the determination of amines. *Anal Biochem* 1975; **64**: 284-288.

23. Commerford SL. Iodination of nucleic acids in vitro. *Biochemistry* 1971; **10**: 1993-2000.
24. Walton MI, Whysong D, O'Connor PM, Hockenbery D, Korsmeyer SJ, Kohn KW. Constitutive expression of human Bcl-2 modulates nitrogen mustard and camptothecin induced apoptosis. *Cancer Res* 1993; **53**: 1853-1861.
25. Win KY, Feng SS. Effects of particle size and surface coating on cellular uptake of polymeric nanoparticles for oral delivery of anticancer drugs. *Biomaterials* 2005; **26**: 2713-2722.
26. He C, Hu Y, Yin L, Tang C, Yin C. Effects of particle size and surface charge on cellular uptake and biodistribution of polymeric nanoparticles. *Biomaterials* 2010; **31**: 3657-3666.
27. Bonnet G, Tyagi S, Libchaber A, Kramer FR. Thermodynamic basis of the enhanced specificity of structured DNA probes. *Proc Natl Acad Sci U S A* 1999; **96**: 6171-6176.
28. Stobiecka M, Chalupa A. DNA Strand Replacement Mechanism in Molecular Beacons Encoded for the Detection of Cancer Biomarkers. *J Phys Chem B* 2016; **120**: 4782-4790.
29. Chen AK, Behlke MA, Tsourkas A. Avoiding false-positive signals with nuclease-vulnerable molecular beacons in single living cells. *Nucleic Acids Res* 2007; **35**: e105.
30. Zhao D, Yang Y, Qu N, Chen M, Ma Z, Krueger CJ *et al.* Single-molecule detection and tracking of RNA transcripts in living cells using phosphorothioate-optimized 2'-O-methyl RNA molecular beacons. *Biomaterials* 2016; **100**: 172-183.
31. Fischer D, Li Y, Ahlemeyer B, Krieglstein J, Kissel T. In vitro cytotoxicity testing of polycations: influence of polymer structure on cell viability and hemolysis. *Biomaterials* 2003; **24**: 1121-1131.
32. Frohlich E. The role of surface charge in cellular uptake and cytotoxicity of medical nanoparticles. *Int J Nanomedicine* 2012; **7**: 5577-5591.
33. Shao XR, Wei XQ, Song X, Hao LY, Cai XX, Zhang ZR *et al.* Independent effect of polymeric nanoparticle zeta potential/surface charge, on their cytotoxicity and affinity to cells. *Cell Prolif* 2015; **48**: 465-474.
34. Jo J, Nagane K, Yamamoto M, Tabata Y. Effect of amine type on the expression of

plasmid DNA by cationized dextran. *J Biomater Sci Polym Ed* 2010; **21**: 225-236.

35. Pommier Y. Topoisomerase I inhibitors: camptothecins and beyond. *Nat Rev Cancer* 2006; **6**: 789-802.

36. Pommier Y, Barcelo JM, Rao VA, Sordet O, Jobson AG, Thibaut L *et al.* Repair of topoisomerase I-mediated DNA damage. *Prog Nucleic Acid Res Mol Biol* 2006; **81**: 179-229.

37. Vermes I, Haanen C, Steffens-Nakken H, Reutelingsperger C. A novel assay for apoptosis. Flow cytometric detection of phosphatidylserine expression on early apoptotic cells using fluorescein labelled Annexin V. *J Immunol Methods* 1995; **184**: 39-51.

38. Goel G, Kumar A, Puniya AK, Chen W, Singh K. Molecular beacon: a multitask probe. *J Appl Microbiol* 2005; **99**: 435-442.

39. Bratu DP, Catrina IE, Marras SA. Tiny molecular beacons for in vivo mRNA detection. *Methods Mol Biol* 2011; **714**: 141-157.

40. Wile BM, Ban K, Yoon YS, Bao G. Molecular beacon-enabled purification of living cells by targeting cell type-specific mRNAs. *Nat Protoc* 2014; **9**: 2411-2424.

PART II

APPLICATION OF GELATIN-BASED CARRIERS FOR IMAGING PROBES TO MULTI-COLOR IMAGING AND THREE-DIMENSIONAL CELLS FABRICATE

Chapter 6

Preparation of cationized gelatin nanospheres incorporating molecular beacon to visualize energy metabolic pathways between undifferentiated and differentiated mouse embryonic stem cells

INTRODUCTION

Cells produce energy via various metabolic pathways for their physiological activities, such as proliferation, survival, and differentiation. Among them, the glycolysis and the oxidative phosphorylation (OXPHOS) are the main pathways of energy production, and the weight of pathways is different for the cell type, situation, and function. For example, it is known as Warburg effect that cancer cells heavily rely the glycolysis even with sufficient supply of oxygen (aerobic glycolysis) [1]. Based on the characteristics of cancer, an enhanced uptake of ^{18}F-fluorodeoxyglucose has been visualized by positron emission tomography (PET) for the clinical cancer diagnosis [2], and extensive trials have been reported to inhibit the metabolic pathways and induce the cancer cell death [3-5]. For stem cells including pluripotent and somatic stem cells, it has been widely recognized that the undifferentiated stem cells mainly rely the energy production on the glycolysis. On the contrary, in the differentiated cells, the OXPHOS is a major part of energy production [6-9]. It is quite important to evaluate the metabolic profile as a function of stem cells. The metabolic shift from the OXPHOS to the glycolysis significantly affects the reprogramming efficiency to generate induced pluripotent stem (iPS) cells [10]. The upregulation of glycolytic genes precedes the expression of pluripotent markers over the reprogramming [11]. On the other hand, it is well accepted that the differentiation of stem cells is actively supported and regulated by the increase of OXPHOS [12]. Based on the metabolic difference, it has been demonstrated that the differentiated cardiomyocytes could be efficiently purified by eliminating the remaining undifferentiated cells [13, 14]. Moreover, the culture of human adipose tissue-derived mesenchymal stem cells (MSC) under a hypoxic condition increased the glycolytic profile, which led to the improvement of proliferation, suppression of senescence, and maintenance of undifferentiated state [15]. It is, thus, indispensable to evaluate the metabolic pathways of energy production for the further development of basic cell research, cancer diagnosis, drug discovery, disease modeling, and regenerative medicine. However, at present, it is technically difficult to directly assess the metabolic profile of individual cells. Under these circumstances, it is of prime importance to develop the imaging technologies and methodologies to visualize the energy metabolic pathways in living cells. The visualization of metabolic profile makes it possible to discriminate the differentiation state of cells and predict the cell potential for reprogramming and differentiation.

Pyruvate dehydrogenase kinase 1 (PDK1) is one of the key enzymes to maintain the glycolysis of cells in an undifferentiated state [16]. PDK1 inhibits the pyruvate dehydrogenase (PDH) of a gatekeeper enzyme which catalyzes the metabolic pathway to combine glycolysis with OXPHOS. The phosphorylation of PDH E1α subunit by the PDK1 activity prevents the conversion of pyruvate into acetyl-coenzyme A, which leads to the maintenance of the high glycolytic profile [4, 17]. On the other hand, peroxisome proliferator-activated receptor γ, coactivator-1α (PGC-1α) is a master regulator of mitochondrial biogenesis. The upregulation of PGC-1α and the resulting transcription of downstream mitochondrial genes induce the enhancement of OXPHOS [3, 18, 19]. Based on the mechanism, it can be hypothesized that the PDK1 and the PGC-1α would be the targets for glycolysis and OXPHOS between undifferentiated and differentiated cells, respectively.

In Chapter 3, it was demonstrated that the feasibility of cationized gelatin nanospheres (cGNS) incorporating molecular beacons (MB) ($\mathrm{cGNS_{MB}}$) to continuously detect intracellular messenger RNA (mRNA) in living cells. In addition, Chapters 4 and 5 demonstrated that the cell apoptosis and proliferation ability of cells can be visualized by the $\mathrm{cGNS_{MB}}$ imaging system. Based on the findings, MB for the mRNA of PDK1 and PGC-1α as the targets for glycolysis and OXPHOS, respectively, are designed to be incorporated in the cGNS. In addition, as a control of constant fluorescence in the cells, MB for the mRNA of β-actin (Actb) is designed due to its constant expression.

In this chapter, a $\mathrm{cGNS_{MB}}$ imaging system to visualize the energy metabolic pathways of cells was developed aiming at the visual discrimination of differentiation state. As one example of stem cells, mouse embryonic stem (mES) cells maintained in the undifferentiated state and that induced the differentiation are focused. Three types of MB (PDK1, PGC-1α, and

Actb MB) were designed to be incorporated in the cGNS. The cell internalization of $\mathrm{cGNS_{MB}}$ was optimized in terms of the internalization amount, the cell viability, and the labeling efficiency. The expression of MB target mRNA and the pluripotency of mES cells after the incubation with $\mathrm{cGNS_{MB}}$ were examined. The $\mathrm{cGNS_{MB}}$ were internalized into the mES cells in the undifferentiated state and that induced early differentiation, as well as the neural differentiation, and the consequent fluorescent intensity was evaluated. The expression of PDK1 and PGC-1α and the phosphorylation of PDH over the differentiations were assessed. In addition, the metabolic profiles of mES cells were investigated by the metabolic indicators of extracellular acidification rate (ECAR) and oxygen consumption rate (OCR). Based on the comparison with the MB fluorescence, the availability of $\mathrm{cGNS_{MB}}$ imaging system to visualize the energy metabolic pathways was evaluated. Finally, cGNS co-incorporating PDK1, PGC-1α, and Actb MB ($\mathrm{cGNS_{multi\ MB}}$) were prepared to simultaneously detect the multiple target mRNA. The multi-color imaging by $\mathrm{cGNS_{multi\ MB}}$ was performed to visualize the metabolic profiles and discriminate the differentiation state in the same cell population.

EXPERIMENTAL

Materials

Gelatin with an isoelectric point of 9.0 and the weight-averaged molecular weight of 99,000, prepared by an acidic process of pig skin, was kindly supplied from Nitta Gelatin Inc., Osaka, Japan. MB composed of DNA bases for mouse mRNA of PDK1, PGC-1α, and Actb were designed by Beacon Designer™ (PREMIER Biosoft, Palo Alto, CA, USA), and synthesized by Integrated DNA Technologies, Inc. Coralville, IA, USA. The secondary structure of MB was estimated by an RNA/DNA folding software (UNAFold, Integrated DNA Technologies, Inc., Coralville, IA, USA.) to confirm the stem-loop structure. Target oligonucleotides of DNA for MB (PDK1, PGC-1α, and Actb specific sequence) were synthesized by Hokkaido System Science Co., Ltd, Sapporo, Japan. The sequences of MB and target oligonucleotides were listed in **Table 1**. Glutaraldehyde (GA, 25 wt% in water), glycine, concentrated hydrochloric acid (HCl), acetone, and 1-ethyl-3-(3-dimethylaminopropyl) carbodiimide hydrochloride salt (EDC) were purchased from Nacalai Tesque. Inc., Kyoto, Japan. Spermine was purchased from Sigma-Aldrich Inc., St. Louis, MO, USA. The reagents were used without further purification.

Table 1. Sequences of MB and target oligonucleotides used.

MB and target oligonucleotides	Sequences (5’ to 3’)
PDK1 MB	[Alexa Fluor®488]-CGCGATCGGAGAACCACAGATAACTCACAGGATCGCG-[IBFQ]
PGC-1α MB	[TYE®563]-CGCGATCGCTCATTGTTGTACTGGTTGGGATCGCG-[IBRQ]
Actb MB	[TYE®665]-CGCGATACCTGGGCCATTCAGAAAATCGCG-[IBRQ]
PDK1 specific target	CTGTGAGTTATCTGTGGTTCTCC
PGC-1α specific target	CCAACCAGTACAACAATGAGC
Actb specific target	TTTCTGAATGGCCCAGGT

MB: molecular beacons
PDK1: pyruvate dehydrogenase kinase 1
PGC-1α: peroxisome proliferator-activated receptor γ, coactivator-1α
Actb: β-actin
IBFQ: Iowa Black®FQ
IBRQ: Iowa Black®RQ
underline: stem structure

Evaluation of hybridization specificity of MB

The hybridization specificity of MB designed was evaluated by incubating with target oligonucleotides with different sequences [20]. The target oligonucleotides (PDK1, PGC-1α, and Actb specific sequence, 0, 50, 100, 500, 1000, and 5000 nM) and the MB (PDK1 MB, PGC-1α MB, and Actb MB, 100 nM) were mixed in phosphate buffered-saline solution (PBS, pH7.4) containing 0.9 mM $CaCl_2$ and 0.5 mM $MgCl_2$. After the incubation for 1 hr at room temperature protected from light, the fluorescent intensity was measured by Multi-mode Microplate Reader (SpectraMax i3x, Molecular Devices Japan Co., Ltd., Tokyo, Japan). The MB (1 μl) and the target oligonucleotides (5 μM) were mixed in PBS and incubated for 1 hr at room temperature, similarly. Then, fluorescent images were taken by LAS-4000 (FUJIFILM Co., Tokyo, Japan).

Preparation of cationized gelatin

According to the preparation procedure described in Chapter 2, spermine of an amine compound was conjugated with gelatin. Briefly, spermine was added at a molar ratio of 50 to the carboxyl group of gelatin into 50 ml of aqueous solution containing 2.0 g of gelatin. The pH of solution was immediately adjusted to 5.0 by adding 11 M HCl. After the addition of double-distilled water (DDW) to give the final volume of 100 ml, EDC was added to the solution at a molar ratio of 3 to the carboxyl group of gelatin. The mixture was agitated for 18 hr at 40 °C, and dialyzed against DDW for 3 days with a dialysis membrane (molecular weight cut off = 12,000 to 14,000, Viskase Companies, Inc., Willowbrook, IL, USA) at room temperature. After the dialysis, the solution was freeze-dried to obtain the cationized gelatin. The percentage of amino groups introduced into gelatin was determined by the conventional 2,4,6-trinitrobenzene sulfonic acid (TNBS, FUJIFILM Wako Pure Chemical Inc., Osaka, Japan) method [21]. The percentage was 59.8 mole% per the carboxyl group of gelatin.

Preparation of cGNS

The cGNS were prepared by the conventional coacervation method as described in Chapter 3 with slight modifications. In brief, aqueous solution of cationized gelatin (50 mg/ml, 1.25 ml) was warmed up to 40 °C. Then, 5 ml of acetone was gradually dropped to the solution to form coacervate. Immediately after that, GA aqueous solution (25 wt%, 20 µl) was added to chemically crosslink the coacervate of cationized gelatin for 6 hr. Next, an excessive amount of glycine aqueous solution (0.5 M, 2 ml) was added to the solution to block the aldehyde groups unreacted, followed by agitation at 40 °C overnight to evaporate the residual acetone. The cGNS were collected by the centrifugation at 16,000 g for 30 min, and resuspended in DDW. The centrifugation and resuspension were repeated three times to wash the cGNS. The concentration of cGNS was determined by the measurement of weight after drying 100 µl of cGNS suspension.

The apparent size of cGNS suspended in PBS was measured by dynamic light scattering (DLS, Zetasizer Nano-ZS, Malvern Instruments Ltd., Worcestershire, UK). The zeta potential of cGNS suspended in 10 mM phosphate buffer (PB, pH7.4) was measured by electrophoresis light scattering (ELS, Zetasizer Nano-ZS, Malvern Instruments Ltd., Worcestershire, UK). The apparent size and the zeta potential of cGNS were 168.0 nm and 8.46 mV, respectively.

Preparation of $cGNS_{MB}$

The $cGNS_{MB}$ were prepared by simply mixing cGNS and MB in DDW. The cGNS (200 μg/ml) and MB (PDK1, PGC-1α, and Actb MB, 4 μM) were mixed in DDW (20 pmole MB/μg cGNS), and incubated for 15 min at room temperature. Then, the mixture was centrifuged at 16,000 g for 15 min, and resuspended in DDW to obtain the $cGNS_{MB}$ ($cGNS_{PDK1\ MB}$, $cGNS_{PGC\text{-}1\alpha\ MB}$, and $cGNS_{Actb\ MB}$). The apparent size and zeta potential of $cGNS_{MB}$ were determined by DLS and ELS measurements, respectively. The measurements were independently performed three times for each of sample unless otherwise mentioned.

To examine the amount of MB incorporated in cGNS, MB were labeled with radioactive iodine (^{125}I) [22] according to the method described in Chapter 2. Briefly, MB (50 μM, 5 μl) was incubated at 60 °C for 50 min with 2 μl of 0.3 mM Na_2SO_3, 5 μl of $Na^{125}I$ (740 MBq/ml in 0.1 M NaOH aqueous solution, PerkinElmer Inc., Waltham, MA, USA), and 5 μl of 4 mM $TlCl_3$. Then, 100 μl of 0.1 M Na_2SO_3, and 900 μl of 0.1 M NaCl, 50 mM Tris, and 1 mM ethylenediaminetetra acetic acid (EDTA) were added to the solution, followed by incubation for 30 min at 60 °C. The unconjugated free ^{125}I was separated from ^{125}I-labeled MB by the gel filtration using PD-10 column (GE Healthcare Bio-Sciences Corp., Piscataway, NJ, USA). The radioactivity of ^{125}I was measured using a gamma counter (Auto Well Gamma System ARC-380 CL, Aloka Co., Ltd, Tokyo, Japan). The $cGNS_{MB}$ were prepared by using the ^{125}I-labeled MB at the same procedure described above, and the amount of MB incorporated was determined by the radioactivity measurement.

Cell culture experiments

EB5 cells of a mES cell line were purchased from RIKEN BioResource Center, Tsukuba, Japan [23, 24]. The cells were cultured on 0.1 wt/vol% gelatin solution (FUJIFILM Wako Pure Chemical Inc., Osaka, Japan)-coated 100 mm cell culture dish (Corning Inc., Corning, NY, USA) in Glasgow's Minimum Essential Medium (GMEM, Thermo Fisher Scientific Inc., Waltham, MA, USA) containing 10 vol% knockout serum replacement (KSR, Thermo Fisher Scientific Inc., Waltham, MA, USA), 1 vol% bovine fetal calf serum (FCS, GE healthcare Life Sciences Hyclone laboratories inc., Logan, UT, USA), 1 mM sodium pyruvate (Thermo Fisher Scientific Inc., Waltham, MA, USA), 0.1 mM non-essential amino acid (NEAA, Thermo Fisher Scientific Inc., Waltham, MA, USA), 0.1 mM 2-mercaptoethanol (Nacalai Tesque. Inc., Kyoto, Japan), 1 vol% penicillin/streptomycin (Nacalai Tesque. Inc., Kyoto, Japan), and 1000 U/ml leukemia inhibitory factor (LIF, Merck Millipore, Burlington, MA, USA). Since the blasticidin S-resistant gene was inserted in one of Oct-3/4 locus, the cells were maintained in the undifferentiated state in the medium supplemented with 20 μg/ml blasticidin S (FUJIFILM Wako Pure Chemical Inc., Osaka, Japan) [25]. The medium was changed every day and the cells were passaged every 2 or 3 days.

Evaluation of cell internalization after incubation with cGNS$_{MB}$

The cells were seeded on each well of 0.1 wt/vol% gelatin solution-coated 6 well multi-dish culture plate (Corning Inc., Corning, NY, USA) at a density of 2×10^5 cells/well, and cultured for 24 hr. The medium was changed to OPTI MEM (Thermo Fisher Scientific Inc., Waltham, MA, USA), and then cGNS$_{Actb\ MB}$ (1, 5, 10, 15, and 20 μg/ml) were added to each well. After the incubation for 0.5, 1, and 3 hr with cGNS$_{Actb\ MB}$, the cells were washed with PBS and observed by a fluorescent microscope BZ-X700 with a 20× objective lens (KEYENCE Co., Ltd., Osaka, Japan). On the other hand, the cells incubated with cGNS$_{Actb\ MB}$ for 1 hr were detached with 0.25 wt% trypsin-containing 1 mM EDTA solution (Nacalai Tesque. Inc., Kyoto, Japan), and analyzed on FACSCanto II flow cytometer and BD FACSDiva software (Becton, Dickinson and Company, Franklin Lakes, NJ, USA) by counting 10,000 cells.

To evaluate the amount of MB internalized into the cells, the cells were similarly incubated with cGNS$_{Actb\ MB}$ which had been labeled with ^{125}I. After that, the cells were washed with PBS and trypsinized to collect. The amount of MB was determined by the radioactivity measurement for the cell suspension.

Evaluation of cell viability after incubation with $\mathrm{cGNS_{MB}}$

The cells were seeded on each well of 0.1 wt/vol% gelatin solution-coated 96 well multi-dish culture plate (Corning Inc., Corning, NY, USA) at a density of 1×10^4 cells/well, and cultured for 24 hr. The cell viability was evaluated using a cell counting kit (Nacalai Tesque. Inc., Kyoto, Japan). After the incubation with $\mathrm{cGNS_{Actb\ MB}}$ at different concentrations and incubation times as described above, 10 μl of 2-(2-methoxy-4-nitrophenyl)-3-(4-nitrophenyl)-5-(2,4-disulfophenyl)-2H-tetrazolium (WST-8) solution was added to each well and further incubated for 1 hr. The absorbance of samples at 450 nm was measured by the microplate reader. The percentage of cell viability was expressed as 100% for cells without incubation of $\mathrm{cGNS_{Actb\ MB}}$.

Fabrication of embryoid body to evaluate differentiation ability for three germ lineages

The embryoid body (EB) was fabricated by the conventional hanging drop method [26] to evaluate the differentiation ability for three germ lineages (endo-, meso-, and ectoderm). Briefly, the original cells and the cells incubated with $\mathrm{cGNS_{PDK1\ MB}}$, $\mathrm{cGNS_{PGC\text{-}1\alpha\ MB}}$, and $\mathrm{cGNS_{Actb\ MB}}$, were detached by the trypsinization and suspended in the medium without LIF. Then, the cell suspension (30 μl containing 500 cells) was dropped on the lid of 100 mm non-adherent cell culture dish (Corning Inc., Corning, NY, USA), and the lid was inverted over the dish filled with PBS. After 2 days, the EB formed was transferred to the 100 mm non-adherent dish and cultured for 6 days in a suspension state. Next, the matured EB was seeded on each well of 0.1 wt/vol% gelatin solution-coated 6 well plate and cultured for further 6 days in an adherent state [27]. The medium was changed every 3 days.

Induction of spontaneous early differentiation and fluorescent imaging

The spontaneous early differentiation of mES cells was induced by the depletion of LIF [28]. In brief, the cells were seeded on each well of 0.1 wt/vol% gelatin solution-coated 6 well plate at a density of 5×10^4 cells/well in the medium supplemented with or without LIF. The medium was changed every day. After the culture for 1, 2, and 3 days, the medium was changed to OPTI MEM, and $\mathrm{cGNS_{PDK1\ MB}}$, $\mathrm{cGNS_{PGC\text{-}1\alpha\ MB}}$, and $\mathrm{cGNS_{Actb\ MB}}$ (10 μg/ml) were added, and incubated for 1 hr. Then, the cells were washed with PBS and observed by the fluorescent microscopy with the 20× objective lens. To evaluate the fluorescent intensity, six images were taken at random and analyzed by BZ-X Analyzer (KEYENCE Co., Ltd., Osaka, Japan). The fluorescent area in the cells was extracted and the averaged brightness of the area was measured as the fluorescent intensity.

Evaluation of cell growth inhibition by metabolic inhibitors

The cells were seeded on each well of 0.1 wt/vol% gelatin solution-coated 24 well multi-dish culture plate (Corning Inc., Corning, NY, USA) at a density of 1×10^4 cells/well in the medium supplemented with or without LIF. Then, different concentrations of 2-deoxy-D-glucose (2-DG, FUJIFILM Wako Pure Chemical Inc., Osaka, Japan) and oligomycin (Cayman Chemical Company, Ann Arbor, MI, USA) were added to the cells, and cultured for 3 days. The medium was changed every day. The cell number at the time point of day 3 was evaluated by determining the DNA amount [29]. Briefly, the cells were washed with PBS and lysed with saline-sodium citrate (SSC) buffer containing 0.2 mg/ml sodium lauryl sulfate (SDS) solution. Next, 40 µl of cell lysate and 160 µl of 1.25 µg/ml bisbenzimide H33258 fluorochrome trihydrochloride (Hoechst 33258) solution (Nacalai Tesque. Inc., Kyoto, Japan) were mixed to measure the fluorescent intensity by the microplate reader. The cell number was evaluated from the DNA amount determined by the standard curve of cell suspension with different cell numbers.

Inhibition of PDK1 activity

The PDK1 activity was inhibited by the addition of dichloroacetate (DCA, Sigma-Aldrich Inc., St. Louis, MO, USA) in the presence of LIF [30, 31]. The cells were seeded on each well of 0.1 wt/vol% gelatin solution-coated 6 well plate (5×10^4 cells/well) in the medium supplemented with both 15 mM DCA and LIF, and the medium was changed every day. The cells were cultured for 3 days, and the $cGNS_{PDK1\ MB}$ and $cGNS_{Actb\ MB}$ (10 µg/ml) were incubated with the cells for 1 hr as described above. Then, the cells were observed by the fluorescent microscopy (20× objective lens) and the fluorescent intensity was evaluated from the six images taken, as well. On the other hand, the PDH activity was measured using Pyruvate Dehydrogenase Activity Colorimetric Assay Kit (BioVision Inc., Milpitas, CA, USA) according to the manufacture's instruction. The enzymatic PDH activity to produce the reduced nicotinamide adenine dinucleotide (NADH) was normalized by the cell number used for the measurement.

Induction of lineage-specific neural differentiation and fluorescent imaging

The cells were similarly seeded on each well of 0.1 wt/vol% gelatin solution-coated 6 well plate at a density of 1 × 10^5 cells/well in the neural differentiation medium NDiff®227 (Takara Bio Inc. Shiga, Japan) [32]. The medium was changed every one or two days, and the cells were cultured for 4, 7, and 9 days to induce the neural differentiation. Then, the $\mathrm{cGNS}_{\mathrm{PDK1\ MB}}$, $\mathrm{cGNS}_{\mathrm{PGC\text{-}1\alpha\ MB}}$, and $\mathrm{cGNS}_{\mathrm{Actb\ MB}}$ (10 μg/ml) were incubated with the cells for 1 hr, and the fluorescent images (20× objective lens) were taken to evaluate the fluorescent intensity at the same procedure as described above.

For the multi-color imaging, cGNS co-incorporating PDK1, PGC-1α, and Actb MB ($\mathrm{cGNS}_{\mathrm{multi\ MB}}$) were prepared by incubating cGNS and the mixture of MB (1:1:1) (total 20 pmole MB/μg cGNS). After the incubation for 15 min, the $\mathrm{cGNS}_{\mathrm{multi\ MB}}$ were obtained by the centrifugation (16,000 g for 15 min). Then, the $\mathrm{cGNS}_{\mathrm{multi\ MB}}$ (10 μg/ml) were similarly incubated with the undifferentiated and the neural differentiation-induced cells (day 9) for 1 hr. The sequential fluorescent images (3 × 3 images for each XY direction) were taken by the fluorescent microscopy (20× objective lens), and the jointed images were reconstructed by BZ-X Analyzer software.

mRNA expression analysis

The total RNA of cells was extracted using RNeasy Plus Mini Kit (QIAGEN, Hilden, Germany) according to the manufacture's instruction. The total RNA was reverse-transcribed to complementary DNA (cDNA) using a SuperScript VILO cDNA synthesis kit (Thermo Fisher Scientific Inc., Waltham, MA, USA). Then, the cDNA synthesized was subjected to quantitative real-time polymerase chain reaction (qPCR) by using Prism 7500 real-time PCR thermal cycler

(Applied Biosystems, Foster City, CA, USA). The qPCR was performed with specific TaqMan probes (TaqMan Gene Expression Assays, Applied Biosystems, Foster City, CA, USA) in the presence of TaqMan Fast Advanced Master Mix (Applied Biosystems, Foster City, CA, USA) as described in the manufacture's instruction. The TaqMan probes used were listed in **Table 2**.

Table 2. TaqMan probes used.

TaqMan Gene Expression Assays	Assay ID
PDK1	Mm00554300_m1
PGC-1α	Mm01208835_m1
Actb	Mm02619580_g1
Tbp	Mm00446973_m1
Oct-3/4 (Pou5f1)	Mm03053917_g1
Sox2	Mm03053810_s1
Nanog	Mm02019550_s1
Gata4	Mm00484689_m1
Gata6	Mm00802636_m1
Sox17	Mm00488363_m1
T (Brachyury)	Mm00436877_m1
Gsc	Mm00650681_g1
Pax6	Mm00443081_m1
Nestin	Mm00450205_m1
Eomes	Mm01351985_m1
Cdx2	Mm01212280_m1
Glut1	Mm00441480_m1
HK2	Mm00443385_m1
PFKFB3	Mm00504650_m1
PK	Mm00834102_gH
Tubb III	Mm00727586_s1

PDK1: pyruvate dehydrogenase kinase 1
PGC-1α: peroxisome proliferator-activated receptor γ, coactivator-1α
Actb: β-actin
Tbp: TATA-box binding protein
Glut1: glucose transporter 1
HK2: hexokinase 2
PFKFB3: 6-phosphofructo-2-kinase/fructose-2,6-biphosphatase 3
PK: pyruvate kinase
Tubb III: βIII tubulin

The following qPCR conditions were used: 50 °C for 2 min and 95 °C for 20 sec, followed by 40 cycles of 95 °C for 3 sec and 60 °C for 30 sec. Actb and TATA-box binding protein (Tbp) were used as a housekeeping gene, and the expression level of mRNA was analyzed by ΔΔCt method.

Immunofluorescent staining

The cells were washed with PBS three times and fixed with 4 vol% paraformaldehyde for 15 min, and permeabilized with 0.2 vol% TritonX-100 for 30 min at room temperature or cold methanol for 15 min on ice. After the blocking (ImmunoBlock^{TM}, KAC Co. Ltd., Kyoto, Japan), primary antibodies were incubated overnight at 4 °C. Then, the cells were washed with PBS three times, followed by the incubation with secondary antibodies for 1 hr at room temperature. The primary and secondary antibodies used were listed in **Table 3**. The cell nuclei were stained with 300 nM 4',6-diamidino-2-phenylindole (DAPI, Thermo Fisher Scientific Inc., Waltham, MA, USA), and then the fluorescent images were taken by the fluorescent microscopy with the 20× objective lens.

Western blotting analysis

The cells were washed with cold PBS three times, and lysed with radioimmunoprecipitation (RIPA) buffer (50 mM Tris-HCl pH7.6, 150 mM NaCl, 1% Nonidet P40 substitute, 0.5% sodium deoxycholate, 0.1% sodium dodecyl sulfate, Nacalai Tesque. Inc., Kyoto, Japan) supplemented with 1 mM Na_3VO_4 and 1 mM phenylmethanesulfonyl fluoride (PMSF). The protein concentration of cell lysates was determined by BCA^{TM} Protein Assay Kit (Thermo Fisher Scientific Inc., Waltham, MA, USA) according to the manufacture's protocol. The cell lysates were boiled at 95 °C for 5 min with Laemmli sample buffer (277.8 mM Tris-HCl pH6.8, 44.4% glycerol, 4.4% lithium dodecyl sulfate, 0.02% bromophenol blue, Bio-Rad Laboratories. Inc., Hercules, CA, USA) supplemented with 2.5% 2-mercaptoethanol. Then, the cell lysate (30 μg) was subjected to the conventional sodium lauryl sulfate-poly(acrylamide) gel electrophoresis (SDS-PAGE), and transferred to a poly(vinyliden difluoride) (PVDF) membrane. The membrane was blocked with the blocking solution (ImmunoBlock^{TM}, KAC Co.

Ltd., Kyoto, Japan) for 45 min at room temperature, and incubated with primary antibodies overnight at 4 °C. The membrane was washed with Tris buffered-saline with Tween 20 (TBST) three times, and incubated with horseradish peroxidase-conjugated secondary antibodies for 60 min at room temperature. The primary and secondary antibodies used were listed in **Table 3**.

Table 3. Antibodies used for immunofluorescent staining and western blotting analysis.

Antibody	Source	Product number	Dilution
Rabbit polyclonal anti-Oct-3/4	Abcam (Cambridge, UK)	ab19857	1:250
Rabbit polyclonal anti-Sox2	Abcam	ab97959	1:250
Rabbit polyclonal anti-Nanog	Abcam	ab80892	1:250
Mouse monoclonal anti-SSEA-1	Thermo Fisher Scientific Inc. (Waltham, MA, USA)	MA1-022	1:250
Rabbit monoclonal anti-α1-fetoprotein	Abcam	ab213328	1:100
Rabbit monoclonal anti-α-smooth muscle actin	Abcam	ab32575	1:250
Rabbit monoclonal anti-βIII tubulin	Abcam	ab52623	1:500
Mouse monoclonal anti-nestin	Abcam	ab11306	1:100
Rabbit monoclonal anti-pyruvate dehydrogenase kinase 1 [a)]	Abcam	ab202468	1:1000
Rabbit polyclonal anti-peroxisome proliferator-activated receptor γ, coactivator-1α	Abcam	ab54481	1:300 [a)] 1:1000 [b)]
Alexa Fluor®488-conjugated goat anti-mouse IgM	Abcam	ab150121	1:1000
Alexa Fluor®488-conjugated goat anti-rabbit IgG	Thermo Fisher Scientific Inc.	A11008	1:1000
Alexa Fluor®546-conjugated goat anti-rabbit IgG	Thermo Fisher Scientific Inc.	A11010	1:1000
Alexa Fluor®568-conjugated donkey anti-mouse IgG	Thermo Fisher Scientific Inc.	A10037	1:1000
Rabbit monoclonal anti-pyruvate dehydrogenase E1α (phosphorylated Ser^{293})	Abcam	ab177461	1:1000
Rabbit monoclonal anti-pyruvate dehydrogenase E1α	Abcam	ab168379	1:1000
Rabbit monoclonal anti-pyruvate dehydrogenase kinase 1 [b)]	Cell Signaling Technology Japan, K.K. (Tokyo, Japan)	#3820	1:1000
Rabbit monoclonal anti-β-actin	Cell Signaling Technology Japan, K.K.	#4970	1:1000
Horseradish peroxidase-conjugated anti-rabbit IgG	Cell Signaling Technology Japan, K.K.	#7074	1:2000

a) The antibody and dilution were used for the immunofluorescent staining.

b) The antibody and dilution were used for the western blotting analysis.

The immunoreactive band was detected by Pierce^{TM} ECL Plus Western Blotting Substrate (Thermo Fisher Scientific Inc., Waltham, MA, USA) with a chemiluminescence imaging system LAS-4000 (FUJIFILM Co., Tokyo, Japan). The chemiluminescent intensity was quantified by ImageJ software (NIH, Bethesda, MD, USA).

Evaluation of energy metabolic profiles

The energy metabolic profiles of cells were evaluated by measuring the extracellular acidification rate (ECAR) and the oxygen consumption rate (OCR) on Seahorse XF^{e}96 Extracellular Flux Analyzer (Agilent Technologies, Inc., Santa Clara, CA, USA). The cells were seeded on each well of 0.1 wt/vol% gelatin solution-coated XF96 cell culture plate at a density of 1×10^3 cells/well in the medium supplemented with or without LIF, and cultured for 3 days to allow cells to induce the early differentiation. Since the cell number at the time point of day 1 was too small to measure the ECAR and OCR, the seeding density of 3×10^3 cells/well were applied to the measurement on day 1. For the neural differentiation, the cells were seeded at a density of 2×10^3 cells/well in the neural differentiation medium, and cultured for 9 days. Glycolysis and mitochondria stress tests were performed to assess the glycolysis and OXPHOS activities, according to the manufacture's protocol. Briefly, the medium was changed to the basal medium of unbuffered Dulbecco's Modified Eagle Medium (DMEM) supplemented with 2 mM L-glutamine (for the glycolysis stress test) or 2 mM L-glutamine, 10 mM glucose, and 1 mM pyruvate (for the mitochondria stress test), and incubated at 37 °C for 1 hr without the CO_2 gas supply. The glycolysis stress test was composed of 4 steps: (i) basal medium, (ii) 10 mM glucose, (iii) 2 μM oligomycin, (iv) 50 mM 2-DG to measure the ECAR. On the other hand, the mitochondria stress test was composed of 4 steps: (i) basal medium, (ii) 2 μM oligomycin, (iii) 1 μM carbonyl cyanide-4-(trifluoromethoxy)phenylhydrazone (FCCP), (iv) 0.5 μM rotenone and 0.5 μM antimycin A to measure the OCR. All reagents were purchased from Agilent Technologies, Inc., Santa Clara, CA, USA. After the measurements, the cells were lysed with the SDS solution, followed by three cycles of freeze and thaw. The protein amount was determined by MicroBCA^{TM} Protein Assay Kit (Thermo Fisher Scientific Inc., Waltham, MA, USA) to normalize the ECAR and OCR values. From the profiles of glycolysis and mitochondria stress tests, the parameters of basal glycolysis and respiration, maximal glycolysis and respiration, and glycolysis and respiration reserves, were calculated according to the manufacture's protocol.

Statistical analysis

The data were expressed as the average ± standard deviation (SD). All the statistical analysis was performed using one-way analysis of variance (ANOVA) with a post-hoc Tukey-Kramer multiple comparison test. *P* values less than 0.05 were considered to be statistically significant.

RESULTS

Characterization of $cGNS_{MB}$

First, the specificity of MB designed in hybridization with the target oligonucleotides was evaluated (**Figure 1**). When PDK1, PGC-1α, and Actb MB were mixed with the target oligonucleotides with non-specific sequences to each MB, no fluorescence was emitted from MB, and the fluorescent intensity was as low as free MB at any concentration. On the other hand, the fluorescence of MB specifically increased as an increase of target concentration with specific sequences to emit the strong signal visualized. **Table 4** shows the amount of MB incorporated in cGNS, the apparent size, and the zeta potential of $cGNS_{PDK1\ MB}$, $cGNS_{PGC\text{-}1\alpha\ MB}$, and $cGNS_{Actb\ MB}$. There was no difference in the values among the MB sequences. The apparent size of $cGNS_{MB}$ was around 250 nm, and the zeta potential was of a positive value.

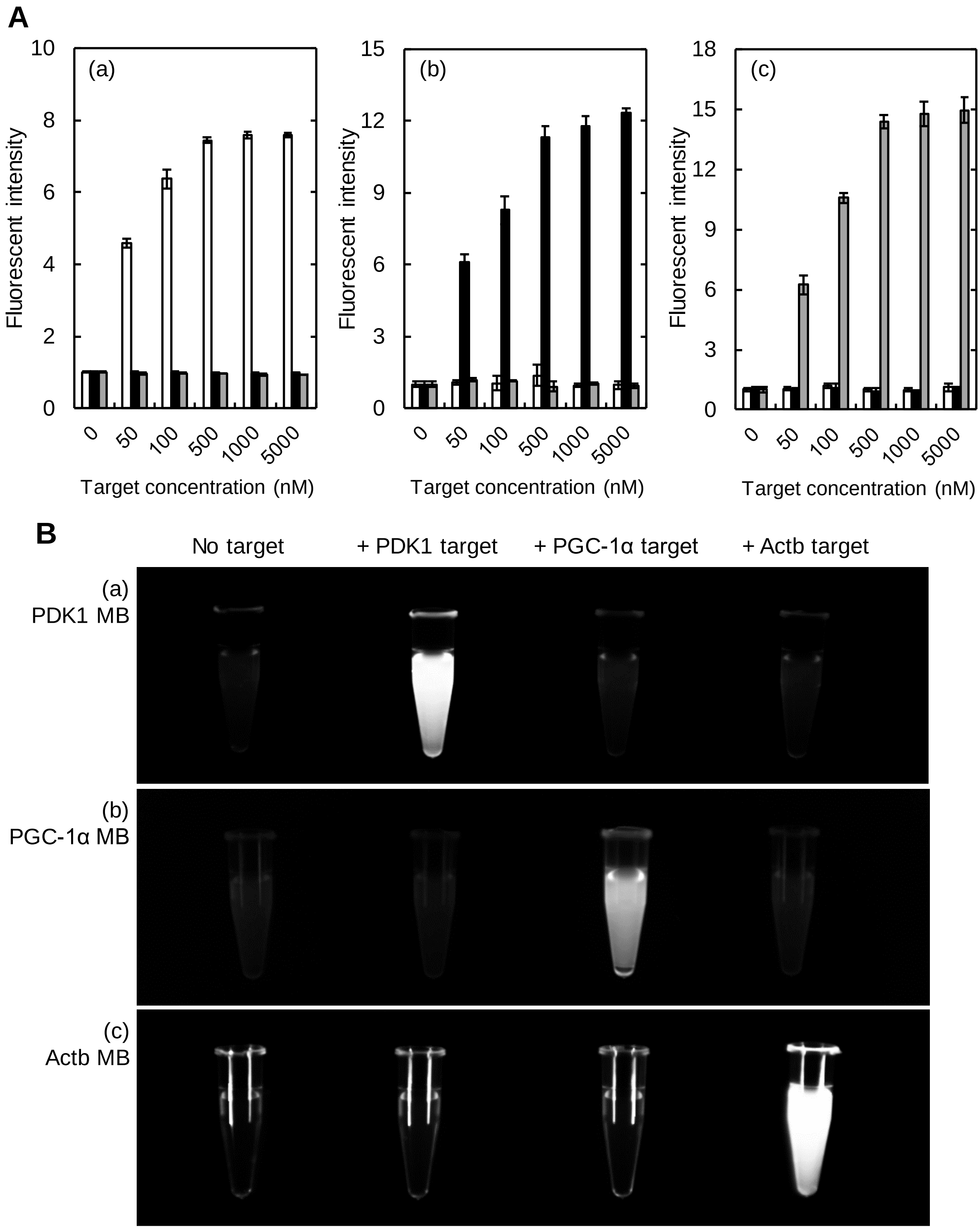

Figure 1. Hybridization specificity of MB designed. (A) The fluorescent intensity of PDK1 (a), PGC-1α (b), and Actb MB (c) mixed with different concentrations of PDK1 (☐), PGC-1α (■), and Actb specific target oligonucleotides (▨). The concentration of MB was all 100 nM. (B) Fluorescent images of PDK1 (a), PGC-1α (b), and Actb MB (c) (1 μM) mixed with PDK1, PGC-1α, and Actb specific target oligonucleotides (5 μM).

Table 4. Physicochemical properties of $\mathrm{cGNS_{MB}}$.

	Amount of MB incorporated (pmole/µg cGNS)	Apparent size (nm)	Zeta potential (mV)
$\mathrm{cGNS_{PDK1\ MB}}$	19.7 ± 0.1 [a)]	260.3 ± 13.0	9.63 ± 0.52
$\mathrm{cGNS_{PGC\text{-}1\alpha\ MB}}$	19.4 ± 0.2	255.5 ± 18.1	10.0 ± 0.41
$\mathrm{cGNS_{Actb\ MB}}$	19.4 ± 0.2	252.8 ± 18.8	9.21 ± 0.76

a) Average ± SD.

Cell internalization, cell viability, and labeling efficiency with $\mathrm{cGNS_{MB}}$

Next, the effect of $\mathrm{cGNS_{MB}}$ concentration and incubation time on the cell internalization and the viability of cells was assessed. **Figure 2A** shows the amount of MB internalized into the cells incubated with different concentrations of $\mathrm{cGNS_{Actb\ MB}}$ with varied incubation times. The amount of cell internalization increased with an increase of both $\mathrm{cGNS_{Actb\ MB}}$ concentration and incubation time other than 1 µg/ml of $\mathrm{cGNS_{Actb\ MB}}$ amount. The cell viability tended to decrease for the incubation time of 3 hr, and the cytotoxicity was observed at the concentration of 20 µg/ml (**Figure 2B**). However, no cytotoxicity was shown in other conditions. When the cells were observed by a fluorescent microscopy, the fluorescence was hardly detected at the concentration of 1 µg/ml at any incubation time (**Figure 2C**). The lower concentration and the shorter incubation time led to the weak fluorescence in the cells. On the other hand, sufficient fluorescence was detected at 10 µg/ml or higher concentration for 1 hr or for longer incubation time. **Figure 3** shows the flow cytometric analysis of cells incubated with different concentrations of $\mathrm{cGNS_{Actb\ MB}}$ for 1 hr. The labeling efficiency with $\mathrm{cGNS_{Actb\ MB}}$ (fluorescent-positive cells) reached around 100% over the concentration of 10 µg/ml. In terms of the cytotoxicity, the sensitivity, and the labeling efficiency, 10 µg/ml and 1 hr incubation was selected for the condition of cell internalization in the following experiments.

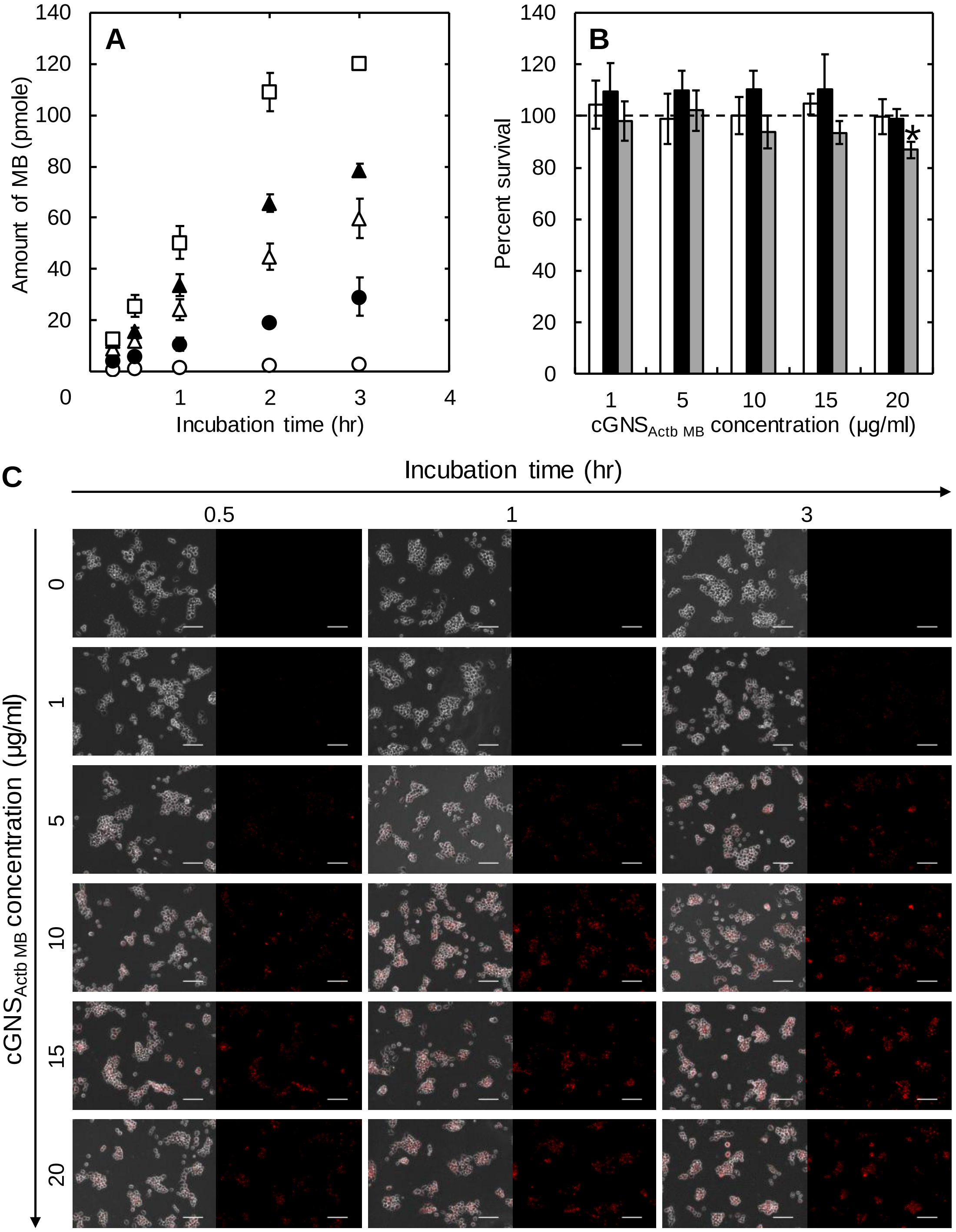

Figure 2. Effect of cGNS$_{Actb\ MB}$ concentration and incubation time on cell internalization and viability of cells. (A) Amount of MB internalized into the cells incubated with 1 (○), 5 (●), 10 (△), 15 (▲), and 20 μg/ml (□) cGNS$_{Actb\ MB}$ for different incubation times. (B) Viability of cells incubated with different concentrations of cGNS$_{Actb\ MB}$ for 0.5 (□), 1 (■), and 3 hr (▨). The viability of cells incubated without cGNS$_{Actb\ MB}$ was expressed as 100%. *, $p < 0.05$; significant against the percent survival of cells without cGNS$_{Actb\ MB}$ incubation. (C) Fluorescent microscopic images of cells incubated with different concentrations of cGNS$_{Actb\ MB}$ for different incubation times. Red: Actb MB. The left panel shows the merged images of phase contrast and MB fluorescence, while the right panel shows the MB fluorescence. Scale bar is 100 μm.

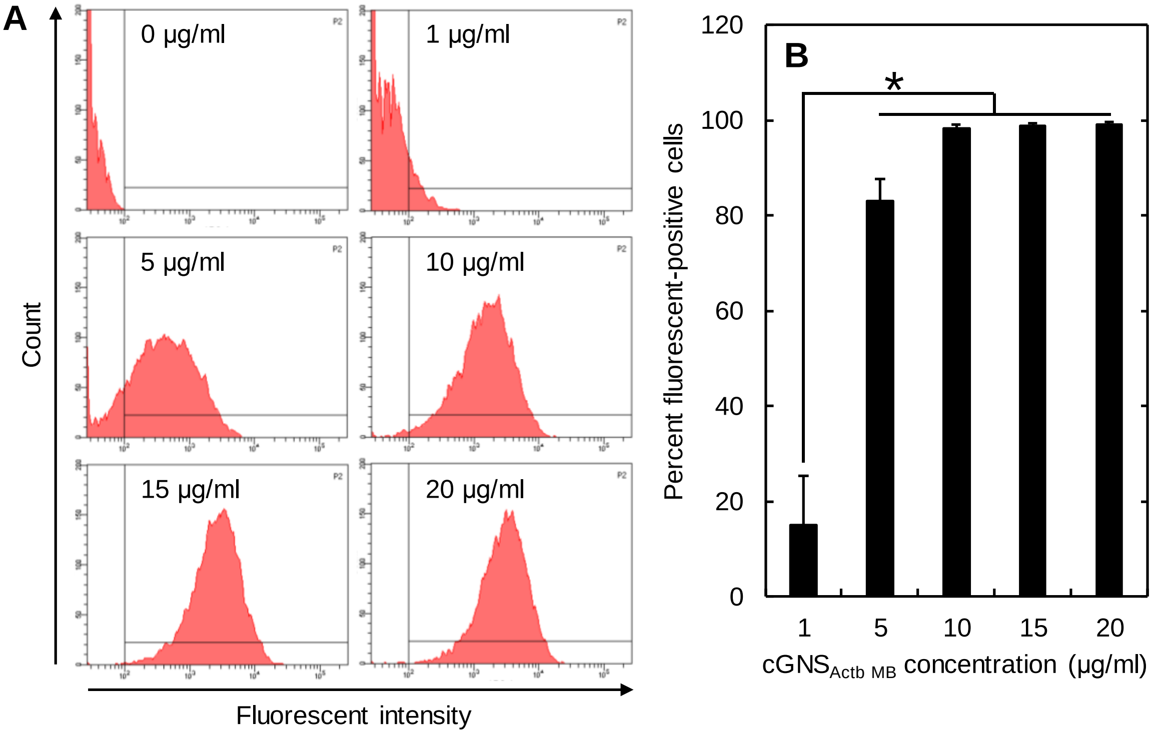

Figure 3. Evaluation of labeling efficiency with cGNS$_{Actb\ MB}$. The cells were incubated with 1, 5, 10, 15, and 20 µg/ml cGNS$_{Actb\ MB}$ for 1 hr, and analyzed on the flow cytometry by counting 10,000 cells. (A) Fluorescent histogram of cells, and (B) percentage of cells labeled with cGNS$_{Actb\ MB}$. The percentage of fluorescent-positive cells was determined by the fluorescent intensity of cells incubated without cGNS$_{Actb\ MB}$ (0 µg/ml). *, $p < 0.05$; significant between the groups.

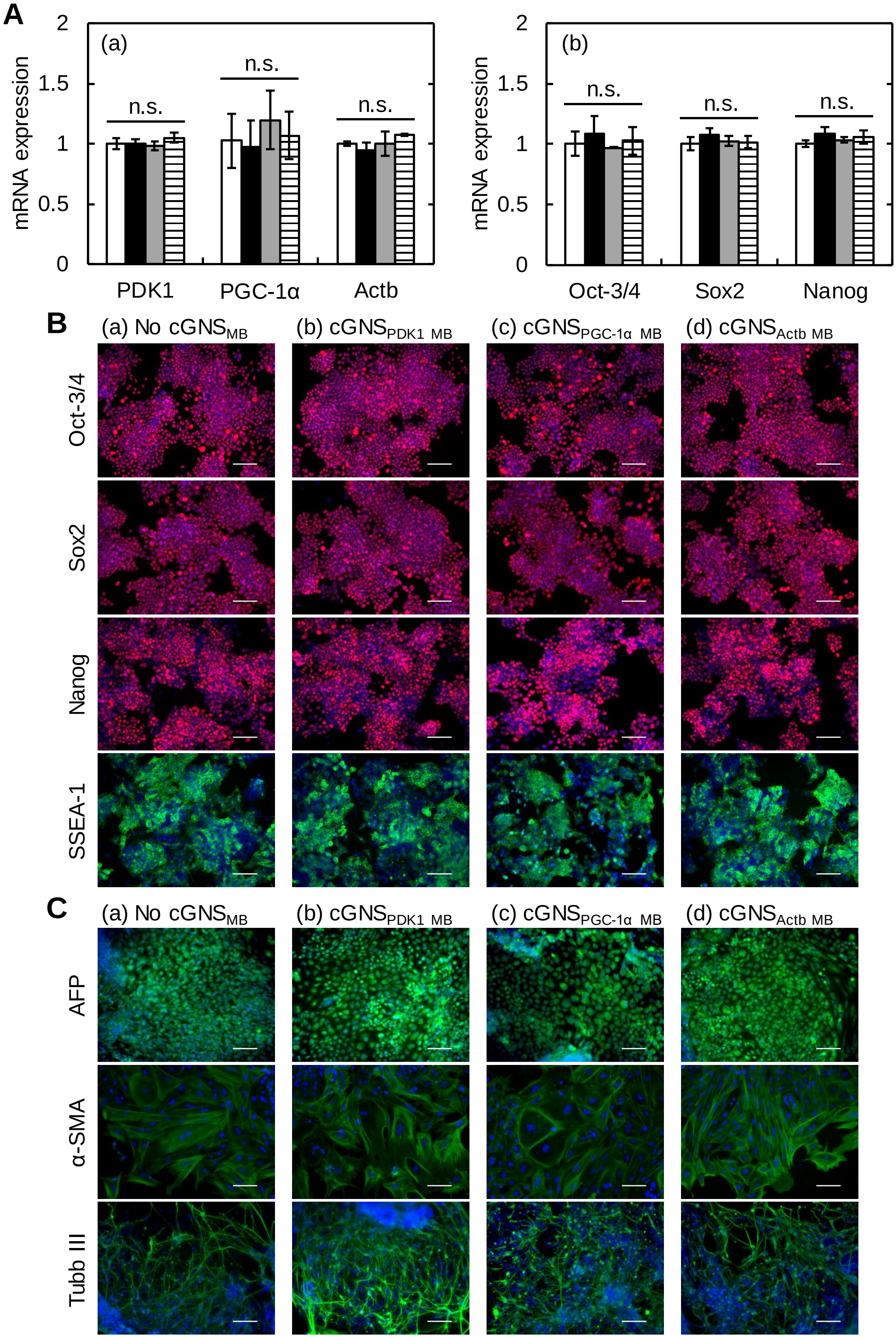
A
(a)
mRNA expression
2
1.5
1
0.5
0
n.s.
n.s.
n.s.
PDK1
PGC-1α
Actb
(b)
mRNA expression
n.s.
n.s.
n.s.
Oct-3/4
Sox2
Nanog
B
(a) No cGNS$_{MB}$
(b) cGNS$_{PDK1\ MB}$
(c) cGNS$_{PGC\text{-}1α\ MB}$
(d) cGNS$_{Actb\ MB}$
Oct-3/4
Sox2
Nanog
SSEA-1
C
(a) No cGNS$_{MB}$
(b) cGNS$_{PDK1\ MB}$
(c) cGNS$_{PGC\text{-}1α\ MB}$
(d) cGNS$_{Actb\ MB}$
AFP
α-SMA
Tubb III

Figure 4

Figure 4. Effect of cGNS$_{\mathrm{MB}}$ incubation on the expression of MB target mRNA and pluripotency. (A) mRNA expression analysis for MB targets (a) and pluripotent markers (b). The cells were incubated with 10 μg/ml cGNS$_{\text{PDK1 MB}}$ (■), cGNS$_{\text{PGC-1}\alpha\text{ MB}}$ (▒), and cGNS$_{\text{Actb MB}}$ (▤) for 1 hr, and the expression level was normalized by that of cells without cGNS$_{\mathrm{MB}}$ incubation (☐). Tbp and Actb were used as a housekeeping gene for (a) and (b), respectively. n.s.; not significant. (B) Immunofluorescent staining of pluripotent markers for the original cells (a) and the cells incubated with cGNS$_{\text{PDK1 MB}}$ (b), cGNS$_{\text{PGC-1}\alpha\text{ MB}}$ (c), and cGNS$_{\text{Actb MB}}$ (d). Red: Oct-3/4, Sox2, and Nanog. Green: SSEA-1. Blue: nuclei (DAPI). Scale bar is 100 μm. (C) Immunofluorescent staining of three germs markers (AFP: endoderm, α-SMA: mesoderm, and Tubb III: ectoderm) for the cells migrated from the matured EB. The EB was fabricated from the original cells (a) and the cells incubated with cGNS$_{\text{PDK1 MB}}$ (b), cGNS$_{\text{PGC-1}\alpha\text{ MB}}$ (c), and cGNS$_{\text{Actb MB}}$ (d). Green: AFP, α-SMA, and Tubb III. Blue: nuclei (DAPI). Scale bar is 100 μm.

mRNA expression of MB target and pluripotency after incubation with cGNS$_{\mathrm{MB}}$

Figure 4 shows the mRNA expression of MB target and the pluripotency of cells incubated with 10 μg/ml cGNS$_{\text{PDK1 MB}}$, cGNS$_{\text{PGC-1}\alpha\text{ MB}}$, and cGNS$_{\text{Actb MB}}$ for 1 hr. It has been reported that some MB have a knockdown effect on the target survivin mRNA of cancer cells as the theranostic application of MB [33]. Inconsistent with the survivin MB, all the mRNA expressions of MB targets (PDK1, PGC-1α, and Actb), as well as pluripotent markers (Oct-3/4, Sox2, and Nanog), were constant after the cGNS$_{\mathrm{MB}}$ incubation (**Figure 4A**). The result suggests that the hybridization of MB with the target sites of mRNA did not affect the expression. In other words, the MB used in this study could detect the target mRNA without interfering the expression, and the resulting function of cells. It is apparent from **Figure 4B** that Oct-3/4, Sox2, Nanog, and SSEA-1 of pluripotent markers were immunofluorescently stained even after the cGNS$_{\mathrm{MB}}$ incubation, which is similar to cells without the incubation. In addition, the differentiation ability for three germ lineages mediated by the formation of EB [26] was evaluated (**Figure 4C**). Even after the incubation with cGNS$_{\mathrm{MB}}$, the three germ markers, *i.e.* α-fetoprotein (AFP) for the endoderm, α-smooth muscle actin (α-SMA) for the mesoderm, and βIII tubulin (Tubb III) for the ectoderm, were similarly stained after the EB formation. These results indicate that the expression of pluripotent markers and the differentiation ability were not affected by the cGNS$_{\mathrm{MB}}$ incubation.

Early differentiation and energy metabolic profiles

Since it is well recognized that the undifferentiated state of mES cells is maintained by the LIF signaling pathways [28], the spontaneous early differentiation by the depletion of LIF was investigated for 3 days. **Figure 5A** shows the mRNA expression of pluripotent and early differentiation markers cultured without LIF. All the expressions of pluripotent markers significantly decreased by the depletion of LIF, and some early differentiation markers, such as Nestin, Eomes, and Cdx2, significantly increased. The result may be due to the inherent character of mES cells that tends to spontaneously differentiate into ectodermal linages [34]. In addition, it has been reported that the expression of Oct-3/4 inhibits the differentiation of mES cells into the trophectoderm [35]. Although the detailed mechanism was not investigated in this study, the mES cells might be differentiated into the ectodermal and trophectodermal linages by the simple withdrawn of LIF. **Figure 5B** shows the mRNA expression of PDK1 and PGC-1α of MB targets cultured with or without LIF. For the undifferentiated cells, the PDK1 expression increased as the culture with LIF, and became significantly higher than that of cells cultured without LIF at days 2 and 3. On the other hand, the PGC-1α expression of cells cultured without LIF, was significantly upregulated and higher than that of cells cultured with LIF at day 3. In addition to the mRNA, the protein expression of PDK1 and PGC-1α at day 3 was evaluated by the western blotting and the immunofluorescent staining (**Figure 6**). As the similar tendency, PDK1 and PGC-1α proteins were upregulated by the culture with or without LIF, respectively. Moreover, the expression ratio of phosphorylated PDH (pPDH) to PDH was higher in the cells cultured with LIF than that cultured without LIF, while the expression level of PDH was a similar extent. To evaluate the contribution of glycolysis and OXPHOS to the cell growth, the cells were cultured with or without LIF for 3 days in the presence of 2-DG of a glycolysis inhibitor and oligomycin of an ATP synthase inhibitor in OXPHOS (**Figure 5C**). The cell number cultured with LIF was significantly smaller than that cultured without LIF at lower concentrations of 2-DG. In contrast, oligomycin showed a tendency to decrease the cell number cultured without LIF rather than with LIF. The results suggest that the proliferation of undifferentiated and early differentiated cells are mainly supported by the glycolysis and the OXPHOS, respectively.

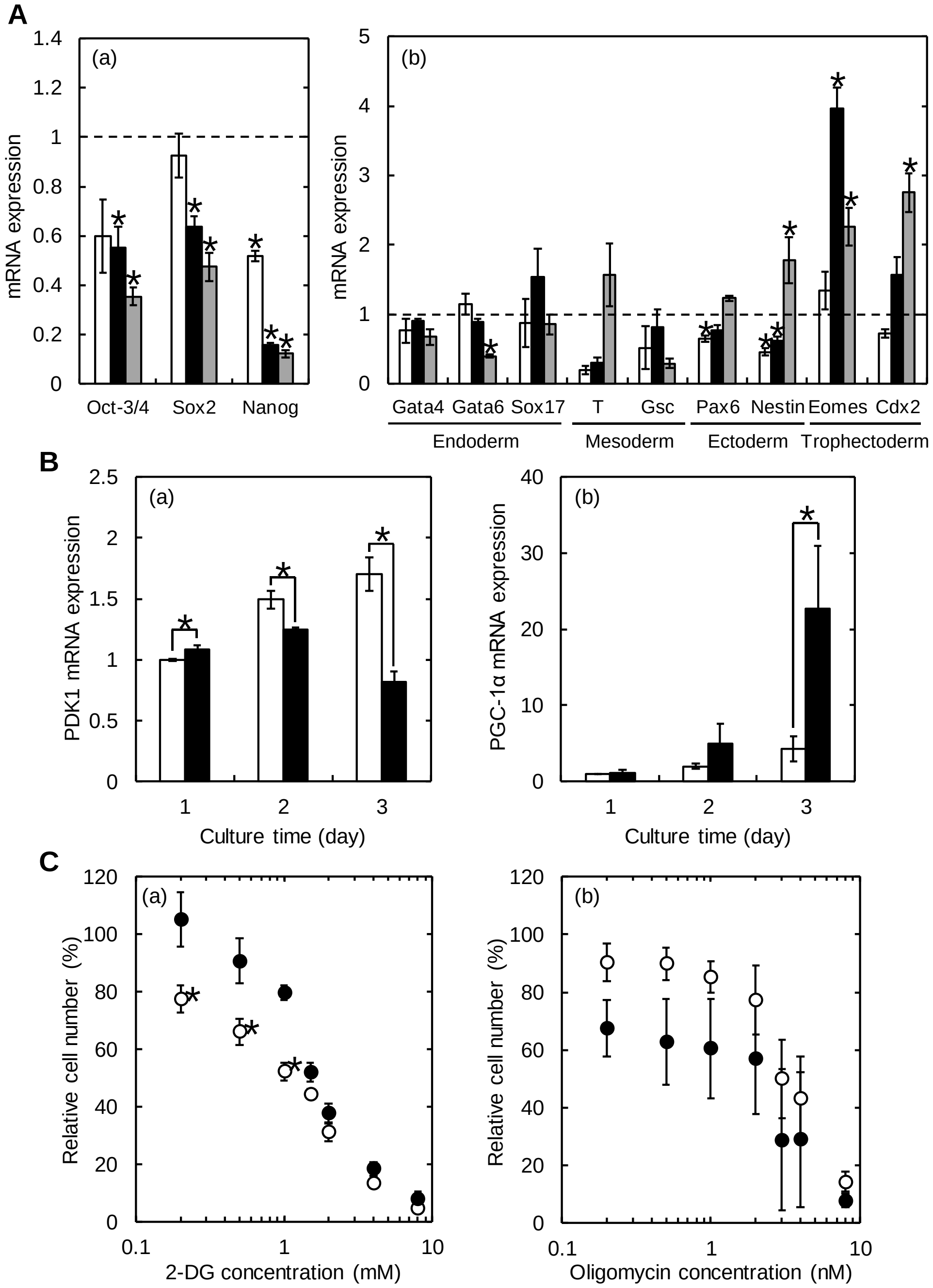

Figure 5. Early differentiation of cells by the depletion of LIF. (A) mRNA expression analysis for pluripotent (a) and early differentiation markers (b). The cells were cultured without LIF for 1 (☐), 2 (■), and 3 days (▨). The expression level was normalized by that of cells cultured with LIF at the corresponding time point. *, $p < 0.05$; significant against the expression level of cells cultured with LIF. (B) mRNA expression analysis for PDK1 (a) and PGC-1α (b). The cells were cultured with (☐) or without LIF (■), and the expression level was normalized by that of cells cultured with LIF at the time point of day 1. Actb was used as a housekeeping gene. *, $p < 0.05$; significant between the groups. (C) Effect of 2-DG (a) and oligomycin concentrations (b) on the cell growth. The cells were cultured with (○) or without LIF (●) for 3 days in the presence of different concentrations of 2-DG and oligomycin. The cell number was normalized by that cultured in the absence of 2-DG and oligomycin. *, $p < 0.05$; significant against the cell number cultured without LIF at the corresponding concentration.

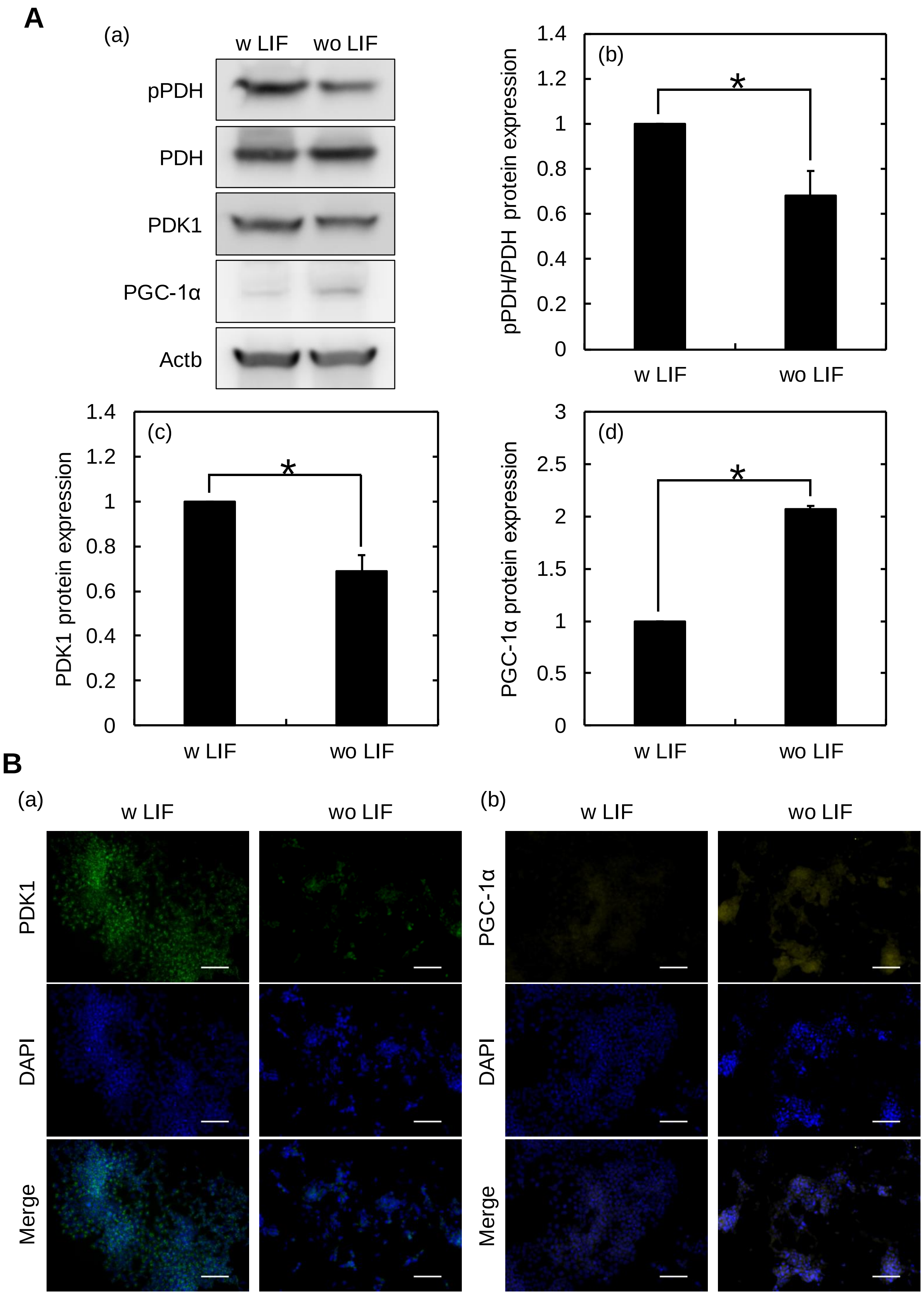
A
(a)
w LIF
wo LIF
pPDH
PDH
PDK1
PGC-1α
Actb
(b)
pPDH/PDH protein expression
1.4
1.2
1
0.8
0.6
0.4
0.2
0
*
w LIF
wo LIF
(c)
PDK1 protein expression
1.4
1.2
1
0.8
0.6
0.4
0.2
0
*
w LIF
wo LIF
(d)
PGC-1α protein expression
3
2.5
2
1.5
1
0.5
0
*
w LIF
wo LIF
B
(a)
w LIF
wo LIF
PDK1
DAPI
Merge
(b)
w LIF
wo LIF
PGC-1α
DAPI
Merge

Figure 6

Figure 6. Evaluation of protein expression for early differentiation. (A) Western blotting analysis of pPDH, PDH, PDK1, and PGC-1α for cells cultured with or without LIF for 3 days. Actb was used as a loading control. Chemiluminescent signal of each band (a) and protein expression analysis for the ratio of pPDH to PDH (b), PDK1 (c) and PGC-1α (d). The expression level was normalized by that of cells cultured with LIF. *, $p < 0.05$; significant between the groups. (B) Immunofluorescent staining of PDK1 (a) and PGC-1α (b) for cells cultured with or without LIF for 3 days. Green: PDK1, Yellow: PGC-1α, Blue: nuclei (DAPI), and Merged fluorescent images. Scale bar is 100 μm.

The metabolic profiles of cells were investigated on the extracellular flux analyzer (**Figure 7**). **Figure 7A** shows the ECAR change over the glycolysis stress test to assess the glycolytic profile. For the undifferentiated cells, the ECAR increased with the addition of glucose and oligomycin, and decreased by the addition of 2-DG, while the increase of ECAR in the early differentiation-induced cells was of a smaller extent. The basal and maximal glycolysis and the glycolysis reserve of cells cultured with LIF significantly became higher than that of cells cultured without LIF at days 2 and 3. **Figure 7B** shows the OCR change over the mitochondria stress test to assess the OXPHOS profile. The addition of oligomycin inhibited the ATP synthase to decrease the OCR, and the FCCP of an uncoupling agent of mitochondrial electron transport chain (ETC) increased the OCR to a maximal level. Finally, the rotenone and antimycin A decreased the OCR to a minimum level by inhibiting the complexes I and III in ETC, respectively. In contrast to the glycolysis stress test, both the basal and maximal respirations of cells cultured without LIF were significantly higher than that of cells cultured with LIF at days 2 and 3. However, there was little difference in the respiration reserve. For the plots of OCR versus ECAR (**Figure 8**), the undifferentiated cells showed a glycolytic profile as the culture with LIF, whereas the early differentiation-induced cells showed an aerobic OXPHOS profile as the culture without LIF. In addition, when the levels of mRNA expression related to the glycolysis were evaluated, the expression of hexokinase 2 (HK2) of the first rate-limiting enzyme in glycolysis was significantly upregulated in the undifferentiated cells (**Figure 9**).

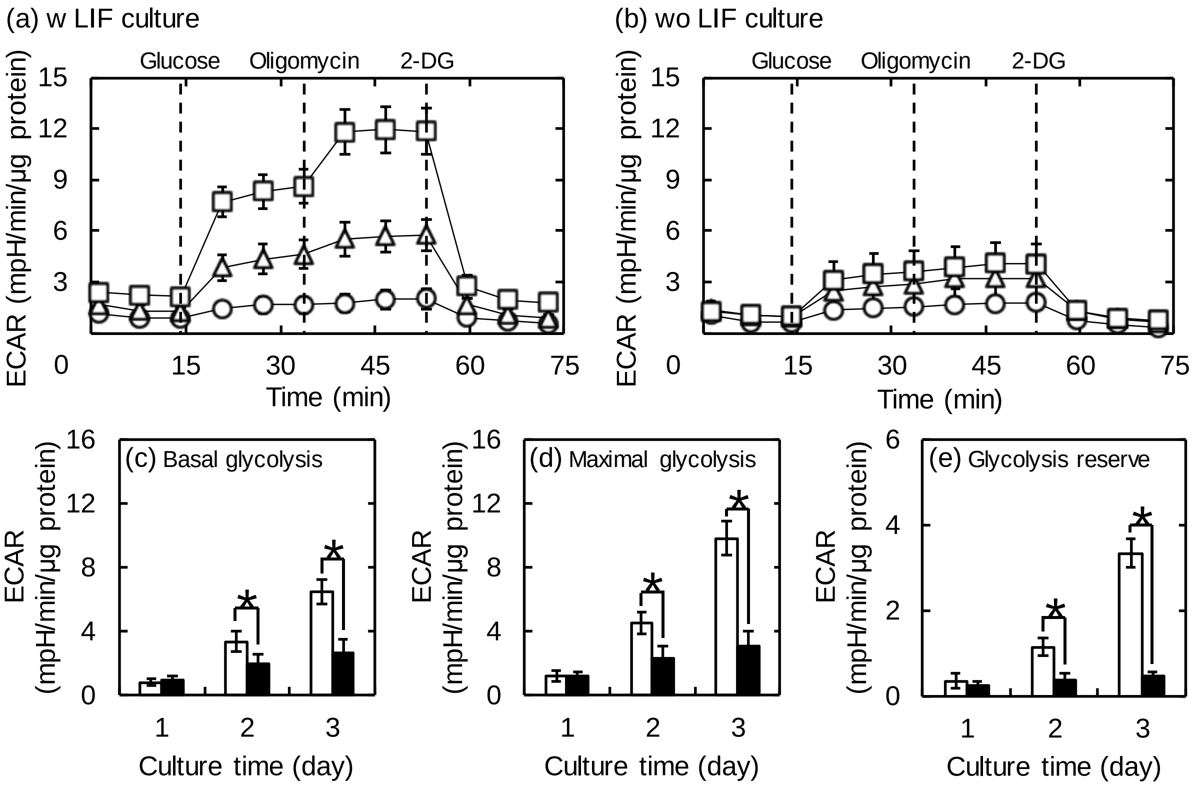

A Glycolysis stress test

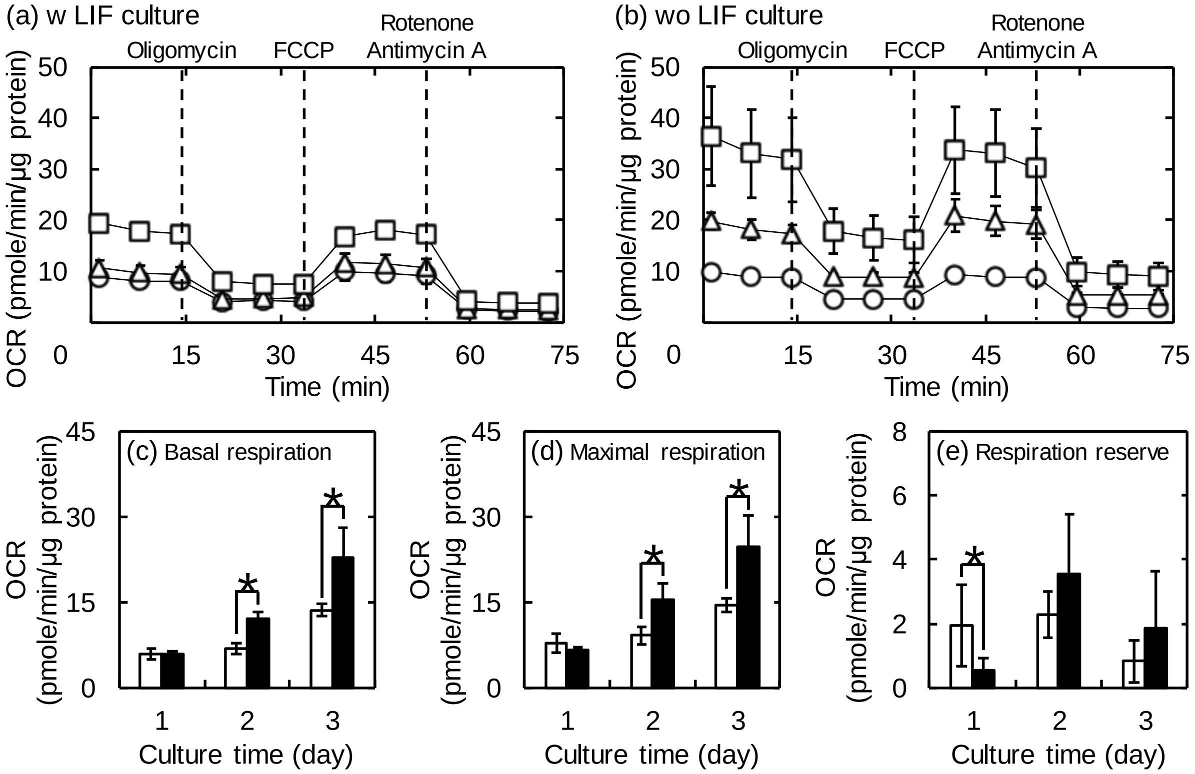

B Mitochondria stress test

Figure 7

Figure 7. Metabolic profiles of undifferentiated and early differentiation-induced cells. (A) ECAR change over the glycolysis stress test (sequential addition of glucose, oligomycin, and 2-DG) on the cells cultured with (a) or without LIF (b) for 1 (○), 2 (△), and 3 days (□). The basal glycolysis (c), maximal glycolysis (d), and glycolysis reserve (e) of cells cultured with (□) or without LIF (■) were determined by the profiles of ECAR change. (B) OCR change over the mitochondria stress test (sequential addition of oligomycin, FCCP, and a mixture of rotenone and antimycin A) on the cells cultured with (a) or without LIF (b) for 1 (○), 2 (△), and 3 days (□). The basal respiration (c), maximal respiration (d), and respiration reserve (e) of cells cultured with (□) or without LIF (■) were determined by the profiles of OCR change. *, $p < 0.05$; significant between the groups.

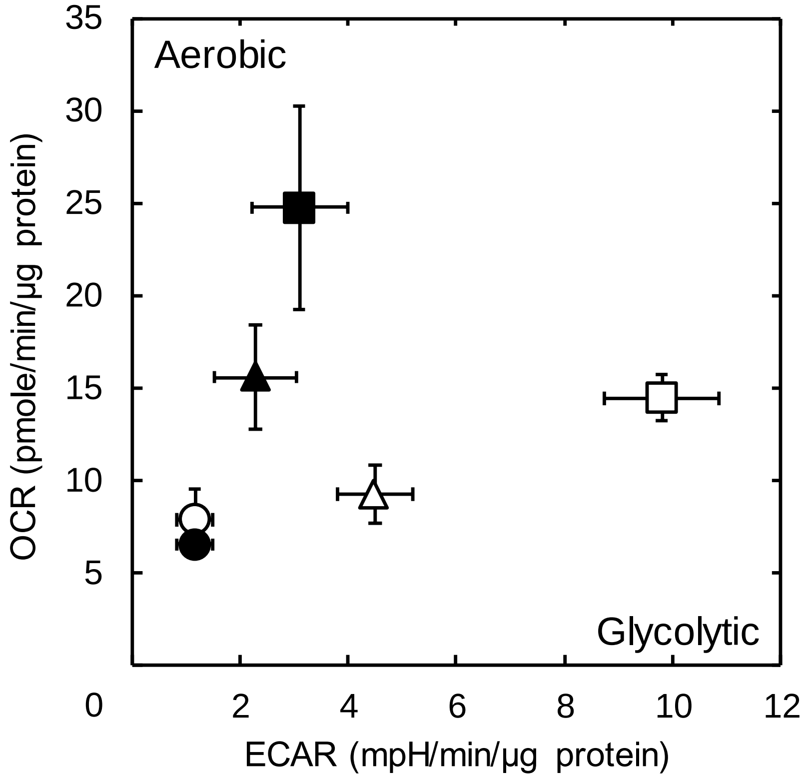

Figure 8. Plots of OCR versus ECAR for undifferentiated and early differentiation-induced cells. The cells were cultured with (white) or without LIF (black) for 1 (○●), 2 (△▲), and 3 days (□■). The ECAR and OCR were the values from maximal glycolysis (Figure 7A (d)) and respiration (Figure 7B (d)), respectively.

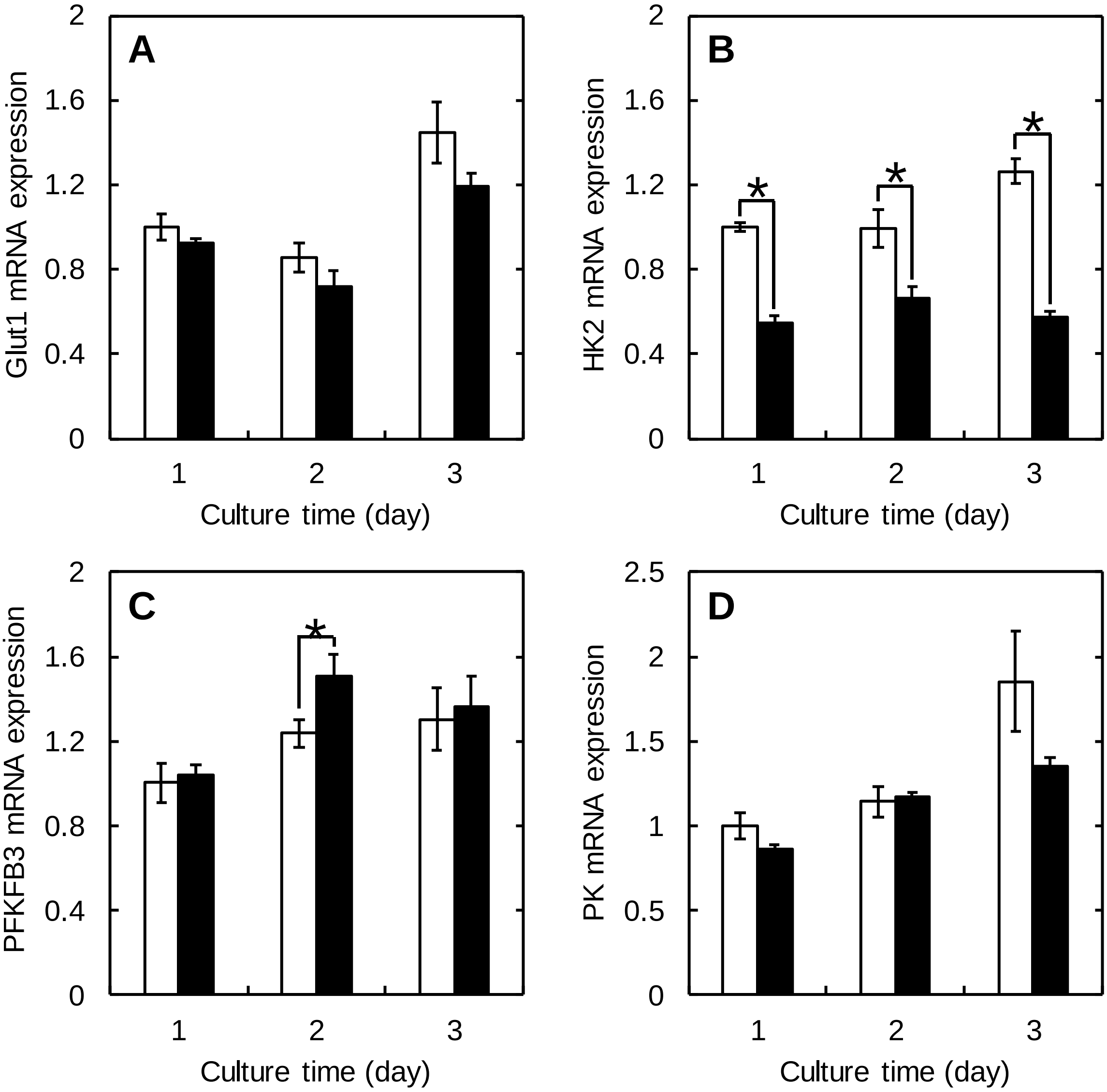

Figure 9. Expression analysis of mRNA related to the glycolysis for early differentiation. The cells were cultured with (☐) or without LIF (■), and the expression level was normalized by that of cells cultured with LIF at the time point of day 1. Actb was used as a housekeeping gene. *, $p < 0.05$; significant between the groups.

Fluorescent imaging of undifferentiated and early differentiation-induced cells after incubation with cGNS$_{\mathrm{MB}}$

The cell internalization of cGNS$_{\mathrm{MB}}$ was evaluated over the maintenance of undifferentiated state and the induction of early differentiation for 3 days (**Figure 10**). Although the amount of MB internalized into the cells increased depending on the culture time period, the MB amount internalized into the cells cultured without LIF for 3 days was significantly lower than that cultured with LIF. This is because the cell number of early differentiation was smaller than that of undifferentiated cells. However, there was no difference in the cell internalization amount among cGNS$_{PDK1\ MB}$, cGNS$_{PGC\text{-}1\alpha\ MB}$, and cGNS$_{Actb\ MB}$. This is due to the similar physicochemical properties of cGNS$_{MB}$, which is independent of the MB sequences (**Table 4**).

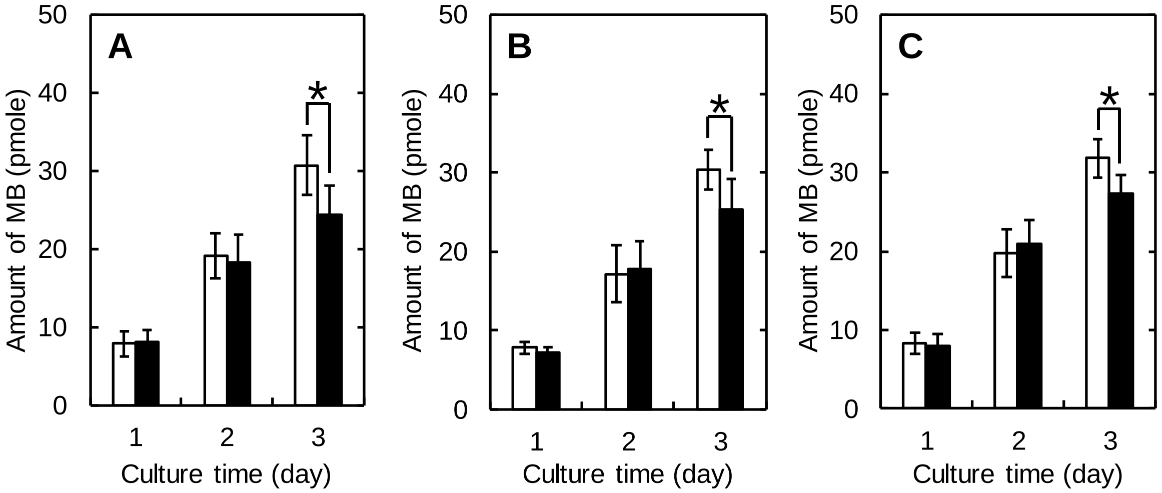

Figure 10. Amount of MB internalized into undifferentiated and early differentiation-induced cells after incubation with cGNS$_{MB}$. The cells were cultured with (☐) or without LIF (■) for 3 days, and incubated with 10 µg/ml cGNS$_{PDK1\ MB}$ (A), cGNS$_{PGC\text{-}1\alpha\ MB}$ (B), and cGNS$_{Actb\ MB}$ (C) for 1 hr at different culture time points. *, $p < 0.05$; significant between the groups.

Figure 11 shows the cGNS$_{MB}$ imaging for undifferentiated and early differentiation-induced cells. The packed colonies as a character of undifferentiated cells cultured with LIF were observed, while the colonies were dissociated as the culture without LIF. The fluorescence of cGNS$_{Actb\ MB}$ was similarly observed at any time point of culture, irrespective of the LIF presence, and the fluorescent intensity was constant. The cGNS$_{PDK1\ MB}$ fluorescence was strongly observed for the undifferentiated cells cultured with LIF than that cultured without LIF, and the fluorescent intensity significantly increased as the culture with LIF. In contrast to the cGNS$_{PDK1\ MB}$, the intense fluorescence of cGNS$_{PGC\text{-}1\alpha\ MB}$ was observed for the early differentiation-induced cells cultured without LIF than that cultured with LIF, and the fluorescent intensity significantly became higher as the culture without LIF. The fluorescent intensity of cGNS$_{PDK1\ MB}$ and cGNS$_{PGC\text{-}1\alpha\ MB}$ showed a similar profile to the mRNA expression of PDK1 and PGC-1α (**Figures 11B** and **5B**).

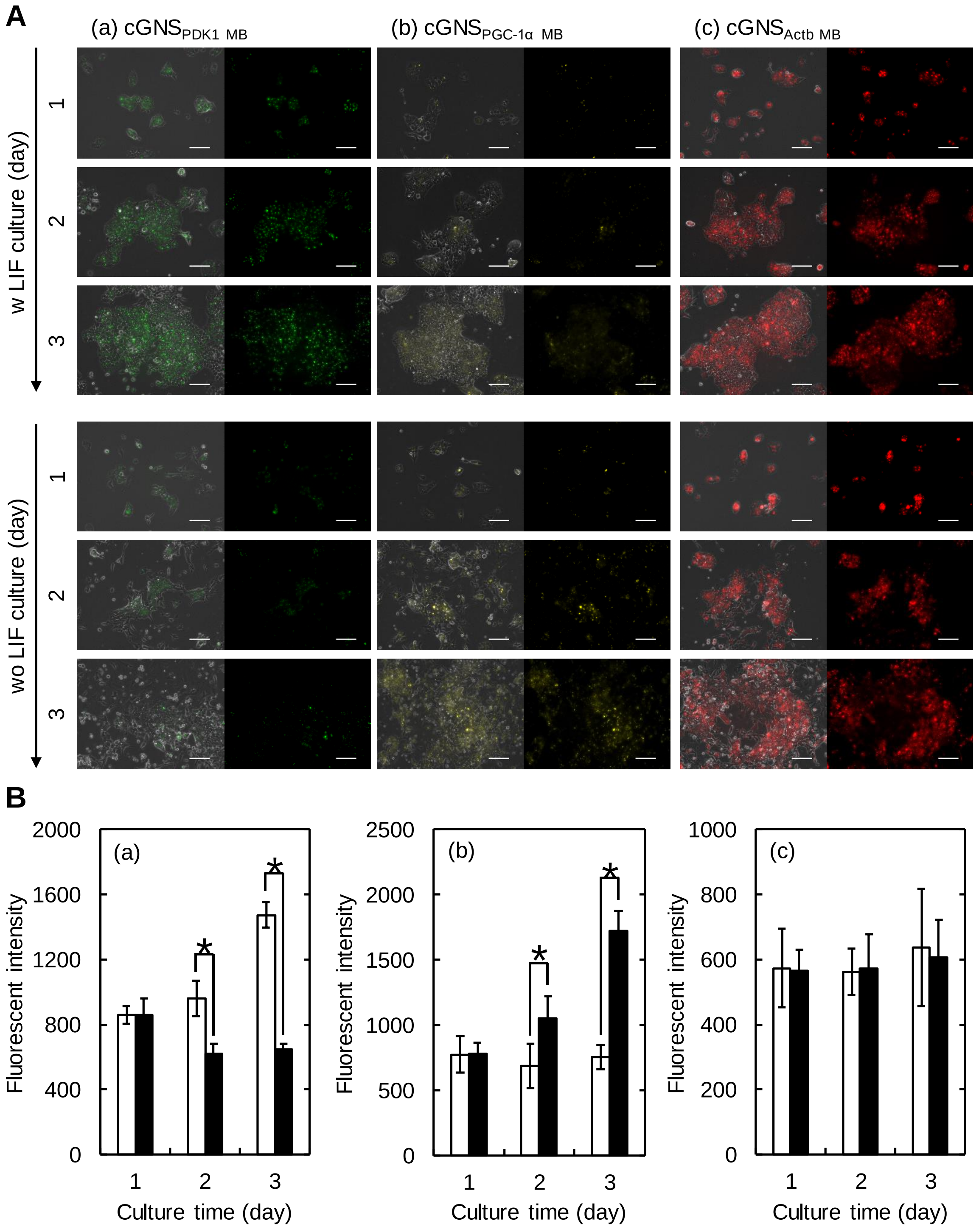

Figure 11. Fluorescent imaging of undifferentiated and early differentiation-induced cells after incubation with cGNS$_{\mathrm{MB}}$. (A) Fluorescent microscopic images of cells incubated with 10 µg/ml cGNS$_{\mathrm{PDK1\ MB}}$ (a), cGNS$_{\mathrm{PGC\text{-}1\alpha\ MB}}$ (b), and cGNS$_{\mathrm{Actb\ MB}}$ (c) for 1 hr at different culture time points. The cells were cultured with or without LIF for 1, 2, and 3 days. Green: PDK1 MB, Yellow: PGC-1α MB, and Red: Actb MB. The left panel shows the merged images of phase contrast and MB fluorescence, while the right panel shows the MB fluorescence. Scale bar is 100 µm. (B) Fluorescent intensity of cells after incubation with cGNS$_{\mathrm{PDK1\ MB}}$ (a), cGNS$_{\mathrm{PGC\text{-}1\alpha\ MB}}$ (b), and cGNS$_{\mathrm{Actb\ MB}}$ (c). The cells were cultured with (□) or without LIF (■) for 1, 2, and 3 days. *, $p < 0.05$; significant between the groups.

For the further evaluation of $cGNS_{MB}$ imaging, the inhibitory experiments of PDK1 activity by the addition of DCA were performed (**Figure 12**). DCA, an analog of the PDH complex substrate pyruvate, has been utilized to inhibit the PDK activity in the fields of cancer research and therapy [4, 30]. As the mechanism of inhibition, it has been reported that the DCA binds to the allosteric site in the amino-terminal domain of the PDK enzymes, leading to the local conformational changes in both the nucleotide- and lipoyl-binding pockets [36]. Despite the cells were cultured with LIF, the addition of 15 mM DCA led to the increased PDH activity and the decreased expression of PDK1 mRNA, which was consistent with the previous report [31]. When the $cGNS_{PDK1\ MB}$ and $cGNS_{Actb\ MB}$ were incubated with the cells, the fluorescent intensity of $cGNS_{PDK1\ MB}$ for the cells supplemented with DCA was significantly lower than that for the cells without DCA, whereas the fluorescent intensity of $cGNS_{Actb\ MB}$ was constant. The fluorescent intensity of $cGNS_{PDK1\ MB}$ was consistent with the decreased expression of PDK1. These results also experimentally indicate that the expression level of target mRNA could be accurately detected by $cGNS_{MB}$.

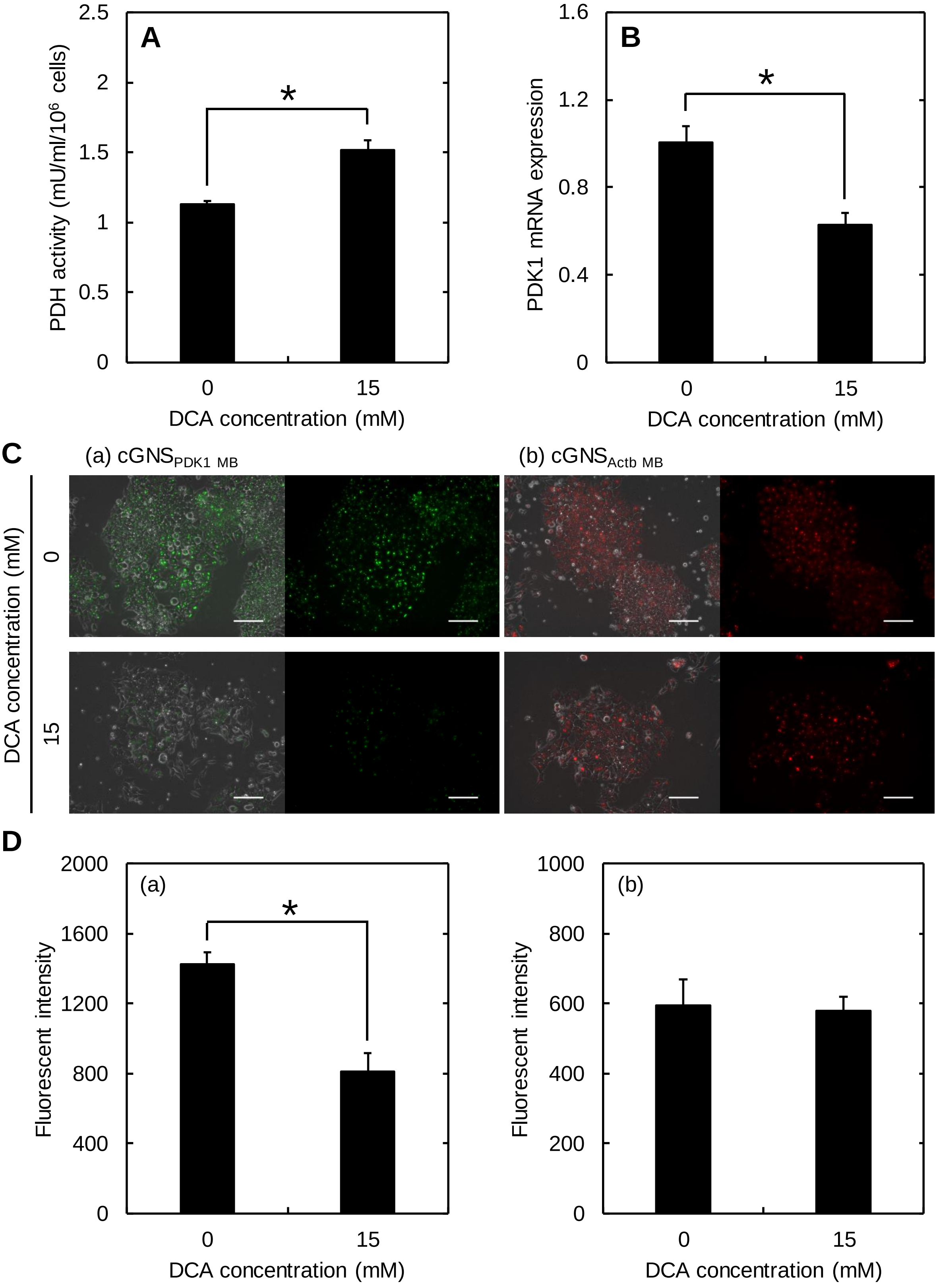
A
PDH activity (mU/ml/10^6 cells)
2.5
2
1.5
1
0.5
0
*
0
15
DCA concentration (mM)
B
PDK1 mRNA expression
1.6
1.2
0.8
0.4
0
*
0
15
DCA concentration (mM)
C
(a) cGNS$_{PDK1\ MB}$
(b) cGNS$_{Actb\ MB}$
DCA concentration (mM)
0
15
D
(a)
Fluorescent intensity
2000
1600
1200
800
400
0
*
0
15
DCA concentration (mM)
(b)
Fluorescent intensity
1000
800
600
400
200
0
0
15
DCA concentration (mM)

Figure 12

Figure 12. Inhibition of PDK1 activity by DCA. (A) PDH activity of cells cultured with 15 mM DCA for 3 days in the presence of LIF. The activity was normalized by the cell number used for the measurement. (B) PDK1 mRNA expression of cells cultured with 15 mM DCA for 3 days in the presence of LIF. The expression level was normalized by that of cells cultured 0 mM DCA. Actb was used as a housekeeping gene. *, $p < 0.05$; significant between the groups. (C) Fluorescent microscopic images of cells after incubation with 10 μg/ml $cGNS_{PDK1\ MB}$ (a) and $cGNS_{Actb\ MB}$ (b) for 1 hr. The cells were cultured with 15 mM DCA for 3 days in the presence of LIF. Green: PDK1 MB, Red: Actb MB. The left panel shows the merged images of phase contrast and MB fluorescence, while the right panel shows the MB fluorescence. Scale bar is 100 μm. (D) Fluorescent intensity of cells after incubation with $cGNS_{PDK1\ MB}$ (a) and $cGNS_{Actb\ MB}$ (b). *, $p < 0.05$; significant between the groups.

Neural differentiation and energy metabolic profiles

In addition to the spontaneous early differentiation, the lineage-specific neural differentiation was induced. The mRNA expression of pluripotent markers (Oct-3/4, Sox2, and Nanog) significantly decreased, while that of neural markers (Pax6, Nestin, and Tubb III) significantly increased as the differentiation culture (**Figure 13A**). As shown in **Figure 13B**, both Nestin and Tubb III of neural progenitor and neuronal markers, respectively, were immunofluorescently stained after the induction of differentiation for 9 days, and the formation of neuronal network was observed. **Figure 13C** shows the mRNA expression of PDK1 and PGC-1α over the neural differentiation. The expression of PDK1 was significantly downregulated, whereas that of PGC-1α was significantly upregulated as the differentiation. The similar tendency was experimentally confirmed by the western blotting analysis (**Figure 14**). The phosphorylation of PDH and the protein expression of PDK1 in the undifferentiated cells were significantly higher than those of the differentiated. On the contrary, the protein expression of PGC-1α was significantly upregulated as the neural differentiation. The results were consistent with the immunofluorescent staining of PDK1 and PGC-1α (**Figure 15**).

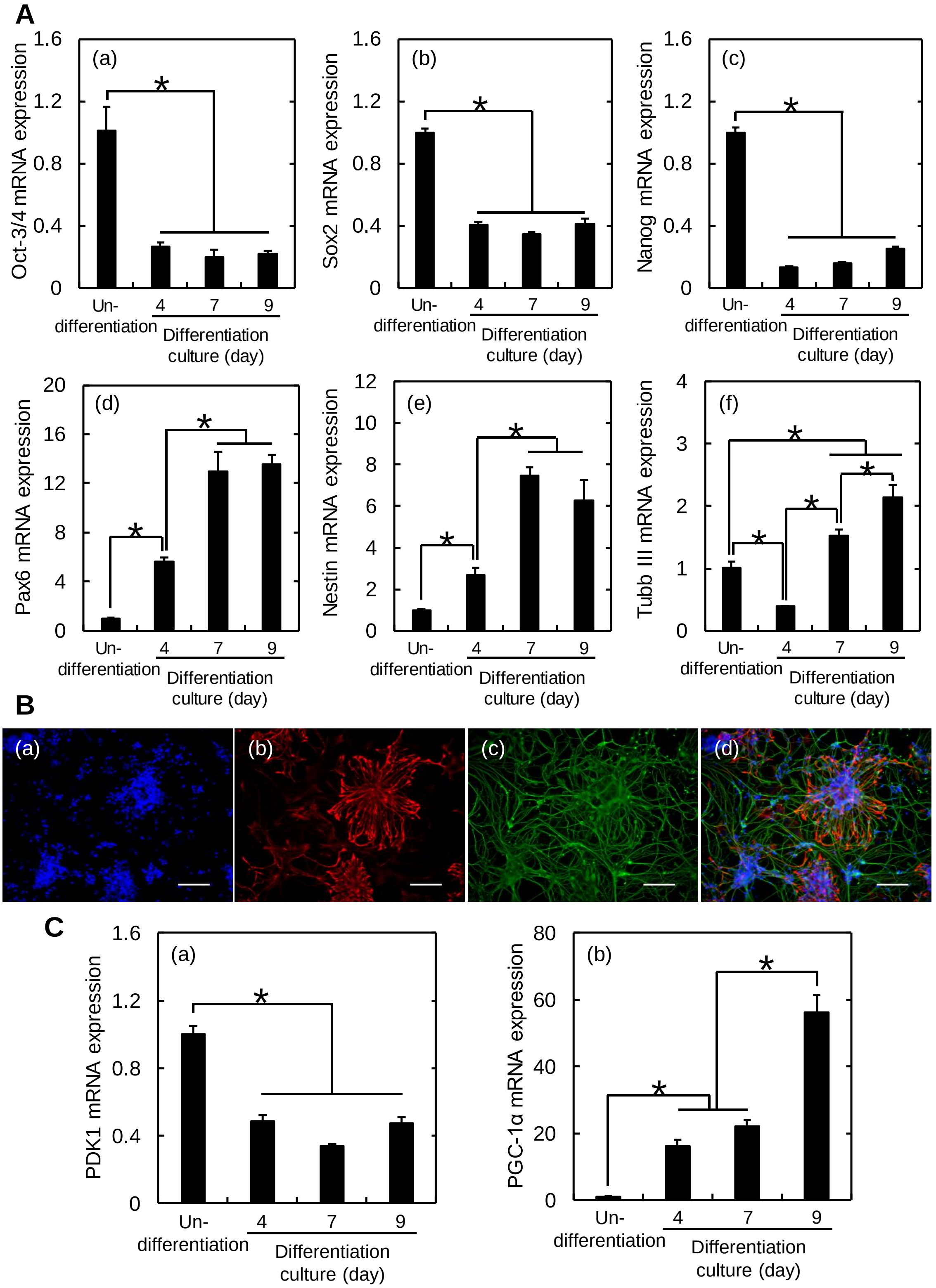

Figure 13. Evaluation of neural differentiation. (A) mRNA expression analysis for pluripotent (a-c) and neural markers (d-f). (B) Immunofluorescent staining of cells after the induction of neural differentiation for 9 days: (a) Blue: nuclei (DAPI), (b) Red: Nestin, (c) Green: Tubb III, and (d) Merged fluorescent images. Scale bar is 100 μm. (C) mRNA expression analysis for PDK1 (a) and PGC-1α (b). The expression level was normalized by that of undifferentiated cells. Actb was used as a housekeeping gene. *, $p < 0.05$; significant between the groups.

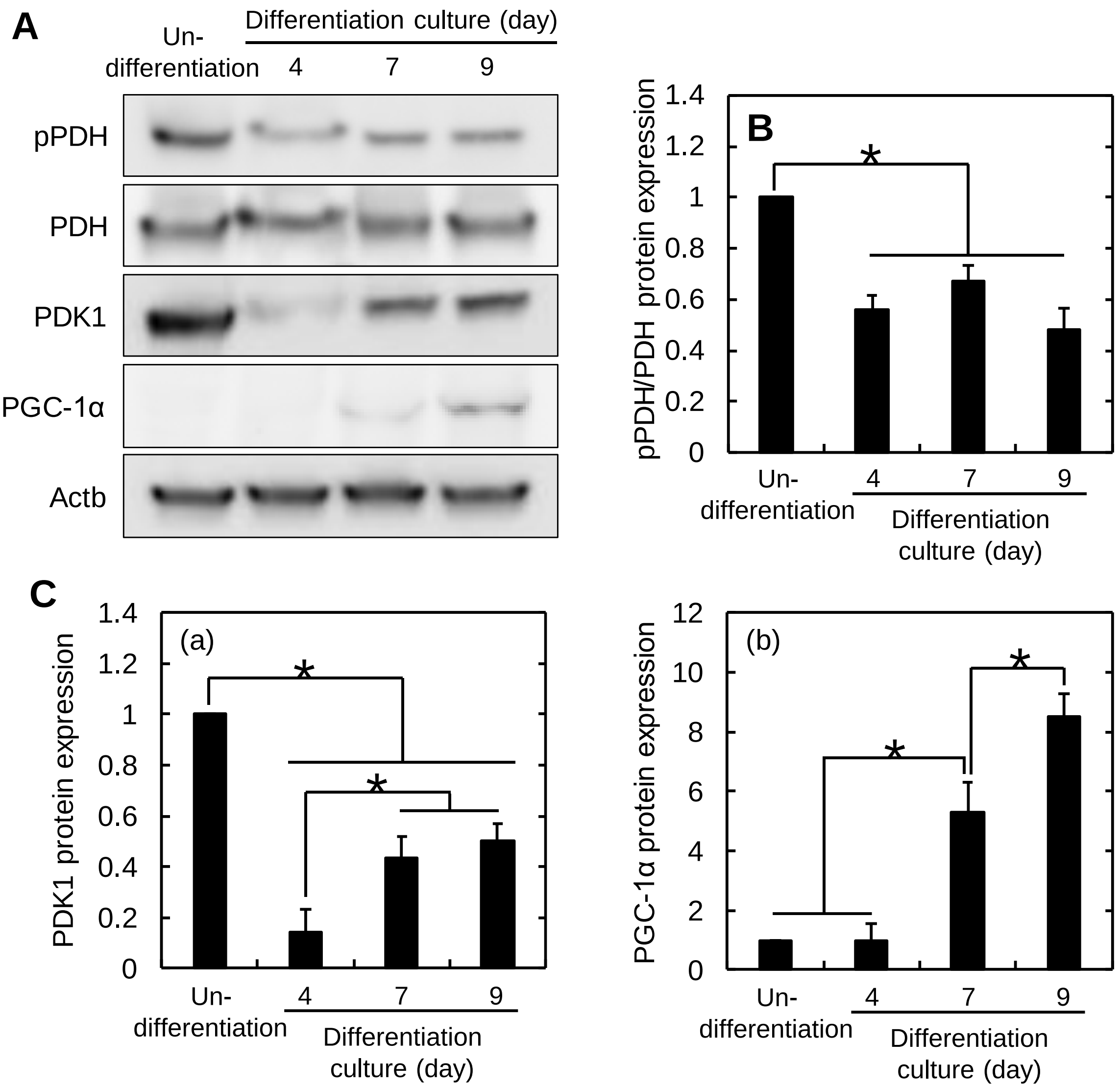

Figure 14. Evaluation of protein expression for neural differentiation. (A) Western blotting analysis of pPDH, PDH, PDK1, and PGC-1α for undifferentiated and neural differentiation-induced cells. Actb was used as a loading control. (B) Protein expression analysis for the ratio of pPDH to PDH. (C) Protein expression analysis for PDK1 (a) and PGC-1α (b). The expression level was normalized by that of undifferentiated cells. *, $p < 0.05$; significant between the groups.

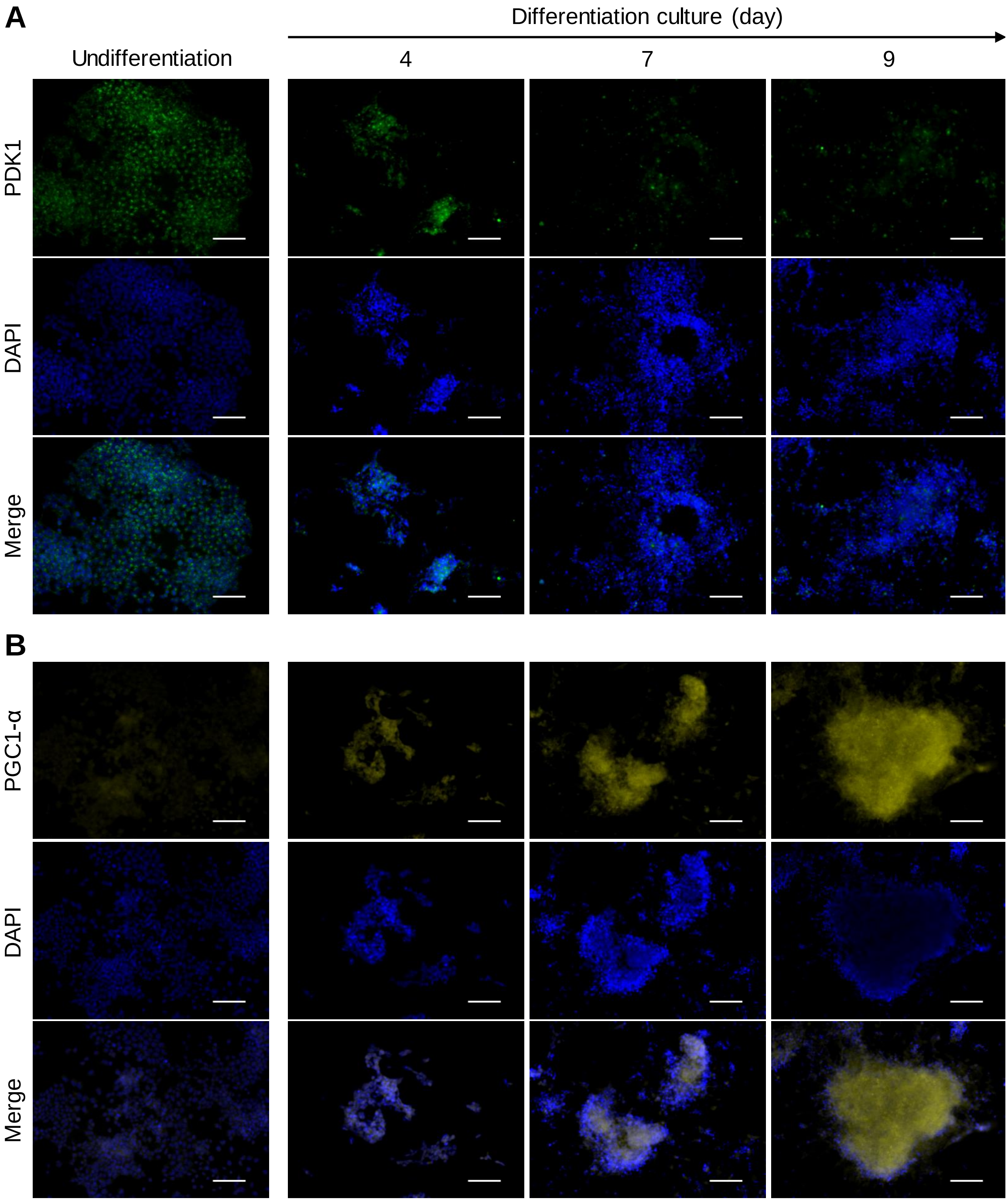

Figure 15. Immunofluorescent staining of PDK1 (A) and PGC-1α (B) for neural differentiation at different time points of culture. Green: PDK1, Yellow: PGC-1α, Blue: nuclei (DAPI), and Merged fluorescent images. Scale bar is 100 μm.

Figure 16 shows the results of glycolysis and mitochondria stress tests on the undifferentiated and neural differentiation-induced cells. All the glycolytic parameters, basal glycolysis, maximal glycolysis, and glycolysis reserve, were significantly higher in the undifferentiated cells than those of the differentiated cells at any time point of differentiation. On the other hand, among the OXHOS parameters, the maximal respiration and the respiration reserve significantly increased as the induction of neural differentiation. In particular, the enhancement of respiration reserve was significantly higher than that in the early differentiation-induced cells. It is known that the neuronal cells heavily rely the energy demand on the OXPHOS [37]. It is likely that the respiration reserve increased to meet the high energy demand in the neuronal OXPHOS. The high level of glycolysis in the undifferentiated cells and the gradual increase of OXPHOS as the neural differentiation were confirmed by the plots of OCR vs ECAR, as well (**Figure 17**). Among the expression of mRNA related to the glycolysis (**Figure 18**), the HK2 mRNA was significantly upregulated in the undifferentiated cells. However, the 6-phosphofructo-2-kinase/fructose-2,6-biphosphatase 3 (PFKFB3) expression increased in the cells induced to neural differentiation for 9 days. The result suggests that HK2 might play a more critical role in the maintenance of glycolysis than other glycolysis markers evaluated in this study, although only the mRNA was investigated.

A Glycolysis stress test

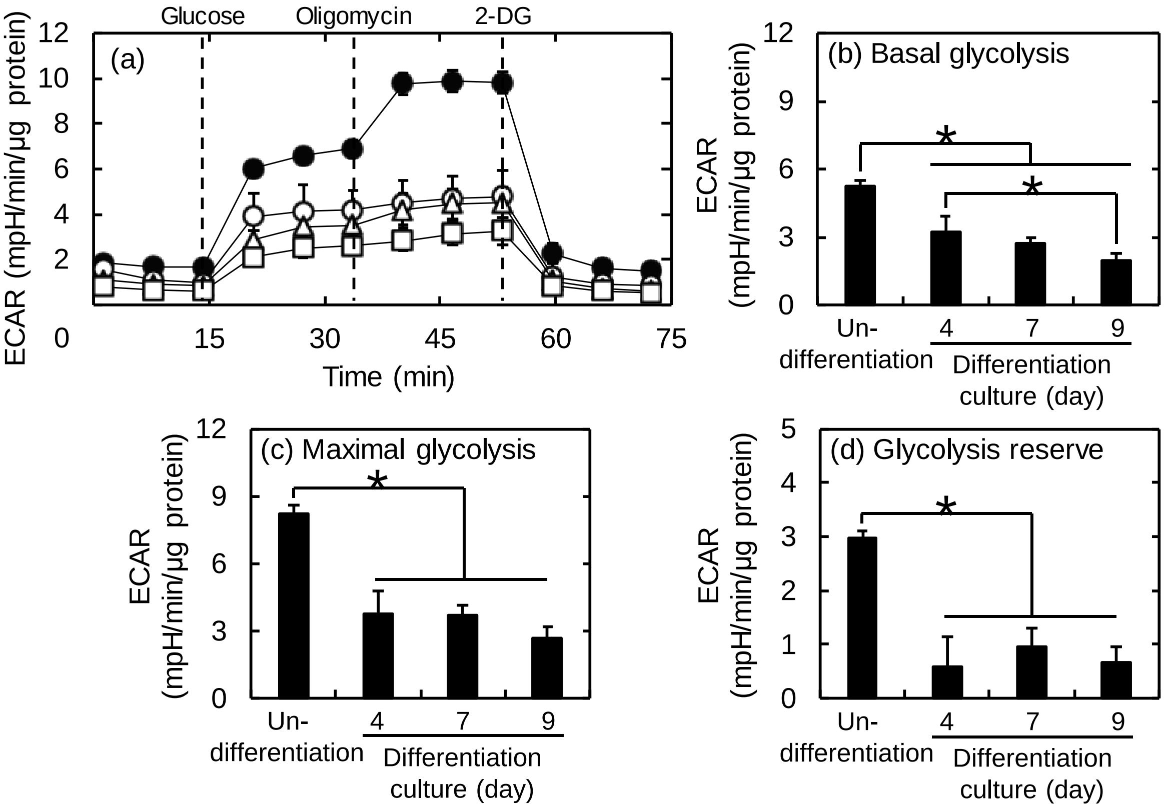

B Mitochondria stress test

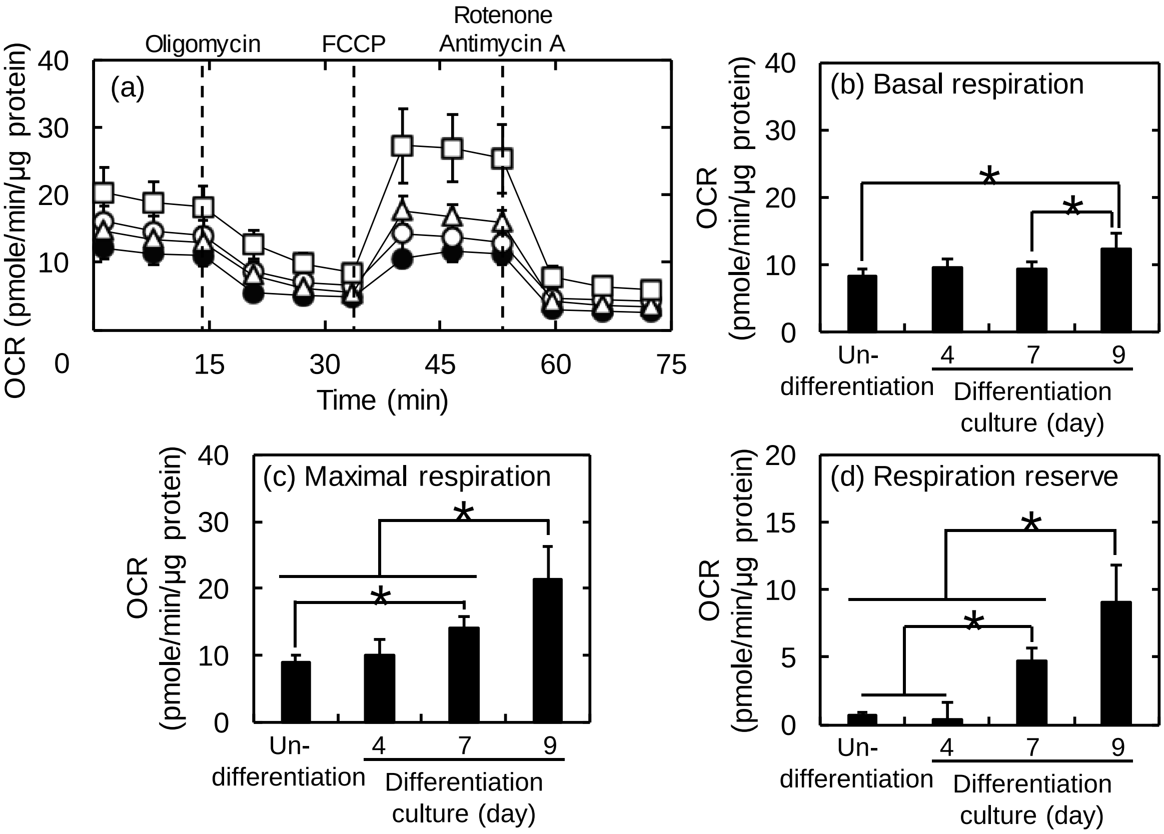

Figure 16

Figure 16. Metabolic profiles of undifferentiated and neural differentiation-induced cells. (A) (a) ECAR change over the glycolysis stress test (sequential addition of glucose, oligomycin, and 2-DG) on the undifferentiated (●) and neural differentiation-induced cells for 4 (○), 7 (△), and 9 days (□). The basal glycolysis (b), maximal glycolysis (c), and glycolysis reserve (d) were determined by the profiles of ECAR change. (B) (a) OCR change over the mitochondria stress test (sequential addition of oligomycin, FCCP, and a mixture of rotenone and antimycin A) on the undifferentiated (●) and neural differentiation-induced cells for 4 (○), 7 (△), and 9 days (□). The basal respiration (b), maximal respiration (c), and respiration reserve (d) were determined by the profiles of OCR change. *, $p < 0.05$; significant between the groups.

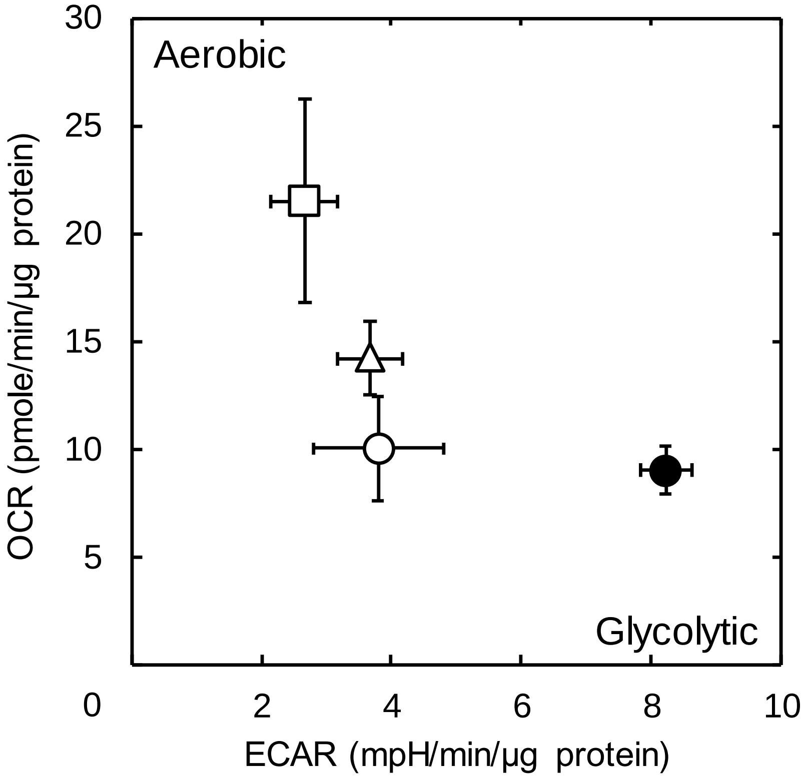

Figure 17. Plots of OCR versus ECAR for undifferentiated and neural differentiation-induced cells. The measurements were performed on the undifferentiated (●) and neural differentiation-induced cells for 4 (○), 7 (△), and 9 days (□). The ECAR and OCR were the values from maximal glycolysis (Figure 16A (c)) and respiration (Figure 16B (c)), respectively.

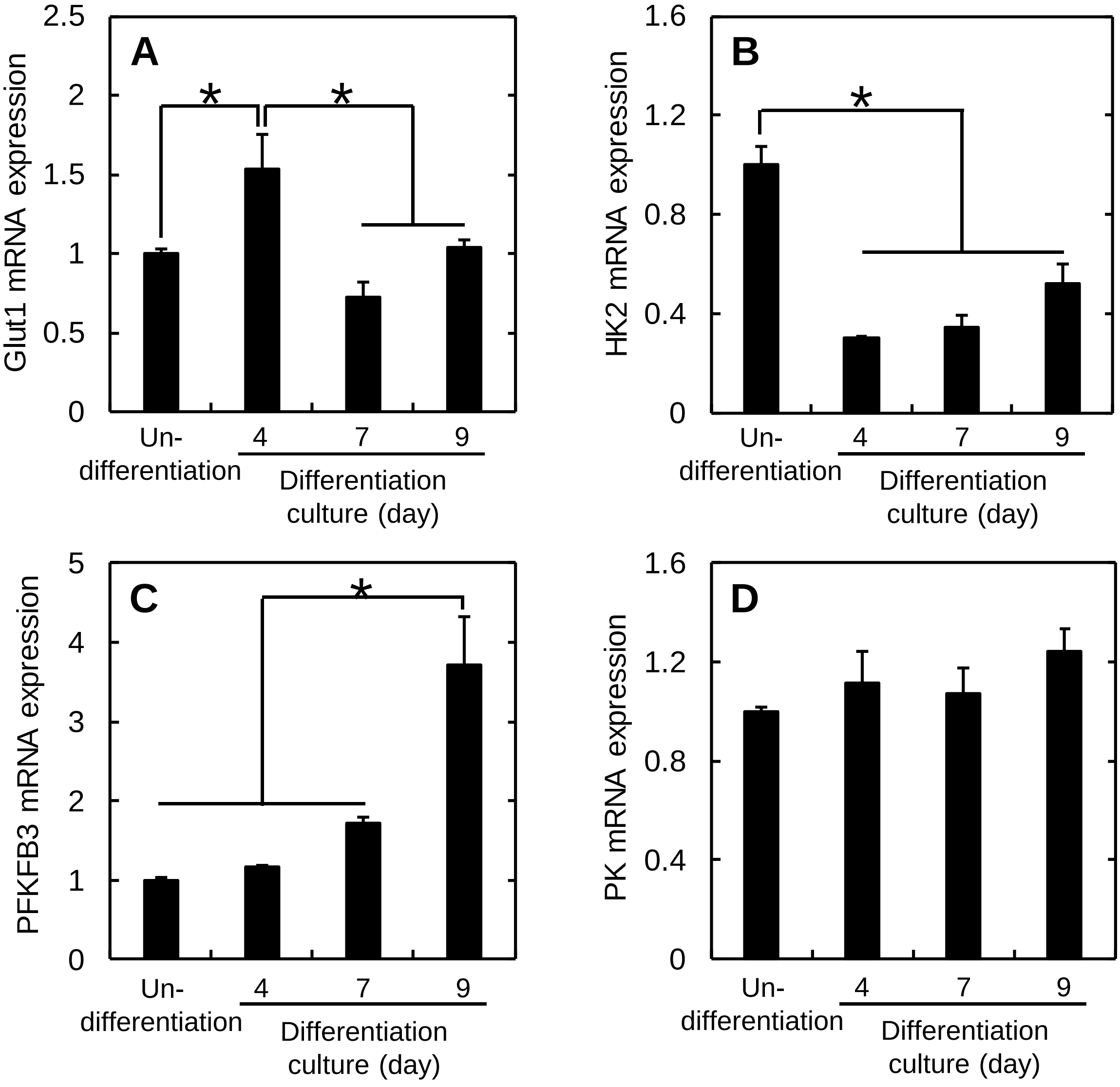

Figure 18. Expression analysis of mRNA related to the glycolysis for neural differentiation. The expression level was normalized by that of undifferentiated cells. Actb was used as a housekeeping gene. *, $p < 0.05$; significant between the groups.

Fluorescent imaging of undifferentiated and neural differentiation-induced cells after incubation with cGNS$_{\text{MB}}$

The cGNS$_{\text{MB}}$ were incubated with the undifferentiated and the neural differentiation-induced cells at different time points of differentiation culture, and the cells were observed by the fluorescent microscopy (**Figure 19**). The fluorescence of cGNS$_{\text{Actb MB}}$ was similarly observed for the undifferentiated and the neural differentiation-induced cells at any time point of induction, and the fluorescent intensity was a constant value. On the other hand, the intense fluorescence of $cGNS_{PDK1\ MB}$ was observed for the undifferentiated cells, and the intensity was significantly higher than that of the neural differentiation-induced cells. In contrast, the $cGNS_{PGC\text{-}1\alpha\ MB}$ fluorescence was strongly observed for the cells induced to neural differentiation, while that of undifferentiated cells was of a weak signal. In addition, the fluorescent intensity of $cGNS_{PGC\text{-}1\alpha\ MB}$ tended to increase depending on the time period of differentiation culture, and became significantly higher than undifferentiated cells 9 days later. The fluorescent intensity of $cGNS_{PDK1\ MB}$ and $cGNS_{PGC\text{-}1\alpha\ MB}$ well corresponded to the mRNA expression of PDK1 and PGC-1α (**Figures 19B** and **13C**), and the profile of MB fluorescence showed a pattern similar to the immunnofluorescent staining (**Figures 19A** and **15**).

As one potential application of $cGNS_{MB}$ imaging system, the multi-color imaging was performed to visualize the difference of energy metabolic pathways in the same cell population. The undifferentiated and the neural differentiation-induced cells for 9 days were incubated with cGNS co-incorporating PDK1, PGC-1α, and Actb MB ($cGNS_{multi\ MB}$), and observed by the fluorescent microscopy with wide fields (**Figure 20**). The fluorescence of Actb MB was detected from almost all of cells in both undifferentiated and differentiated cells. For the undifferentiated cells, fluorescence of PDK1 MB was homogenously observed, whereas that of PGC-1α MB was weak. On the other hand, the fluorescent signal of PDK1 MB was detected around the intense signal of PGC-1α MB in the cells induced to neural differentiation.

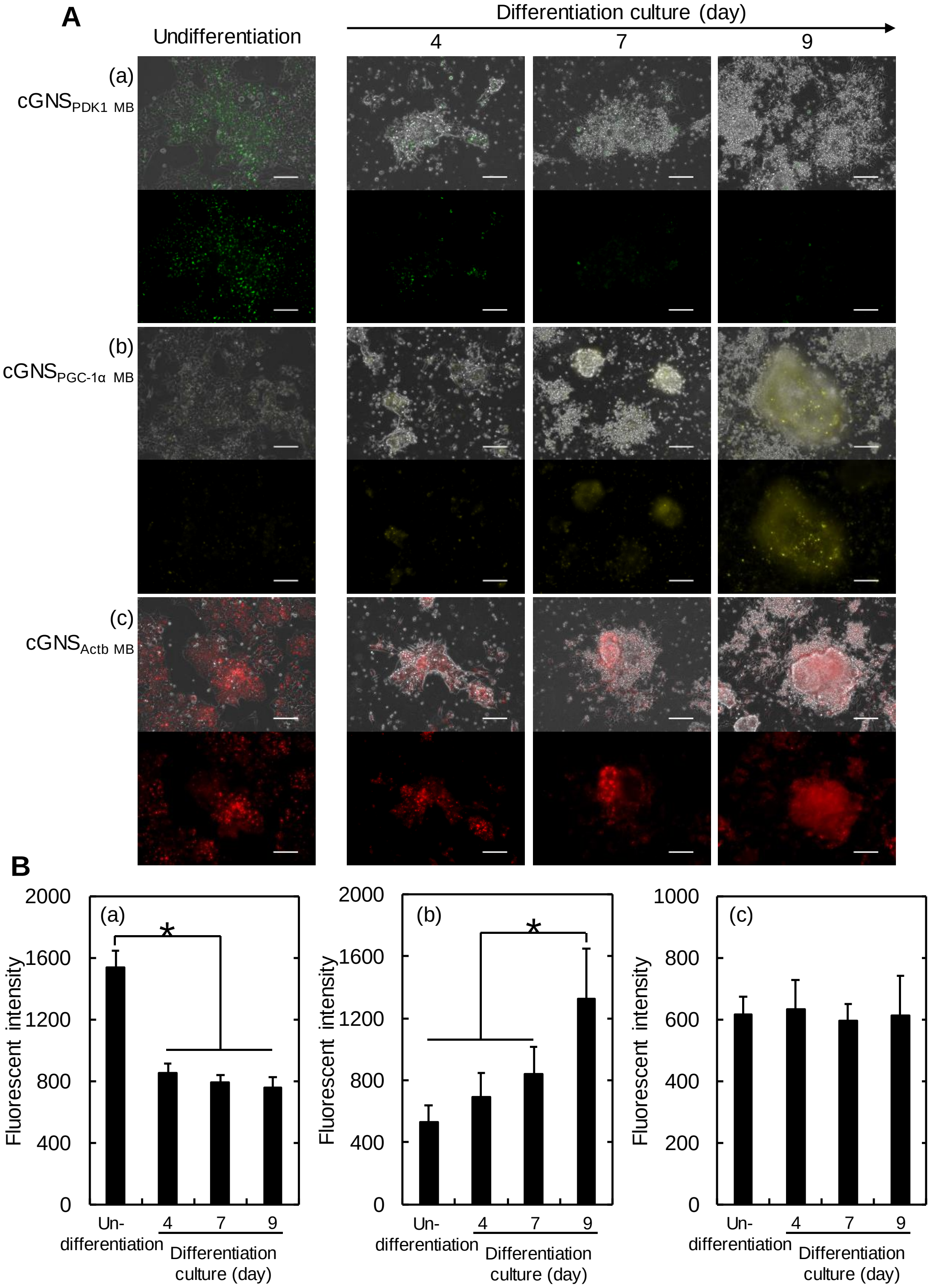

Figure 19. Fluorescent imaging of undifferentiated and neural differentiation-induced cells after incubation with cGNS$_{\text{MB}}$. (A) Fluorescent microscopic images of cells incubated with 10 μg/ml cGNS$_{\text{PDK1 MB}}$ (a), cGNS$_{\text{PGC-1α MB}}$ (b), and cGNS$_{\text{Actb MB}}$ (c) for 1 hr at different time points of differentiation culture. Green: PDK1 MB, Yellow: PGC-1α MB, and Red: Actb MB. The upper panel shows the merged images of phase contrast and MB fluorescence, while the lower panel shows the MB fluorescence. Scale bar is 100 μm. (B) Fluorescent intensity of cells after incubation with cGNS$_{\text{PDK1 MB}}$ (a), cGNS$_{\text{PGC-1α MB}}$ (b), and cGNS$_{\text{Actb MB}}$ (c). *, $p < 0.05$; significant between the groups.

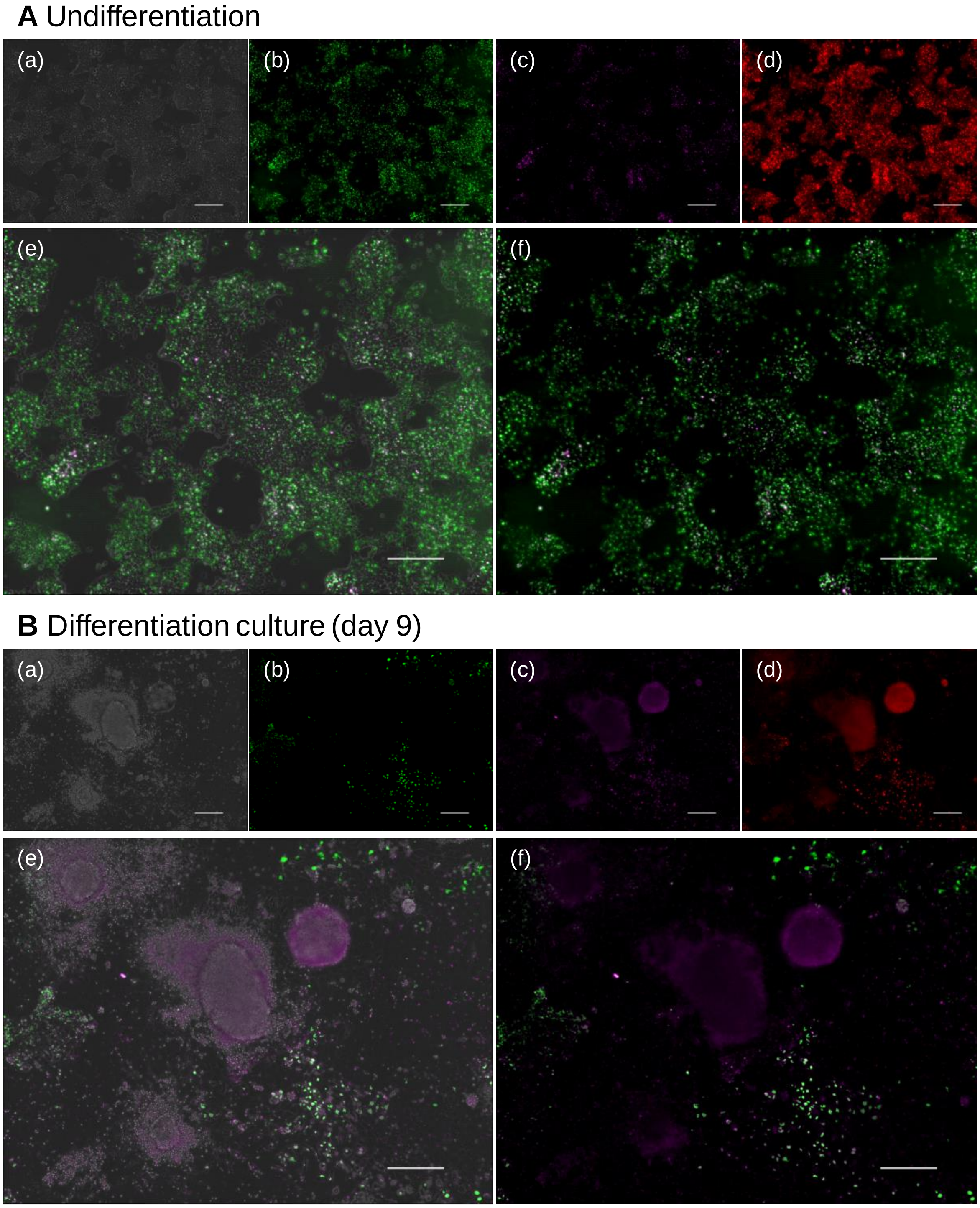

Figure 20. Multi-color fluorescent imaging of undifferentiated and neural differentiation-induced cells after incubation with cGNS$_{\text{multi MB}}$. Fluorescent microscopic images of undifferentiated (A) and neural differentiation-induced cells at day 9 (B) incubated with 10 µg/ml cGNS$_{\text{multi MB}}$ for 1 hr. The fluorescence of MB was expressed as a pseudo color to visualize the co-localization: (a) Phase contrast, (b) Green: PDK1 MB, (c) Magenta: PGC-1α MB, (d) Red: Actb MB. Merged fluorescent images: (e) Phase contrast, PDK1 MB, and PGC-1α MB, and (f) PDK1 MB and PGC-1α MB. Scale bar is 200 µm.

DISCUSSION

The present study clearly demonstrates that undifferentiated and differentiated cells could be discriminated from the energy metabolic pathways by making use of the cGNS_{MB} imaging system. The cGNS_{MB} prepared were readily internalized into the mES cells to allow MB to efficiently label, without modifying their pluripotency. The PDK1 was significantly upregulated in the undifferentiated cells, and the resulting phosphorylation of PDH was maintained in a high level. On the other hand, the expression of PGC-1α significantly increased as the early differentiation by the depletion of LIF, as well as the neural differentiation. The analysis of metabolic profile by the measurements of ECAR and OCR revealed that the undifferentiated cells showed an enhanced glycolytic profile. In contrast, the OXPHOS profile increased as the early and neural differentiations were induced. For the cGNS_{MB} imaging, the intense fluorescence of $\text{cGNS}_{\text{PDK1 MB}}$ was detected for the undifferentiated cells. On the contrary, the fluorescence of $\text{cGNS}_{\text{PGC-1}\alpha\text{ MB}}$ significantly increased by the induction of early and neural differentiations, while the $\text{cGNS}_{\text{Actb MB}}$ fluorescence was similarly observed for both the undifferentiated and differentiated cells. The fluorescence of MB showed a good accordance with the metabolic profiles of undifferentiated and differentiated cells. To our knowledge, this study is the first trial to discriminate the differentiation state of cells from the energy metabolic pathways based on the MB imaging system.

The cGNS_{MB} were efficiently internalized into the mES cells at the concentration of 10 μg/ml and the incubation time for only 1 hr to emit the sufficient fluorescence (**Figure 2**) and achieve the labeling efficiency of around 100% (**Figure 3**). The condition of cell internalization did not show any cytotoxicity. The efficient cell internalization results from the small size of 250 nm and the positive surface charge of cGNS_{MB} (**Table 4**), which is advantageous for the cell internalization [38, 39]. Importantly, the expression of pluripotent markers and the differentiation ability for three germ layers of mES cells were preserved even after the internalization of cGNS_{MB} (**Figure 4**). In addition, the proliferation of MSC did not change after the cGNS_{MB} internalization (data not shown). This might be due to the efficient internalization property of cGNS_{MB}, and the consequent mild internalization condition. In Chapters 3 and 5, as the mechanism of cell internalization, it has been demonstrated that the

$cGNS_{MB}$ were internalized into cells via an endocytotic pathway, followed by the endosomal escape into the cytosol due to the pH buffering effect of spermine [40]. The MB were intracellularly released into the cytosol accompanied with the degradation of cGNS. The release profile is readily regulated by the degradability of hydrogels, and gelatin fragments degraded showed no cytotoxicity. The MB fluorescence did not become weak over the cell division due to the high retention of MB in the cytosol, which made it possible to detect the target mRNA over 2 weeks without the digestion of nuclease. The sequence specificity of MB in the hybridization was experimentally confirmed (**Figure 1**). Taken together, it is highly conceivable that the $cGNS_{MB}$ used in this study could specifically detect the target mRNA based on the intracellular controlled release with little influence on the cell function. The low cytotoxicity, susceptibility to cell internalization, high labeling efficiency, and the easy regulation of degradability and the consequent release profile of MB, are advantageous characteristics of $cGNS_{MB}$ over other carrier materials [41-43]. The intracellular controlled release of MB enables the time-course tracing of same cells, which is quite important in the biological and medical research fields.

The PDK1 expression and the consequent phosphorylation level of PDH were significantly upregulated in the undifferentiated cells. The results well agreed with the previous papers on the energy metabolism of stem cells [44, 45]. The high expression of PDK1 and its enzymatic activity led to the phosphorylation of PDH and the inhibited activity, resulted in the limitation of metabolic flux into the OXPHOS and the maintenance of enhanced glycolysis in the undifferentiated cells (**Figures 7A** and **16A**). On the other hand, the increased expression of PGC-1α was observed for the cells induced to both early and neural differentiations. The increase of PGC-1α well corresponded to the increased OXPHOS over the differentiations (**Figures 7B** and **16B**). The PGC-1α is known to regulate the biogenesis of mitochondria to enhance the OXPHOS, and the upregulation has been reported over the differentiation of stem cells, such as osteogenic [46] and adipogenic [47] differentiations of human MSC, and the neuronal differentiation of human neural stem [48] and progenitor cells [37], which is consistent with the results in this study. It is, thus, highly possible that the PDK1 and the PGC-1α would synergistically play a key role in the regulation of balance between the glycolysis and the

OXPHOS, and it would be reasonable to select as the targets of MB.

The fluorescence of cGNS$_{\text{PDK1 MB}}$ increased as the maintenance of undifferentiated state, and significantly higher than that in the early and neural differentiations-induced cells. In contrast, the cGNS$_{\text{PGC-1}\alpha\text{ MB}}$ fluorescence gradually increased with the induction of early and neural differentiations to give the mirror images with cGNS$_{\text{PDK1 MB}}$ (**Figures 11** and **19**). The fluorescent intensity of cGNS$_{\text{PDK1 MB}}$ and cGNS$_{\text{PGC-1}\alpha\text{ MB}}$ reflected the expression levels of target mRNA (**Figures 5B** and **13C**). The fluorescence of cGNS$_{\text{Actb MB}}$ was similarly observed between undifferentiated and differentiated cells at any time point, and the fluorescent intensity was constant. In other words, cGNS$_{\text{Actb MB}}$ worked well as a reference fluorescence of cGNS$_{\text{MB}}$, although the internalization amount was varied in the differentiation state of cells (**Figure 10**). This is due to the constant expression of Actb mRNA in each cell. As the mechanism of mRNA detection, it is likely that the excessive MB over the target mRNA could be released into the cytosol from cGNS, whereas most of MB are in a quenched state. Therefore, the fluorescent signal of MB reacted with the target mRNA reflects the expression level of mRNA in individual cells, which was independent of the internalization amount of MB.

When the cGNS$_{\text{MB}}$ imaging was compared with the results of extracellular flux analyzer, the fluorescence of MB showed a good accordance with the metabolic profiles of undifferentiated and differentiated cells. Among the parameters of glycolysis and OXPHOS in both the early and neural differentiations, the ECAR of maximal glycolysis (**Figures 7A (d)** and **16A (c)**) and the OCR of maximal respiration (**Figures 7B (d)** and **16B (c)**) well corresponded to the fluorescent intensity of cGNS$_{\text{PDK1 MB}}$ (**Figures 11B (a)** and **19B (a)**) and cGNS$_{\text{PGC-1}\alpha\text{ MB}}$ (**Figures 11B (b)** and **19B (b)**), respectively. The maximal glycolysis and respiration represent the metabolically stressed and enhanced glycolysis and OXPHOS, respectively. On the other hand, the PDK1 is a critical regulator in the inhibition of metabolic flux to maintain the glycolysis, while the PGC-1α is a master regulator of mitochondrial biogenesis, which is an upstream of OXPHOS. Therefore, the change of its mRNA accompanied with the differentiation might reflect the capacity of glycolysis and OXPHOS, and the consequent values of maximal glycolysis and respiration. The difference of energy metabolic pathways, especially maximal glycolysis and respiration, would be detected by the

MB fluorescence.

The extracellular flux analyzer is a powerful tool to evaluate the cellular metabolic profiles measuring the ECAR and OCR as the indicators of glycolysis and OXPHOS [49], and the differentiation state of stem cells has been investigated based on the metabolic profiles [37, 47, 48, 50, 51]. However, the ECAR and OCR are measured as the total values to only indicate the metabolic state as a cell population. On the other hand, the advantage of $cGNS_{MB}$ imaging system is to visualize the metabolic pathways in individual cells. Based on the advantage, the multi-color imaging was performed between the undifferentiated and the neural differentiation-induced cells (**Figure 20**). It is highly conceivable that the $cGNS_{multi\ MB}$ were internalized into nearly 100% of cells because the fluorescence of Actb MB as an internal reference was detected from almost all of cells. This is experimentally supported by the labeling efficiency of around 100% (**Figure 3**). The intense fluorescence of PDK1 MB was homogenously observed in the undifferentiated cells (**Figure 20A**). The finding suggests that the metabolic state of undifferentiated cells should be relatively homogenous and the glycolysis is the main pathway. On the contrary, for the neural differentiation-induced cells, some fluorescence of PDK1 MB was observed around the intense PGC-1α MB fluorescence (**Figure 20B**). It has been conventionally recognized that there are heterogeneous cell populations after the differentiation of mES cells. Recent technologies on the RNA-sequence have revealed the dynamic heterogeneity over the differentiation in a single cell level [52]. In this study, it is possible that various cell types, such as matured neuron, neural progenitor/stem cells, and remaining undifferentiated cells, with different metabolic states would be induced. The heterogeneity of cell population would lead to the different localizations of MB fluorescence. The $cGNS_{MB}$ imaging system developed in this study might have a potential to visualize the metabolic heterogeneity in the same cell population.

It has been recognized on the heterogeneity of energy metabolism in cancer, which might be one possible reason of resistance against therapies. The energy metabolism of some cancer stem cells (CSC), *e.g.* glioma stem cells [53], breast CSC [54], and pancreatic CSC [55], is reported to be different from other cancer cells, although the weight of glycolysis and OXPHOS seems to depend on the cancer type. In the case of immune cells, including T cells [56], dendritic cells [57], and macrophages [58, 59], the energy metabolic pathways are different in its subsets and activation patterns against immune stimulations. For pluripotent stem cells, the different metabolic states between naive and primed human iPS cells [60], as well as human ES cells [61], have been reported. It is important to claim here that the decisive role of PDK1 and PGC-1α as the metabolic regulators has been recognized in these research fields. This technological universality would expand the biological and medical applications of $\mathrm{cGNS_{MB}}$ imaging system. In the future, the metabolic heterogeneity in various cell types and states would be visually discriminated by making use of the $\mathrm{cGNS_{MB}}$ imaging system to contribute to the development of basic cell research, drug discovery, and regenerative medicine.

REFERENCES

1. Warburg O. On the origin of cancer cells. *Science* 1956; **123**: 309-314.
2. Kostakoglu L, Agress H, Jr., Goldsmith SJ. Clinical role of FDG PET in evaluation of cancer patients. *Radiographics* 2003; **23**: 315-340.
3. Wolf DA. Is Reliance on Mitochondrial Respiration a "Chink in the Armor" of Therapy-Resistant Cancer? *Cancer Cell* 2014; **26**: 788-795.
4. Stacpoole PW. Therapeutic Targeting of the Pyruvate Dehydrogenase Complex/Pyruvate Dehydrogenase Kinase (PDC/PDK) Axis in Cancer. *J Natl Cancer Inst* 2017; **109**: djx071.
5. DeWaal D, Nogueira V, Terry AR, Patra KC, Jeon SM, Guzman G *et al.* Hexokinase-2 depletion inhibits glycolysis and induces oxidative phosphorylation in hepatocellular carcinoma and sensitizes to metformin. *Nat Commun* 2018; **9**: 446.
6. Folmes CD, Dzeja PP, Nelson TJ, Terzic A. Metabolic plasticity in stem cell homeostasis and differentiation. *Cell Stem Cell* 2012; **11**: 596-606.
7. Zhang J, Nuebel E, Daley GQ, Koehler CM, Teitell MA. Metabolic regulation in pluripotent stem cells during reprogramming and self-renewal. *Cell Stem Cell* 2012; **11**: 589-595.
8. Ito K, Suda T. Metabolic requirements for the maintenance of self-renewing stem cells. *Nat Rev Mol Cell Biol* 2014; **15**: 243-256.
9. Teslaa T, Teitell MA. Pluripotent stem cell energy metabolism: an update. *EMBO J* 2015; **34**: 138-153.
10. Sone M, Morone N, Nakamura T, Tanaka A, Okita K, Woltjen K *et al.* Hybrid Cellular Metabolism Coordinated by Zic3 and Esrrb Synergistically Enhances Induction of Naive Pluripotency. *Cell Metab* 2017; **25**: 1103-1117.
11. Folmes CD, Nelson TJ, Martinez-Fernandez A, Arrell DK, Lindor JZ, Dzeja PP *et al.* Somatic oxidative bioenergetics transitions into pluripotency-dependent glycolysis to facilitate nuclear reprogramming. *Cell Metab* 2011; **14**: 264-271.
12. Tormos KV, Anso E, Hamanaka RB, Eisenbart J, Joseph J, Kalyanaraman B *et al.* Mitochondrial complex III ROS regulate adipocyte differentiation. *Cell Metab* 2011; **14**:

537-544.

13. Tohyama S, Hattori F, Sano M, Hishiki T, Nagahata Y, Matsuura T *et al.* Distinct metabolic flow enables large-scale purification of mouse and human pluripotent stem cell-derived cardiomyocytes. *Cell Stem Cell* 2013; **12**: 127-137.
14. Tohyama S, Fujita J, Fujita C, Yamaguchi M, Kanaami S, Ohno R *et al.* Efficient Large-Scale 2D Culture System for Human Induced Pluripotent Stem Cells and Differentiated Cardiomyocytes. *Stem Cell Reports* 2017; **9**: 1406-1414.
15. Moriyama H, Moriyama M, Isshi H, Ishihara S, Okura H, Ichinose A *et al.* Role of notch signaling in the maintenance of human mesenchymal stem cells under hypoxic conditions. *Stem Cells Dev* 2014; **23**: 2211-2224.
16. Bukowiecki R, Adjaye J, Prigione A. Mitochondrial function in pluripotent stem cells and cellular reprogramming. *Gerontology* 2014; **60**: 174-182.
17. Golias T, Kery M, Radenkovic S, Papandreou I. Microenvironmental control of glucose metabolism in tumors by regulation of pyruvate dehydrogenase. *Int J Cancer* 2019; **144**: 674-686.
18. Mootha VK, Handschin C, Arlow D, Xie X, St Pierre J, Sihag S *et al.* Errα and Gabpa/b specify PGC-1α-dependent oxidative phosphorylation gene expression that is altered in diabetic muscle. *Proc Natl Acad Sci U S A* 2004; **101**: 6570-6575.
19. Rohas LM, St-Pierre J, Uldry M, Jager S, Handschin C, Spiegelman BM. A fundamental system of cellular energy homeostasis regulated by PGC-1α. *Proc Natl Acad Sci U S A* 2007; **104**: 7933-7938.
20. Desai HV, Voruganti IS, Jayasuriya C, Chen Q, Darling EM. Live-cell, temporal gene expression analysis of osteogenic differentiation in adipose-derived stem cells. *Tissue Eng Part A* 2014; **20**: 899-907.
21. Snyder SL, Sobocinski PZ. An improved 2,4,6-trinitrobenzenesulfonic acid method for the determination of amines. *Anal Biochem* 1975; **64**: 284-288.
22. Commerford SL. Iodination of nucleic acids in vitro. *Biochemistry* 1971; **10**: 1993-2000.
23. Niwa H, Masui S, Chambers I, Smith AG, Miyazaki J. Phenotypic complementation establishes requirements for specific POU domain and generic transactivation function

of Oct-3/4 in embryonic stem cells. *Mol Cell Biol* 2002; **22**: 1526-1536.

24. Ogawa K, Matsui H, Ohtsuka S, Niwa H. A novel mechanism for regulating clonal propagation of mouse ES cells. *Genes Cells* 2004; **9**: 471-477.
25. Izumi Y, Wakita S, Kanbara C, Nakai T, Akaike A, Kume T. Integrin α5β1 expression on dopaminergic neurons is involved in dopaminergic neurite outgrowth on striatal neurons. *Sci Rep* 2017; **7**: 42111.
26. Kurosawa H. Methods for inducing embryoid body formation: in vitro differentiation system of embryonic stem cells. *J Biosci Bioeng* 2007; **103**: 389-398.
27. Yamasaki S, Taguchi Y, Shimamoto A, Mukasa H, Tahara H, Okamoto T. Generation of human induced pluripotent stem (iPS) cells in serum- and feeder-free defined culture and TGF-β1 regulation of pluripotency. *PLoS One* 2014; **9**: e87151.
28. Niwa H, Ogawa K, Shimosato D, Adachi K. A parallel circuit of LIF signalling pathways maintains pluripotency of mouse ES cells. *Nature* 2009; **460**: 118-122.
29. Anamizu M, Tabata Y. Design of injectable hydrogels of gelatin and alginate with ferric ions for cell transplantation. *Acta Biomater* 2019; **100**: 184-190.
30. Michelakis ED, Webster L, Mackey JR. Dichloroacetate (DCA) as a potential metabolic-targeting therapy for cancer. *Br J Cancer* 2008; **99**: 989-994.
31. Rodrigues AS, Correia M, Gomes A, Pereira SL, Perestrelo T, Sousa MI *et al.* Dichloroacetate, the Pyruvate Dehydrogenase Complex and the Modulation of mESC Pluripotency. *PLoS One* 2015; **10**: e0131663.
32. Ying QL, Stavridis M, Griffiths D, Li M, Smith A. Conversion of embryonic stem cells into neuroectodermal precursors in adherent monoculture. *Nat Biotechnol* 2003; **21**: 183-186.
33. Carpi S, Fogli S, Giannetti A, Adinolfi B, Tombelli S, Da Pozzo E *et al.* Theranostic properties of a survivin-directed molecular beacon in human melanoma cells. *PLoS One* 2014; **9**: e114588.
34. Kamiya D, Banno S, Sasai N, Ohgushi M, Inomata H, Watanabe K *et al.* Intrinsic transition of embryonic stem-cell differentiation into neural progenitors. *Nature* 2011; **470**: 503-509.

35. Niwa H, Toyooka Y, Shimosato D, Strumpf D, Takahashi K, Yagi R *et al.* Interaction between Oct3/4 and Cdx2 determines trophectoderm differentiation. *Cell* 2005; **123**: 917-929.
36. Saunier E, Benelli C, Bortoli S. The pyruvate dehydrogenase complex in cancer: An old metabolic gatekeeper regulated by new pathways and pharmacological agents. *Int J Cancer* 2016; **138**: 809-817.
37. Zheng X, Boyer L, Jin M, Mertens J, Kim Y, Ma L *et al.* Metabolic reprogramming during neuronal differentiation from aerobic glycolysis to neuronal oxidative phosphorylation. *Elife* 2016; **5**: e13374.
38. Win KY, Feng SS. Effects of particle size and surface coating on cellular uptake of polymeric nanoparticles for oral delivery of anticancer drugs. *Biomaterials* 2005; **26**: 2713-2722.
39. He C, Hu Y, Yin L, Tang C, Yin C. Effects of particle size and surface charge on cellular uptake and biodistribution of polymeric nanoparticles. *Biomaterials* 2010; **31**: 3657-3666.
40. Jo J, Nagane K, Yamamoto M, Tabata Y. Effect of amine type on the expression of plasmid DNA by cationized dextran. *J Biomater Sci Polym Ed* 2010; **21**: 225-236.
41. Xue HY, Wong HL. Tailoring nanostructured solid-lipid carriers for time-controlled intracellular siRNA kinetics to sustain RNAi-mediated chemosensitization. *Biomaterials* 2011; **32**: 2662-2672.
42. Prabhakar N, Zhang J, Desai D, Casals E, Gulin-Sarfraz T, Nareoja T *et al.* Stimuli-responsive hybrid nanocarriers developed by controllable integration of hyperbranched PEI with mesoporous silica nanoparticles for sustained intracellular siRNA delivery. *Int J Nanomedicine* 2016; **11**: 6591-6608.
43. Wiraja C, Yeo DC, Chong MS, Xu C. Nanosensors for Continuous and Noninvasive Monitoring of Mesenchymal Stem Cell Osteogenic Differentiation. *Small* 2016; **12**: 1342-1350.
44. Varum S, Rodrigues AS, Moura MB, Momcilovic O, Easley CAt, Ramalho-Santos J *et al.* Energy metabolism in human pluripotent stem cells and their differentiated

counterparts. *PLoS One* 2011; **6**: e20914.

45. Prigione A, Rohwer N, Hoffmann S, Mlody B, Drews K, Bukowiecki R *et al.* HIF1α modulates cell fate reprogramming through early glycolytic shift and upregulation of PDK1-3 and PKM2. *Stem Cells* 2014; **32**: 364-376.

46. Chen CT, Shih YR, Kuo TK, Lee OK, Wei YH. Coordinated changes of mitochondrial biogenesis and antioxidant enzymes during osteogenic differentiation of human mesenchymal stem cells. *Stem Cells* 2008; **26**: 960-968.

47. Zhang Y, Marsboom G, Toth PT, Rehman J. Mitochondrial respiration regulates adipogenic differentiation of human mesenchymal stem cells. *PLoS One* 2013; **8**: e77077.

48. O'Brien LC, Keeney PM, Bennett JP, Jr. Differentiation of Human Neural Stem Cells into Motor Neurons Stimulates Mitochondrial Biogenesis and Decreases Glycolytic Flux. *Stem Cells Dev* 2015; **24**: 1984-1994.

49. Zhang J, Nuebel E, Wisidagama DR, Setoguchi K, Hong JS, Van Horn CM *et al.* Measuring energy metabolism in cultured cells, including human pluripotent stem cells and differentiated cells. *Nat Protoc* 2012; **7**: 1068-1085.

50. Cliff TS, Wu T, Boward BR, Yin A, Yin H, Glushka JN *et al.* MYC Controls Human Pluripotent Stem Cell Fate Decisions through Regulation of Metabolic Flux. *Cell Stem Cell* 2017; **21**: 502-516.

51. Hopkinson BM, Desler C, Kalisz M, Vestentoft PS, Juel Rasmussen L, Bisgaard HC. Bioenergetic Changes during Differentiation of Human Embryonic Stem Cells along the Hepatic Lineage. *Oxid Med Cell Longev* 2017; **2017**: 5080128.

52. Semrau S, Goldmann JE, Soumillon M, Mikkelsen TS, Jaenisch R, van Oudenaarden A. Dynamics of lineage commitment revealed by single-cell transcriptomics of differentiating embryonic stem cells. *Nat Commun* 2017; **8**: 1096.

53. Vlashi E, Lagadec C, Vergnes L, Matsutani T, Masui K, Poulou M *et al.* Metabolic state of glioma stem cells and nontumorigenic cells. *Proc Natl Acad Sci U S A* 2011; **108**: 16062-16067.

54. Peng F, Wang JH, Fan WJ, Meng YT, Li MM, Li TT *et al.* Glycolysis gatekeeper PDK1 reprograms breast cancer stem cells under hypoxia. *Oncogene* 2018; **37**: 1062-1074.

55. Sancho P, Burgos-Ramos E, Tavera A, Bou Kheir T, Jagust P, Schoenhals M *et al.* MYC/PGC-1α Balance Determines the Metabolic Phenotype and Plasticity of Pancreatic Cancer Stem Cells. *Cell Metab* 2015; **22**: 590-605.
56. Gerriets VA, Rathmell JC. Metabolic pathways in T cell fate and function. *Trends Immunol* 2012; **33**: 168-173.
57. Pearce EJ, Everts B. Dendritic cell metabolism. *Nat Rev Immunol* 2015; **15**: 18-29.
58. Tan Z, Xie N, Cui H, Moellering DR, Abraham E, Thannickal VJ *et al.* Pyruvate dehydrogenase kinase 1 participates in macrophage polarization via regulating glucose metabolism. *J Immunol* 2015; **194**: 6082-6089.
59. Saha S, Shalova IN, Biswas SK. Metabolic regulation of macrophage phenotype and function. *Immunol Rev* 2017; **280**: 102-111.
60. Zhang J, Ratanasirintrawoot S, Chandrasekaran S, Wu Z, Ficarro SB, Yu C *et al.* LIN28 Regulates Stem Cell Metabolism and Conversion to Primed Pluripotency. *Cell Stem Cell* 2016; **19**: 66-80.
61. Sperber H, Mathieu J, Wang Y, Ferreccio A, Hesson J, Xu Z *et al.* The metabolome regulates the epigenetic landscape during naive-to-primed human embryonic stem cell transition. *Nat Cell Biol* 2015; **17**: 1523-1535.

Chapter 7

Preparation of gelatin nanospheres incorporating quantum dots and iron oxide nanoparticles to visualize human induced pluripotent stem cells-derived three-dimensional cartilage tissue

INTRODUCTION

Recently, many studies on the three-dimensional (3D) fabrication of cells have been extensively performed and applied to wide research fields which make use of cell functions enhanced in the 3D state [1-8]. Under these circumstances, it is indispensable to develop the imaging technologies and methodologies for non-invasive visualization of 3D cells fabricated. To visualize the 3D cells fabricated, it is technically necessary to develop the labeling method as well as imaging probes. Based on the results in Chapter 1, it was demonstrated that the gelatin nanospheres (GNS) incorporating quantum dots (QD) and iron oxide nanoparticles (IONP) ($\mathrm{GNS_{QD+IONP}}$) were feasible as a multimodal imaging probe. The $\mathrm{GNS_{QD+IONP}}$ treated with octa-arginine (R8) were readily internalized into human chondrocytes, and visualized by both the fluorescent and magnetic resonance (MR) imaging modalities. QD is one of the useful imaging probes for the cellular labeling, and a lot of carrier materials of QD including the use of R8 have been reported [9-13]. However, most of the studies focused on the use of single QD. In this study, a multi-modal and multi-color imaging probe by utilizing three kinds of QD with different fluorescent wavelengths and IONP was designed. The multi-color imaging is potentially useful to visualize different intracellular targets as well as the enhancement of imaging reliability.

In this chapter, the labeling method of human induced pluripotent stem (iPS) cells-derived 3D cartilage tissue with the GNS co-incorporating three kinds of QD and IONP ($\mathrm{GNS_{3QD+IONP}}$) was developed. To label the human iPS cells-derived 3D cartilage tissue, two labeling approaches were tried. One is that the cartilage tissue was labeled directly by incubating with R8-$\mathrm{GNS_{3QD+IONP}}$ (direct labeling method). The other one is a “dissociation and labeling method”. First, the cartilage tissue was dissociated to cells in a single dispersed state. Then, the cells were incubated with R8-$\mathrm{GNS_{3QD+IONP}}$ in a monolayer culture. Finally, the cells labeled were fabricated to 3D pellets or cell sheets. The labeling efficiency was compared in terms of the fluorescent visualization. In addition, the immunohistological evaluation of cartilage tissue after the labeling with $GNS_{3QD+IONP}$ was performed to assess the cartilage properties.

EXPERIMENTAL

Materials

Gelatin with an isoelectric point of 5.0 and the weight-averaged molecular weight of 100,000, prepared by an alkaline treatment of bovine bone collagen, was kindly supplied from Nitta Gelatin Inc., Osaka, Japan. Qdot 525, 605, and 705 ITK Carboxyl Quantum Dots (QD525, 605, and 705, 8 µM in water) were purchased from Invitrogen Co., Tokyo, Japan. Alkali-treated dextran-coated magnetic iron oxide nanoparticle (IONP, 5 mg Fe/ml in water) was purchased from Meito Sangyo Co., Ltd, Nagoya, Japan. Isooctane, poly(oxyethylene) sorbitan monooleate (Tween 80), glutaraldehyde (GA, 25 wt% in water), glycine, and concentrated hydrochloric acid (HCl) were purchased from Nacalai Tesque. Inc., Kyoto, Japan. Sorbitan monooleate (Span 80) was purchased from Tokyo Chemical Industry Co., Ltd, Tokyo, Japan. R8 was purchased from Sigma-Aldrich Inc., St. Louis, MO, USA. The reagents were used without further purification.

Preparation of $GNS_{3QD+IONP}$

According to the preparation procedure described in Chapter 1, the $GNS_{3QD+IONP}$ were prepared by the conventional emulsion method. Briefly, QD525 (200 nM), QD605 (80 nM), QD705 (160 nM), and IONP (25 µg Fe/ml) were mixed with 2 ml of gelatin aqueous solution (5 mg/ml). The mixed solution was added into 40 ml of isooctane containing Tween 80 (480 mg) and Span 80 (480 mg), and then sonicated for 3 min at room temperature to obtain gelatin/isooctane emulsion. Next, 0.5 wt% GA aqueous solution (200 µl) was mixed with isooctane (40 ml) containing Tween 80 (480 mg) and Span 80 (480 mg), followed by sonication to prepare the GA/isooctane emulsion. Then, the gelatin/isooctane and GA/isooctane emulsions were mixed and sonicated for 3 min on ice, and the mixture was agitated for 3 hr at 4 °C to allow gelatin to crosslink in emulsion with GA. After that, the glycine/isooctane emulsion prepared similarly was added to block the aldehyde groups unreacted. The final reactant was centrifuged at 8,500 rpm for 60 min at 4 °C to collect the $GNS_{3QD+IONP}$. The nanospheres were washed with acetone, and then double-distilled water (DDW) by the centrifugation of 5,000 rpm for 5 min at 4 °C and 20,000 rpm for 30 min at 4 °C, respectively. Finally, the $GNS_{3QD+IONP}$ were dispersed in 1 ml of DDW.

Characterization of $GNS_{3QD+IONP}$

The apparent size and polydispersity index of $GNS_{3QD+IONP}$ resuspended in 10 mM phosphate buffered-saline solution (PBS, pH7.4) were measured by dynamic light scattering (DLS, Zetasizer Nano-ZS, Malvern Instruments Ltd., Worcestershire, UK). The zeta potential of $GNS_{3QD+IONP}$ resuspended in 10 mM phosphate buffered solution (PB, pH7.4) was measured by electrophoresis light scattering (ELS, Zetasizer Nano-ZS, Malvern Instruments Ltd., Worcestershire, UK). The amount of QD and IONP incorporated in the $GNS_{3QD+IONP}$ was measured by an atomic absorption spectrophotometer of Cd and Fe (AA-6800, Shimadzu Corp., Kyoto, Japan) after the degradation with concentrated HCl. The fluorescent intensity of $GNS_{3QD+IONP}$ was measured by a microplate reader (SpectraMax i3x, Molecular Devices Japan Co., Ltd., Tokyo, Japan). The excitation wavelength was 350 nm, and the emission wavelengths were 525, 605, and 705 nm, respectively. The experiments were independently performed three times unless otherwise mentioned.

Cell culture experiments

Cartilage tissue differentiated from human iPS cells (human iPS cells-derived cartilage tissue) was kindly supplied from Professor Tsumaki's laboratory [14]. The cartilage tissue was suspended to maintain in Dulbecco's Modified Eagle Medium (DMEM, Sigma-Aldrich Inc., St. Louis, MO, USA) supplemented with 1 vol% bovine fetal calf serum (FCS, GE healthcare Life Sciences Hyclone laboratories inc., Logan, UT, USA), 1 vol% insulin, transferrin, selenium, and ethanolamine solution (ITS-X, Thermo Fisher Scientific Inc., Waltham, MA, USA), 1 mM sodium pyruvate (Thermo Fisher Scientific Inc., Waltham, MA, USA), 0.1 mM non-essential amino acid (NEAA, Thermo Fisher Scientific Inc., Waltham, MA, USA), 5 mg/ml L-ascorbic acid phosphate (FUJIFILM Wako Pure Chemical Inc., Osaka, Japan), 10 ng/ml bone morphogenic protein-2 (BMP-2, PeproTech Inc., Rocky Hill, NJ, USA), 10 ng/ml transforming growth factor-β1 (TGF-β1, PeproTech Inc., Rocky Hill, NJ, USA), 10 ng/ml growth differentiation factor-5 (GDF-5, ProSpec, Ness Ziona, Israel), and 1 vol% penicillin/streptomycin (Nacalai Tesque. Inc., Kyoto, Japan) at 37 °C in a 5% CO_2-95% air atmospheric condition.

Direct labeling of human iPS cells-derived cartilage tissue with $GNS_{3QD+IONP}$

The human iPS cells-derived cartilage tissue was directly labeled with $GNS_{3QD+IONP}$. In brief, $GNS_{3QD+IONP}$ were mixed with R8 in OPTI MEM (Thermo Fisher Scientific Inc., Waltham, MA, USA) for 15 min at room temperature (R8-$GNS_{3QD+IONP}$). The cartilage tissue was transferred to a 15 ml centrifuge tube (Greiner Bio-One International GmbH, Kremsmünster, Austria), and incubated with R8-$GNS_{3QD+IONP}$ (final concentrations of R8 and averaged QD were 8 μM and 8 nM, respectively) in OPTI MEM for 3 hr. After that, the cartilage tissue was washed with PBS, and the fluorescent images were taken by LAS-4000 (FUJIFILM Co., Tokyo, Japan), with UV light (365 nm) excitation and 515 nm filter (QD525), 605 nm filter (QD605), and 670 nm filter (QD705). The labeled cartilage tissue was gradually fixed with 4 vol% paraformaldehyde, and 15 and 30 wt% sucrose. After the fixation, the tissue was embedded in Tissue-Tek OCT compound (Sakura Finetek Inc., Tokyo, Japan), followed by freezing in liquid nitrogen. The cryosection was prepared by Cryostat (Leica CM3030S, Leica Biosystems Ltd., Germany) and observed by confocal laser microscopy FV1000-D IX81 (OLYMPUS Co., Ltd., Tokyo, Japan).

Dissociation and labeling of human iPS cells-derived cartilage tissue with $GNS_{3QD+IONP}$

The human iPS cells-derived cartilage tissue was completely dissociated to cells in the single dispersed state [15], and the monolayerd cells were labeled with $GNS_{3QD+IONP}$ as described in Chapter 1. Briefly, the cartilage tissue was incubated with 0.25 wt% trypsin-containing 1 mM ethylenediaminetetra acetic acid (EDTA) solution (Nacalai Tesque. Inc., Kyoto, Japan) for 1 hr, and then washed with PBS. Collagenase D solution (4 mg/ml) (Roche Diagnostics, Indianapolis, IN, USA) was added, and incubated for 3 hr. After the incubation, the cartilage tissue was dissociated by pipetting to obtain the chondrocytes suspension.

The chondrocytes were seeded on each well of 6 well multi-dish culture plate (Corning Inc., Corning, NY, USA) at a density of 1×10^5 cells/well, and cultured for 24 hr. The medium was changed to OPTI MEM, and the R8-$GNS_{3QD+IONP}$ (8 μM R8 and 8 nM QD) were added to each well. After the incubation for 3 hr, the cells were washed with PBS and observed by the confocal laser microscopy. The percentage of labeled cells was evaluated by the flow cytometry analysis (FACSCant II, Becton Dickinson and Company, Franklin Lakes, NJ, USA).

Fabrication of 3D cartilage pellets after the dissociation and labeling with $GNS_{3QD+IONP}$

The chondrocytes labeled were detached by the trypsinization, and 3×10^5 cells were resuspended in the 15 ml centrifuge tube. After the centrifugation at 1,000 rpm for 5 min, the cell pellet was cultured for 1, 2, 3, and 4 weeks to fabricate the 3D cartilage pellet. The fluorescent images were taken and the cryosection prepared as described above was observed by the confocal laser microscopy.

Fabrication of cell sheets after the dissociation and labeling with $GNS_{3QD+IONP}$

The chondrocytes dissociated from the cartilage tissue were seeded on each well of 24 well multi-dish culture plate (Corning Inc., Corning, NY, USA) at a density of 1×10^5 cells/well, and cultured for 24 hr. The cells were incubated with R8-$GNS_{3QD+IONP}$ at the same procedure described above, and cultured for 1 week to fabricate the cell sheet. The cell sheet was detached by the pipetting and collected by Cell Shifter^{TM} (CellSeed Inc., Tokyo, Japan) according to the manufacture’s instruction. The fluorescent images were taken and the cryosection prepared as described above was observed by the confocal laser microscopy similarly.

Histological analysis

To immunohistologically evaluate the 3D pellets and 2D sheets, the original human iPS cells-derived cartilage tissue, the 3D cartilage pellet (4 weeks after the labeling with $GNS_{3QD+IONP}$), and the cell sheet (1 week after the labeling with $GNS_{3QD+IONP}$) were stained with the conventional hematoxylin and eosin (HE), alcian blue, and saflanin O / fast green. The expression of collagen types I and II was evaluated by the immunohistochemical staining. In brief, the sections were treated with 0.3 vol% hydrogen peroxide in methanol solution, and blocked with 1 wt% bovine serum albumin in PBS for 30 min. Then, primary antibodies (1:20, goat anti-collagen type I and type II, SouthernBiotech, Birmingham, AL, USA) were incubated overnight at 4 °C. Following the incubation, the samples were treated with peroxidase-conjugated secondary antibody (Simple Stain^{TM} MAX PO (G), Nichirei Biosciences Inc., Tokyo, Japan). The immunoreactions were visualized by 3,3'-diaminobenzidine (DAB) substrate in chromogen solution (Agilent Technologies Inc., Santa Clara, CA, USA). The samples were counter stained with hematoxylin, and observed by a microscope (BZ-X700, KEYENCE Co., Ltd., Osaka, Japan).

RESULTS

Physicochemical and fluorescent properties of $GNS_{3QD+IONP}$

Table 1 shows the physicochemical properties of $GNS_{3QD+IONP}$. The apparent size was around 200 nm, and the zeta potential was of a negative charge. The percentage of averaged QD incorporation was around 60%. On the other hand, the fluorescent efficiency of $GNS_{3QD+IONP}$ at each wavelength was lower than the percentage of QD incorporated (**Table 2**).

Table 1. Physicochemical properties of $GNS_{3QD+IONP}$.

Apparent size (nm)	221.8 ± 9.93 [a)]
Polydispersity index	0.220 ± 0.02
Zeta potential (mV)	-12.4 ± 1.17
Averaged QD percent incorporated	61.5 ± 7.07
Averaged amount of QD incorporated (nmole/mg GNS)	0.71 ± 0.15
IONP percent incorporated	52.0 ± 7.05
Amount of IONP incorporated (Fe-µg/mg GNS)	67.3 ± 8.34

a) Average ± standard deviation.

Table 2. Fluorescent properties of GNS$_{3QD+IONP}$.

Fluorescent efficiency [a)] (525 nm)	11.7 ± 3.00 [b)]
Fluorescent efficiency (605 nm)	16.9 ± 2.75
Fluorescent efficiency (705 nm)	35.2 ± 1.95

a) Percentage of fluorescent intensity relative to QD aqueous solution (200 nM QD525, 80 nM QD605, and 160 nM QD705).
b) Average ± standard deviation.

Direct labeling of human iPS cells-derived cartilage tissue with GNS$_{3QD+IONP}$

The human iPS cells-derived cartilage tissue was tried to label directly with GNS$_{3QD+IONP}$ (direct labeling method). **Figure 1A** shows the fluorescent images of cartilage tissue co-incubated with R8-GNS$_{3QD+IONP}$. Fluorescence was hardly observed for any QD. **Figure 1B** shows the confocal microscopic images of cryosectional cartilage tissue. The fluorescence of cells was detected only at the surrounding site of cartilage tissue.

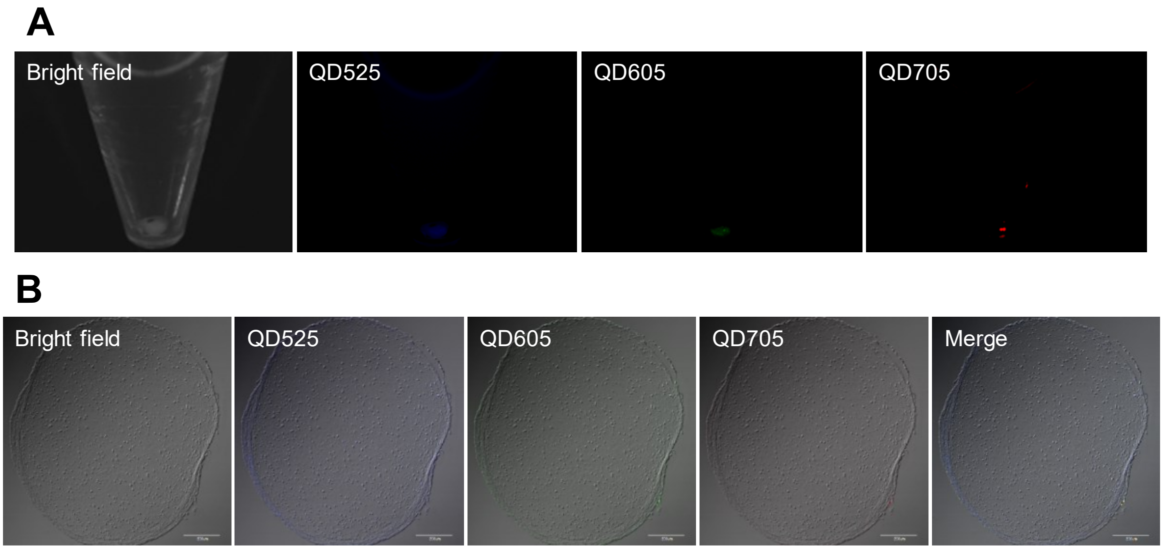

Figure 1. Direct labeling of human iPS cells-derived cartilage tissue with GNS$_{3QD+IONP}$. Fluorescent images of cartilage tissue in 15 ml centrifuge tube incubated with R8-GNS$_{3QD+IONP}$ (A). Confocal microscopic images of cryosectional cartilage tissue (B). Scale bar is 200 μm. The experiments are performed at least three times to confirm the reproducibility, and the representative images are shown.

Dissociation and labeling of human iPS cells-derived cartilage tissue with GNS$_{\mathrm{3QD+IONP}}$

The cartilage tissue was dissociated and the cells of a single state were labeled with GNS$_{\mathrm{3QD+IONP}}$ in the monolayer culture (dissociation and labeling method). The GNS$_{\mathrm{3QD+IONP}}$ were efficiently internalized into the monolayer cells and the fluorescence was observed (**Figure 2A**). **Figure 2B** shows the flow cytometric analysis after the incubation with R8-GNS$_{\mathrm{3QD+IONP}}$ in the monolayer culture. Almost 100% cells were fluorescently positive for QD605 and QD705, whereas around 40% cells were positive for QD525.

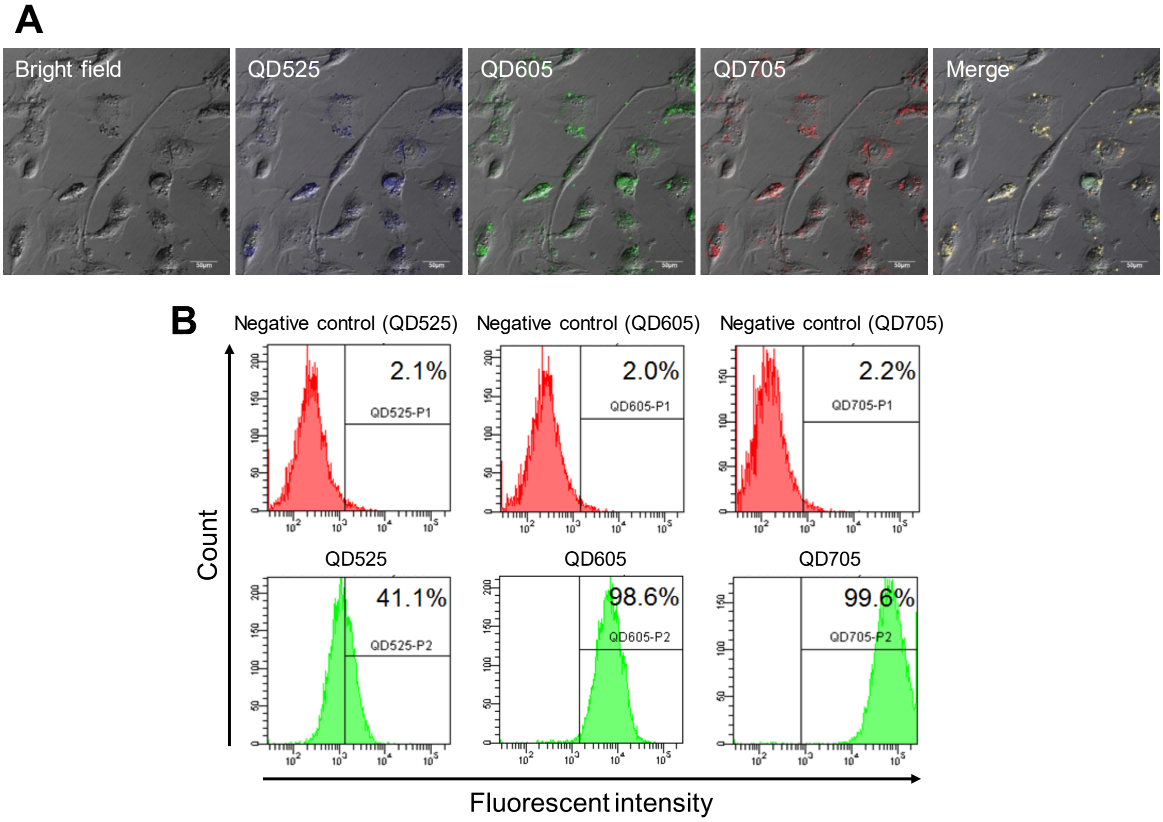

Figure 2. Labeling after dissociation of human iPS cells-derived cartilage tissue with GNS$_{\mathrm{3QD+IONP}}$. Confocal microscopic images of monolayer cells incubated with R8-GNS$_{\mathrm{3QD+IONP}}$ (A). Scale bar is 50 µm. Flow cytometric histograms of cells incubated with or without GNS$_{\mathrm{3QD+IONP}}$ (negative control) and the percentage of fluorescent positive cells (B). The experiments are performed at least three times to confirm the reproducibility, and the representative images are shown.

Fabrication of 3D cartilage pellets and cell sheets

The labeled cells with GNS$_{3QD+IONP}$ were cultured in a pellet state to fabricate the 3D cartilage pellets, and the 3D pellets were fluorescently visualized (**Figure 3A**). The fluorescence of GNS$_{3QD+IONP}$ was homogenously observed in the pellet cryosection (**Figure 3B**). **Figure 4** shows the fluorescent time course of pellets labeled with GNS$_{3QD+IONP}$. All the fluorescence of pellet (QD525, 605, and 705) could be detected even 4 weeks later. **Figure 5** shows the fluorescent observation of cell sheets labeled with GNS$_{3QD+IONP}$. The cells of sheet were fluorescently visualized for all wavelength of QD.

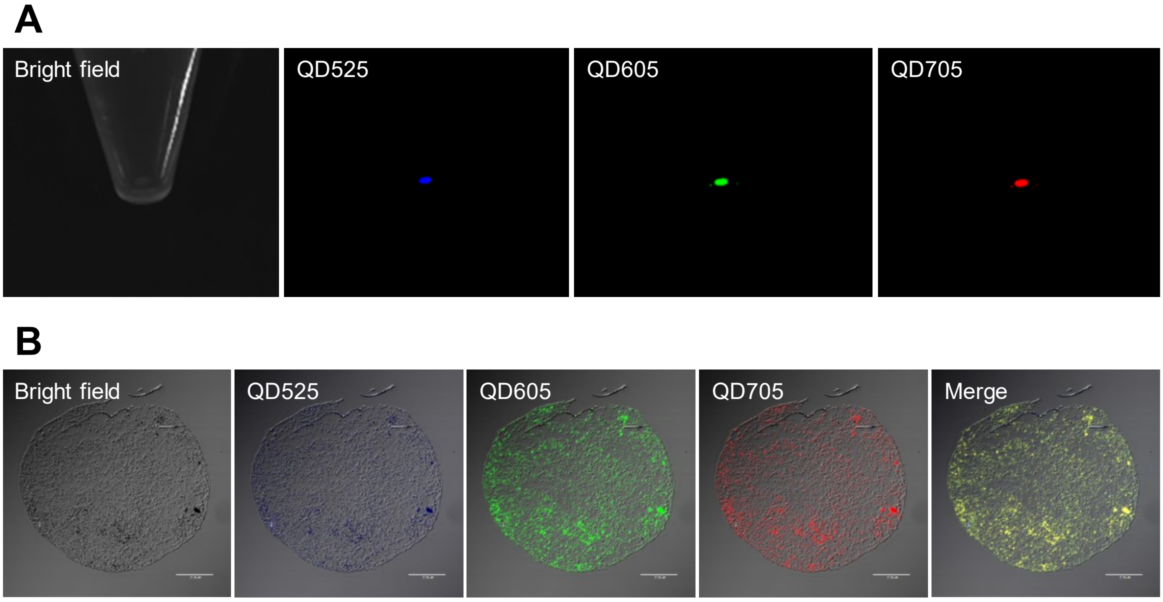

Figure 3. Fabrication of 3D cartilage pellet from cells labeled with GNS$_{3QD+IONP}$. Fluorescent images of cartilage pellet in 15 ml centrifuge tube (A). Confocal microscopic images of cryosectional cartilage pellet (B). Scale bar is 200 µm. The experiments are performed at least three times to confirm the reproducibility, and the representative images are shown.

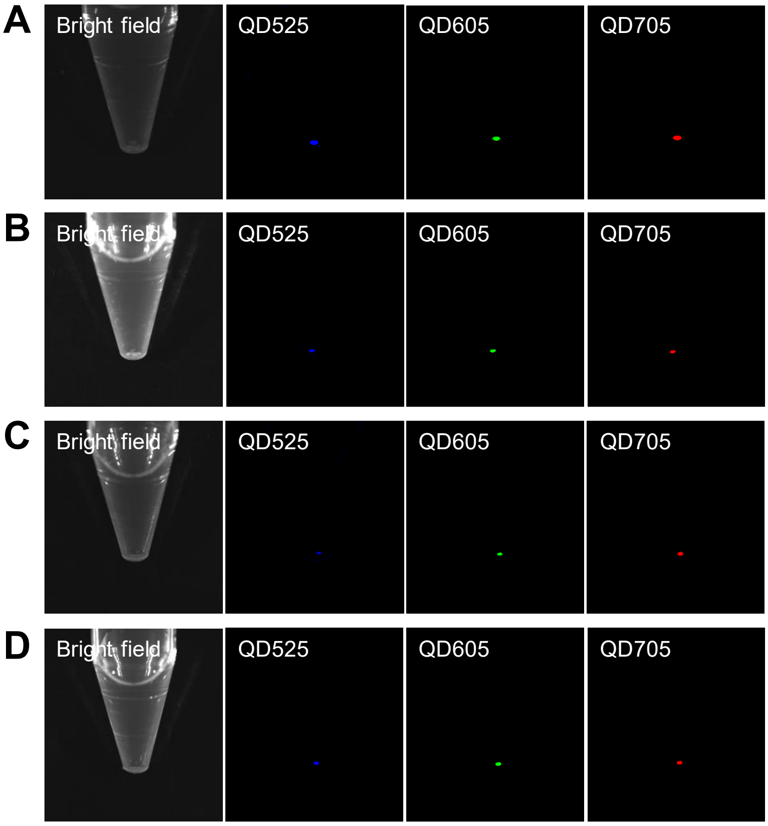

Figure 4. Fluorescent time course of 3D cartilage pellet from cells labeled with GNS$_{3QD+IONP}$. Fluorescent images of cartilage pellet prepared 1 (A), 2 (B), 3 (C), and 4 weeks after incubation (D). The experiments are performed at least three times to confirm the reproducibility, and the representative images are shown.

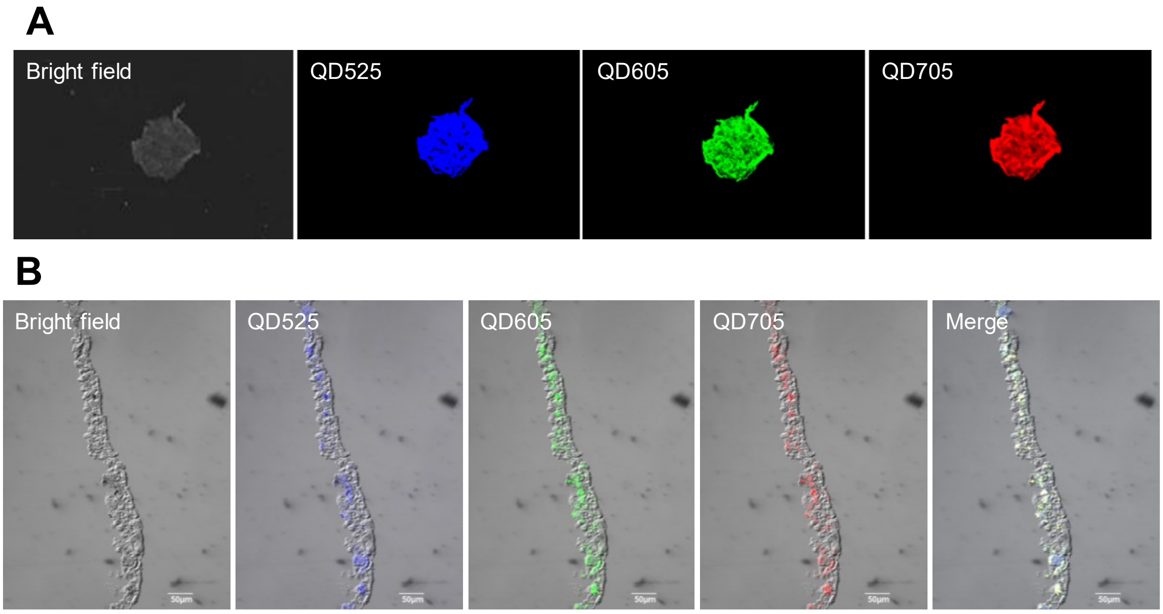

Figure 5. Fluorescent images of cell sheet prepared 1 week after incubation with R8-GNS$_{3QD+IONP}$ (A). Confocal microscopic images of cryosectional cell sheet (B). Scale bar is 50 μm. The experiments are performed at least three times to confirm the reproducibility, and the representative images are shown.

Histological analysis

The histological analysis was performed for the original cartilage tissue (**Figure 6A**), the cartilage pellet 4 weeks after label with $GNS_{3QD+IONP}$ (**Figure 6B**), and the cell sheet 1 week after the label with $GNS_{3QD+IONP}$ (**Figure 6C**). Both the pellet and sheet of cells labeled with $GNS_{3QD+IONP}$ were stained with the cartilage specific staining (alcian blue, safranin O / fast green, collagen type I, and II) to a similar extent as the original cartilage tissue.

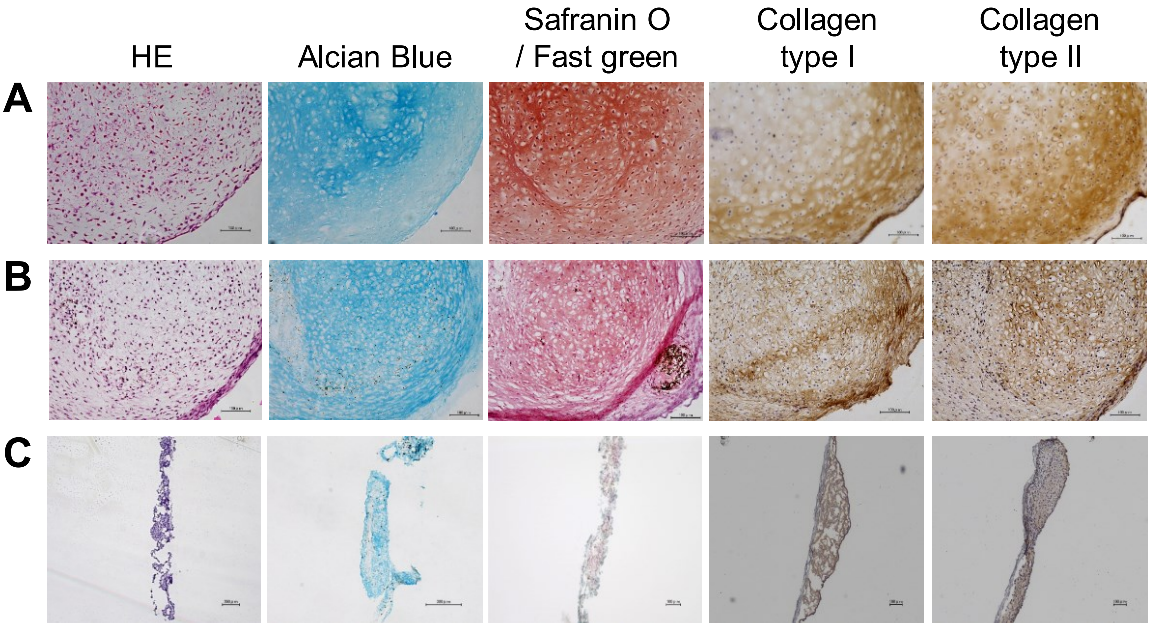

Figure 6. Histological analysis for the original cartilage tissue (A), cartilage pellet prepared 4 weeks after incubation with R8-$GNS_{3QD+IONP}$ (B), and cell sheet prepared 1 week after incubation with R8-$GNS_{3QD+IONP}$ (C). Scale bars are 100 µm (A, B, and C for the staining of safranin O / fast green and collagen type I and II) and 300 µm (C for the staining of HE and alcian blue). The experiments are performed at least three times to confirm the reproducibility, and the representative images are shown.

DISCUSSION

The present study demonstrates that the $GNS_{3QD+IONP}$ were prepared to visualize cells in the 3D formation. The human iPS cells-derived 3D cartilage tissue was directly incubated with R8-treated $GNS_{3QD+IONP}$ (direct labeling method). However, in this case, only cells residing in the surrounding site of cartilage tissue were labeled. On the other hand, the 3D cartilage pellet and the cell sheet prepared by the "dissociation and labeling method" were homogenously and fluorescently labeled. Both the pellet and the sheet of cells labeled with $GNS_{3QD+IONP}$ were cartilage-specifically stained to the similar extent as the original cartilage tissue.

The apparent size of $GNS_{3QD+IONP}$ was around 200 nm, and this small size is advantageous for the cell internalization [16]. On the other hand, the zeta potential of $GNS_{3QD+IONP}$ was negative charge. R8 is one of common cell-penetrating peptides (CPP) to enhance the cell internalization via an endocytotic pathway [17]. The electrostatic interaction between the negative charge of $GNS_{3QD+IONP}$ and the positive charge of R8 would permit the surface modification of $GNS_{3QD+IONP}$. This modification may also be advantageous for the cell internalization due to the easy interaction with the negative charge of cell membrane [18]. Although the percentage of averaged QD incorporation was around 60% (**Table 1**), the fluorescent efficiency of $GNS_{3QD+IONP}$ at each wavelength was lower than the percentage of QD incorporated (**Table 2**). The reason why the fluorescent intensity decreased relative to the QD aqueous solution is not clear at present. It is highly conceivable that the fluorescence of QD interacts with IONP, and the interaction may increase in the hydrogel of GNS in the concentrated state.

By the direct labeling method, only cells present in the surrounding site of human iPS cells-derived 3D cartilage tissue were labeled (**Figure 1**). This is due to the poor penetration of $GNS_{3QD+IONP}$ to the interior of tissue. In general, it is known that the natural cartilage tissue is surrounded by extracellular matrix (ECM) to maintain the mechanical structures [19]. The human iPS cells-derived cartilage tissue used in this study also has rich ECM. It is possible that the ECM presence of cartilage tissue prevents $GNS_{3QD+IONP}$ from the penetration into the inside of tissue.

As one trial to label the cartilage tissue homogenously, the “dissociation and labeling method” was performed. The cartilage tissue was enzymatically dissociated to cells of a single state due to the ECM degradation by the trypsin and collagenase treatments [15]. Then, the R8-$GNS_{3QD+IONP}$ were efficiently internalized into the monolayer cells dissociated from the cartilage tissue (**Figure 2A**). In the previous studies, under the QD concentration of 8 nM, QD neither showed the cytotoxicity and affected the cell proliferation [20]. In addition, the 8 μM R8-treated GNS did not show the cytotoxicity, either (Chapter 1). Therefore, it is highly conceivable that the labeling condition used in this study has no cytotoxicity. The fluorescence of all QD was well co-localized in the cells. Although the fluorescence of QD was observed from the cytosol (**Figure 2A**), the detail localization is not clear at present. However, it has been reported that the liposomes modified with R8 had an ability for endosomal escape [17]. It is likely that the R8-$\mathrm{GNS}_{\mathrm{3QD+IONP}}$ were internalized into the cells via an endocytotic pathway, followed by their endosomal escape into the cytosol. On the other hand, the flow cytometric assay revealed that almost 100% cells were fluorescently positive for QD605 and QD705, while around 40% cells were positive for QD525 (**Figure 2B**). The difference might be due to the weak fluorescence of QD525 (**Table 2**). The poor incorporation in the GNS and the weak fluorescence of QD525 might lead to the low detection level of flow cytometry. However, it is important to claim here that the 3D cartilage pellet fabricated after the labeling with $\mathrm{GNS}_{\mathrm{3QD+IONP}}$ was fluorescently visualized for all wavelength of QD (**Figure 3A**). In addition, the homogenous fluorescence of $\mathrm{GNS}_{\mathrm{3QD+IONP}}$ from the 3D cartilage pellet was observed (**Figure 3B**). The homogenous labeling should be lead to the retention of fluorescence even 4 weeks later (**Figure 4**). Another advantage of the “dissociation and labeling method” is the versatility to fabricate various structures of cells after the labeling. In this study, in addition to the 3D cartilage pellet, the cell sheet was fabricated after the labeling. The cell sheet was fluorescently visualized for all wavelength of QD (**Figure 5A**), while it was homogenously labeled as well (**Figure 5B**). **Figure 6** shows the histological evaluation for the pellet and the sheet of cells labeled with $\mathrm{GNS}_{\mathrm{3QD+IONP}}$. Both of 3D cartilage pellets and sheets were cartilage-specifically stained. The alcian blue and safranin O / fast green stainings revealed the glycosaminoglycans in the cartilage ECM. In addition, both the collagen types I and II in the cartilage ECM were stained, while no homogenous staining was observed. Although it is further necessary to quantitatively evaluate the expression of cartilage markers, the results indicate that the cartilage properties were maintained even after the process of dissociation and labeling.

It is well recognized that the homogenous labeling of cells in the 3D fabricate is sometimes difficult due to the poor penetration of imaging probes into the cell fabricates [21, 22]. Therefore, some researches on the construction of 3D structure of cells, such as neurosphere [23], embryoid body (EB) [24], and spheroid of mesenchymal stem cells (MSC) [25], after the cellular labeling in a monolayer culture, have been reported. The 3D cells fabricated after the labeling could be visualized for several weeks after the transplantation *in vivo*. However, those often focus on the cellular labeling with a single imaging probe. In this study, a multimodal imaging probe of gelatin nanospheres co-incorporating three kinds of QD and IOPN was designed. The multimodal imaging is one of the promising approaches to enhance the reliability of visualization by compensating the disadvantages of each imaging modality [26-29]. The multimodal imaging probe, such as liposomes [30], poly(lactic-co-glycolic acid) (PLGA) nanoparticles [31], and other polymeric nanoparticles [32] co-incorporating QD and IONP, have been reported. In addition to the use of single QD and IONP, in this study, three kinds of QD were used to perform the multi-color imaging. One of the advantages for multi-color imaging is to visualize different intracellular targets by one single probe. On the other hand, functionalized QD which changes the fluorescent signal based on the fluorescence resonance energy transfer (FRET) responding to the intracellular environment, have been investigated [33]. Combination with the functionalized QD may allow the imaging system of $\mathrm{GNS}_{\mathrm{3QD+IONP}}$ to visualize an intracellular environmental change more pleiotropically.

Since the self-repairing and regeneration abilities of cartilages are poor, the cell transplantation therapy is one of the promising approaches for cartilage injuries [34, 35]. Some researches using animal models demonstrated that therapeutic potential of human iPS cells-derived 3D cartilage tissue [14, 15]. The labeling technology developed in this study may be a powerful tool to evaluate the localization and distribution of cartilage tissues transplanted. In the future, the labeled cartilage tissue with $\mathrm{GNS}_{\mathrm{3QD+IONP}}$ will be transplanted to an animal model, and the fluorescent and MR imaging should be performed to evaluate the *in vivo* efficacy.

REFERENCES

1. Zanoni M, Piccinini F, Arienti C, Zamagni A, Santi S, Polico R *et al.* 3D tumor spheroid models for in vitro therapeutic screening: a systematic approach to enhance the biological relevance of data obtained. *Sci Rep* 2016; **6**: 19103.
2. Fang Y, Eglen RM. Three-Dimensional Cell Cultures in Drug Discovery and Development. *SLAS Discov* 2017; **22**: 456-472.
3. Petrenko Y, Sykova E, Kubinova S. The therapeutic potential of three-dimensional multipotent mesenchymal stromal cell spheroids. *Stem Cell Res Ther* 2017; **8**: 94.
4. Drost J, Clevers H. Organoids in cancer research. *Nat Rev Cancer* 2018; **18**: 407-418.
5. Lee SH, Hu W, Matulay JT, Silva MV, Owczarek TB, Kim K *et al.* Tumor Evolution and Drug Response in Patient-Derived Organoid Models of Bladder Cancer. *Cell* 2018; **173**: 515-528.
6. Ong CS, Zhou X, Han J, Huang CY, Nashed A, Khatri S *et al.* In vivo therapeutic applications of cell spheroids. *Biotechnol Adv* 2018; **36**: 494-505.
7. Ronaldson-Bouchard K, Vunjak-Novakovic G. Organs-on-a-Chip: A Fast Track for Engineered Human Tissues in Drug Development. *Cell Stem Cell* 2018; **22**: 310-324.
8. Antunes J, Gaspar VM, Ferreira L, Monteiro M, Henrique R, Jeronimo C *et al.* In-air production of 3D co-culture tumor spheroid hydrogels for expedited drug screening. *Acta Biomater* 2019; **94**: 392-409.
9. Fan YY, Liu HL, Han RC, Huang L, Shi H, Sha YL *et al.* Extremely High Brightness from Polymer-Encapsulated Quantum Dots for Two-photon Cellular and Deep-tissue Imaging. *Sci Rep* 2015; **5**: 9908.
10. Li ZS, Xu W, Wang YT, Shah BR, Zhang CL, Chen YJ *et al.* Quantum dots loaded nanogels for low cytotoxicity, pH-sensitive fluorescence, cell imaging and drug delivery. *Carbohyd Polym* 2015; **121**: 477-485.
11. Aizik G, Waiskopf N, Agbaria M, Levi-Kalisrnan Y, Banin U, Golomb G. Delivery of Liposomal Quantum Dots via Monocytes for Imaging of Inflamed Tissue. *Acs Nano* 2017; **11**: 3038-3051.
12. Okumura H, Nanizawa E, Nakanishi A, Yukawa H, Hashita T, Iwao T *et al.* Effective

Transplantation of 2D and 3D Cultured Hepatocyte Spheroids Confirmed by Quantum Dot Imaging. *Adv Biosys* 2018; **2**: 1800137.

13. Aizik G, Waiskopf N, Agbaria M, Ben-David-Naim M, Nordling-David MM, Jbara-Agbaria D *et al.* Targeting and imaging of monocyte-derived macrophages in rat's injured artery following local delivery of liposomal quantum dots. *J Control Release* 2020; **318**: 145-157.
14. Yamashita A, Morioka M, Yahara Y, Okada M, Kobayashi T, Kuriyama S *et al.* Generation of scaffoldless hyaline cartilaginous tissue from human iPSCs. *Stem Cell Reports* 2015; **4**: 404-418.
15. Kimura T, Yamashita A, Ozono K, Tsumaki N. Limited Immunogenicity of Human Induced Pluripotent Stem Cell-Derived Cartilages. *Tissue Eng Part A* 2016; **22**: 1367-1375.
16. He C, Hu Y, Yin L, Tang C, Yin C. Effects of particle size and surface charge on cellular uptake and biodistribution of polymeric nanoparticles. *Biomaterials* 2010; **31**: 3657-3666.
17. Khalil IA, Kimura S, Sato Y, Harashima H. Synergism between a cell penetrating peptide and a pH-sensitive cationic lipid in efficient gene delivery based on double-coated nanoparticles. *J Control Release* 2018; **275**: 107-116.
18. Frohlich E. The role of surface charge in cellular uptake and cytotoxicity of medical nanoparticles. *Int J Nanomedicine* 2012; **7**: 5577-5591.
19. Tsumaki N, Okada M, Yamashita A. iPS cell technologies and cartilage regeneration. *Bone* 2015; **70**: 48-54.
20. Yukawa H, Kagami Y, Watanabe M, Oishi K, Miyamoto Y, Okamoto Y *et al.* Quantum dots labeling using octa-arginine peptides for imaging of adipose tissue-derived stem cells. *Biomaterials* 2010; **31**: 4094-4103.
21. Ma HL, Jiang Q, Han S, Wu Y, Cui Tomshine J, Wang D *et al.* Multicellular tumor spheroids as an in vivo-like tumor model for three-dimensional imaging of chemotherapeutic and nano material cellular penetration. *Mol Imaging* 2012; **11**: 487-498.

22. Jarockyte G, Dapkute D, Karabanovas V, Daugmaudis JV, Ivanauskas F, Rotomskis R. 3D cellular spheroids as tools for understanding carboxylated quantum dot behavior in tumors. *Biochim Biophys Acta Gen Subj* 2018; **1862**: 914-923.

23. Chen CC, Ku MC, D MJ, Lai JS, Hueng DY, Chang C. Simple SPION incubation as an efficient intracellular labeling method for tracking neural progenitor cells using MRI. *PLoS One* 2013; **8**: e56125.

24. Du V, Luciani N, Richard S, Mary G, Gay C, Mazuel F *et al.* A 3D magnetic tissue stretcher for remote mechanical control of embryonic stem cell differentiation. *Nat Commun* 2017; **8**: 400.

25. Mazza M, Lozano N, Vieira DB, Buggio M, Kielty C, Kostarelos K. Liposome-Indocyanine Green Nanoprobes for Optical Labeling and Tracking of Human Mesenchymal Stem Cells Post-Transplantation In Vivo. *Adv Healthc Mater* 2017; **6**: 1700374.

26. Louie A. Multimodality imaging probes: design and challenges. *Chem Rev* 2010; **110**: 3146-3195.

27. Lee DE, Koo H, Sun IC, Ryu JH, Kim K, Kwon IC. Multifunctional nanoparticles for multimodal imaging and theragnosis. *Chem Soc Rev* 2012; **41**: 2656-2672.

28. Mitra RN, Doshi M, Zhang X, Tyus JC, Bengtsson N, Fletcher S *et al.* An activatable multimodal/multifunctional nanoprobe for direct imaging of intracellular drug delivery. *Biomaterials* 2012; **33**: 1500-1508.

29. Li X, Zhang XN, Li XD, Chang J. Multimodality imaging in nanomedicine and nanotheranostics. *Cancer Biol Med* 2016; **13**: 339-348.

30. Xu HL, Yang JJ, ZhuGe DL, Lin MT, Zhu QY, Jin BH *et al.* Glioma-Targeted Delivery of a Theranostic Liposome Integrated with Quantum Dots, Superparamagnetic Iron Oxide, and Cilengitide for Dual-Imaging Guiding Cancer Surgery. *Adv Healthc Mater* 2018; **7**: e1701130.

31. Ye F, Barrefelt A, Asem H, Abedi-Valugerdi M, El-Serafi I, Saghafian M *et al.* Biodegradable polymeric vesicles containing magnetic nanoparticles, quantum dots and anticancer drugs for drug delivery and imaging. *Biomaterials* 2014; **35**: 3885-3894.

32. Wen X, Wang Y, Zhang F, Zhang X, Lu L, Shuai X *et al.* In vivo monitoring of neural stem cells after transplantation in acute cerebral infarction with dual-modal MR imaging and optical imaging. *Biomaterials* 2014; **35**: 4627-4635.

33. Mattera L, Bhuckory S, Wegner KD, Qiu X, Agnese F, Lincheneau C *et al.* Compact quantum dot-antibody conjugates for FRET immunoassays with subnanomolar detection limits. *Nanoscale* 2016; **8**: 11275-11283.

34. Newman AP. Articular cartilage repair. *Am J Sports Med* 1998; **26**: 309-324.

35. Yanaga H, Yanaga K, Imai K, Koga M, Soejima C, Ohmori K. Clinical application of cultured autologous human auricular chondrocytes with autologous serum for craniofacial or nasal augmentation and repair. *Plast Reconstr Surg* 2006; **117**: 2019-2030.

Chapter 8

Preparation of cationized gelatin nanospheres incorporating molecular beacon to visualize apoptosis in three-dimensional cell aggregates

INTRODUCTION

It has been recognized that cells improve their biological functions in a three-dimensional (3D) state compared with a two-dimensional (2D) state cultured in the conventional cell culture dish or plate. In the 3D environments of cells like living bodies, the biochemical and mechanical signals are upregulated due to the increased cell-cell and cell-extracellular matrix (ECM) contacts [1, 2]. Therefore, a variety of 3D cells fabricates have been extensively studied to allow the cell functions to enhance *in vitro*. For example, aggregates or spheroids of mesenchymal stem cells (MSC) which are one of 3D multi-cellular structures, enhance the therapeutic potential by improving the anti-inflammatory and angiogenic properties, stemness, and survival after transplantation *in vivo* [3-7]. However, at present, it is technically difficult to evaluate the cell functions in living 3D cell aggregates. As the conventional assays, biochemical and histological techniques have been widely utilized to evaluate the functions of cell aggregates, while the destruction or fixation are required. The destruction and fixation of cell aggregates result in the loss of information on the position and time-course change of cell functions in the 3D structure. Under these circumstances, it is of prime importance to develop the imaging technology to visualize cell functions in the 3D cell aggregates without the destruction of aggregates. The cell apoptosis is one of fundamental cell functions to be visualized. For the cell transplantation therapy in regenerative medicine, the prevention of cell apoptosis and the enhancement of cell survival *in vivo* are the keys to improve the therapeutic efficiency [8]. In addition, the visualization of cell apoptosis in the 3D cell aggregates, spheroids, and organoids, would contribute to their quality control *in vitro* in the use of drug screening [9], disease modeling [10], and cell transplantation therapy [11].

In Chapter 5, it was demonstrated that the cell apoptosis can be visualized by making use of cationized gelatin nanospheres (cGNS) incorporating molecular beacons (MB) in a 2D culture condition. In addition, Chapter 7 demonstrated that the cells labeled with gelatin nanospheres incorporating imaging probes in the 2D culture, can be fabricated into the 3D structure. The 3D cells fabricated were homogenously labeled with the imaging probes. Based on the findings, it is expected that the 3D cell aggregates are prepared from the cells labeled with $\mathrm{cGNS_{MB}}$ in the 2D culture, and the apoptosis in aggregates could be detected by the MB fluorescence.

In this chapter, a $\mathrm{cGNS_{MB}}$ imaging system to visualize apoptosis in 3D cell aggregates was developed. Two types of MB for messenger RNA (mRNA) were used: caspase-3 MB of a target for apoptosis and glyceraldehyde-3-phosphate dehydrogenase (GAPDH) MB as a control of stable fluorescence in cells. The cGNS incorporating caspase-3 and GAPDH MB ($\mathrm{cGNS_{casp3\ MB}}$ and $\mathrm{cGNS_{GAP\ MB}}$, respectively) were prepared. In addition to the single type of MB, cGNS co-incorporating caspase-3 and GAPDH MB ($\mathrm{cGNS_{dual\ MB}}$) were prepared to perform the dual-color imaging for the same aggregate. The $\mathrm{cGNS_{MB}}$ were incubated with KUM6 cells of a mouse bone marrow-derived MSC line to allow cells to label with MB in the 2D culture. Then, the cell apoptosis was induced by an anti-Fas antibody to agonistically stimulate the Fas receptor, so-called "death receptor" [12]. The fluorescent intensity of MB in response to the Fas-mediated apoptosis was evaluated in terms of the MB function to visualize the cell apoptosis. In addition, the ratiometric intensity of MB fluorescence (caspase-3 MB / GAPDH MB) was compared with that of single MB to assess the availability of dual-color imaging. The 3D cell aggregates were prepared from the MB-labeled cells, and the Fas-mediated apoptosis was induced to the aggregates. As a different type of apoptosis inducer, camptothecin of a low-molecular weight compound was used as well. The fluorescence of MB was evaluated between the Fas-mediated and camptothecin-induced apoptosis to investigate the localization of apoptotic cells in the 3D aggregates. Finally, the distribution of anti-Fas antibody in the aggregates was examined to compare with the fluorescent localization of MB.

EXPERIMENTAL

Materials

Gelatin with an isoelectric point of 9.0 and the weight-averaged molecular weight of

99,000, prepared by an acidic process of pig skin, was kindly supplied from Nitta Gelatin Inc., Osaka, Japan. MB for mouse mRNA of caspase-3 and GAPDH were designed by NIPPON GENE Co., Ltd, Tokyo, Japan, and synthesized by Integrated DNA Technologies, Inc. Coralville, IA, USA. The sequences of MB were listed in **Table 1**. Glutaraldehyde (GA, 25 wt% in water), glycine, concentrated hydrochloric acid (HCl), acetone, and 1-ethyl-3-(3-dimethylaminopropyl) carbodiimide hydrochloride salt (EDC) were purchased from Nacalai Tesque. Inc., Kyoto, Japan. Spermine was purchased from Sigma-Aldrich Inc., St. Louis, MO, USA. The reagents were used without further purification.

Table 1. Sequences of MB used.

MB	Sequences (5' to 3')
Caspase-3 MB	[Alexa Fluor®488]-GTCACATACAGGAAGTCAGCCTCCACCGTGAC-[IBFQ]
GAPDH MB	[TYE®665]-CTGGTAATCCGTTCACACCGACCTTCACCAG-[IBRQ]

MB: molecular beacons
GAPDH: glyceraldehyde-3-phosphate dehydrogenase
IBFQ: Iowa Black®FQ
IBRQ: Iowa Black®RQ
underline: stem structure

Preparation of cationized gelatin

Cationized gelatin was prepared by conjugating spermine with the carboxyl groups of gelatin as described in Chapter 2. In brief, spermine was added at a molar ratio of 50 to the carboxyl groups of gelatin into 50 ml of gelatin aqueous solution (40 mg/ml). Immediately after that, the solution pH was adjusted to 5.0 by adding 11 M HCl. Double-distilled water (DDW) was added to give the final volume of 100 ml. Next, EDC was added at a molar ratio of 3 to the carboxyl groups of gelatin, followed by the agitation at 40 °C for 18 hr and dialysis against DDW for 3 days with a dialysis membrane (molecular weight cut off = 12,000 to 14,000, Viskase Companies, Inc., Willowbrook, IL, USA) at room temperature. The dialyzed solution was freeze-dried to obtain the cationized gelatin. The percentage of amino groups introduced into gelatin was determined by the conventional 2,4,6-trinitrobenzene sulfonic acid (TNBS, FUJIFILM Wako Pure Chemical Inc., Osaka, Japan) method [13]. The percentage was 59.8 mole% per the carboxyl groups of gelatin.

Preparation of cGNS

According to the preparation procedure described in Chapter 3, cGNS were prepared by the conventional coacervation method. Briefly, aqueous solution of cationized gelatin (50 mg/ml, 1.25 ml) was warmed up to 40 °C. Then, 5 ml of acetone was gradually dropped to the solution to form coacervate. Aqueous solution of 25 wt% GA (20 μl) was immediately added to the solution, followed by chemically crosslinking of cationized gelatin for 6 hr. After that, an excessive amount of 0.5 M glycine aqueous solution (2 ml) was added for the blocking of aldehyde groups unreacted. The resulting solution was agitated overnight at 40 °C and the residual acetone was evaporated. Then, cGNS were collected by the centrifugation of 16,000 g for 30 min at 25 °C and resuspended in DDW. The centrifugation and resuspension procedures were repeated three times to wash cGNS. The concentration of cGNS was determined by the measurement of weight after drying 100 μl of cGNS suspension.

The apparent size of cGNS dispersed in 10 mM phosphate buffered-saline solution (PBS, pH7.4) was measured by dynamic light scattering (DLS, Zetasizer Nano-ZS, Malvern Instruments Ltd., Worcestershire, UK). On the other hand, the zeta potential of cGNS dispersed in 10 mM phosphate buffer (PB, pH7.4) was measured by electrophoresis light scattering (ELS, Zetasizer Nano-ZS, Malvern Instruments Ltd., Worcestershire, UK). The apparent size and zeta potential of cGNS were 151.8 ± 0.98 nm and 8.44 ± 0.39 mV, respectively.

Preparation of cGNS_{MB}

The cGNS_{MB} were prepared by simply incubating cGNS with MB in DDW. The cGNS (200 μg) and MB (caspase-3 and GAPDH MB, each 4 μM) were mixed in DDW at the MB/cGNS ratio of 20 pmole/μg. After the incubation for 15 min at room temperature, the mixture was centrifuged at 16,000 g for 15 min at 25 °C and resuspended in DDW to obtain cGNS incorporating caspase-3 and GAPDH MB ($\text{cGNS}_{\text{casp3 MB}}$ and $\text{cGNS}_{\text{GAP MB}}$, respectively). On the other hand, cGNS co-incorporating caspase-3 and GAPDH MB ($\text{cGNS}_{\text{dual MB}}$) were prepared by incubating cGNS and the mixed solution of caspase-3 and GAPDH MB (1:1) (total 20 pmole MB/μg cGNS). After the incubation for 15 min, the $\text{cGNS}_{\text{dual MB}}$ were obtained by the centrifugation and resuspension in DDW as well. The apparent size and zeta potential of cGNS_{MB} were determined by DLS and ELS measurements, respectively. The measurements were performed independently three times for each of sample unless otherwise mentioned.

Cell culture experiments

KUM6 cells (JCRB1202) of a mouse bone marrow-derived MSC line were purchased from JCRB Cell Bank (National Institute of Biomedical Innovation, Health and Nutrition, Osaka, Japan). The cells were cultured in Iscove's Modified Dulbecco's Medium (IMDM, Thermo Fisher Scientific Inc., Waltham, MA, USA) supplemented with 10 vol% bovine fetal calf serum (FCS, GE healthcare Life Sciences Hyclone laboratories inc., Logan, UT, USA) and 1 vol% penicillin and streptomycin (Nacalai Tesque. Inc., Kyoto, Japan) at 37 °C in a 5% CO_2-95% air atmospheric condition. The cells were detached with 0.25 wt% trypsin-containing 1 mM ethylenediaminetetra acetic acid (EDTA) solution (Nacalai Tesque. Inc., Kyoto, Japan) and continued to culture in 100 mm cell culture dish (Corning Inc., Corning, NY, USA) to allow to grow until to 80% confluency.

Immunofluorescent staining

The cells were seeded on a glass bottom dish of 35 mm in diameter (Matsunami Glass Industries Ltd., Tokyo, Japan) at a density of 1×10^5 cells/dish. After the incubation for 24 hr, the cells were fixed with 4 vol% paraformaldehyde for 20 min at room temperature. After the blocking (ImmunoBlock™, KAC Co. Ltd., Kyoto, Japan), the cells were incubated with the rabbit monoclonal anti-Fas antibody (1:50, 50027-R004, Sino Biological, Inc., Beijing, China) overnight at 4 °C. Next, the cells were washed with PBS three times, followed by the incubation with the secondary goat anti-rabbit IgG (H + L) antibody conjugated with Alexa Fluor®488 (1:1000, A11008, Thermo Fisher Scientific Inc., Waltham, MA, USA) for 1 hr at room temperature. The cell nuclei were stained with 300 nM 4',6-diamidino-2-phenylindole (DAPI, Thermo Fisher Scientific Inc., Waltham, MA, USA), and then the fluorescent images were taken by a fluorescent microscope (BZ-X700, KEYENCE Co., Ltd., Osaka, Japan).

Induction of Fas-mediated apoptosis

The Fas-mediated apoptosis was induced by the agonistic stimulation of Fas receptor with the anti-Fas antibody (Fas Ab) in the presence of actinomycin D (Act D) [14, 15]. Briefly, cells were seeded in each well of 6 well multi-dish culture plate (Corning Inc., Corning, NY, USA) at a density of 1 × 10^5 cells/well, and cultured for 24 hr. Next, 1 μg/ml hamster monoclonal Fas Ab (clone: Jo2, 554255, Becton, Dickinson and Company, Franklin Lakes, NJ, USA) and 0.1 μg/ml Act D (Enzo Life Sciences, Inc., Farmingdale, NY, USA) were added to the cells, and cultured for further 16 hr to induce the apoptosis. The cell apoptosis was evaluated by the flow cytometric analysis using fluorescein isothiocyanate (FITC) Annexin V Apoptosis Detection Kit I (Becton, Dickinson and Company, Franklin Lakes, NJ, USA) according to the manufacture's instruction. The cells cultured with Fas Ab and Act D were collected by the trypsinization and washed with cold PBS twice. Then, the cells were resuspended in 10 mM HEPES/NaOH solution containing 140 mM NaCl and 2.5 mM $CaCl_2$ (pH7.4), and FITC-conjugated annexin V and propidium iodide (PI) were added to the suspension. The cell suspension was analyzed on FACSCanto II flow cytometer and FACSDiva software (Becton Dickinson and Company, Franklin Lakes, NJ, USA) by counting 10,000 cells.

Fluorescent imaging of apoptosis in the 2D culture

The cells were similarly seeded on the glass bottom dish at a density of 1 × 10^5 cells/dish, and cultured for 24 hr. The medium was changed to OPTI MEM (Thermo Fisher Scientific Inc., Waltham, MA, USA), and $\mathrm{cGNS_{MB}}$ ($\mathrm{cGNS_{casp3\ MB}}$, $\mathrm{cGNS_{GAP\ MB}}$, and $\mathrm{cGNS_{dual\ MB}}$) were added to the cells at the concentration of 10 μg/ml. After the incubation for 1 hr with $\mathrm{cGNS_{MB}}$, the cells were washed with PBS and cultured for further 5 hr. Then, 1 μg/ml Fas Ab and 0.1 μg/ml Act D were added to the $\mathrm{cGNS_{MB}}$-incubated cells to induce the Fas-mediated apoptosis. After the apoptosis induction for 16 hr, the cells were observed by the fluorescent microscope BZ-X700. To evaluate the fluorescent intensity, six images were taken at random and analyzed by BZ-X Analyzer (KEYENCE Co., Ltd., Osaka, Japan). The fluorescent area in the cells was extracted and the averaged brightness of the area was measured as the fluorescent intensity.

Preparation of cell aggregates labeled with MB

The cells were similarly seeded in each well of 6 well plate at a density of 1 × 10^5 cells/well, and cultured for 24 hr. After the medium change to OPTI MEM, the $\mathrm{cGNS_{MB}}$ were added to the cells (10 μg/ml), and incubated for 1 hr to allow cells to label with MB in the 2D culture. The MB-labeled cells were detached by the trypsinization 5 hr later, and the cell number was counted.

Poly(vinyl alcohol) (PVA) (degree of polymerization = 1,800 and saponification = 88 mole%) was kindly supplied from Unitika Ltd., Tokyo, Japan. The PVA solution (1 wt%, dissolved in PBS) was added to each well of round-bottomed (U-bottomed) 96 well culture plate (Greiner Bio-One International GmbH, Kremsmünster, Austria) to coat wells with PVA (100 μl/well). After the incubation for 15 min at 37 °C, the PVA solution was removed and the wells were washed with PBS twice. Then, the MB-labeled cells were added to each well (500 cells/well, 200 μl/well), and cultured for 3 days to form the aggregates. The cell aggregates were transferred to the glass bottom dish, and observed by confocal laser microscopy IX73/CSU-W1 (OLYMPUS Co., Ltd., Tokyo, Japan) to take the fluorescent images of optical sections and construct the 3D images. On the other hand, the size of cell aggregates prepared from MB-labeled cells or original cells was measured from 20 images using the software BZ-X Analyzer to calculate the average diameter.

Fluorescent imaging of apoptosis in the 3D cell aggregates

The cells were similarly incubated with $\mathrm{cGNS_{dual\ MB}}$ in the 2D culture, and the cell aggregates were prepared from the MB-labeled cells as described above. After the aggregate culture for 3 days, the half of medium was changed to the medium containing Fas Ab and Act D (final concentration of 1 and 0.1 μg/ml, respectively). In addition, camptothecin (5 μM, Enzo Life Sciences, Inc., Farmingdale, NY, USA) of a DNA-topoisomerase I inhibitor was used to induce the apoptosis [16-18]. The cell aggregates induced apoptosis for 16 hr were transferred to the glass bottom dish, and observed by the fluorescent microscopy BZ-X700 with an optical sectioning module. The optical sections of cell aggregates were taken based on the structured illumination in a grid pattern and the projection onto only the focused areas of sample [19]. The fluorescent intensity as a line-profile of optical sections was evaluated by BZ-X Analyzer.

To investigate the distribution of Fas Ab in the aggregates, the Fas Ab was fluorescently labeled using HiLyte Fluor^{TM} 555 Labeling Kit-NH_2 (Dojindo Laboratories, Kumamoto, Japan) according to the manufacture's protocol. Then, the cell aggregates were incubated with 1 µg/ml Fas Ab labeled with HiLyte Fluor 555 and 0.1 µg/ml Act D for 16 hr. After the incubation, the cell aggregates were collected and washed with PBS, and the fluorescent intensity as a line-profile of optical section taken by the fluorescent microscopy was similarly evaluated.

Statistical analysis

The data were expressed as the average ± standard deviation (SD). All the statistical analysis was performed using one-way analysis of variance (ANOVA) with a post-hoc Tukey-Kramer multiple comparison test. *P* values less than 0.05 were considered to be statistically significant.

RESULTS

Characterization of $cGNS_{MB}$

Table 2 shows the apparent size and zeta potential of $cGNS_{MB}$ prepared. There was no difference in the values among $cGNS_{casp3\ MB}$, $cGNS_{GAP\ MB}$, and $cGNS_{dual\ MB}$.

Table 2. Physicochemical properties of $cGNS_{MB}$.

	Apparent size (nm)	Zeta potential (mV)
$cGNS_{casp3\ MB}$	211.9 ± 11.2 $^{a)}$	9.40 ± 0.35
$cGNS_{GAP\ MB}$	220.1 ± 2.40	9.38 ± 0.28
$cGNS_{dual\ MB}$	222.0 ± 1.66	9.41 ± 0.16

a) Average ± SD.

Analysis of Fas-mediated apoptosis

The expression of Fas in KUM6 cells was evaluated by the immunofluorescent staining (**Figure 1**). The Fas expression was experimentally confirmed by the positive staining. **Figure 2** shows the flow cytometric analysis of Fas-mediated apoptosis induced by the addition of 1 µg/ml Fas Ab, 0.1 µg/ml Act D, and 1 µg/ml Fas Ab plus 0.1 µg/ml Act D for 16 hr. The cells treated with only Fas Ab or Act D were double negative for annexin V and PI. On the other hand, the combination of Fas Ab and Act D significantly increased the percentage of apoptotic (annexin V-positive) cells.

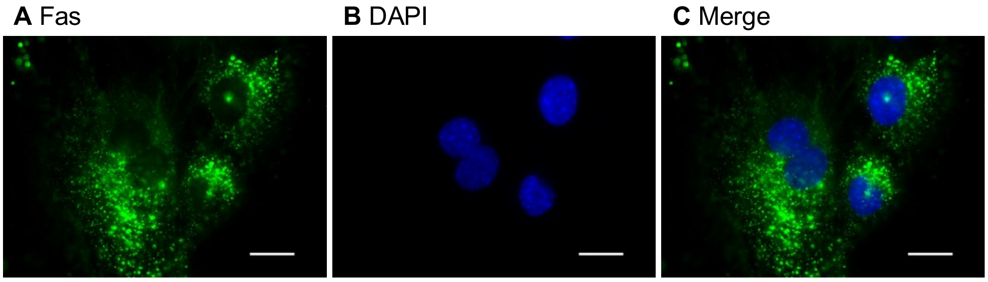

Figure 1. Immunofluorescent staining of Fas: (A) Green: Fas, (B) Blue: DAPI (nuclei), and (C) Merged fluorescent image. Scale bar is 20 µm.

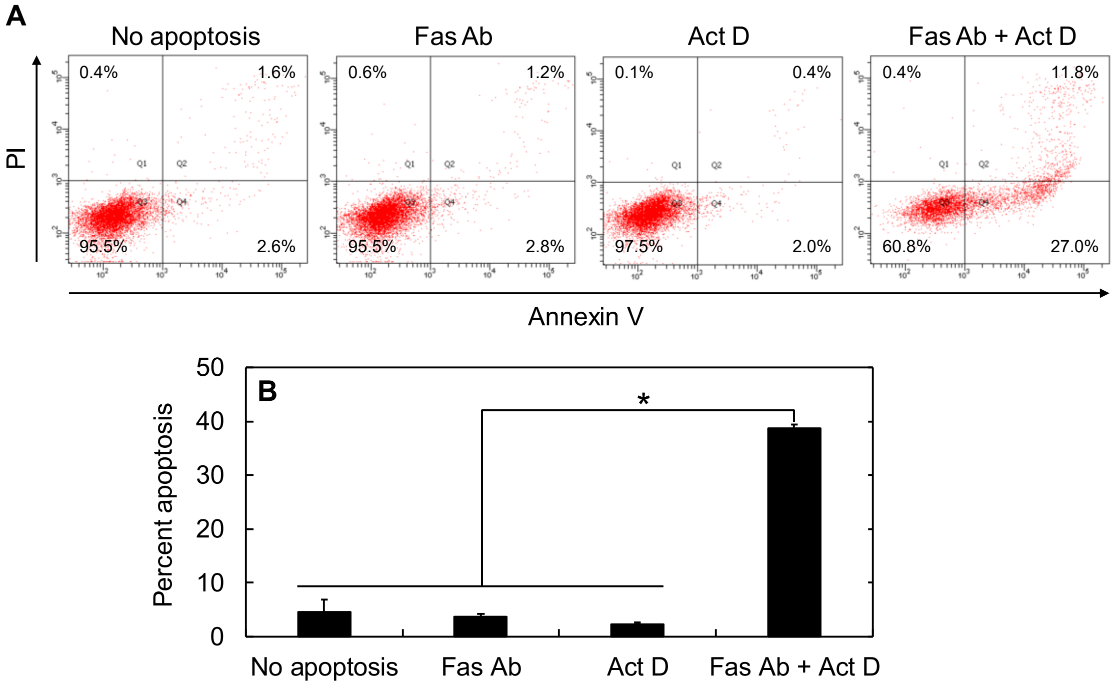

Figure 2. Analysis of Fas-mediated apoptosis. (A) Flow cytometric plots of cell population and (B) the percentage of apoptotic (annexin V-positive) cells 16 hr after incubation with 1 µg/ml Fas Ab, 0.1 µg/ml Act D, and 1 µg/ml Fas Ab plus 0.1 µg/ml Act D. *, $p < 0.05$; significant between the groups.

Fluorescent imaging of apoptosis in the 2D culture

The cells were incubated with cGNS_{MB}, followed by the addition of Fas Ab and Act D to induce the Fas-mediated apoptosis for 16 hr, and observed by the fluorescent microscopy. **Figure 3A** shows the fluorescent microscopic images of cells incubated with $\text{cGNS}_{\text{casp3 MB}}$ and $\text{cGNS}_{\text{GAP MB}}$. The fluorescence of $\text{cGNS}_{\text{GAP MB}}$ was similarly observed for both no apoptotic and Fas apoptosis-induced cells, while the intense fluorescence of $\text{cGNS}_{\text{casp3 MB}}$ was observed for only the Fas apoptosis-induced cells. When the fluorescent intensity was evaluated (**Figure 3B**), the intensity of $\text{cGNS}_{\text{GAP MB}}$ was constant between the no apoptotic and Fas apoptosis-induced cells. On the other hand, the fluorescent intensity of $\text{cGNS}_{\text{casp3 MB}}$ significantly increased in response to the Fas-mediated apoptosis.

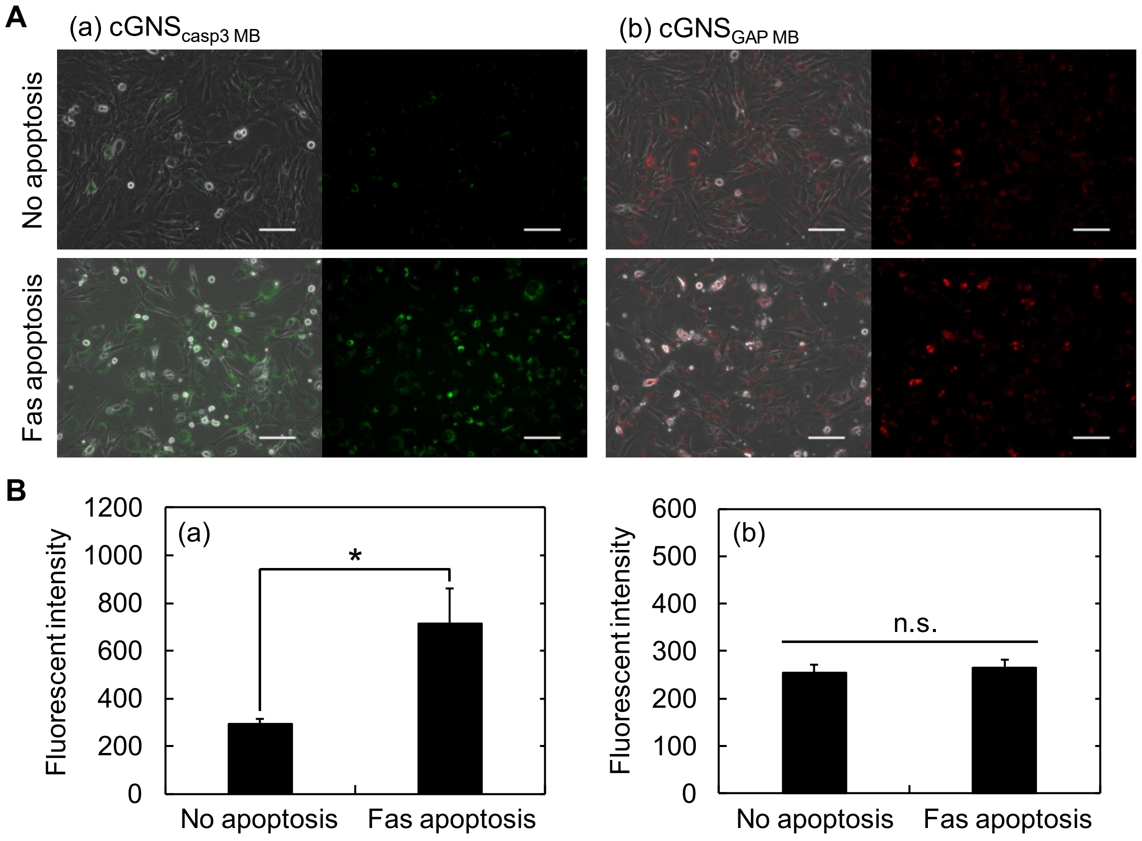

Figure 3. Fluorescent imaging of apoptosis in the 2D culture with single color. (A) Fluorescent microscopic images of cells incubated with 10 μg/ml $\text{cGNS}_{\text{casp3 MB}}$ (a) and $\text{cGNS}_{\text{GAP MB}}$ (b) for 1 hr. The Fas-mediated apoptosis was induced by the addition of 1 μg/ml Fas Ab and 0.1 μg/ml Act D for further 16 hr. The left panel shows the merged images of phase contrast and MB fluorescence, while the right panel shows the MB fluorescence. Scale bar is 100 μm. (B) Fluorescent intensity of cells incubated with $\text{cGNS}_{\text{casp3 MB}}$ (a) and $\text{cGNS}_{\text{GAP MB}}$ (b). The Fas-mediated apoptosis was induced by the addition of Fas Ab and Act D for further 16 hr. n.s.; not significant. *, $p < 0.05$; significant between the groups.

Next, the cells were incubated with $\text{cGNS}_{\text{dual MB}}$, and the Fas Ab and Act D were similarly added to perform the dual-color imaging of Fas-mediated apoptosis in the 2D culture condition (**Figure 4**). It is apparent from **Figure 4A** that the fluorescence of caspase-3 MB was strongly observed for apoptotic cells. **Figure 4B** shows the ratiometric fluorescent intensity of $\text{cGNS}_{\text{dual MB}}$ (caspase-3 MB / GAPDH MB). The ratio of fluorescent intensity significantly increased with the Fas-mediated apoptosis. In addition, the increase of fluorescent ratio showed a profile similar to that of $\text{cGNS}_{\text{casp3 MB}}$ fluorescent intensity (**Figure 3B (a)**).

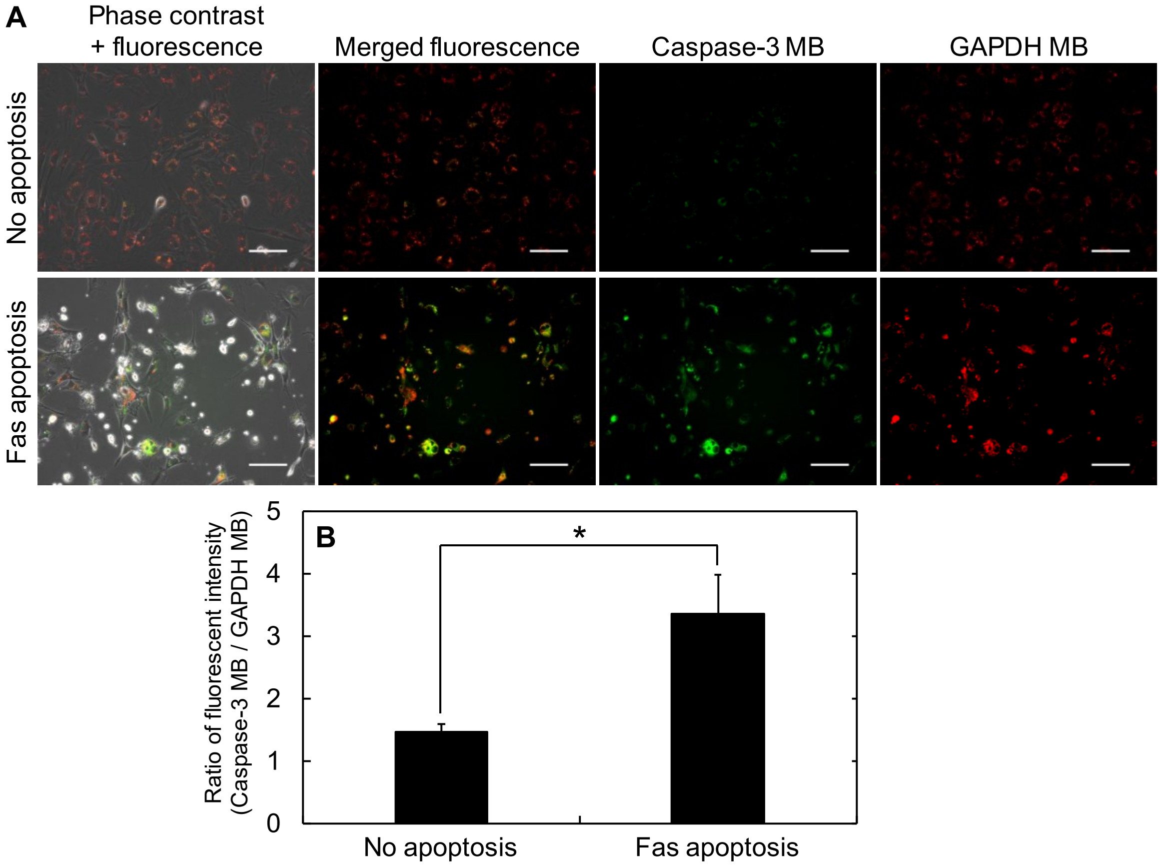

Figure 4. Fluorescent imaging of apoptosis in the 2D culture with dual colors. (A) Fluorescent microscopic images of cells incubated with 10 µg/ml $\text{cGNS}_{\text{daul MB}}$ for 1 hr. The Fas-mediated apoptosis was induced by the addition of 1 µg/ml Fas Ab and 0.1 µg/ml Act D for further 16 hr. Green: caspase-3 MB. Red: GAPDH MB. Scale bar is 100 µm. (B) Ratiometric fluorescent intensity of cells incubated with $\text{cGNS}_{\text{daul MB}}$. The Fas-mediated apoptosis was induced by the addition of Fas Ab and Act D for further 16 hr. *, $p < 0.05$; significant between the groups.

Preparation of cell aggregate labeled with MB

The cell aggregates were prepared from the cells incubated with $\mathrm{cGNS_{MB}}$ in the 2D culture (MB-labeled cells), and observed by the confocal laser microscopy. **Figure 5** shows the confocal microscopic images of cell aggregates labeled with GAPDH MB. Almost all of the cells emitted the fluorescence of GAPDH MB even in the 3D aggregates, and spatially distributed in homogenous. In addition, there was no difference in the size of cell aggregates prepared form the original or MB-labeled cells (**Figure 6**). The size of cell aggregates was around 100 μm.

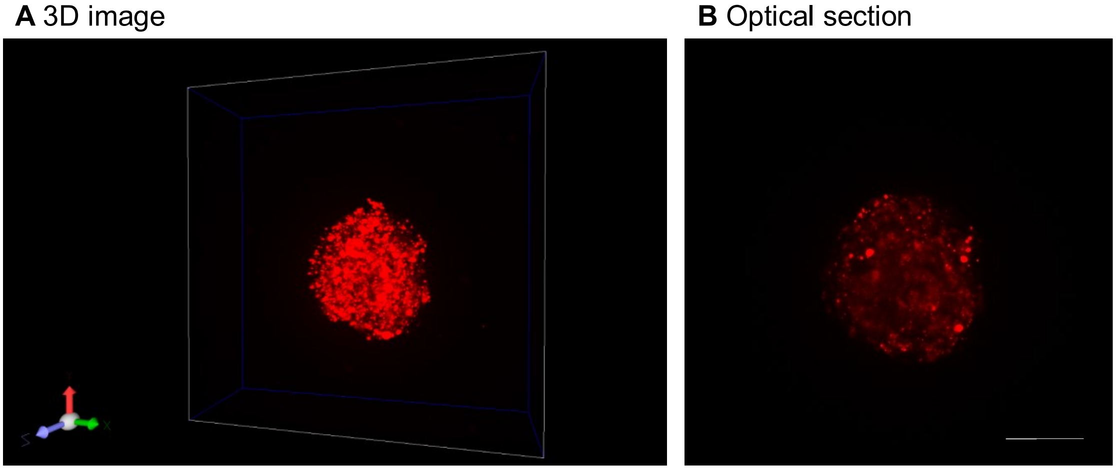

Figure 5. Confocal microscopic images of cell aggregates labeled with MB. The cell aggregates were prepared from the $\mathrm{cGNS_{GAP\ MB}}$-incubated cells, and observed by the confocal laser microscopy. TYE®563 was used as a 5'-fluorophore of GAPDH MB to adjust the optimal laser excitation and emission. (A) 3D image of cell aggregate and (B) optical section of the cell aggregate (center image of z-axis). Scale bar is 50 μm.

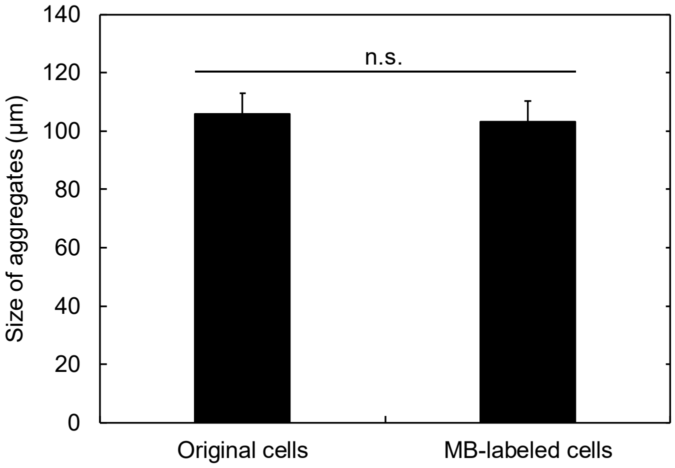

Figure 6. Size of cell aggregates labeled with MB. The cell aggregates were prepared from the $\mathrm{cGNS_{dual\ MB}}$-incubated cells (MB-labeled cells) or the original cells. n.s.; not significant.

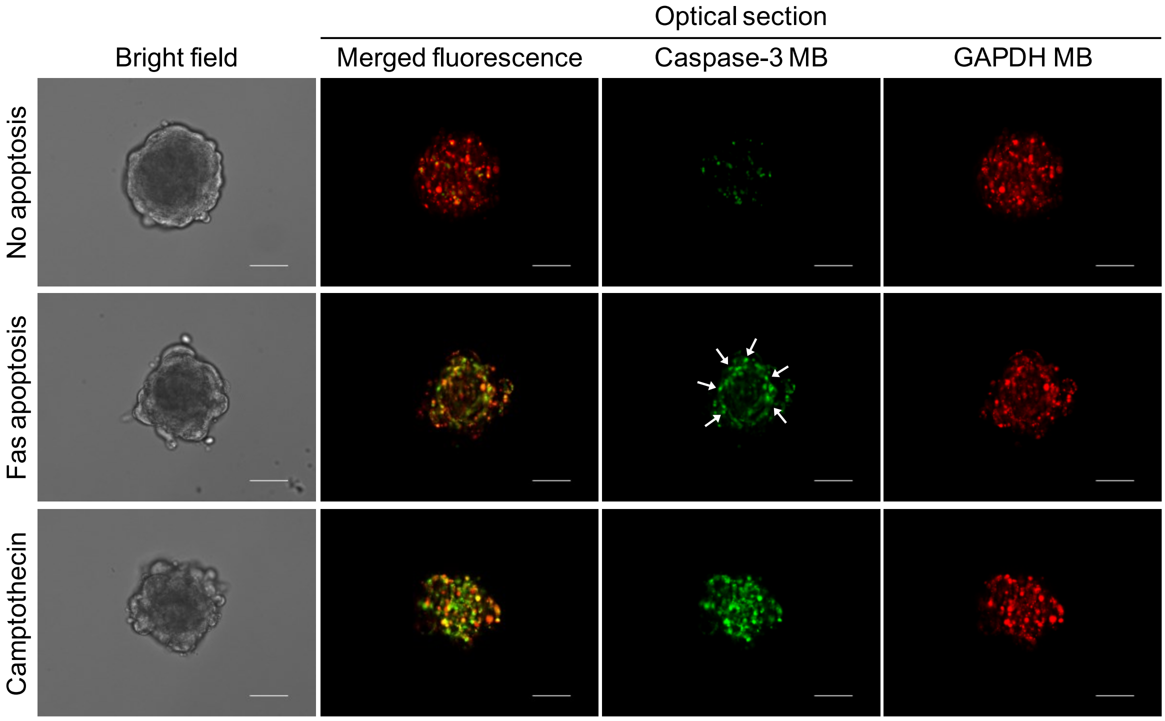

Figure 7. Fluorescent imaging of apoptosis in the 3D cell aggregates with dual colors. The cell aggregates were prepared from the cGNS$_{\text{dual MB}}$-incubated cells, and the apoptosis was induced by the addition of 1 μg/ml Fas Ab and 0.1 μg/ml Act D (Fas apoptosis), as well as 5 μM camptothecin for further 16 hr. Green: caspase-3 MB. Red: GAPDH MB. The arrows indicate the cells which emit the strong fluorescence of caspase-3 MB at the surrounding site of aggregates. Scale bar is 50 μm.

Fluorescent imaging of apoptosis in the 3D cell aggregates

The apoptosis was induced to the cell aggregates prepared from cGNS$_{\text{dual MB}}$-incubated cells, and the optical sections were observed to investigate the response of MB in the 3D cell aggregates (**Figure 7**). In addition to the Fas-mediated apoptosis, camptothecin of a low-molecular weight compound was used to induce the apoptosis. The fluorescence of GAPDH MB was observed for every condition (no apoptosis, Fas apoptosis, and camptothecin apoptosis), whereas that of caspase-3 MB in both the Fas- and camptothecin-induced apoptotic conditions was strongly observed compared with the no apoptosis. For the fluorescence distribution of MB, the intense fluorescence of caspase-3 MB was detected in cells at the surface surrounding site of Fas-mediated apoptotic aggregates rather than the center site, while that of GAPDH MB was detected even in the interior site of aggregates. On the other hand, in the camptothecin-induced apoptotic aggregates, both caspae-3 and GAPDH MB fluorescence were detected from the interior site of aggregates as well as the surrounding site. **Figure 8** shows the line-profiles of fluorescent intensity in the cell aggregates. In the aggregate of Fas apoptosis, the peaks of caspase-3 MB fluorescence were mainly distributed at the edge sites although the GAPDH MB showed the fluorescent peaks even in the interior site. On the contrary, the fluorescent peaks of caspase-3 MB in the camptothecin-treated aggregates were distributed at both the edge and interior sites. Then, the distribution of Fas Ab in the cell aggregates was investigated (**Figure 9**). As the similar result of caspase-3 MB, the fluorescence of Fas Ab was strongly observed in the periphery of aggregates compared with the center site. The fluorescent peaks of Fas Ab at the edge sites were higher than that in the interior sites.

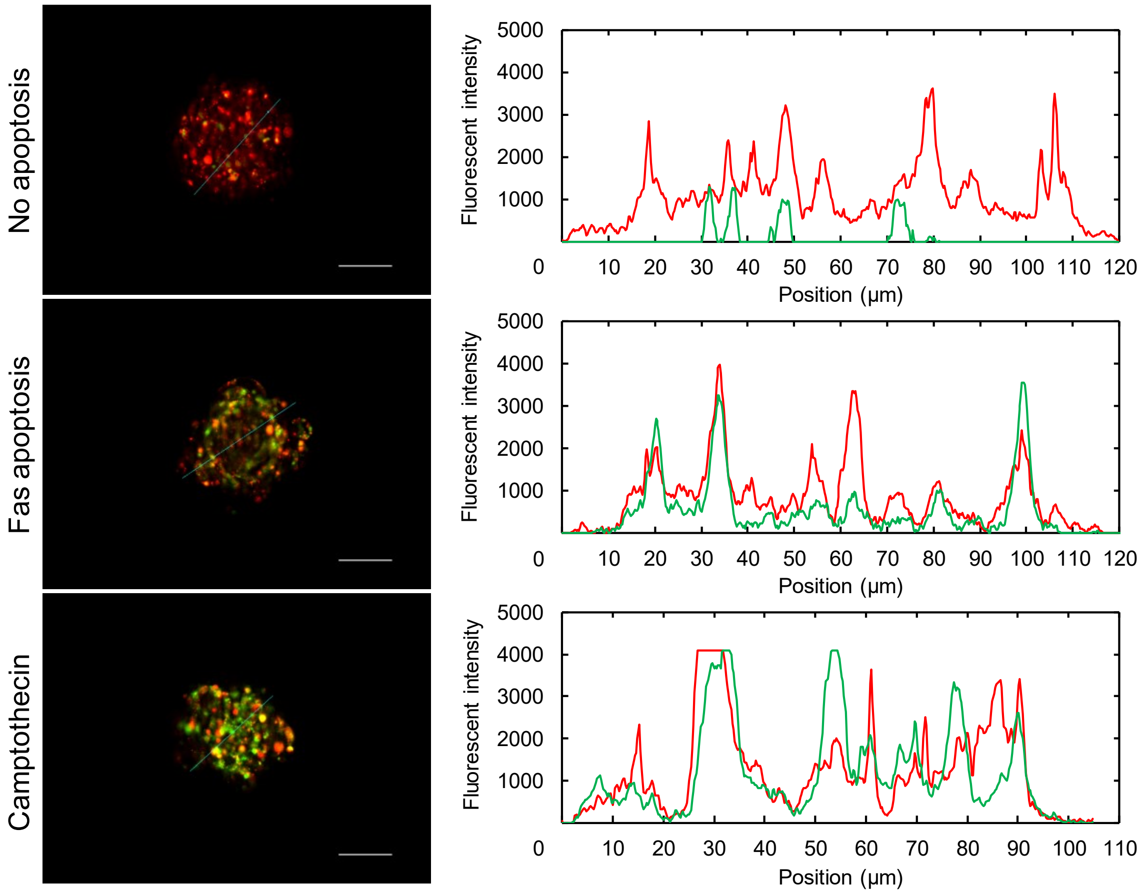

Figure 8. Evaluation of apoptosis in the 3D cell aggregates. Left images are the merged fluorescence of caspase-3 MB (green) and GAPDH MB (red) in Figure 7, and the fluorescent intensity as a line-profile (cyan lines) was evaluated (right graphs). Green line: fluorescent intensity of caspase-3 MB. Red line: fluorescent intensity of GAPDH MB.

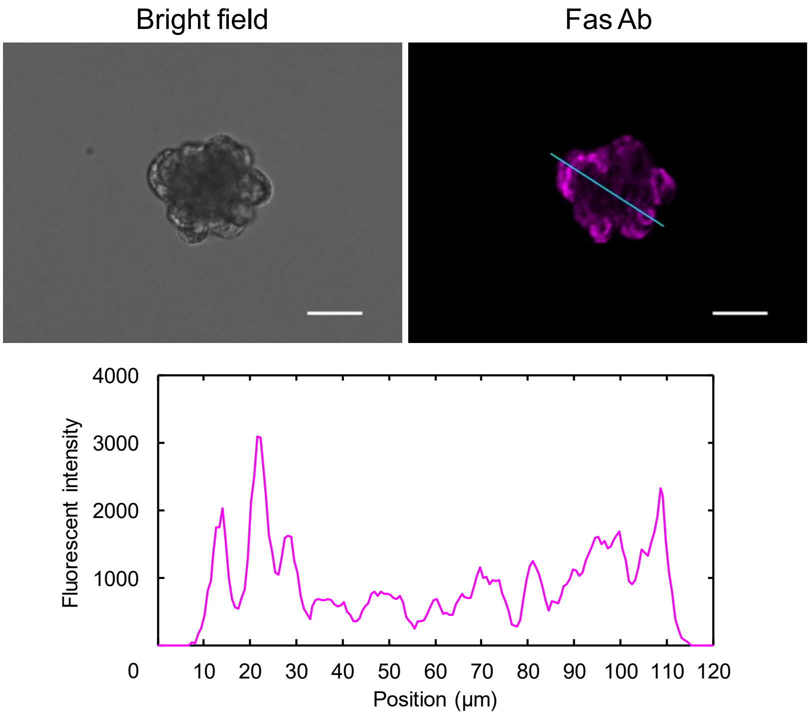

Figure 9. Evaluation of Fas Ab distribution in the 3D cell aggregates. The Fas Ab labeled with HiLyte Fluor^{TM} 555 (1 μg/ml) and Act D (0.1 μg/ml) were added to the cell aggregates for 16 hr, and the optical section was taken by the fluorescent microscopy to evaluate the fluorescent intensity as a line-profile (cyan line). Magenta: Fas Ab. Scale bar is 50 μm.

DISCUSSION

The present study demonstrates that cell apoptosis in 3D cell aggregates could be visualized by making use of the cGNS$_{MB}$ imaging system. The cGNS$_{MB}$ were incubated with the cells to label with MB in the 2D culture, and the Fas-mediated apoptosis was induced by the addition of Fas Ab and Act D. The fluorescence of cGNS$_{casp3\ MB}$ significantly enhanced with the apoptosis induction, whereas that of cGNS$_{GAP\ MB}$ was constant, irrespective of the cell apoptosis. In addition, the apoptosis was ratiometrically detected by the cGNS$_{dual\ MB}$ to the same extent as single MB. The cell aggregates were prepared from MB-labeled cells, and the MB fluorescence was detected from almost all of the cells even in the 3D aggregates to show the homogenous distribution. In addition to the Fas-mediated apoptosis, the aggregates were treated with camptothecin of a low-molecular weight apoptosis inducer. The fluorescence of caspase-3 MB was mainly distributed at the surface surrounding site of Fas-mediated apoptotic aggregates rather than the center site, while that of GAPDH MB was detected even in the interior site. The distribution of caspase-3 MB fluorescence showed a profile similar to that of Fas Ab in the aggregates. On the other hand, in the camptothecin-induced apoptotic aggregates, both caspae-3 and GAPDH MB fluorescence emission were detected from the interior site of aggregates as well as the surrounding site.

There was no difference in the apparent size and zeta potential among $\mathrm{cGNS_{casp3\ MB}}$, $\mathrm{cGNS_{GAP\ MB}}$, and $\mathrm{cGNS_{dual\ MB}}$ prepared (**Table 2**). The apparent size was around 220 nm, and the zeta potential was of a positive value. The result indicates that the physicochemical properties of $\mathrm{cGNS_{MB}}$ did not depend on the type of MB, as well as the co-incorporation of different MB types. In Chapters 3 and 5, it has been demonstrated that the $\mathrm{cGNS_{MB}}$ were internalized into the cells via an endocytotic pathway, followed by the endosomal escape into the cytosol. The intracellular release of MB according to the degradation of carrier cGNS enabled the detection of target mRNA (Chapter 3). The specificity of caspase-3 and GAPDH MB for the target nucleotides in hybridization and the stability against nucleases were experimentally demonstrated (Chapter 5). In addition, at the $\mathrm{cGNS_{MB}}$ concentration lower than 10 μg/ml, the incubation time for 1 hr did not show any cytotoxicity. This is due to the high susceptibility of $\mathrm{cGNS_{MB}}$ to cell internalization and the resulting mild internalization condition. Taken together, it is highly conceivable that the $\mathrm{cGNS_{casp3\ MB}}$, $\mathrm{cGNS_{GAP\ MB}}$, and $\mathrm{cGNS_{dual\ MB}}$ were efficiently internalized into the cells to label with MB, and the target mRNA of caspase-3 and GAPDH could be specifically detected based on the intracellular controlled release of MB.

The Fas-mediated apoptosis was induced by the agonistic stimulation of Fas receptor with Fas Ab in the presence of Act D. The immunofluorescent staining experimentally confirmed the Fas expression in KUM6 cells used in this study (**Figure 1**). The flow cytometric analysis with annexin V / PI staining was performed to assess the Fas-mediated apoptosis (**Figure 2**). PI only permeates the damaged cell membrane to stain the nucleus of late apoptotic and dead cells, while the annexin V specifically conjugates with the phosphatidylserine on the surface of apoptotic cell membrane [20]. The cell population treated with only Fas Ab or Act D was double negative for annexin V and PI, which indicates that the apoptosis was hardly induced. On the contrary, the apoptosis was significantly induced by the combination of Fas Ab and Act D. The finding suggests that the Fas Ab and Act D synergistically cause the Fas-mediated apoptosis, which is consistent with the previous reports [21]. Fas (also known as Apo-1/CD95) is one of death receptors widely expressed in many cell types [14, 15, 21-23]. The stimulation of Fas with Fas-ligands including the agonistic antibody, results in the downstream cascade of signal transduction in the apoptosis pathway. It has been reported in mouse cardiomyocytes that the apoptotic signal transduction in the treatment with Fas Ab and Act D is composed of c-Jun N-terminal kinase (JNK) activation, Bcl-2-associated X protein (Bax) upregulation, and caspase-3 upregulation at both mRNA and protein levels [21]. It is important to claim here that the caspase-3, so-called "effector caspase", is finally upregulated in almost all pathways to execute the apoptosis [24]. Therefore, it would be reasonable to select the caspase-3 mRNA as the target for MB in terms of the visualization of apoptosis as a versatile system.

After the cell incubation with cGNS$_{MB}$ for internalization and labeling with MB, a Fas-mediated apoptosis was induced by the addition of Fas Ab and Act D in the 2D culture condition. In agreement with the results in Chapter 5, the fluorescence of cGNS$_{GAP\ MB}$ was similarly observed for both no apoptotic and Fas-apoptotic cells, and the fluorescent intensity was constant. On the other hand, the cGNS$_{casp3\ MB}$ fluorescence significantly enhanced in the apoptotic condition (**Figure 3**). The result would be due to the increased expression of caspase-3 mRNA by the Fas-mediated apoptosis induction and the constant expression of GAPDH mRNA in cells [21]. When the dual-color imaging was performed by utilizing cGNS$_{dual\ MB}$, the fluorescence of caspase-3 MB was strongly observed in the Fas apoptosis condition (**Figure 4**). The increased ratio of fluorescent intensity (caspase-3 MB / GAPDH MB) well corresponded to the increased fluorescent intensity of single caspase-3 MB (**Figures 3B** and **4B**). These results strongly suggest that the cell apoptosis could be successfully visualized by the dual-color imaging as well as the use of single MB.

The 3D cell aggregates were readily prepared only by using the cells labeled with MB in the 2D culture. The PVA-coated U-shaped bottom of wells gives cells an environment suitable for the efficient formation of aggregates. The cell adhesion on the well is inhibited by the PVA-coating [25]. In addition, the U-shaped bottom allows cells to accumulate in the center of the wells, where the frequency of cell to cell contact is enhanced to form the aggregates [25].

The confocal microscopic images show that the cells labeled with MB were spatially distributed in a homogenous manner, and almost all of cells emitted the fluorescence of MB (**Figure 5**). It was confirmed that the labeling efficiency with cGNS$_{MB}$ was around 100% after the incubation in the 2D culture (Chapter 6). In addition, it has been demonstrated that the intracellular fluorescence of MB maintained over 2 weeks (Chapter 3). Taken together, nearly 100% of cells were labeled with MB, and the MB fluorescence was sufficiently retained even in the 3D cell aggregates. In some cases, it is difficult to label the 3D constructs of cells due to the poor penetration of imaging probes into the interior of constructs [26, 27]. Therefore, some researches on the construction of 3D structures following the cell labeling in a 2D culture have been reported [28-30]. This labeling strategy is advantageous for the homogenous labeling of cells in the 3D constructs with varied shapes (Chapter 7). The homogenous labeling with MB makes it possible to visualize the change of cell functions in the 3D environments. The size of cell aggregates prepared was around 100 μm, which was not affected by the labeling with MB (**Figure 6**). In general, it is well recognized that the excess size of aggregates results in the cell death in the core of aggregates due to the insufficient supply of nutrients and oxygen [31, 32]. On the other hand, it has been reported in hepatocyte spheroids that under the size of 100-150 μm in diameter showed no significant cell death [33, 34]. It is, thus, highly possible that the cell death hardly occurred in the aggregates prepared in this study without the induction of apoptosis.

It is apparent form **Figure 7** that the fluorescence of caspase-3 MB was strongly observed for the Fas-mediated and camptothecin-treated apoptotic aggregates compared with non-apoptotic aggregates, while that of GAPDH MB was detected in every condition. The result suggests that the apoptosis of cell aggregates was detected by the fluorescence of caspase-3 MB, and the GAPDH MB worked well as an internal reference. The availability of internal reference in the same cell aggregate is one of advantages in the dual-color imaging. In Chapter 5, the addition of 5 μM camptothecin caused the significant cell apoptosis (around 40% in cell population), which is a similar extent to the Fas-mediated apoptosis in this study (**Figure 2**). In the Fas-mediated apoptotic aggregates, the fluorescent peaks of caspase-3 MB were mainly distributed at the surface site of aggregates, while that of GAPDH MB was detected even in the interior site (**Figure 8**). On the other hand, in the case of camptothecin-treated aggregates, the fluorescent peaks of caspase-3 and GAPDH MB were distributed at both the surface and interior sites. The difference in the fluorescent distribution between the Fas-mediated and camptothecin-induced apoptosis would be due to the molecular size of apoptosis inducers and their penetration into the aggregates. The Fas Ab (IgG) is a macromolecule with a Y-shaped structure. The typical dimensions of IgG are approximately 14.5 nm × 8.5 nm × 4.0 nm [35]. The large molecular size of Fas Ab might prevent the penetration into the interior site of cell aggregates. It has been reported that the penetration of cetuximab (monoclonal antibody for epidermal growth factor receptor) into tumor spheroids (around 400 μm in diameter) was limited in the periphery after 16 hr of addition although the penetration was observed in time- and dose-dependent manners [36]. When the penetration and distribution of Fas Ab in the aggregates were investigated (**Figure 9**), the fluorescent peaks of Fas Ab showed a similar pattern to those of caspase-3 MB (**Figure 8**). These findings experimentally support that the poor penetration of Fas Ab into the interior of cell aggregates, and the resulting cell apoptosis was significantly enhanced at the surface site compared with the interior site. On the other hand, camptothecin has a low-molecular weight of 348.4, and induces the cell apoptosis by conjugating with DNA-topoisomerase I to inhibit the activity [16-18]. As another type of low-molecular weight drug, doxorubicin (molecular weight of 543.5) showed the rapid penetration into the interior site of tumor spheroid (around 300 μm in diameter) within 8 hr [37]. Considering the findings, it is highly possible that the camptothecin sufficiently penetrated into the interior site of aggregates due to the small molecular size, and caused the cell apoptosis over the entire aggregates. Taken together, it is likely that the MB fluorescence reflected the localization of apoptotic position as well as the expression level of target caspase-3 mRNA in the 3D cell aggregates, which is caused by the different penetration patterns of apoptosis inducers into the aggregates.

The visualization of apoptosis without the destruction of cell aggregates was achieved by the cGNS$_{MB}$ imaging system, which facilitated the discrimination of apoptotic position in the 3D structure. This is one of advantages over the conventional biochemical techniques like western blotting and polymerase chain reaction (PCR). As the histological analysis, terminal deoxynucleotidyl transferase (TdT)-mediated dUTP nick-end labeling (TUNEL) assay has been applied to evaluate the apoptotic position in the 3D cells constructs, as well as the tissue samples. The TUNEL assay can reveal the localization of late apoptotic cells by staining the DNA fragments. However, it is necessary to prepare the histological section for the reaction with TdT and the following labeling procedures. Therefore, it would be difficult to analyze the entire 3D structures of construct. In addition, it is theoretically impossible to apply the TUNEL assay to the living samples. A fluorescent staining by the LIVE/DEAD$^{\text{TM}}$ assay (calcein-AM for live cells and ethidium homodimer-1 for dead cells) has been widely utilized as well. The advantage of LIVE/DEAD assay is to stain both live and dead cells by simply incubating with the fluorescent dyes. However, in the case of 3D constructs, the incubation condition often requires the optimization to confirm the complete penetration of fluorescent dyes into the interior site of constructs. On the other hand, the labeling strategy of 3D cell aggregates with cGNS$_{\text{MB}}$ (construction of 3D aggregates following the MB-labeling in a 2D culture) can validate the homogenous labeling even in the interior site of constructs. This is another advantage of cGNS$_{\text{MB}}$ imaging system.

Since the MB can be designed against theoretically every mRNA and miRNA, it is possible to visualize various cell functions in a versatile imaging system. The present study demonstrates the feasibility of cGNS$_{\text{MB}}$ imaging system to visualize the apoptosis in 3D cell aggregates, especially the localization of apoptotic position without the destruction of aggregates. As the limitation of this study, the apoptosis in cell aggregates was visualized as the end-point assay. Further study should be performed to trace the time-course of Fas Ab penetration and the consequent apoptosis in the cell aggregates. On the other hand, the intracellular controlled release of MB from the cGNS (Chapter 3) and biodegradable poly(lactic-co-glycolic acid) (PLGA) nanoparticles [38] achieved the continuous and long-term detection of target mRNA. The time-course tracing of cell functions in the same cell and aggregate is quite important in the biological and biomedical research fields. In the near future, in addition to the apoptosis, various cell functions in the 3D environments will be continuously visualized for a long time period based on the intracellular controlled release of MB.

REFERENCES

1. Griffith LG, Swartz MA. Capturing complex 3D tissue physiology in vitro. *Nat Rev Mol Cell Biol* 2006; **7**: 211-224.
2. Baker BM, Chen CS. Deconstructing the third dimension: how 3D culture microenvironments alter cellular cues. *J Cell Sci* 2012; **125**: 3015-3024.
3. Bhang SH, Lee S, Shin JY, Lee TJ, Kim BS. Transplantation of cord blood mesenchymal stem cells as spheroids enhances vascularization. *Tissue Eng Part A* 2012; **18**: 2138-2147.
4. Zhang S, Liu P, Chen L, Wang Y, Wang Z, Zhang B. The effects of spheroid formation of adipose-derived stem cells in a microgravity bioreactor on stemness properties and therapeutic potential. *Biomaterials* 2015; **41**: 15-25.
5. Cesarz Z, Tamama K. Spheroid Culture of Mesenchymal Stem Cells. *Stem Cells Int* 2016; **2016**: 9176357.
6. Follin B, Juhl M, Cohen S, Pedersen AE, Kastrup J, Ekblond A. Increased Paracrine Immunomodulatory Potential of Mesenchymal Stromal Cells in Three-Dimensional Culture. *Tissue Eng Part B Rev* 2016; **22**: 322-329.
7. Petrenko Y, Sykova E, Kubinova S. The therapeutic potential of three-dimensional multipotent mesenchymal stromal cell spheroids. *Stem Cell Res Ther* 2017; **8**: 94.
8. Hyun JS, Tran MC, Wong VW, Chung MT, Lo DD, Montoro DT *et al.* Enhancing stem cell survival in vivo for tissue repair. *Biotechnol Adv* 2013; **31**: 736-743.
9. Zanoni M, Piccinini F, Arienti C, Zamagni A, Santi S, Polico R *et al.* 3D tumor spheroid models for in vitro therapeutic screening: a systematic approach to enhance the biological relevance of data obtained. *Sci Rep* 2016; **6**: 19103.
10. Dutta D, Heo I, Clevers H. Disease Modeling in Stem Cell-Derived 3D Organoid Systems. *Trends Mol Med* 2017; **23**: 393-410.
11. Zhang X, Hu MG, Pan K, Li CH, Liu R. 3D Spheroid Culture Enhances the Expression of Antifibrotic Factors in Human Adipose-Derived MSCs and Improves Their Therapeutic Effects on Hepatic Fibrosis. *Stem Cells Int* 2016; **2016**: 4626073.
12. Peter ME, Krammer PH. The CD95(APO-1/Fas) DISC and beyond. *Cell Death Differ* 2003; **10**: 26-35.

13. Snyder SL, Sobocinski PZ. An improved 2,4,6-trinitrobenzenesulfonic acid method for the determination of amines. *Anal Biochem* 1975; **64**: 284-288.

14. Park MA, Pejovic V, Kerisit KG, Junius S, Thoene JG. Increased apoptosis in cystinotic fibroblasts and renal proximal tubule epithelial cells results from cysteinylation of protein kinase Cδ. *J Am Soc Nephrol* 2006; **17**: 3167-3175.

15. Liu W, Jing ZT, Xue CR, Wu SX, Chen WN, Lin XJ *et al.* PI3K/AKT inhibitors aggravate death receptor-mediated hepatocyte apoptosis and liver injury. *Toxicol Appl Pharmacol* 2019; **381**: 114729.

16. Walton MI, Whysong D, O'Connor PM, Hockenbery D, Korsmeyer SJ, Kohn KW. Constitutive expression of human Bcl-2 modulates nitrogen mustard and camptothecin induced apoptosis. *Cancer Res* 1993; **53**: 1853-1861.

17. Pommier Y. Topoisomerase I inhibitors: camptothecins and beyond. *Nat Rev Cancer* 2006; **6**: 789-802.

18. Pommier Y, Barcelo JM, Rao VA, Sordet O, Jobson AG, Thibaut L *et al.* Repair of topoisomerase I-mediated DNA damage. *Prog Nucleic Acid Res Mol Biol* 2006; **81**: 179-229.

19. Tanei T, Pradipta AR, Morimoto K, Fujii M, Arata M, Ito A *et al.* Cascade Reaction in Human Live Tissue Allows Clinically Applicable Diagnosis of Breast Cancer Morphology. *Adv Sci* 2019; **6**: 1801479.

20. Vermes I, Haanen C, Steffens-Nakken H, Reutelingsperger C. A novel assay for apoptosis. Flow cytometric detection of phosphatidylserine expression on early apoptotic cells using fluorescein labelled Annexin V. *J Immunol Methods* 1995; **184**: 39-51.

21. Aoyama T, Takemura G, Maruyama R, Kosai K, Takahashi T, Koda M *et al.* Molecular mechanisms of non-apoptosis by Fas stimulation alone versus apoptosis with an additional actinomycin D in cultured cardiomyocytes. *Cardiovasc Res* 2002; **55**: 787-798.

22. Zhang J, Cado D, Chen A, Kabra NH, Winoto A. Fas-mediated apoptosis and activation-induced T-cell proliferation are defective in mice lacking FADD/Mort1. *Nature* 1998; **392**: 296-300.

23. Forster A, Falcone FH, Gibbs BF, Preussner LM, Fiebig BS, Altunok H *et al.* Anti-Fas/CD95 and tumor necrosis factor-related apoptosis-inducing ligand (TRAIL) differentially regulate apoptosis in normal and neoplastic human basophils. *Leuk Lymphoma* 2013; **54**: 835-842.

24. Elmore S. Apoptosis: a review of programmed cell death. *Toxicol Pathol* 2007; **35**: 495-516.

25. Hayashi K, Tabata Y. Preparation of stem cell aggregates with gelatin microspheres to enhance biological functions. *Acta Biomater* 2011; **7**: 2797-2803.

26. Ma HL, Jiang Q, Han S, Wu Y, Cui Tomshine J, Wang D *et al.* Multicellular tumor spheroids as an in vivo-like tumor model for three-dimensional imaging of chemotherapeutic and nano material cellular penetration. *Mol Imaging* 2012; **11**: 487-498.

27. Jarockyte G, Dapkute D, Karabanovas V, Daugmaudis JV, Ivanauskas F, Rotomskis R. 3D cellular spheroids as tools for understanding carboxylated quantum dot behavior in tumors. *Biochim Biophys Acta Gen Subj* 2018; **1862**: 914-923.

28. Chen CC, Ku MC, D MJ, Lai JS, Hueng DY, Chang C. Simple SPION incubation as an efficient intracellular labeling method for tracking neural progenitor cells using MRI. *PLoS One* 2013; **8**: e56125.

29. Du V, Luciani N, Richard S, Mary G, Gay C, Mazuel F *et al.* A 3D magnetic tissue stretcher for remote mechanical control of embryonic stem cell differentiation. *Nat Commun* 2017; **8**: 400.

30. Mazza M, Lozano N, Vieira DB, Buggio M, Kielty C, Kostarelos K. Liposome-Indocyanine Green Nanoprobes for Optical Labeling and Tracking of Human Mesenchymal Stem Cells Post-Transplantation In Vivo. *Adv Healthc Mater* 2017; **6**: 1700374.

31. Kellner K, Liebsch G, Klimant I, Wolfbeis OS, Blunk T, Schulz MB *et al.* Determination of oxygen gradients in engineered tissue using a fluorescent sensor. *Biotechnol Bioeng* 2002; **80**: 73-83.

32. Malda J, Klein TJ, Upton Z. The roles of hypoxia in the in vitro engineering of tissues.

Tissue Eng 2007; **13**: 2153-2162.

33. Glicklis R, Merchuk JC, Cohen S. Modeling mass transfer in hepatocyte spheroids via cell viability, spheroid size, and hepatocellular functions. *Biotechnol Bioeng* 2004; **86**: 672-680.

34. Curcio E, Salerno S, Barbieri G, De Bartolo L, Drioli E, Bader A. Mass transfer and metabolic reactions in hepatocyte spheroids cultured in rotating wall gas-permeable membrane system. *Biomaterials* 2007; **28**: 5487-5497.

35. Tan YH, Liu M, Nolting B, Go JG, Gervay-Hague J, Liu GY. A nanoengineering approach for investigation and regulation of protein immobilization. *ACS Nano* 2008; **2**: 2374-2384.

36. Ingargiola M, Runge R, Heldt JM, Freudenberg R, Steinbach J, Cordes N *et al.* Potential of a Cetuximab-based radioimmunotherapy combined with external irradiation manifests in a 3-D cell assay. *Int J Cancer* 2014; **135**: 968-980.

37. Gong X, Lin C, Cheng J, Su J, Zhao H, Liu T *et al.* Generation of Multicellular Tumor Spheroids with Microwell-Based Agarose Scaffolds for Drug Testing. *PLoS One* 2015; **10**: e0130348.

38. Wiraja C, Yeo DC, Chong MS, Xu C. Nanosensors for Continuous and Noninvasive Monitoring of Mesenchymal Stem Cell Osteogenic Differentiation. *Small* 2016; **12**: 1342-1350.

SUMMARY

Chapter 1.

The objective of this chapter is to prepare a multimodal imaging probe which can simultaneously visualize cells by fluorescent and MR imaging modalities. Various types of GNS, such as empty GNS, GNS_{QD}, GNS_{IONP}, and $GNS_{QD+IONP}$, were prepared by the conventional emulsion method. The apparent size and percentage of QD and IONP incorporated in GNS_{QD} and GNS_{IONP}, respectively, were changed by the concentration of gelatin used. At the same gelatin concentration in the $GNS_{QD+IONP}$ preparation, the apparent size and zeta potential of $GNS_{QD+IONP}$ were not affected by the GA concentration. On the other hand, the percentage of QD incorporated in $GNS_{QD+IONP}$ tended to decrease as the GA concentration increased, whereas that of IONP was constant. In terms of the efficient QD and IONP incorporation, as well as the apparent size suitable for cell internalization, $GNS_{QD+IONP}$ prepared at 5.0 mg/ml of gelatin and 0.5 wt% of GA were used in the cell imaging experiments. When $GNS_{QD+IONP}$ were treated with R8 of a CPP and incubated with human articular chondrocytes, $GNS_{QD+IONP}$ were efficiently internalized into the cells although their cytotoxicity was observed at the R8 concentration of 320 μM. The cells internalizing $GNS_{QD+IONP}$ could be visualized by both fluorescent and MR imaging modalities. It is concluded that the $GNS_{QD+IONP}$ are promising for the probe of multimodal cell imaging.

Chapter 2.

The objective of this chapter is to prepare cationized gelatin-MB complexes for the visualization of intracellular mRNA. The complexes were prepared from spermine-introduced cationized gelatins with different extents of cationization and different mixing ratios of MB to cationized gelatin. The apparent size of complexes was almost similar, while the zeta potential was different among the complexes. Irrespective of the preparation conditions, the complexes had a sequence specificity against the target oligonucleotides in hybridization. Upon incubating mouse bone marrow-derived MSC with complexes, the cell viability was low for the complexes prepared with a high cationic extent at a low mixing ratio. On the other hand, the amount of

MB internalized depended on the type of complexes and the mixing ratio. The highest fluorescent intensity of MB in cells was observed for the SM50 complex prepared at a medium mixing ratio. This can be explained by the balance between the cytotoxicity and the amount of MB internalized into cells. Taking the balance into consideration, the SM50 complex prepared with the mixing ratio at 20 pmole MB/μg cationized gelatin was the most effective to visualize the GAPDH mRNA endogenously present. In addition, the EGFP mRNA exogenously transfected was also detected by this complex system. It is concluded that both the endogenous and exogenous mRNA can be visualized in living cells by making use of cationized gelatin-MB complexes designed.

Chapter 3.

The objective of this chapter is to prepare cationized gelatin-MB complexes and $\mathrm{cGNS_{MB}}$, and evaluate the time period of mRNA visualization. The cGNS with different degradabilities were prepared by changing the amount of GA to incorporate the MB for GAPDH mRNA. There was no difference in the apparent size and zeta potential between the complexes and the $\mathrm{cGNS_{MB}}$, while the MB release from the complexes was faster than that from the $\mathrm{cGNS_{MB}}$. When mouse bone marrow-derived MSC were incubated with the complexes and $\mathrm{cGNS_{MB}}$, the amount of MB internalized into cells and cytotoxicity of complexes was higher than those of $\mathrm{cGNS_{MB}}$. However, in the amount range of non-cytotoxicity, the amount of MB internalized was at a similar level among them. The complexes and $\mathrm{cGNS_{MB}}$ were readily internalized into the cells via an endocytotic pathway, but not co-localized with lysosomes. The intracellular fluorescence of $\mathrm{cGNS_{MB}}$ was observed over 14 days, whereas that of complexes disappeared within 5 days. This is because the intracellular decrease of $\mathrm{cGNS_{MB}}$ was slower than that of complexes. In addition, the time period of $\mathrm{cGNS_{MB}}$ remaining in the cells prolonged with the increase of GA amount used in $\mathrm{cGNS_{MB}}$ preparation. As the result, it is likely that the intracellular fluorescence was retained at a high level for longer time periods. It is concluded that the $\mathrm{cGNS_{MB}}$ are a promising system to achieve the intracellular controlled release of MB for the long-term and continuous visualization of mRNA.

Chapter 4.

The objective of this chapter is to visualize the proliferation ability of cells based on the $cGNS_{MB}$ imaging system. Two types of MB to detect mRNA were used. One is a Ki67 MB of a target for cell proliferation ability. The other one is a GAPDH MB as a control of stable fluorescence in cells. The cGNS incorporating Ki67 MB and GAPDH MB ($cGNS_{Ki67\ MB}$ and $cGNS_{GAP\ MB}$) were prepared, respectively. There was no difference in the physicochemical properties and the cell internalization between the $cGNS_{Ki67\ MB}$ and $cGNS_{GAP\ MB}$. When bFGF was added to mouse bone marrow-derived MSC, the mRNA and protein expression of Ki67 increased as the increase of bFGF concentration, and the level was saturated over 20 ng/ml. In addition, the cell proliferation was significantly accelerated by the bFGF addition. After the incubation for the cell internalization of $cGNS_{MB}$, the cells were further incubated for 24 hr with or without different concentrations of bFGF. The fluorescent intensity of $cGNS_{Ki67\ MB}$ significantly increased in response to the concentration of bFGF added, whereas that of $cGNS_{GAP\ MB}$ was constant, irrespective of the bFGF concentration. The fluorescent increase of $cGNS_{Ki67\ MB}$ well corresponded to the mRNA expression of Ki67. A timelapse imaging assay revealed that a fast enhancement of $cGNS_{Ki67\ MB}$ fluorescence after the bFGF addition compared with no bFGF addition. On the other hand, the constant fluorescence of $cGNS_{GAP\ MB}$ was observed even at any time point after the bFGF addition. Moreover, the $cGNS_{GAP\ MB}$ fluorescence was maintained at an almost same level over the cell division. It is concluded that the $cGNS_{MB}$ are a promising system for the chronological visualization of proliferation ability in living cells.

Chapter 5.

The objective of this chapter is to visualize the cell apoptosis based on the $cGNS_{MB}$ imaging system. Two types of MB to detect mRNA of caspase-3 as a target for cell apoptosis and GAPDH MB were incorporated in cGNS, respectively ($cGNS_{casp3\ MB}$ and $cGNS_{GAP\ MB}$). The apparent size of $cGNS_{MB}$ increased, whereas the zeta potential tended to decrease as the amount of MB added. Since the $cGNS_{MB}$ have a positive surface charge and a small size of 200 nm suitable for cell internalization, the $cGNS_{MB}$ prepared at the ratio of 20 pmole MB/μg cGNS were selected, although the MB amount increased with an increase in the MB/cGNS ratio. There was no difference in the physicochemical properties between $\mathrm{cGNS}_{\mathrm{casp3\ MB}}$ and $\mathrm{cGNS}_{\mathrm{GAP\ MB}}$. A hybridization assay revealed that both the caspase-3 and GAPDH MB incorporated in cGNS showed the sequence specificity against the target oligonucleotides. In addition, the cGNS incorporation enabled MB to enhance the stability against nuclease to a significantly great extent compared with free MB. The $\mathrm{cGNS}_{\mathrm{GAP\ MB}}$ were internalized into the mouse bone marrow-derived MSC by an endocytotic pathway, and were not distributed at the lysosomes. After the incubation with $\mathrm{cGNS}_{\mathrm{MB}}$, the cell apoptosis was induced at different concentrations of camptothecin. The fluorescence of cells incubated with $\mathrm{cGNS}_{\mathrm{GAP\ MB}}$ was constant at any camptothecin concentration. On the other hand, the fluorescence of cells incubated with $\mathrm{cGNS}_{\mathrm{casp3\ MB}}$ was significantly increased after the addition of camptothecin. When compared with the conventional apoptosis analysis of annexin V / PI staining, $\mathrm{cGNS}_{\mathrm{MB}}$ enabled the apoptosis detection in the earlier stage at the lower concentrations of camptothecin. It is concluded that the $\mathrm{cGNS}_{\mathrm{MB}}$ are a promising system for the visualization of cell apoptosis.

Chapter 6.

The objective of this chapter is to develop a $\mathrm{cGNS}_{\mathrm{MB}}$ imaging system to visualize the energy metabolic pathways of cells aiming at visual discrimination of differentiation state. PDK1 and PGC-1α are key regulators in the balance between glycolysis and OXPHOS. MB for the mRNA of PDK1 and PGC-1α, as well as Actb of a constant expressing gene, were designed to be incorporated in cGNS. The $\mathrm{cGNS}_{\mathrm{MB}}$ prepared were efficiently internalized into mES cells without modifying their pluripotency. The PDK1 was significantly upregulated in the undifferentiated cells, and the resulting phosphorylation of PDH was maintained in a high level. On the other hand, the expression of PGC-1α significantly increased as the spontaneous early differentiation by the depletion of LIF, as well as the lineage-specific neural differentiation. The analysis of metabolic profile by the measurements of ECAR and OCR revealed that the undifferentiated cells showed an enhanced glycolytic profile. In contrast, the OXPHOS profile increased as the early and neural differentiations were induced. For the $\mathrm{cGNS}_{\mathrm{MB}}$ imaging, the intense fluorescence of $\mathrm{cGNS}_{\mathrm{PDK1\ MB}}$ was detected for the undifferentiated cells. On the contrary, the fluorescence of $\mathrm{cGNS}_{\mathrm{PGC\text{-}1\alpha\ MB}}$ significantly increased by the induction of early and neural differentiations, while the $\mathrm{cGNS}_{\mathrm{Actb\ MB}}$ fluorescence was similarly observed for both the undifferentiated and differentiated cells. The fluorescence of MB showed a good accordance with the metabolic profiles of undifferentiated and differentiated cells evaluated by the change of ECAR and OCR values. When the multi-color imaging with $\mathrm{cGNS}_{\mathrm{multi\ MB}}$ was performed, the intense fluorescence of PDK1 MB was homogenously observed for the undifferentiated cells. On the other hand, for the neural differentiation-induced cells, some fluorescence of PDK1 MB was observed around the intense PGC-1α MB fluorescence. The multi-color imaging showed the potential to visualize the heterogeneous metabolic pathways in the same cell population. It is concluded that the $\mathrm{cGNS}_{\mathrm{MB}}$ imaging system is a promising tool to visually discriminate the differentiation state of cells from energy metabolic pathways.

Chapter 7.

The objective of this chapter is to develop the labeling method of human iPS cells-derived 3D cartilage tissue with $\mathrm{GNS}_{\mathrm{3QD+IONP}}$. To label the 3D cartilage tissue, two labeling approaches, *i.e.* “direct labeling method” and “dissociation and labeling method”, were tried. In the “direct labeling method”, a cartilage tissue was labeled directly by incubating with R8-treated $\mathrm{GNS}_{\mathrm{3QD+IONP}}$. However, in this case, only cells residing in the surrounding site of cartilage tissue were labeled. This is due to the poor penetration of $\mathrm{GNS}_{\mathrm{3QD+IONP}}$ to the interior of tissue. On the other hand, for the “dissociation and labeling method”, the cartilage tissue was enzymatically dissociated to cells in a single dispersed state by the trypsin and collagenase treatments. Then, the R8-$\mathrm{GNS}_{\mathrm{3QD+IONP}}$ were efficiently internalized into the monolayer cells dissociated from the cartilage tissue. Finally, the cells labeled were fabricated to 3D pellets or cell sheets. As the results, the 3D cartilage pellets and the cell sheets were homogenously labeled, and maintained fluorescently visualized over 4 weeks for all wavelength of QD. In addition, the cartilage properties were histologically detected even after the process of dissociation and labeling. It is concluded that the homogenous labeling and visualization of human iPS cells-derived 3D cartilage tissue was achieved by the dissociation and labeling method with $\mathrm{GNS}_{\mathrm{3QD+IONP}}$.

Chapter 8.

The objective of this chapter is to visualize the cell apoptosis in 3D cell aggregates based on the $cGNS_{MB}$ imaging system. The cGNS incorporating caspase-3 and GAPDH MB ($cGNS_{casp3\ MB}$ and $cGNS_{GAP\ MB}$, respectively) were prepared. In addition, cGNS co-incorporating caspase-3 and GAPDH MB ($cGNS_{dual\ MB}$) were prepared to perform the dual-color imaging for the same aggregate. The $cGNS_{MB}$ were incubated with mouse bone marrow-derived MSC to label with MB in the 2D culture, and the Fas-mediated apoptosis was induced by the addition of Fas Ab and Act D. The fluorescence of $cGNS_{casp3\ MB}$ significantly enhanced with the apoptosis induction, whereas that of $cGNS_{GAP\ MB}$ was constant, irrespective of the cell apoptosis. Moreover, the apoptosis was ratiometrically detected by the $cGNS_{dual\ MB}$ to the same extent as single MB. The cell aggregates were prepared from MB-labeled cells, and the MB fluorescence was detected from almost all of the cells even in the 3D aggregates to show the homogenous distribution. In addition to the Fas-mediated apoptosis, the aggregates were treated with camptothecin of a low-molecular weight apoptosis inducer. The fluorescence of caspase-3 MB was mainly distributed at the surface surrounding site of Fas-mediated apoptotic aggregates rather than the center site, while that of GAPDH MB was detected even in the interior site. On the other hand, in the camptothecin-induced apoptotic aggregates, both caspae-3 and GAPDH MB fluorescence emission were detected from the interior site of aggregates as well as the surrounding site. It is likely that the MB fluorescence reflected the localization of apoptotic position caused by the different molecular sizes of apoptosis inducer and the consequent penetration into the aggregates. It is concluded that the $cGMS_{MB}$ are a promising system to visualize cell apoptosis in 3D cell aggregates without the destruction of aggregates.

LIST OF PUBLICATIONS

Chapter 1.

Yuki Murata, Jun-ichiro Jo, and Yasuhiko Tabata. Preparation of gelatin nanospheres incorporating quantum dots and iron oxide nanoparticles for multimodal cell imaging. *Journal of Biomaterials Science, Polymer Edition*, **28**(6), 555-568, 2017.

Chapter 2.

Sho Takehana, **Yuki Murata**, Jun-ichiro Jo, and Yasuhiko Tabata. Complexation design of cationized gelatin and molecular beacon to visualize intracellular mRNA. *PLOS ONE*, in press.

Chapter 3.

Yuki Murata, Jun-ichiro Jo, and Yasuhiko Tabata. Intracellular Controlled Release of Molecular Beacon Prolongs the Time Period of mRNA Visualization. *Tissue Engineering Part A*, **25**(21-22), 1527-1537, 2019.

Chapter 4.

Yuki Murata, Jun-ichiro Jo, and Yasuhiko Tabata. Molecular Beacon Imaging to Visualize Ki67 mRNA for Cell Proliferation Ability. *Tissue Engineering Part A*, in press.

Chapter 5.

Yuki Murata, Jun-ichiro Jo, and Yasuhiko Tabata. Preparation of cationized gelatin nanospheres incorporating molecular beacon to visualize cell apoptosis. *Scientific Reports*, **8**, 14839, 2018.

Chapter 6.

Yuki Murata, Jun-ichiro Jo, and Yasuhiko Tabata. A molecular beacon imaging system to discriminate the differentiation state of cells from energy metabolic pathways, submitted.

Chapter 7.

Yuki Murata, Jun-ichiro Jo, Hiroshi Yukawa, Noriyuki Tsumaki, Yoshinobu Baba, and Yasuhiko Tabata. Visualization of Human Induced Pluripotent Stem Cells-Derived Three-Dimensional Cartilage Tissue by Gelatin Nanospheres. *Tissue Engineering Part C: Methods*, **26**(5), 244-252, 2020.

Chapter 8.

Yuki Murata, Jun-ichiro Jo, and Yasuhiko Tabata. Visualization of apoptosis in three-dimensional cell aggregates based on molecular beacon imaging, submitted.

OTHER PUBLICATIONS

Hideki Maeda, Daisuke Kami, Ryotaro Maeda, **Yuki Murata**, Jun-ichiro Jo, Tomoya Kitani, Yasuhiko Tabata, Satoaki Matoba, and Satoshi Gojo. TAT-dextran–mediated mitochondrial transfer enhances recovery from models of reperfusion injury in cultured cardiomyocytes. *Journal of Cellular and Molecular Medicine*, **24**(9), 5007-5020, 2020.

ACKNOWLEDGEMENTS

This research was carried out under the guidance of Dr. Yasuhiko Tabata, Professor of Institute for Frontier Life and Medical Sciences, Kyoto University, Japan. The author is deeply indebted to Professor Yasuhiko Tabata for his constant guidance, encouragement, valuable discussion, informative advice, and rational criticism on the manuscript as well as experiments. Professor Tabata gave the author an opportunity to perform experiments, present in societies, publish papers, and especially study for the degree of Ph. D. The author has learned a lot of invaluable things under his great mentorship. The completion of the present research has been an exciting project and one which would not have been realized without his guidance.

To the committee members of this thesis, Professor Kazunari Akiyoshi and Professor Keiji Numata, Graduate School of Engineering, Kyoto University, the author is grateful and deeply appreciated the time they took out of their busy schedule to discuss the present research.

The author wishes to express his special thanks to Dr. Masaya Yamamoto, Professor of Graduate School of Engineering, Tohoku University, Japan, and Dr. Jun-ichiro Jo, Assistant Professor of Institute for Frontier Life and Medical Sciences, Kyoto University, for their thoughtful guidance, encouragement, cooperation, valuable advice and discussion, and their great help for preparation of this manuscript. The author has been professionally and personally supported by their kindness, and greatly motivated through the discussion from various perspectives.

The author wishes to his deeply thanks to Dr. Yoshinobu Baba and Dr. Hiroshi Yukawa, Professor and Designated Associate Professor of Institute of Nano-Life-Systems, Institutes of Innovation for Future Society, Nagoya University, Japan, and Dr. Noriyuki Tsumaki, Professor of Center for iPS Cell Research and Application, Kyoto University, Japan, for their cooperation, advice, and discussion in Chapter 7 of this manuscript.

The author wishes to express his thanks to Ms. Nami Yoshioka, Ms. Chiaki Okada, and Ms. Kaori Takahashi, Secretary to Professor Yasuhiko Tabata and other members and collaborators of Professor Tabata’s Laboratory for their help and kindness.

Finally, the author is deeply indebted to his wife, Yukino, and his parents, Masami and Emi, for their constant support and warm encouragement.

November, 2020

Kyoto

Yuki Murata